

Through Iron & Ice: Searching for Sterile Neutrinos at the IceCube Neutrino Observatory

by

Alejandro Diaz

B.A., University of Chicago (2016)

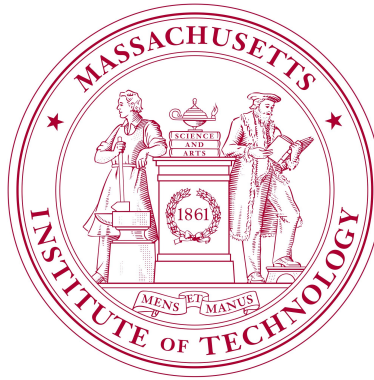
Submitted to the Department of Physics
in partial fulfillment of the requirements for the degree of

Doctor of Philosophy

at the

MASSACHUSETTS INSTITUTE OF TECHNOLOGY

February 2023



© Massachusetts Institute of Technology 2023. All rights reserved.

Author
Department of Physics
September 30, 2022

Certified by
Janet M. Conrad
Professor of Physics
Thesis Supervisor

Accepted by
Lindley Winslow
Associate Department Head of Physics

arXiv:2210.09418v1 [hep-ex] 17 Oct 2022

Through Iron & Ice: Searching for Sterile Neutrinos at the IceCube Neutrino Observatory

by
Alejandro Diaz

Submitted to the Department of Physics
on September 30, 2022, in partial fulfillment of the
requirements for the degree of
Doctor of Philosophy

Abstract

Despite the rapid progression in our understanding of neutrinos over the last half century, much is left unknown about their properties. This leaves neutrinos as the most promising portal for Beyond Standard Model (BSM) physics, and neutrinos have already provided fruitful surprises.

A number of neutrino experiments in the last three decades have observed anomalous oscillation signals consistent with a mass-squared splitting of $\Delta m^2 \sim 1 \text{ eV}^2$, motivating the existence and search for sterile neutrinos. On the other hand, other experiments have failed to see such a signal.

In this thesis, we present two analyses. The first is an update to the sterile neutrino global fits with the inclusion of recent experimental data. We find that the 3+1 model provides a better fit to the global data set compared to the null, with an improvement of $\Delta\chi^2 = 51$ with the addition of only 3 degrees of freedom, corresponding to 6.6σ . While a substantial improvement, we also find a irreconcilable tension between the data sets of 5.1σ , calculated using the parameter goodness-of-fit test. This motivates the exploration of expanded models: a 3+2 model, and a 3+1+Decay model. In the 3+2 model, we find negligible improvement to the fit, and an even worse tension of 5.5σ . In the more exotic 3+1+Decay model, we find the tension reduced to 3.6σ . While a substantial improvement compared to the 3+1 model with the introduction of only one additional parameter, the tension is still too large to assuage concerns.

The second analysis is the results of an expanded IceCube sterile neutrino search. A previous sterile neutrino search found no evidence for sterile neutrinos, finding a p-value of 8%. Of the three sterile mixing angles, θ_{14} , θ_{24} , and θ_{34} , only θ_{24} was fitted for, as θ_{14} was negligible and $\theta_{34} = 0$ was considered a conservative assumption. We present results of an analysis where we include θ_{34} to the fitted model. Both a frequentist and Bayesian analysis were conducted, with fits done in terms of the mass-squared splitting Δm_{41}^2 and the mixing matrix parameters $|U_{\mu 4}|^2$ and $|U_{\tau 4}|^2$. The frequentist analysis finds a best fit at $\Delta m_{41}^2 = 5.0 \text{ eV}^2$, $|U_{\mu 4}|^2 = 0.04$, and $|U_{\tau 4}|^2 = 0.006$, with a p-value of 5.2% assuming Wilks' Theorem with 3 degrees of freedom. Pseudoexperiments are indicating a smaller p-value 2.7%. The Bayesian analysis finds a similar best fit point at $\Delta m_{41}^2 = 5.0 \text{ eV}^2$, $|U_{\mu 4}|^2 = 0.02$, and $|U_{\tau 4}|^2 = 0.006$, with a Bayes factor indicating a "Very Strong" preference for this sterile hypothesis over the null hypothesis.

Thesis Supervisor: Janet M. Conrad
Title: Professor of Physics

Acknowledgments

It's impossible to properly acknowledge and thank everyone who has had an impact on me over the last six years, but I will try.

First, I have to thank my advisor, Professor Janet Conrad. An omnipotent force, Janet has guided me through the maze of neutrino physics with an uncanny intuition towards the profound and interesting. The scientist I am today would not have existed without Janet's hard work and dedication to my success. Thank you, Janet, for having reached out to me after I submitted my application to MIT.

Along with Janet, any success of mine must be shared with the whole of the Conrad research group. The work in this thesis is truly the outcome of a collaborative effort amongst this formidable group of up-and-coming scientists.

To the postdocs, Carlos Argüelles, Daniel Winklehner, Taritree Wongjirad, Adrien Hourlier, David Vannerom, Austin Schneider, and John Hardin: while only a few years stand between myself and them, their knowledge and experience feels decades ahead of mine. Beyond the physics, they have taught me what the life of an academic entails. In particular, I'd like to thank (now Professor) Carlos Argüelles. His first task as a postdoc with Janet was to talk to me as a prospective student; and I'm grateful, both professionally and personally, to have known him through my entire grad school career.

To Janet's grad students that I got to know well, Gabriel Collin, Spencer Axani, Jarrett Moon, Marjon Moulai, Lauren Yates, Loyd Waits, Joe Smolsky, and Nick Kamp: my relationship with each of you has been lopsided, having gained more from you than you did from me. Either in teaching me all the research know-how, or having the shared experience of stumbling through neutrino physics, I'm indebted to each of you.

To the younger grad students, Darcy Newmark and Philip Weigel: unfortunately, world-wide circumstances took away our chance to learn from each other. I only have one piece of wisdom: Don't work so hard, you're fine.

Outside of my research group, I've been blessed with a multitude of people that have ridden through MIT alongside me. To Field, Joe, Efrain, Cedric, Afro, Nick, Sangbaek, Francesco, and Dani: You know I hate to do things alone, and that includes struggling. Thank you for being there with me while we studied and cried, played board and video games, and explored bits of the world outside of Cambridge. To my roommate, Michael Calzadilla: thank you for the late-night company and the frequent trips for ice cream; I'm sorry for inflicting my social needy-ness onto you. To the Astro and LIGO boys and girls, Ben, Chris, Kaley, David, and Nick: thank you for soaking up the sun with me at Provincetown and Spectacle Island, and for taking spontaneous trips to Walden Pond and Iceland. Outside of MIT, I'd like to thank Chris Barnes and Adam Lister for keeping me sane in Fermilab. And to Alejandro Buendia, thank you for your support and comfort throughout the pain of the last year.

I'm lucky to have kept in touch with my closest friends from UChicago, and fortunate that many lived near where my research took me. I'm thankful to have spent Thanksgivings with Max, Tres, Brian, and Hunter, and celebrating a New Year with Jenni and Sal at Medieval Times. As I'm currently sitting on a plane to Los Angeles for the bachelor party, I'd like to wish Jenni and Sal a happy life together. I'd also like to thank Raul Zaldaña-Calles, for having to deal with me in my first years at MIT from a distance.

To those in my hometown of Miami, Lazaro Rodriguez, Brandon Castro, and Carlos Morales: thank you for maintaining our friendships, despite the months and years that pass between our hangouts.

I'd like to thank my family, my dad and sister (the real doctor in the family), for having supported and encouraged me throughout my entire academic career. I also need to thank my extended family in Colombia, for providing invaluable support especially over the last year.

Above and beyond, I have to thank my mother, Angela Maria. I adore her, and any success in my life should be attributed to her love, care, and unreasonable pride for me. I miss her dearly, *Te quiero*.

Contents

1	Neutrino Oscillations	9
1.1	Theory	9
1.2	Two Neutrinos	10
1.3	Three Neutrinos	12
1.3.1	Best Fit	12
1.4	Neutrino Oscillation in Matter	14
2	Anomalous Results & Sterile Neutrinos	17
2.1	Accelerator Source Neutrinos	17
2.1.1	LSND	17
2.1.2	MiniBooNE	18
2.2	Sterile Neutrino?	19
2.3	Reactor Neutrinos	20
2.4	Gallium Anomalies	21
2.5	Sterile Neutrino Models	23
2.5.1	3+1 Neutrinos	24
2.5.2	3+2 Model	25
2.5.3	3+1+Decay Model	27
3	MiniBooNE	31
	<i>Publication: Significant Excess of Electronlike Events in the MiniBooNE Short-Baseline Neutrino Experiment</i>	32
3.1	Current Results	39
4	Global Data Fits to Sterile Neutrino Models	41
4.1	Experiments	42
4.1.1	$P(\nu_\mu \rightarrow \nu_e)$ & $P(\bar{\nu}_\mu \rightarrow \bar{\nu}_e)$	42
4.1.2	$P(\nu_e \rightarrow \nu_e)$ & $P(\bar{\nu}_e \rightarrow \bar{\nu}_e)$	45
4.1.3	$P(\nu_\mu \rightarrow \nu_\mu)$ & $P(\bar{\nu}_\mu \rightarrow \bar{\nu}_\mu)$	56
4.2	Methodology	61
4.3	Results	64
4.3.1	3+1 Model	64
4.3.2	3+2 Model	68
4.3.3	3+1+Decay Model	70
4.4	Discussion	75

5	Summary of the Previous Sterile Neutrino Search in IceCube	77
5.1	IceCube in a Nutshell	77
5.2	Sterile-Induced Neutrino Oscillation in Matter	77
5.3	8-year Sterile Neutrino Search	79
5.3.1	ν_μ Flux	80
5.3.2	ν_μ Interactions Near the Detector	81
5.3.3	Results	82
6	MEOWS+θ_{34}	85
6.1	Oscillograms	85
6.2	Neutrino Sources	87
6.2.1	Atmospheric Neutrinos	87
6.2.2	Astrophysical Neutrinos	88
6.3	Neutrino Propagation Through the Earth	88
6.4	Neutrino Interactions Near the Detector	89
6.5	Muon Reconstruction	91
6.6	Event Selection	92
6.7	Systematic Parameters	94
6.7.1	Conventional Flux Parameters	95
6.7.2	Detector Parameters	96
6.7.3	Astrophysics Parameters	97
6.7.4	Cross Section Parameters	97
7	Analysis Procedure and Results	99
7.1	Physics Parameters	99
7.2	Binning & Likelihood	99
7.3	Frequentist Analysis	100
7.4	Bayesian Analysis	101
7.5	Sensitivity	102
7.6	Pre-Unblinding Checks	102
7.7	Results	104
7.7.1	Frequentist	104
7.7.2	Bayesian	112
7.8	Discussion	112
8	Conclusion	121
A	Specific Contributions	123
B	Neutrino Oscillations Derivation	125
C	MiniBooNE Supplementary Material	131

Chapter 1

Neutrino Oscillations

1.1 Theory

Let us consider neutrino oscillation in the case of N -neutrino mixing. In this discussion, we will denote the neutrino mass states with Latin subscripts (e.g. ν_i, ν_j), and the neutrino flavor states with Greek subscripts (e.g. ν_α, ν_β), unless otherwise stated. The neutrino mass states are related to the flavor states by the $N \times N$ matrix

$$\begin{pmatrix} \nu_\alpha \\ \nu_\beta \\ \vdots \end{pmatrix} = \begin{pmatrix} U_{\alpha 1} & U_{\alpha 2} & \cdots \\ U_{\beta 1} & U_{\beta 2} & \cdots \\ \vdots & & \ddots \end{pmatrix} \begin{pmatrix} \nu_1 \\ \nu_2 \\ \vdots \end{pmatrix}. \quad (1.1)$$

For now, we simply quote here the N -neutrino oscillation formula.

$$\begin{aligned} P(\nu_\alpha \rightarrow \nu_\beta) &= \delta_{\alpha\beta} - 4 \sum_{i < j} \Re(U_{\alpha i}^* U_{\beta i} U_{\alpha j} U_{\beta j}^*) \sin^2 \left(1.27 \Delta m_{ji}^2 [\text{eV}] \frac{L[\text{km}]}{E[\text{GeV}]} \right) \\ &\quad - 2 \sum_{i < j} \Im(U_{\alpha i}^* U_{\beta i} U_{\alpha j} U_{\beta j}^*) \sin \left(2.54 \Delta m_{ji}^2 [\text{eV}] \frac{L[\text{km}]}{E[\text{GeV}]} \right), \end{aligned} \quad (1.2)$$

where the mass-squared splitting $\Delta m_{ji}^2 = m_j^2 - m_i^2$. The notation “ $P(\nu_\alpha \rightarrow \nu_\beta)$ ” is understood as the probability that a neutrino of original flavor ν_α is later measured as ν_β . In the case that $\alpha \neq \beta$, “ $P(\nu_\alpha \rightarrow \nu_\beta)$ ” is referred to as an *appearance* probability, and an experiment that makes this kind of measurement is referred to as an appearance experiment. When $\alpha = \beta$, “ $P(\nu_\alpha \rightarrow \nu_\alpha)$ ” is referred to as a *disappearance* probability, and an experiment that makes this measurement is called a disappearance experiment.

In Equation (1.2), the mass-squared splitting Δm_{ji}^2 is in units of eV^2 , the neutrino energy E in GeV, and the distance L in kilometers. This is the standard in the neutrino community, and we will use these units unless otherwise stated. A complete derivation of Equation (1.2) is provided in Appendix B.

Let’s quickly note some CP-related properties of Equation (1.2). To get the CP conjugated oscillation equation $\hat{C}\hat{P}P(\nu_\alpha \rightarrow \nu_\beta) = P(\bar{\nu}_\alpha \rightarrow \bar{\nu}_\beta)$, we would simply replace each mixing matrix parameter with its complex conjugate $U \rightarrow U^*$. This results in flipping the

sign of the second line of Equation (1.2). Therefore, if the mixing matrix contains complex terms, $P(\nu_\alpha \rightarrow \nu_\beta) \neq P(\bar{\nu}_\alpha \rightarrow \bar{\nu}_\beta)$ and CP-symmetry is violated in the neutrino sector. An exception occurs when we consider $\nu_\beta = \nu_\alpha$ (disappearance). In that case, the term $U_{\alpha i}^* U_{\beta i} U_{\alpha j} U_{\beta j}^*$ becomes $|U_{\alpha i}|^2 |U_{\alpha j}|^2$, which is entirely real. Therefore $\Im(U_{\alpha i}^* U_{\beta i} U_{\alpha j} U_{\beta j}^*) = 0$ and Equation (1.2) does not change with the transformation $U \rightarrow U^*$. CP-violation in the lepton sector is thus not observable in disappearance experiments.

1.2 Two Neutrinos

As an example, it is useful to first consider the case where we have only two neutrinos mixing. We'll consider the weak eigenstates ν_e & ν_μ , and the two neutrino mass eigenstates ν_1 & ν_2 .

We write our mixing relationship as

$$\begin{pmatrix} \nu_e \\ \nu_\mu \end{pmatrix} = \begin{pmatrix} U_{e1} & U_{e2} \\ U_{\mu 1} & U_{\mu 2} \end{pmatrix} \begin{pmatrix} \nu_1 \\ \nu_2 \end{pmatrix}. \quad (1.3)$$

As we'll come to see, the mixing matrix is frequently written as a rotation matrix, with the matrix elements written in terms of some mixing "angle." In the two-neutrino case this is

$$\begin{pmatrix} \nu_e \\ \nu_\mu \end{pmatrix} = \begin{pmatrix} \cos \theta & \sin \theta \\ -\sin \theta & \cos \theta \end{pmatrix} \begin{pmatrix} \nu_1 \\ \nu_2 \end{pmatrix}, \quad (1.4)$$

where the mixing is parameterized by the single angle θ (the remaining degrees of freedom for the 2×2 unitary matrix can be absorbed into the definition of the neutrino states).

Reading off Equation (1.2) and using some trigonometric identities, we end up with the oscillation equations

$$P(\nu_e \rightarrow \nu_\mu) = \sin^2(2\theta) \sin^2 \left(1.27 \frac{\Delta m^2 L}{E} \right) \quad (1.5)$$

$$= P(\bar{\nu}_e \rightarrow \bar{\nu}_\mu) \quad (1.6)$$

$$= P(\nu_\mu \rightarrow \nu_e) \quad (1.7)$$

$$= P(\bar{\nu}_\mu \rightarrow \bar{\nu}_e) \quad (1.8)$$

$$P(\nu_e \rightarrow \nu_e) = 1 - \sin^2(2\theta) \sin^2 \left(1.27 \frac{\Delta m^2 L}{E} \right) \quad (1.9)$$

$$= P(\bar{\nu}_e \rightarrow \bar{\nu}_e) \quad (1.10)$$

$$= P(\nu_\mu \rightarrow \nu_\mu) \quad (1.11)$$

$$= P(\bar{\nu}_\mu \rightarrow \bar{\nu}_\mu). \quad (1.12)$$

Suppose that we have a 1 GeV ν_μ beam produced at some source, and we measure the flavor composition some distance L away. For the mixing parameters $\sin^2(2\theta) = 0.8$ and $\Delta m^2 = 1 \text{ eV}^2$, we would have an oscillation probability as a function of distance L as shown in Figure 1-1. In the figure, the oscillation amplitude is determined by $\sin^2(2\theta)$ and the

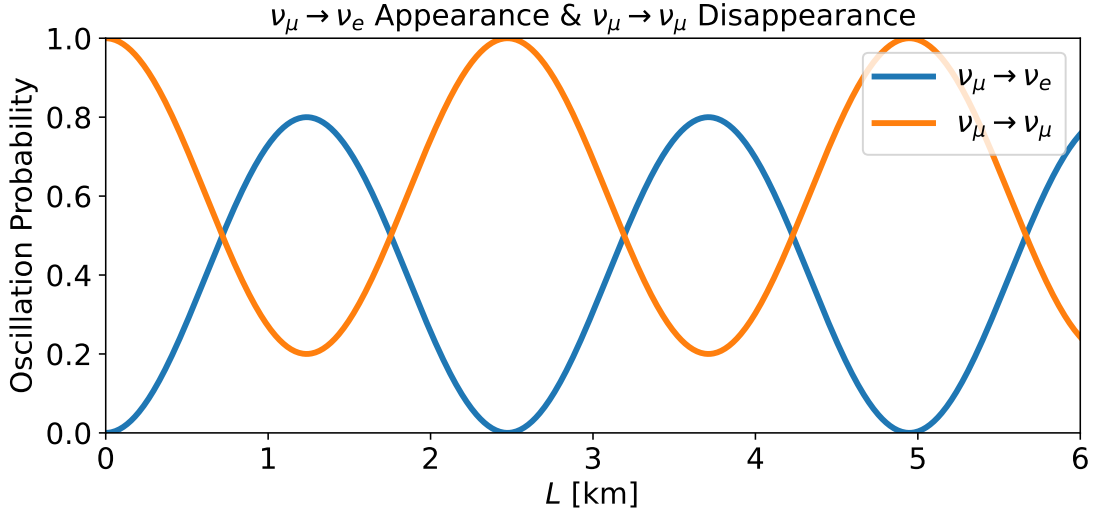


Figure 1-1: Appearance probability $P(\nu_\mu \rightarrow \nu_e)$ and disappearance probability $P(\nu_\mu \rightarrow \nu_\mu)$, as a function of baseline L , for a ν_μ beam of 1 GeV and oscillation parameters $\sin^2(2\theta) = 0.8$ and $\Delta m^2 = 1 \text{ eV}^2$.

frequency by Δm^2 .

It is convenient for us to define the *oscillation length*

$$L_o = \frac{\pi E}{1.27 \Delta m^2}, \quad (1.13)$$

which is the propagation distance over which a complete oscillation takes place. In Figure 1-1, this would be about 2.5 km.

The oscillation length also dictates the Δm^2 an experiment is sensitive to given an L and E ; or, alternatively, what L and E to choose given a known Δm^2 . In the example of Figure 1-1, where we assume to know Δm^2 and have a fixed E , we would like to place our detector at $L_o/2$ where the oscillation is at its maximum.

In practice, if a detector is placed $L \gg L_o$, then uncertainties in L and E (due to production and detection uncertainties) will cause the oscillation curves to average out, such that $\sin^2\left(1.27 \frac{\Delta m^2 L}{E}\right) \rightarrow 1/2$, and

$$P(\nu_\alpha \rightarrow \nu_\beta) = \frac{1}{2} \sin^2(2\theta) \quad \beta \neq \alpha \quad (1.14)$$

$$P(\nu_\alpha \rightarrow \nu_\alpha) = 1 - \frac{1}{2} \sin^2(2\theta). \quad (1.15)$$

In this case, the experiment will have no sensitivity to Δm^2 , only the mixing angle θ .

If, on the other hand, the detector is placed such that $L \ll L_o$, then the neutrinos will have propagated for too little distance (i.e. time) to have observably oscillated. Therefore, there is no sensitivity to any oscillation parameters.

While nature is known to have more than two neutrinos, the two-neutrino model is often

a valid approximation. For N neutrinos, there are oscillation lengths corresponding to each pair of Δm^2

$$L_{o_{ij}} = \frac{\pi E}{1.27 \Delta m_{ij}^2}. \quad (1.16)$$

If there exists a Δm^2 (or a set of degenerate Δm^2 s) that is much larger than the remaining Δm^2 s, then the corresponding oscillation length L_o^* would be much shorter than the remaining oscillation lengths \bar{L}_o^* s. If the detector is placed such that $L \sim L_o^* \ll \bar{L}_o^*$, then the detector would be sensitive only to the one larger Δm^2 , approximating two-neutrino oscillations.

1.3 Three Neutrinos

In the Standard Model (SM), there are three neutrinos, and therefore a 3×3 mixing matrix, called the Pontecorvo-Maki-Nakagawa-Sakata (PMNS) matrix.

$$\begin{pmatrix} \nu_e \\ \nu_\mu \\ \nu_\tau \end{pmatrix} = \begin{pmatrix} U_{e1} & U_{e2} & U_{e3} \\ U_{\mu1} & U_{\mu2} & U_{\mu3} \\ U_{\tau1} & U_{\tau2} & U_{\tau3} \end{pmatrix} \begin{pmatrix} \nu_1 \\ \nu_2 \\ \nu_3 \end{pmatrix}. \quad (1.17)$$

We will refer to Ref. [1] for the details of three neutrino oscillations. For now, we will only note that three neutrino oscillations, like two neutrino oscillations, is typically written in terms of unitary rotations. In this convention, the PMNS matrix is written as

$$U_{\text{PMNS}} = R^{23}(\theta_{23})R^{13}(\theta_{13}, \delta)R^{12}(\theta_{12}), \quad (1.18)$$

or,

$$\begin{pmatrix} U_{e1} & U_{e2} & U_{e3} \\ U_{\mu1} & U_{\mu2} & U_{\mu3} \\ U_{\tau1} & U_{\tau2} & U_{\tau3} \end{pmatrix} = \begin{pmatrix} 1 & 0 & 0 \\ 0 & c_{23} & s_{23} \\ 0 & -s_{23} & c_{23} \end{pmatrix} \begin{pmatrix} c_{13} & 0 & s_{13}e^{-i\delta} \\ 0 & 1 & 0 \\ -s_{13}e^{i\delta} & 0 & c_{13} \end{pmatrix} \begin{pmatrix} c_{12} & s_{12} & 0 \\ -s_{12} & c_{12} & 0 \\ 0 & 0 & 1 \end{pmatrix}, \quad (1.19)$$

where s_{ij} and c_{ij} is shorthand for $\sin \theta_{ij}$ and $\cos \theta_{ij}$ respectively.

In this model, there are 6 independent parameters, $\Delta m_{21}^2, \Delta m_{31}^2, \theta_{12}, \theta_{13}, \theta_{23}$, and δ .

1.3.1 Best Fit

Combined fits of the three neutrino model parameters are periodically conducted by the NuFit organization. The results of their most recent fit [2] are printed in Table 1.1.

With these parameters, NuFit finds the 3σ range of the mixing parameters to be

$$|U|_{3\sigma} = \begin{pmatrix} 0.801 \rightarrow 0.845 & 0.513 \rightarrow 0.579 & 0.143 \rightarrow 0.156 \\ 0.233 \rightarrow 0.507 & 0.461 \rightarrow 0.694 & 0.631 \rightarrow 0.778 \\ 0.261 \rightarrow 0.526 & 0.471 \rightarrow 0.701 & 0.611 \rightarrow 0.761 \end{pmatrix}. \quad (1.20)$$

A visualization of the mass-squared splittings and the mixing elements are shown in Figure 1-2.

	Normal Ordering (best fit)		Inverted Ordering ($\Delta\chi^2 = 2.7$)	
	bfp $\pm 1\sigma$	3σ range	bfp $\pm 1\sigma$	3σ range
$\sin^2 \theta_{12}$	$0.304^{+0.013}_{-0.012}$	$0.269 \rightarrow 0.343$	$0.304^{+0.013}_{-0.012}$	$0.269 \rightarrow 0.343$
$\theta_{12}/^\circ$	$33.44^{+0.78}_{-0.75}$	$31.27 \rightarrow 35.86$	$33.45^{+0.78}_{-0.75}$	$31.27 \rightarrow 35.87$
$\sin^2 \theta_{23}$	$0.570^{+0.018}_{-0.024}$	$0.407 \rightarrow 0.618$	$0.575^{+0.017}_{-0.021}$	$0.411 \rightarrow 0.621$
$\theta_{23}/^\circ$	$49.0^{+1.1}_{-1.4}$	$39.6 \rightarrow 51.8$	$49.3^{+1.0}_{-1.2}$	$39.9 \rightarrow 52.0$
$\sin^2 \theta_{13}$	$0.02221^{+0.00068}_{-0.00062}$	$0.02034 \rightarrow 0.02430$	$0.02240^{+0.00062}_{-0.00062}$	$0.02053 \rightarrow 0.02436$
$\theta_{13}/^\circ$	$8.57^{+0.13}_{-0.12}$	$8.20 \rightarrow 8.97$	$8.61^{+0.12}_{-0.12}$	$8.24 \rightarrow 8.98$
$\delta_{\text{CP}}/^\circ$	195^{+51}_{-25}	$107 \rightarrow 403$	286^{+27}_{-32}	$192 \rightarrow 360$
$\frac{\Delta m_{21}^2}{10^{-5} \text{ eV}^2}$	$7.42^{+0.21}_{-0.20}$	$6.82 \rightarrow 8.04$	$7.42^{+0.21}_{-0.20}$	$6.82 \rightarrow 8.04$
$\frac{\Delta m_{3\ell}^2}{10^{-3} \text{ eV}^2}$	$+2.514^{+0.028}_{-0.027}$	$+2.431 \rightarrow +2.598$	$-2.497^{+0.028}_{-0.028}$	$-2.583 \rightarrow -2.412$

Table 1.1: Best fit three-neutrino oscillation parameters as fitted by the NuFit group [2]. The first column gives the best fit values assuming normal ordering (i.e. $\Delta m_{31}^2 > 0$), while the second column gives the best fit values assuming inverted ordering (i.e. $\Delta m_{31}^2 < 0$).

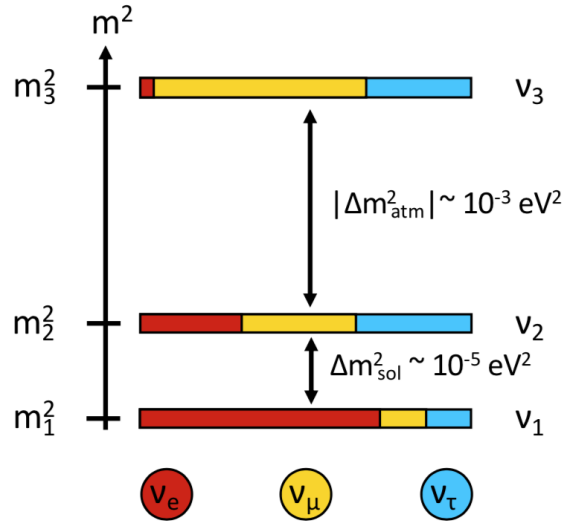


Figure 1-2: A visualization of the mass-squared splittings and mixing of the three neutrinos in the SM. Each horizontal bar corresponds to a neutrino mass state ν_i , where their spacing illustrates the mass squared differences (normal ordering, $\Delta m_{31}^2 > 0$, is assumed). The colors within each bar represents the content of the flavor eigenstates ν_α within each mass state. Figure taken from Ref. [3].

1.4 Neutrino Oscillation in Matter

In the preceding sections, we have described neutrinos oscillating specifically in a *vacuum*. In reality, neutrinos will propagate through matter, interacting with the particles it traverses. While all three SM neutrino types will experience neutral-current (NC) interactions, only electron neutrinos will experience charged-current (CC) interactions since matter contains free electrons but no free muons or taus. This will alter how the neutrinos will oscillate compared with how neutrinos oscillate through vacuum.

The following description follows Ref. [1]. In the flavor basis, the neutrino evolution equation can be written as

$$i \frac{d}{dx} \Psi_\alpha = \mathcal{H}_F \Psi_\alpha, \quad (1.21)$$

where time t usually found in the Schrödinger equation is replaced by x (due to the approximation that $x = t$, as done in Appendix B), Ψ_α is a column vector describing a neutrino state initially produced in the α state, and \mathcal{H}_F is the effective Hamiltonian in the flavor basis. In matter, \mathcal{H}_F is described by

$$\mathcal{H}_F = \frac{1}{2E} (U \mathbb{M}^2 U^\dagger + \mathbb{A}), \quad (1.22)$$

where, U is the neutrino mixing matrix. For three neutrinos,

$$\Psi_\alpha = \begin{pmatrix} \psi_{\alpha e} \\ \psi_{\alpha \mu} \\ \psi_{\alpha \tau} \end{pmatrix}, \quad \mathbb{M}^2 = \begin{pmatrix} 0 & 0 & 0 \\ 0 & \Delta m_{21}^2 & 0 \\ 0 & 0 & \Delta m_{31}^2 \end{pmatrix}, \quad \mathbb{A} = \begin{pmatrix} A_{CC} & 0 & 0 \\ 0 & 0 & 0 \\ 0 & 0 & 0 \end{pmatrix}, \quad (1.23)$$

with

$$A_{CC} \equiv 2EV_{CC} = 2\sqrt{2}EG_F N_e, \quad (1.24)$$

where G_F is the Fermi constant and N_e is the density of electrons in the propagation medium. NC interactions are ignored since all neutrino types would undergo NC interactions in matter equally; the NC terms in \mathbb{A} can therefore be removed by a common phase.

After simplifying our problem to two neutrinos, and applying a phase shift,

$$\psi_{\alpha\beta}(x) \rightarrow \psi_{\alpha\beta}(x) e^{-i\Delta m^2 x/4E - \frac{i}{2} \int_0^x V_{CC}(x') dx'}. \quad (1.25)$$

the evolution equation can be written as

$$i \frac{d}{dx} \begin{pmatrix} \psi_{\alpha e} \\ \psi_{\alpha \mu} \end{pmatrix} = \frac{1}{4E} \begin{pmatrix} -\Delta m^2 \cos 2\theta + A_{CC} & \Delta m^2 \sin 2\theta \\ \Delta m^2 \sin 2\theta & \Delta m^2 \cos 2\theta - A_{CC} \end{pmatrix} \begin{pmatrix} \psi_{\alpha e} \\ \psi_{\alpha \mu} \end{pmatrix}, \quad (1.26)$$

where θ is the two-neutrino mixing angle, as in Equation (1.4). We can diagonalize this matrix, giving us the effective Hamiltonian matrix in the mass basis when in matter of constant density,

$$U_M^T \mathcal{H}_F U_M = \mathcal{H}_M, \quad (1.27)$$

where

$$\mathcal{H}_M = \frac{1}{4E} \text{diag}(-\Delta m_M^2, \Delta m_M^2) \quad (1.28)$$

is the effective Hamiltonian in the mass basis. The mixing matrix U_M is given by

$$U_M = \begin{pmatrix} \cos \theta_M & \sin \theta_M \\ -\sin \theta_M & \cos \theta_M \end{pmatrix}. \quad (1.29)$$

The new parameters Δm_M^2 and θ_M are given by

$$\Delta m_M^2 = \sqrt{(\Delta m^2 \cos 2\theta - A_{CC})^2 + (\Delta m^2 \sin 2\theta)^2}. \quad (1.30)$$

and

$$\tan 2\theta_M = \frac{\tan 2\theta}{1 - \frac{A_{CC}}{\Delta m^2 \cos 2\theta}}, \quad (1.31)$$

or

$$\cos 2\theta_M = \frac{\Delta m^2 \cos 2\theta - A_{CC}}{\Delta m_M^2} = \frac{\Delta m^2 \cos 2\theta - A_{CC}}{\sqrt{(\Delta m^2 \cos 2\theta - A_{CC})^2 + (\Delta m^2 \sin 2\theta)^2}} \quad (1.32)$$

$$\sin 2\theta_M = \frac{\Delta m^2 \sin 2\theta}{\Delta m_M^2} = \frac{\Delta m^2 \sin 2\theta}{\sqrt{(\Delta m^2 \cos 2\theta - A_{CC})^2 + (\Delta m^2 \sin 2\theta)^2}}. \quad (1.33)$$

In this scenario, where the matter density is constant, we find that the oscillation parameters Δm^2 and θ pick up an effective value Δm_M^2 and θ_M . They would simply replace the parameters as seen in Equations (1.5) to (1.12).

An interesting phenomena can be seen in Equation (1.33). If we set

$$A_{CC}^R = \Delta m^2 \cos 2\theta, \quad (1.34)$$

which is equivalent to setting the electron density to

$$N_e^R = \frac{\Delta m^2 \cos 2\theta}{2\sqrt{2}EG_F}, \quad (1.35)$$

then $\sin \theta_M$ is maximised to a value of 1, i.e. we see complete disappearance of the produced flavor eigenstate. This is regardless of the vacuum value of θ . The phenomena of matter oscillation was first described in [4-6].

While a treatment of neutrino oscillation through *changing* matter density is beyond the scope of this thesis, a complete treatment can be found in [1, 7].

For the experiments used in our global fits describe in Chapter 4, the neutrino energies are too low, the baselines too short, and the medium too low density to make matter effects observable. Therefore, we simply assume vacuum oscillations for those experiments. Matter oscillations will only become relevant when we discuss IceCube in Chapters 5 to 7.

Chapter 2

Anomalous Results & Sterile Neutrinos

In this chapter, we will first introduce a number of experiments and observations that have motivated the search for sterile neutrinos. These experiments can typically be categorized into three types: accelerator-source neutrinos, reactor-source neutrinos, and radioactive-source neutrinos. We will then introduce a handful of sterile neutrino models and their phenomenology.

2.1 Accelerator Source Neutrinos

2.1.1 LSND

The earliest experiment that suggested the existence of sterile neutrinos was the Liquid Scintillator Neutrino Detector (LSND) experiment [8], which ran 1993-1998 at Los Alamos National Laboratory (LANL).

The purpose of the experiment was to observe $\bar{\nu}_\mu$ of energy 20 – 52.8 MeV oscillating into $\bar{\nu}_e$ over a 30 m baseline. Referring to Equation (1.13), this gave LSND sensitivity to an oscillation with $\Delta m^2 \sim 1 \text{ eV}^2$, while being insensitive to the two SM mass squared splittings given in Section 1.3.1.

The decay-at-rest (DAR) neutrino source was created by impinging a $\sim 1 \text{ mA}$ beam of 798 MeV protons on a target, producing mainly pions. The negatively charged π^- 's are mostly absorbed. On the other hand, the positively charged π^+ 's are likely to decay as $\pi^+ \rightarrow \mu^+ \nu_\mu$. The μ^+ 's then decay at rest as $\mu^+ \rightarrow e^+ \nu_e \bar{\nu}_\mu$. The fact that the μ^+ 's decay at rest means that the $\bar{\nu}_\mu$ energy distribution is well understood with an end point at 52.8 MeV.

The detector was a cylindrical tank filled with 167 metric tons of mineral oil acting as a liquid scintillator. The event of interest, a $\bar{\nu}_e + p \rightarrow e^+ + n$ interaction, would produce two correlated signals. First, the outgoing positron produces scintillation light, while the outgoing neutron later captures on a free proton and emits a 2.2 MeV photon.

LSND observed an excess of $87.9 \pm 22.4 \pm 6.0$ $\bar{\nu}_e$ events above the expected backgrounds with no oscillations. This excess is shown Figure 2-1a. If this event distribution is modeled as two-neutrino oscillations, the best fit parameters would predict an excess of 89.5 events, agreeing very well with the observed data. The favored oscillation parameters are shown in Figure 2-1b. The plot shows a best fit regions with $\Delta m^2 > 10^{-2} \text{ eV}^2$, a Δm^2 larger than the SM Δm^2 's discussed in Section 1.3.1. Ultimately, in the neutrino oscillation picture,

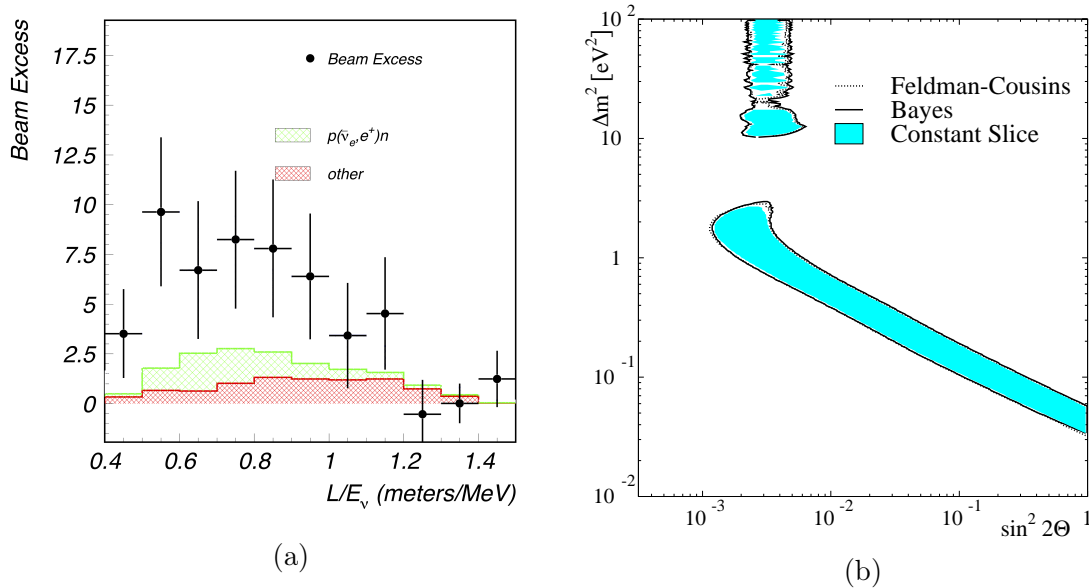


Figure 2-1: (a) The beam excess event distribution observed by LSND. The colored histograms are the expected beam-on backgrounds, while beam-off backgrounds have been subtracted. The figure is a modified figure from Ref. [8]. (b) The 90% confidence level of the LSND observation when fitted to a two-neutrino oscillation model. Figure taken from Ref. [8].

the observed LSND data hints towards a mass splitting Δm^2 inconsistent with those in the three neutrino SM picture: Δm_{21}^2 and Δm_{31}^2 . To reiterate, any oscillations observed by LSND would not be due to Δm_{21}^2 or Δm_{31}^2 , since the corresponding oscillation lengths would be too long for LSND to observe.

2.1.2 MiniBooNE

The MiniBooNE experiment was another accelerator neutrino experiment conducted to further study the LSND anomaly [9]. MiniBooNE is located at Fermilab, having collected data 2002–2019.

Unlike LSND, MiniBooNE used a decay-in-flight (DIF) neutrino beam. An 8 GeV proton beam from Fermilab’s Booster Neutrino Beam (BNB) was impinged on a beryllium target, where the resulting mesons then travel down a decay pipe and decay in flight to produce ν_μ ’s or $\bar{\nu}_\mu$ ’s. These neutrinos then travel ~ 500 meters before reaching the MiniBooNE detector. A magnetic focusing horn placed around the target allowed the experiment to selectively focus positive π^+/K^+ mesons or negative π^-/K^- mesons, letting the experiment run in either neutrino or antineutrino mode. The ν_μ flux peaked at around 600 MeV, while the $\bar{\nu}_\mu$ flux peaked at around 400 MeV. This gave the MiniBooNE experiment a $L/E \sim 1$, similar to LSND and thus giving MiniBooNE sensitivity to the same Δm^2 parameter space. Further information on the MiniBooNE detector can be found in Chapter 3.

In its 17 years of running, MiniBooNE observed an excess above expectation in both neutrino and antineutrino modes [9, 10]. In neutrino mode, the excess was 560.6 ± 119.6

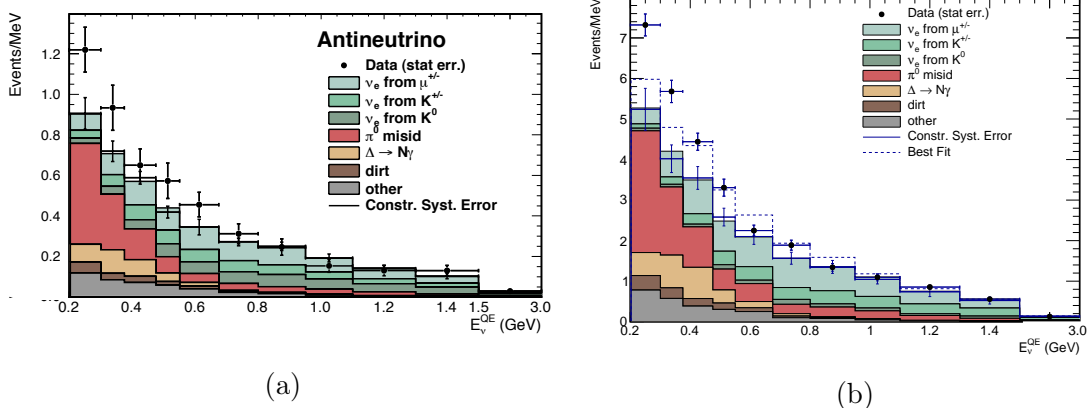


Figure 2-2: (a) The event distribution of $\bar{\nu}_e$ -like events observed by MiniBooNE in antineutrino mode. The data are given by the black crosses, while the colored histograms are the expected background events. Figure taken from Ref. [10]. (b) The event distribution of ν_e -like events observed in neutrino mode. Figure taken from Ref. [9].

events, while the excess in antineutrino mode was 78.4 ± 28.5 . Combined, this is a 4.8σ observed anomaly, corresponding to a p-value of $p = 1.59 \times 10^{-6}$. The excess is plotted for antineutrino mode in Figure 2-2a, and for neutrino mode in Figure 2-2b.

When the data are fitted to a two neutrino model, the preferred sterile parameters are shown in Figure 2-3. Using the best fit point as the hypothesis, the p-value of the data increases dramatically to $p = 0.123$. Like LSND, the best fit parameters are found to be at a Δm^2 larger than the SM neutrinos. Furthermore, the MiniBooNE preferred parameters have considerable overlap with LSND's.

2.2 Sterile Neutrino?

Before going over the other types of experiments that have seen anomalous data, let's first briefly introduce the focus of this thesis, *sterile neutrinos*.

The SM already predicts three neutrinos, with two corresponding independent mass-squared splittings, Δm_{21}^2 and Δm_{31}^2 . This model is very well established with overwhelming data supporting it. However, as seen in Section 2.1, LSND and MiniBooNE have observed an excess of neutrino events above the SM expectation. If attributed to neutrino oscillations, then remarkable agreement is found between the data and model. Further, LSND and MiniBooNE would predict neutrino oscillation parameters compatible with each other.

As Figure 2-1 and Figure 2-3 show, the Δm^2 of such an oscillation would be too large to be compatible with the two established mass splittings, $\Delta m_{21}^2 \approx 7.4 \pm 0.2 \text{ eV}^2$ and $|\Delta m_{31}^2| \approx 2.5 \pm 0.03 \text{ eV}^2$. Therefore, interpreting the LSND and MiniBooNE results as neutrino oscillations would require the introduction of a *third* independent mass-squared splitting, and a *fourth* neutrino mass state, ν_4 . Building off of Figure 1-2, the addition of a fourth mass state ν_4 with mass-squared splitting $\Delta m_{41}^2 \sim 1 \text{ eV}^2$ can be represented as in Figure 2-4.

However, LEP data has shown that the Z-boson only decays to *three* neutrino types with

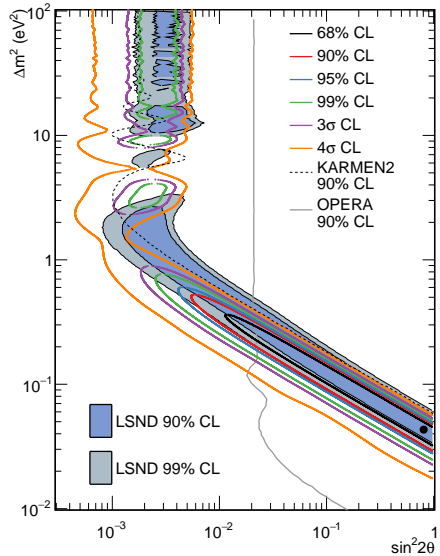


Figure 2-3: The hollow contours show the preferred parameter space for a two neutrino oscillation model given the MiniBooNE neutrino-antineutrino combined data. Also shown are the LSND best fit contours. KARMEN2 and OPERA are other experiments which did not see an anomalous signal, but will not be discussed in this section.

mass $m_\nu < m_Z/2 \approx 45.6 \text{ GeV}$ [11]. Therefore, in order to have an additional mass and weak neutrino state to contribute to oscillations, we require that the new weak eigenstate ν_s does not interact weakly, i.e. it is a *sterile* neutrino.

Because we are considering a third mass-squared splitting Δm_{41}^2 that is much larger than Δm_{21}^2 and $|\Delta m_{31}^2|$, we are justified in treating our observations as simply following two-neutrino oscillations, as described in Section 1.2 and as will be further demonstrated in Section 2.5.1. This approximation, in the context of sterile neutrino oscillations, is referred to as the Short-Baseline (SBL) approximation. Further, experiments that are sensitive to this Δm_{41}^2 are referred to as SBL experiments.¹

2.3 Reactor Neutrinos

Nuclear reactors are a good source of $\mathcal{O}(1) \text{ MeV}$ $\bar{\nu}_e$'s. Up until the start of the last decade, good agreement was found between the expected flux of reactor $\bar{\nu}_e$'s versus the observed $\bar{\nu}_e$ event rates. However, in 2011, a reevaluation of the expected reactor $\bar{\nu}_e$ flux [12, 13] resulted in the observed event rate to now have a $\sim 6\%$ deficit compared to the models [14]. This reevaluated flux model is commonly referred to as the “Huber-Mueller” (HM) flux, while the observed deficit of reactor $\bar{\nu}_e$'s is referred to as the Reactor Antineutrino Anomaly (RAA). The RAA is an established phenomena observed over a range of reactors, detectors, and

¹“Short-Baseline” is a bit of a misnomer. “Short Baseline” refers to relatively small values of L/E , not just L .

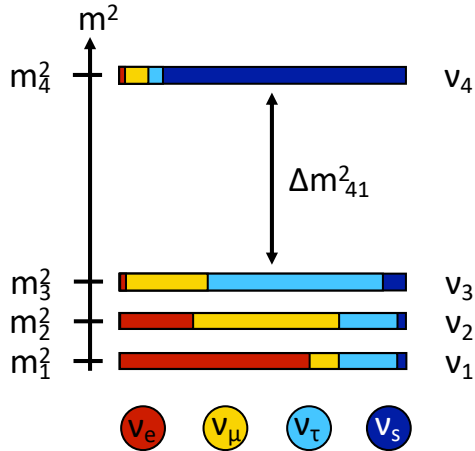


Figure 2-4: A visualization of the mass squared splittings and mixing, with the introduction of a fourth neutrino mass state ν_4 and weak state ν_s . Figure taken from Ref. [3].

baselines, as shown in Figure 2-5.

Like the SBL accelerator results described in Section 2.1, the observed deficit of reactor $\bar{\nu}_e$'s versus expectation can be fit to a neutrino oscillation model. Figure 2-6 shows the best fit oscillation region when this is done. Again, as seen in Section 2.1, a $\Delta m^2 > 0.1 \text{ eV}^2$ can explain the anomalous observations.

Before continuing, we must note that the RAA is a deficit compared to nuclear reactor models. Therefore, there does exist the possibility that it's the models that are overestimating the $\bar{\nu}_e$ flux, as opposed to a real disappearance of $\bar{\nu}_e$. In fact, the HM model is known to be incorrect since a spectral distortion is found at $\sim 5 \text{ MeV}$ in observed prompt energy [17–19], referred to as the “5 MeV bump,” which cannot be explained by neutrino oscillations. Further, as more reactor models have been published, some strengthen the RAA [20], while others weaken it [21]. The conclusion to draw is that the reactor $\bar{\nu}_e$ flux is difficult to predict, and these models are not reliable enough to let the RAA be convincing proof of neutrino oscillations. In Section 4.1.2, we discuss modern reactor experiments that work around this limitation.

2.4 Gallium Anomalies

GALLEX[22] and SAGE[23] were two solar neutrino experiments that used ^{71}Ga detectors to observe solar ν_e 's through the process



The produced ^{71}Ge would then be collected and counted to calculate the ν_e flux.

Both experiments used intense radioactive electron-capture ν_e sources to calibrate their

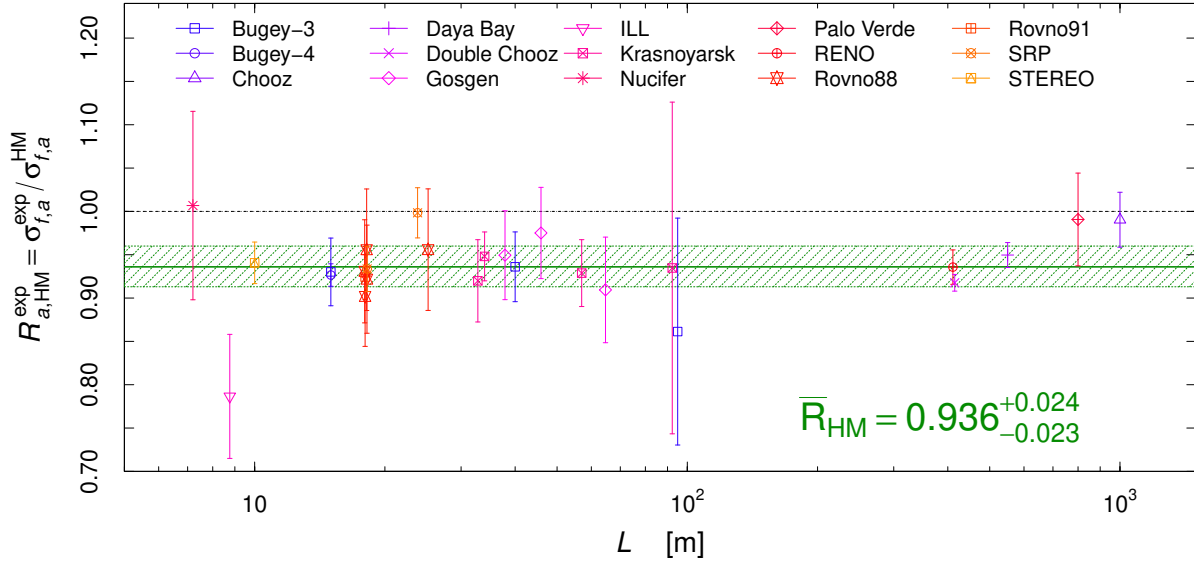


Figure 2-5: Ratios of the observed inverse beta decay (IBD) yields over the expectation from the HM model. The plot shows that the deficit is baseline independent, and universal amongst various reactors and detectors. Figure taken from Ref. [15].

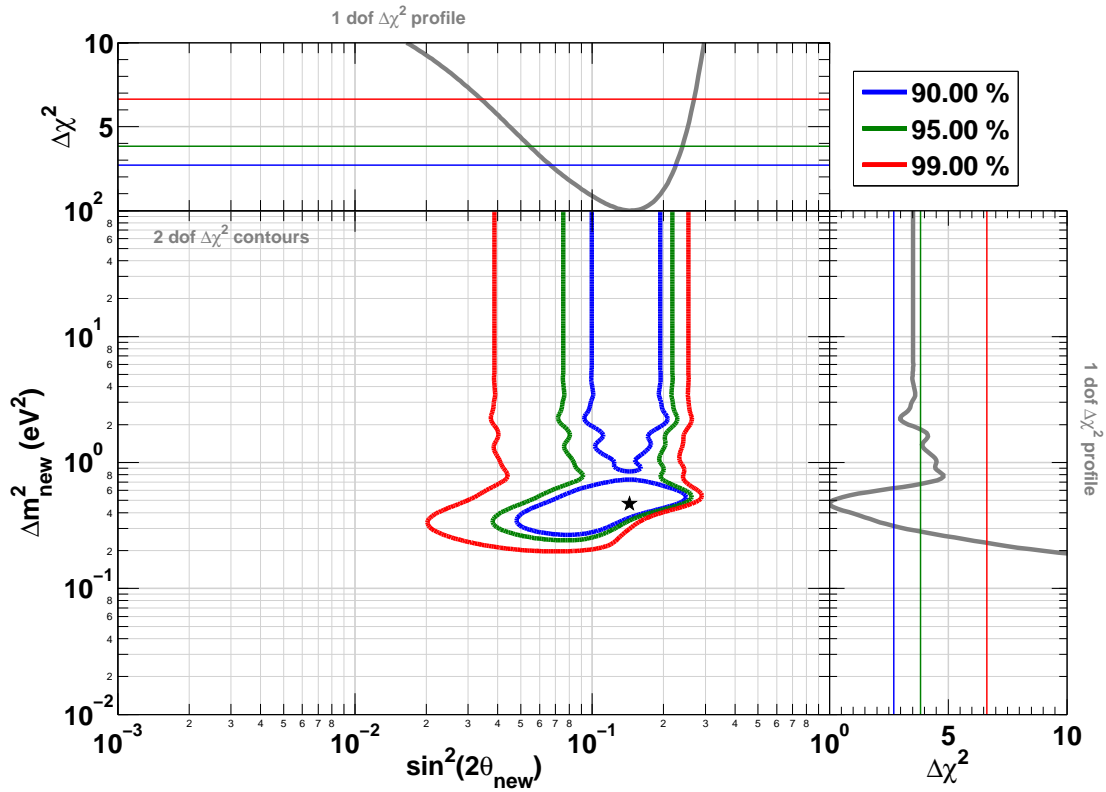


Figure 2-6: The plot shows the best fit oscillation parameters when the RAA is modeled as neutrino oscillations. Figure taken from Ref. [16].

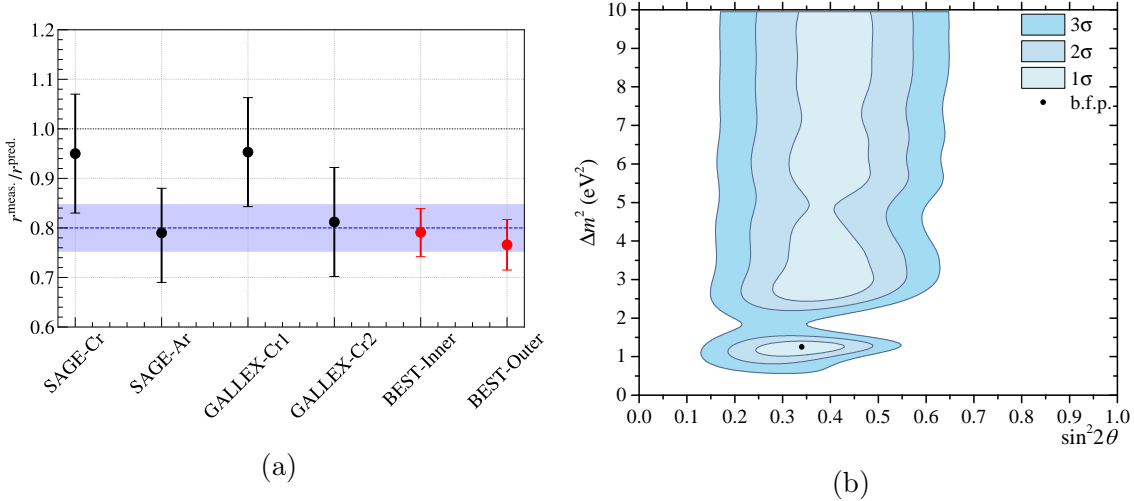


Figure 2-7: (a) The observed ^{71}Ge production rate over expectation for the various runs for SAGE, GALLEX, and BEST. Figure taken from Ref. [25]. (b) Allowed parameter regions of the combined SAGE, GALLEX, and BEST data when modeled as two neutrino oscillations. Figure taken from Ref. [24].

detectors. GALLEX ran two measurements of ^{51}Cr , while SAGE ran once with ^{51}Cr and again with ^{37}Ar . These isotopes would decay like



producing mono-energetic ν_e lines to use as calibration.

Combined, the observed ratio of observed ^{71}Ge production to expectation was $R = 0.87 \pm 0.05$. Like the $\bar{\nu}_e$'s from reactors, it appeared as if the ν_e 's from the sources were disappearing before interacting with the detector.

More recently, the BEST experiment [24, 25] ran to probe this ‘‘gallium anomaly.’’ A ^{51}Cr source was placed within two concentric containers filled with ^{71}Ga . Again, a deficit of ^{71}Ge production was observed with an observed over expected ratio of $R_{\text{In}} = 0.79 \pm 0.05$ in the inner shell, and $R_{\text{Out}} = 0.77 \pm 0.05$ in the outer shell.

The ratios of observed ^{71}Ge production over expectations are shown in Figure 2-7a. Figure 2-7b shows the best fit regions of the oscillation parameters if the data were fitted to neutrino oscillations. Like the previous anomalies, these results fit well within a neutrino oscillation picture, with a $\Delta m^2 > 1 \text{ eV}^2$.

2.5 Sterile Neutrino Models

Now that we have summarized the experimental observations that have motivated the search for sterile neutrinos, let us now introduce some phenomenological models of sterile neutrinos. These models will be the basis of the global fit results which will be presented in Chapter 4.

2.5.1 3+1 Neutrinos

Suppose that there exists an additional neutrino on top of the three SM neutrinos. In this scenario, we simply expand the mixing matrix to

$$\begin{pmatrix} \nu_e \\ \nu_\mu \\ \nu_\tau \\ \nu_s \end{pmatrix} = \begin{pmatrix} U_{e1} & U_{e2} & U_{e3} & U_{e4} \\ U_{\mu1} & U_{\mu2} & U_{\mu3} & U_{\mu4} \\ U_{\tau1} & U_{\tau2} & U_{\tau3} & U_{\tau4} \\ U_{s1} & U_{s2} & U_{s3} & U_{s4} \end{pmatrix} \begin{pmatrix} \nu_1 \\ \nu_2 \\ \nu_3 \\ \nu_4 \end{pmatrix}. \quad (2.4)$$

Per usual, the mixing matrix can be written out as a series of unitary rotations

$$U = R^{34}(\theta_{34})R^{24}(\theta_{24}, \delta_{24})R^{14}(\theta_{14}, \delta_{14})R^{23}(\theta_{23})R^{13}(\theta_{13}, \delta_{13})R^{12}(\theta_{12}). \quad (2.5)$$

This increases the number of free parameters to 12, introducing Δm_{41}^2 , θ_{14} , θ_{24} , θ_{34} , δ_{14} , and δ_{24} on top of the parameters in the three neutrino model.

Now, let us assume that this additional neutrino state ν_4 has a mass much larger than the other neutrinos such that $\Delta m_{41}^2 \gg \Delta m_{31}^2 > \Delta m_{21}^2 \approx 0$. Further, let us also suppose that our experiments are set up such that $L/E \ll \Delta m_{21}^2 < \Delta m_{31}^2$. We'll refer to these assumptions as the Short-Baseline (SBL) approximation, as mentioned earlier. Under these assumptions, we take Equation (1.2) and set $\Delta m_{31}^2 = \Delta m_{21}^2 = 0$, and $\Delta m_{41}^2 = \Delta m_{42}^2 = \Delta m_{43}^2$, giving

$$\begin{aligned} P(\nu_\alpha \rightarrow \nu_\beta) &= \delta_{\alpha\beta} - 4 \sum_{i<4} \Re(U_{\alpha i}^* U_{\beta i} U_{\alpha 4} U_{\beta 4}^*) \sin^2 \left(1.27 \Delta m_{41}^2 [\text{eV}] \frac{L[\text{km}]}{E[\text{GeV}]} \right) \\ &\quad - 2 \sum_{i<4} \Im(U_{\alpha i}^* U_{\beta i} U_{\alpha 4} U_{\beta 4}^*) \sin \left(2.54 \Delta m_{41}^2 [\text{eV}] \frac{L[\text{km}]}{E[\text{GeV}]} \right) \\ &= \delta_{\alpha\beta} - 4 \sin^2 \left(1.27 \Delta m_{41}^2 [\text{eV}] \frac{L[\text{km}]}{E[\text{GeV}]} \right) \Re \left(\sum_{i<4} U_{\alpha i}^* U_{\beta i} U_{\alpha 4} U_{\beta 4}^* \right) \\ &\quad - 2 \sin \left(2.54 \Delta m_{41}^2 [\text{eV}] \frac{L[\text{km}]}{E[\text{GeV}]} \right) \Im \left(\sum_{i<4} U_{\alpha i}^* U_{\beta i} U_{\alpha 4} U_{\beta 4}^* \right). \end{aligned} \quad (2.6)$$

We can rewrite $\sum_{i<4} U_{\alpha i}^* U_{\beta i} U_{\alpha 4} U_{\beta 4}^*$, utilizing the unitarity of the mixing matrix

$$\sum_{i<4} U_{\alpha i}^* U_{\beta i} U_{\alpha 4} U_{\beta 4}^* = U_{\alpha 4} U_{\beta 4}^* \sum_{i<4} U_{\alpha i}^* U_{\beta i} = U_{\alpha 4} U_{\beta 4}^* (\delta_{\alpha\beta} - U_{\alpha 4}^* U_{\beta 4}). \quad (2.7)$$

Note that the above equation is real regardless if $\alpha = \beta$ or $\alpha \neq \beta$; therefore, we can drop the imaginary term in Equation (2.6) to give us

$$P(\nu_\alpha \rightarrow \nu_\beta) = \delta_{\alpha\beta} - 4 U_{\alpha 4} U_{\beta 4}^* (\delta_{\alpha\beta} - U_{\alpha 4}^* U_{\beta 4}) \sin^2 \left(1.27 \Delta m_{41}^2 [\text{eV}] \frac{L[\text{km}]}{E[\text{GeV}]} \right). \quad (2.8)$$

$\sin^2 2\theta_{ee}$	$= \sin^2 2\theta_{14}$	$= 4(1 - U_{e4} ^2) U_{e4} ^2$
$\sin^2 2\theta_{\mu\mu}$	$= 4 \cos^2 \theta_{14} \sin^2 \theta_{24} (1 - \cos^2 \theta_{14} \sin^2 \theta_{24})$	$= 4(1 - U_{\mu4} ^2) U_{\mu4} ^2$
$\sin^2 2\theta_{\tau\tau}$	$= 4 \cos^2 \theta_{14} \cos^2 \theta_{24} \sin^2 \theta_{34} (1 - \cos^2 \theta_{14} \cos^2 \theta_{24} \sin^2 \theta_{34})$	$= 4(1 - U_{\tau4} ^2) U_{\tau4} ^2$
$\sin^2 2\theta_{\mu e}$	$= \sin^2 2\theta_{14} \sin^2 \theta_{24}$	$= 4 U_{\mu4} ^2 U_{e4} ^2$
$\sin^2 2\theta_{e\tau}$	$= \sin^2 2\theta_{14} \cos^2 \theta_{24} \sin^2 \theta_{34}$	$= 4 U_{e4} ^2 U_{\tau4} ^2$
$\sin^2 2\theta_{\mu\tau}$	$= \sin^2 2\theta_{24} \cos^4 \theta_{14} \sin^2 \theta_{34}$	$= 4 U_{\mu4} ^2 U_{\tau4} ^2$

Table 2.1: 3+1 neutrino model mixing parameters with the SBL approximation.

For the specific case of appearance ($\alpha \neq \beta$), this gives

$$P(\nu_\alpha \rightarrow \nu_\beta) = 4|U_{\alpha4}|^2|U_{\beta4}|^2 \sin^2 \left(1.27 \Delta m_{41}^2 [\text{eV}] \frac{L[\text{km}]}{E[\text{GeV}]} \right) \quad (\alpha \neq \beta), \quad (2.9)$$

while for disappearance ($\alpha = \beta$) we get

$$P(\nu_\alpha \rightarrow \nu_\alpha) = 1 - 4|U_{\alpha4}|^2(1 - |U_{\alpha4}|^2) \sin^2 \left(1.27 \Delta m_{41}^2 [\text{eV}] \frac{L[\text{km}]}{E[\text{GeV}]} \right). \quad (2.10)$$

Notice the similarities between Equations (2.9) and (2.10) and Equations (1.5) to (1.12). The analogies become clearer when we use effective mixing angles

$$\sin^2 2\theta_{\alpha\beta} \equiv 4|U_{\alpha4}|^2|U_{\beta4}|^2 \quad (\alpha \neq \beta), \quad \sin^2 2\theta_{\alpha\alpha} \equiv 4|U_{\alpha4}|^2(1 - |U_{\alpha4}|^2) \quad (2.11)$$

so that Equation (2.9) and Equation (2.10) can be written as

$$P(\nu_\alpha \rightarrow \nu_\beta) = \sin^2 2\theta_{\alpha\beta} \sin^2 \left(1.27 \Delta m_{41}^2 [\text{eV}] \frac{L[\text{km}]}{E[\text{GeV}]} \right) \quad (\alpha \neq \beta) \quad (2.12)$$

$$P(\nu_\alpha \rightarrow \nu_\alpha) = 1 - \sin^2 2\theta_{\alpha\alpha} \sin^2 \left(1.27 \Delta m_{41}^2 [\text{eV}] \frac{L[\text{km}]}{E[\text{GeV}]} \right). \quad (2.13)$$

We therefore see the similarities between a 3+1 neutrino model under the SBL approximation and a simple two-neutrino model.

In order to keep track of the different mixing parameter conventions, Table 2.1 provides the relations between these different conventions.

2.5.2 3+2 Model

An obvious extension to the 3+1 would be to simply add more neutrinos. In our global fits, we consider a 3+2 model. If we continue to use the SBL approximation, where $\Delta m_{51}^2 > \Delta m_{41}^2 \gg \Delta m_{31}^2 > \Delta m_{21}^2 \approx 0$ and $L/E \ll \Delta m_{21}^2 < \Delta m_{31}^2$, then the general oscillation

equation Equation (1.2) can be written as

$$\begin{aligned}
P(\nu_\alpha \rightarrow \nu_\beta) &= \delta_{\alpha\beta} - 4 \sum_{i < j} \Re(U_{\alpha i}^* U_{\beta i} U_{\alpha j} U_{\beta j}^*) \sin^2(1.27 \Delta m_{ji}^2 L/E) \\
&\quad - 2 \sum_{i < j} \Im(U_{\alpha i}^* U_{\beta i} U_{\alpha j} U_{\beta j}^*) \sin(2.54 \Delta m_{ji}^2 L/E) \\
&= \delta_{\alpha\beta} - 4 \Re(U_{\alpha 4}^* U_{\beta 4} U_{\alpha 5} U_{\beta 5}^*) \sin^2(1.27 \Delta m_{54}^2 L/E) \\
&\quad - 2 \Im(U_{\alpha 4}^* U_{\beta 4 i} U_{\alpha 5} U_{\beta 5}^*) \sin(2.54 \Delta m_{54}^2 L/E) \\
&\quad - 4 \sum_{i < 4} \Re(U_{\alpha i}^* U_{\beta i} U_{\alpha 4} U_{\beta 4}^*) \sin^2(1.27 \Delta m_{4i}^2 L/E) \\
&\quad - 2 \sum_{i < 4} \Im(U_{\alpha i}^* U_{\beta i} U_{\alpha 4} U_{\beta 4}^*) \sin(2.54 \Delta m_{4i}^2 L/E) \\
&\quad - 4 \sum_{i < 4} \Re(U_{\alpha i}^* U_{\beta i} U_{\alpha 5} U_{\beta 5}^*) \sin^2(1.27 \Delta m_{5i}^2 L/E) \\
&\quad - 2 \sum_{i < 4} \Im(U_{\alpha i}^* U_{\beta i} U_{\alpha 5} U_{\beta 5}^*) \sin(2.54 \Delta m_{5i}^2 L/E) \\
&= \delta_{\alpha\beta} - 4 \Re(U_{\alpha 4}^* U_{\beta 4} U_{\alpha 5} U_{\beta 5}^*) \sin^2(1.27 \Delta m_{54}^2 L/E) \\
&\quad - 2 \Im(U_{\alpha 4}^* U_{\beta 4 i} U_{\alpha 5} U_{\beta 5}^*) \sin(2.54 \Delta m_{54}^2 L/E) \\
&\quad - 4(\Re(\delta_{\alpha\beta} U_{\alpha 4} U_{\beta 4}^* - U_{\alpha 5}^* U_{\beta 5} U_{\alpha 4} U_{\beta 4}^*) - |U_{\alpha 4} U_{\beta 4}^*|^2) \sin^2(1.27 \Delta m_{41}^2 L/E) \\
&\quad - 2 \Im(\delta_{\alpha\beta} U_{\alpha 4} U_{\beta 4}^* - U_{\alpha 5}^* U_{\beta 5} U_{\alpha 4} U_{\beta 4}^*) \sin(2.54 \Delta m_{41}^2 L/E) \\
&\quad - 4(\Re(\delta_{\alpha\beta} U_{\alpha 5} U_{\beta 5}^* - U_{\alpha 4}^* U_{\beta 4} U_{\alpha 5} U_{\beta 5}^*) - |U_{\alpha 5}^* U_{\beta 5}|^2) \sin^2(1.27 \Delta m_{51}^2 L/E) \\
&\quad - 2 \Im(\delta_{\alpha\beta} U_{\alpha 5} U_{\beta 5}^* - U_{\alpha 4}^* U_{\beta 4} U_{\alpha 5} U_{\beta 5}^*) \sin(2.54 \Delta m_{51}^2 L/E), \tag{2.14}
\end{aligned}$$

where the last step uses Equation (2.7).

For an appearance experiment,

$$\begin{aligned}
P(\nu_\alpha \rightarrow \nu_\beta) &= -4 |U_{\alpha 4}^* U_{\beta 4} U_{\alpha 5} U_{\beta 5}^*| \cos(\phi_{\alpha\beta}) \sin^2(1.27 \Delta m_{54}^2 L/E) \\
&\quad + 2 |U_{\alpha 4}^* U_{\beta 4} U_{\alpha 5} U_{\beta 5}^*| \sin(\phi_{\alpha\beta}) \sin(2.54 \Delta m_{54}^2 L/E) \\
&\quad + 4(|U_{\alpha 5}^* U_{\beta 5} U_{\alpha 4} U_{\beta 4}^*| \cos(\phi_{\alpha\beta}) + |U_{\alpha 4} U_{\beta 4}^*|^2) \sin^2(1.27 \Delta m_{41}^2 L/E) \\
&\quad + 2 |U_{\alpha 5}^* U_{\beta 5} U_{\alpha 4} U_{\beta 4}^*| \sin(\phi_{\alpha\beta}) \sin(2.54 \Delta m_{41}^2 L/E) \\
&\quad + 4(|U_{\alpha 4}^* U_{\beta 4} U_{\alpha 5} U_{\beta 5}^*| \cos(\phi_{\alpha\beta}) + |U_{\alpha 5}^* U_{\beta 5}|^2) \sin^2(1.27 \Delta m_{51}^2 L/E) \\
&\quad - 2 |U_{\alpha 4}^* U_{\beta 4} U_{\alpha 5} U_{\beta 5}^*| \sin(\phi_{\alpha\beta}) \sin(2.54 \Delta m_{51}^2 L/E) \tag{2.15}
\end{aligned}$$

where

$$\phi_{\alpha\beta} = \arg(U_{\alpha 4}^* U_{\beta 4 i} U_{\alpha 5} U_{\beta 5}^*). \tag{2.16}$$

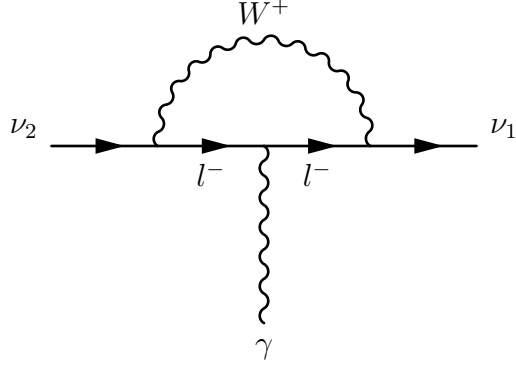


Figure 2-8: An example of a Standard Model $\nu_2 \rightarrow \nu_1 + \gamma$ decay.

For a disappearance experiment,

$$\begin{aligned}
 P(\nu_\alpha \rightarrow \nu_\alpha) = & 1 - 4|U_{\alpha 4}|^2|U_{\alpha 5}|^2 \sin^2(1.27\Delta m_{54}^2 L/E) \\
 & - 4(1 - |U_{\alpha 4}|^2 - |U_{\alpha 5}|^2)|U_{\alpha 4}|^2 \sin^2(1.27\Delta m_{41}^2 L/E) \\
 & - 4(1 - |U_{\alpha 4}|^2 - |U_{\alpha 5}|^2)|U_{\alpha 5}|^2 \sin^2(1.27\Delta m_{51}^2 L/E).
 \end{aligned} \tag{2.17}$$

Similar to the case when we reached three neutrinos in Section 1.3, we now have a CP-violating phase $\phi_{\alpha\beta}$ appearing in the appearance equation. In this scenario, switching from ν to $\bar{\nu}$ flips $\phi_{\alpha\beta} \rightarrow -\phi_{\alpha\beta}$, leading to different oscillation equations for $P(\nu_\alpha \rightarrow \nu_\beta)$ versus $P(\bar{\nu}_\alpha \rightarrow \bar{\nu}_\beta)$.

We choose to stop at 3+2 since since any further sterile neutrinos lead to too many parameters that could be fit for, and the experimental data are too limited to be used to fit to so many parameters.

2.5.3 3+1+Decay Model

We now consider a more exotic model of sterile neutrinos: an unstable sterile neutrino.

Strictly speaking, the Standard Model neutrinos are already unstable. Figure 2-8 shows an example of a $\nu_2 \rightarrow \nu_1 + \gamma$ decay.

Lifetimes for $\nu_2 \rightarrow \nu_1 + \gamma$ and $\nu_2 \rightarrow \nu_1 + \gamma + \gamma$ decays are printed below.

$$\nu_2 \rightarrow \nu_1 + \gamma \quad \tau \approx \mathcal{O}(10^{36}) (m_2/\text{eV})^{-5} \text{ years [26]} \tag{2.18}$$

$$\nu_2 \rightarrow \nu_1 + \gamma + \gamma \quad \tau \approx \mathcal{O}(10^{66}) (m_2/\text{eV})^{-9} \text{ years [27]} \tag{2.19}$$

These lifetimes are well beyond the age of the universe, so for practical purposes the SM neutrinos are treated as stable particles.

However, models can be introduced where neutrinos are allowed to decay through some new interaction, e.g. $\nu_i \rightarrow \nu_j + \phi$ [28].

Beyond Standard Model (BSM) decays of SM neutrinos have been used in the past to explain ν_μ disappearance in atmospheric data [29]. And a decaying sterile neutrino model

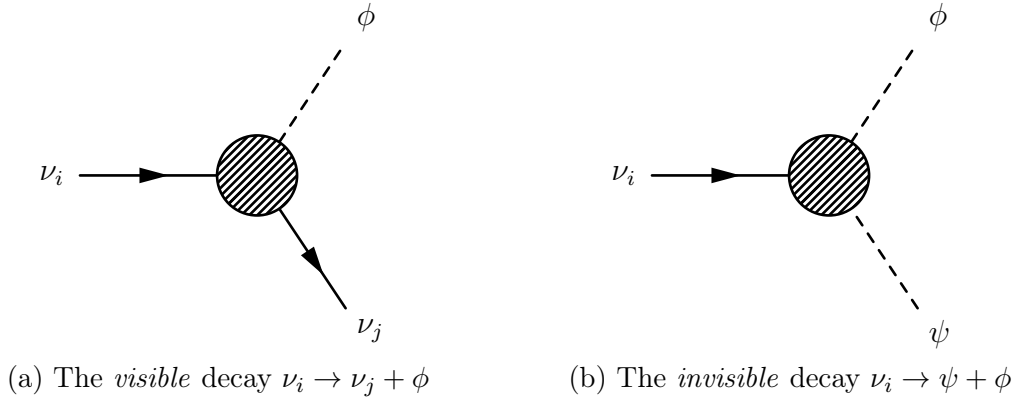


Figure 2-9

has been used to explain the LSND anomaly [30].

For our studies, we consider sterile neutrino decays as described in Ref. [31] and shown in Figure 2-9. Here, the mostly-sterile mass state ν_4 is allowed to decay into some scalar ϕ , with the Lagrangian [28, 32]

$$\mathcal{L}_{\text{int}} = \frac{g_{4j}^s}{2} \bar{\nu}_j \nu_4 \phi + i \frac{g_{4j}^p}{2} \bar{\nu}_j \gamma_5 \nu_4, \quad (2.20)$$

where g_{4j}^s is the scalar coupling between ν_4 and ν_j , and g_{4j}^p is the pseudoscalar coupling. In the limit where $m_4 \gg m_j$, both the helicity-preserving and helicity-violating decay rates are given as

$$\Gamma(\nu_4 \rightarrow \nu_j) = \Gamma(\nu_4 \rightarrow \bar{\nu}_j) = \frac{(g_{4j}^s)^2 + (g_{4j}^p)^2}{32\pi E_4} m_4^2. \quad (2.21)$$

In Ref. [31], both decays in Figure 2-9 were considered in the context of the IceCube experiment. The $\nu_4 \rightarrow \nu_j + \phi$ decay in Figure 2-9a is referred to as a *visible* decay, since ν_j is taken to be an active neutrino that can be detected, in principle. The $\nu_4 \rightarrow \psi + \phi$ decay shown in Figure 2-9b, on the other hand, is referred to as an *invisible* decay, since ψ is considered to be some fermion that cannot be detected through conventional means. For our work, we only consider the invisible decay shown in Figure 2-9b. We also assume that the coupling is either purely scalar or pseudo-scalar.

To model the invisible decay, we use the non-Hermitian Hamiltonian

$$H = H_0 - i \frac{1}{2} \Gamma(E), \quad (2.22)$$

where Γ is a diagonal matrix with $\Gamma_{ii} = \Gamma_i(E)$ and $\Gamma_i(E)$ is the decay rate for the i^{th} neutrino given by *twice* Equation (2.21). The factor of two comes from the fact that Equation (2.21) gives the decay width for only the helicity-preserving or helicity-violating decay. The total decay width would be the sum of the two. In our model, we assume that the only non-zero term is Γ_4 , so that only the fourth mass state ν_4 decays.

The neutrino vacuum Hamiltonian H_0 in the ultra-relativistic limit can be written as

$H_{0ii} = \frac{\Delta m_i^2}{2E}$, where $\Delta m_i^2 = m_i^2 - m_1^2$. Further, we again take the SBL approximation and assume that $\Delta m_{31}^2 = \Delta m_{21}^2 = 0$. Finally, the $\Gamma(E)$ described above is given in the lab frame. When we later wish to compare the decay coupling between different experiments, it's more convenient to deal with the *rest-frame* coupling. Therefore, we make the shift $\Gamma(E) \rightarrow \Gamma/\gamma = \Gamma m_4/E$, where γ is the lorentz factor. Together, this gives

$$H = \frac{1}{2E} \begin{pmatrix} 0 & 0 & 0 & 0 \\ 0 & 0 & 0 & 0 \\ 0 & 0 & 0 & 0 \\ 0 & 0 & 0 & \Delta m^2 - im_4\Gamma \end{pmatrix}. \quad (2.23)$$

The oscillation probabilities can be found by evaluating

$$P(\nu_\beta \rightarrow \nu_\alpha) = \langle \nu_\beta | U \exp[-iHL] U^\dagger | \nu_\alpha \rangle. \quad (2.24)$$

We simply write the solution below for appearance

$$P(\nu_\alpha \rightarrow \nu_\beta) = 4|U_{\alpha 4}|^2 |U_{\beta 4}|^2 \left(\sinh^2 \left(\frac{\Gamma L m_4}{4E} \right) + \sin^2 \left(\frac{\Delta m^2 L}{4E} \right) \right) e^{-\frac{\Gamma L m_4}{2E}} \quad (\alpha \neq \beta) \quad (2.25)$$

and disappearance

$$P(\nu_\alpha \rightarrow \nu_\alpha) = 2(1 - |U_{\alpha 4}|^2) |U_{\alpha 4}|^2 \cos \left(\frac{\Delta m^2 L}{2E} \right) e^{-\frac{\Gamma L m_4}{2E}} + |U_{\alpha 4}|^4 e^{-\frac{\Gamma L m_4}{E}} + (1 - |U_{\alpha 4}|^2)^2. \quad (2.26)$$

Written in terms of the 3+1 effective angles

$$\sin^2 2\theta_{\alpha\beta} \equiv 4|U_{\alpha 4}|^2 |U_{\beta 4}|^2 \quad (\alpha \neq \beta), \quad \sin^2 2\theta_{\alpha\alpha} \equiv 4|U_{\alpha 4}|^2 (1 - |U_{\alpha 4}|^2), \quad (2.27)$$

the decay oscillation equations can be rewritten as

$$P(\nu_\alpha \rightarrow \nu_\beta) = \sin^2 2\theta_{\alpha\beta} \left(\sinh^2 \left(\frac{\Gamma L m_4}{4E} \right) + \sin^2 \left(\frac{\Delta m^2 L}{4E} \right) \right) e^{-\frac{\Gamma L m_4}{2E}} \quad (\alpha \neq \beta) \quad (2.28)$$

and

$$P(\nu_\alpha \rightarrow \nu_\alpha) = \frac{1}{2} \sin^2 2\theta_{\alpha\alpha} \cos \left(\frac{\Delta m^2 L}{2E} \right) e^{-\frac{\Gamma L m_4}{2E}} + \sin^4 \theta_{\alpha\alpha} e^{-\frac{\Gamma L m_4}{E}} + \cos^4 \theta_{\alpha\alpha}. \quad (2.29)$$

Chapter 3

MiniBooNE

Below we present the MiniBooNE publication [33] on which the author had the lead contribution. The Letter provides a concise description of the MiniBooNE detector and analysis. The corresponding Supplemental Material for this work is also provided in Appendix C.

The most recent MiniBooNE results are given in Section 3.1 for completeness.

Significant Excess of Electronlike Events in the MiniBooNE Short-Baseline Neutrino Experiment

A. A. Aguilar-Arevalo,¹³ B. C. Brown,⁶ L. Bugel,¹² G. Cheng,⁵ J. M. Conrad,¹² R. L. Cooper,^{10,15} R. Dharmapalan,^{1,2} A. Diaz,¹² Z. Djurcic,² D. A. Finley,⁶ R. Ford,⁶ F. G. Garcia,⁶ G. T. Garvey,¹⁰ J. Grange,⁷ E.-C. Huang,¹⁰ W. Huelsnitz,¹⁰ C. Ignarra,¹² R. A. Johnson,³ G. Karagiorgi,⁵ T. Katori,^{12,16} T. Kobilarcik,⁶ W. C. Louis,¹⁰ C. Mariani,¹⁹ W. Marsh,⁶ G. B. Mills,^{10,*} J. Mirabal,¹⁰ J. Monroe,¹⁸ C. D. Moore,⁶ J. Mousseau,¹⁴ P. Nienaber,¹⁷ J. Nowak,⁹ B. Osmanov,⁷ Z. Pavlovic,⁶ D. Perevalov,⁶ H. Ray,⁷ B. P. Roe,¹⁴ A. D. Russell,⁶ M. H. Shaevitz,⁵ J. Spitz,¹⁴ I. Stancu,¹ R. Tayloe,⁸ R. T. Thornton,¹⁰ M. Tzanov,^{4,11} R. G. Van de Water,¹⁰ D. H. White,^{10,*} D. A. Wickremasinghe,³ and E. D. Zimmerman⁴

(MiniBooNE Collaboration)

¹University of Alabama, Tuscaloosa, Alabama 35487, USA

²Argonne National Laboratory, Argonne, Illinois 60439, USA

³University of Cincinnati, Cincinnati, Ohio 45221, USA

⁴University of Colorado, Boulder, Colorado 80309, USA

⁵Columbia University, New York, New York 10027, USA

⁶Fermi National Accelerator Laboratory, Batavia, Illinois 60510, USA

⁷University of Florida, Gainesville, Florida 32611, USA

⁸Indiana University, Bloomington, Indiana 47405, USA

⁹Lancaster University, Lancaster LA1 4YB, United Kingdom

¹⁰Los Alamos National Laboratory, Los Alamos, New Mexico 87545, USA

¹¹Louisiana State University, Baton Rouge, Louisiana 70803, USA

¹²Massachusetts Institute of Technology, Cambridge, Massachusetts 02139, USA

¹³Instituto de Ciencias Nucleares, Universidad Nacional Autónoma de México, CDMX 04510, Mexico

¹⁴University of Michigan, Ann Arbor, Michigan 48109, USA

¹⁵New Mexico State University, Las Cruces, New Mexico 88003, USA

¹⁶Queen Mary University of London, London E1 4NS, United Kingdom

¹⁷Saint Mary's University of Minnesota, Winona, Minnesota 55987, USA

¹⁸Royal Holloway, University of London, Egham TW20 0EX, United Kingdom

¹⁹Center for Neutrino Physics, Virginia Tech, Blacksburg, Virginia 24061, USA

 (Received 30 May 2018; revised manuscript received 28 September 2018; published 26 November 2018)

The MiniBooNE experiment at Fermilab reports results from an analysis of ν_e appearance data from 12.84×10^{20} protons on target in neutrino mode, an increase of approximately a factor of 2 over previously reported results. A ν_e charged-current quasielastic event excess of 381.2 ± 85.2 events (4.5σ) is observed in the energy range $200 < E_\nu^{\text{QE}} < 1250$ MeV. Combining these data with the $\bar{\nu}_e$ appearance data from 11.27×10^{20} protons on target in antineutrino mode, a total ν_e plus $\bar{\nu}_e$ charged-current quasielastic event excess of 460.5 ± 99.0 events (4.7σ) is observed. If interpreted in a two-neutrino oscillation model, $\nu_\mu \rightarrow \nu_e$, the best oscillation fit to the excess has a probability of 21.1%, while the background-only fit has a χ^2 probability of 6×10^{-7} relative to the best fit. The MiniBooNE data are consistent in energy and magnitude with the excess of events reported by the Liquid Scintillator Neutrino Detector (LSND), and the significance of the combined LSND and MiniBooNE excesses is 6.0σ . A two-neutrino oscillation interpretation of the data would require at least four neutrino types and indicate physics beyond the three neutrino paradigm. Although the data are fit with a two-neutrino oscillation model, other models may provide better fits to the data.

DOI: [10.1103/PhysRevLett.121.221801](https://doi.org/10.1103/PhysRevLett.121.221801)

Evidence for short-baseline neutrino anomalies at an $L/E_\nu \sim 1$ m/MeV, where E_ν is the neutrino energy and L is the distance that the neutrino traveled before detection, comes from both neutrino appearance and disappearance experiments. The appearance anomalies include the excess of ν_e and $\bar{\nu}_e$ charge-current quasielastic (CCQE) events observed by the Liquid Scintillator Neutrino Detector (LSND) [1] and MiniBooNE [2,3] experiments, while the disappearance anomalies, although not completely consistent, include the deficit of ν_e and $\bar{\nu}_e$ events observed by reactor [4] and radioactive-source experiments [5]. As the masses and mixings within the three-generation neutrino matrix have been attached to solar and long-baseline neutrino experiments, more exotic models are typically used to explain these anomalies, including, for example, $3 + N$ neutrino oscillation models involving three active neutrinos and N additional sterile neutrinos [6–14], resonant neutrino oscillations [15], Lorentz violation [16], sterile neutrino decay [17], sterile neutrino nonstandard interactions [18], and sterile neutrino extra dimensions [19]. This Letter presents improved MiniBooNE ν_e and $\bar{\nu}_e$ appearance results, assuming two-neutrino oscillations with probability $P = \sin^2(2\theta) \sin^2(1.27\Delta m^2 L/E)$, where θ is the mixing angle, Δm^2 (eV^2/c^4) is the difference in neutrino mass eigenstates squared, L (m) is the distance traveled by the neutrino, and E (MeV) is the neutrino energy.

The booster neutrino beam (BNB) at Fermilab delivers to the MiniBooNE experiment a flux of neutrinos and antineutrinos that is simulated using information from external measurements [20]. The BNB is produced by 8 GeV protons from the Fermilab booster interacting on a beryllium target inside a magnetic focusing horn. Depending on the polarity of the horn, either π^+ are focused and π^- are defocused to produce a fairly pure beam of ν_μ , or π^- are focused and π^+ are defocused to produce a somewhat pure beam of $\bar{\nu}_\mu$. In neutrino mode, the ν_μ , $\bar{\nu}_\mu$, ν_e , and $\bar{\nu}_e$ flux contributions at the detector are 93.5%, 5.9%, 0.5%, and 0.1%, respectively, while in antineutrino mode, the flux contributions are 15.7%, 83.7%, 0.2%, and 0.4%, respectively. The ν_μ and $\bar{\nu}_\mu$ fluxes peak at approximately 600 and 400 MeV, respectively.

The MiniBooNE detector is described in detail in Ref. [21]. The detector consists of a 12.2 m diameter sphere filled with 818 tonnes of pure mineral oil (CH_2) and is located 541 m from the beryllium target. The detector is covered by 1520 8-inch photomultiplier tubes (PMTs), where 1280 PMTs are in the interior detector region and 240 PMTs are located in the optically isolated outer veto region. Charged particles produced by neutrino interactions in the mineral oil emit both directed Cherenkov light and isotropic scintillation light that is detected by the PMTs. Event reconstruction [22] and particle identification make use of the hit PMT charge and time information, and the reconstructed neutrino energy E_ν^{QE} is estimated from the

measured energy and angle of the outgoing muon or electron, assuming the kinematics of CCQE scattering [23].

From 2002–2017, the MiniBooNE experiment has collected a total of 11.27×10^{20} protons on target (POT) in antineutrino mode, 12.84×10^{20} POT in neutrino mode, and a further 1.86×10^{20} POT in a special beam-off target mode to search for sub-GeV dark matter [24]. The neutrino sample has approximately doubled in size since the previous publication [3]. The published neutrino-mode data correspond to 6.46×10^{20} POT, while 6.38×10^{20} POT were obtained in 2016 and 2017. During the 15 years of running, the BNB and MiniBooNE detector have been stable to within 2% in neutrino energy.

The analysis is optimized to measure ν_e and $\bar{\nu}_e$ induced CCQE events, and the event reconstruction [22] and selection are identical to the previous analysis [3]. The average selection efficiency is $\sim 20\%$ ($\sim 0.1\%$) for ν_e -induced CCQE events (ν_μ -induced background events) generated over the fiducial volume. The fraction of CCQE events in antineutrino mode that are from wrong-sign neutrino events was determined from the angular distributions of muons created in CCQE interactions and by measuring CC single π^+ events [25].

The predicted but unconstrained ν_e and $\bar{\nu}_e$ CCQE background events for the neutrino energy range $200 < E_\nu^{\text{QE}} < 1250$ MeV are shown in Table I for both neutrino

TABLE I. The expected (unconstrained) number of events for the $200 < E_\nu^{\text{QE}} < 1250$ MeV neutrino energy range from all of the backgrounds in the ν_e and $\bar{\nu}_e$ appearance analysis before using the constraint from the CC ν_μ events. Also shown are the constrained background, as well as the expected number of events corresponding to the LSND best fit oscillation probability of 0.26%, assuming oscillations at large Δm^2 . The table shows the diagonal-element systematic plus statistical uncertainties, which become substantially reduced in the oscillation fits when correlations between energy bins and between the electron and muon neutrino events are included. The antineutrino numbers are from a previous analysis [3].

Process	Neutrino mode	Antineutrino mode
ν_μ & $\bar{\nu}_\mu$ CCQE	73.7 ± 19.3	12.9 ± 4.3
NC π^0	501.5 ± 65.4	112.3 ± 11.5
NC $\Delta \rightarrow N\gamma$	172.5 ± 24.1	34.7 ± 5.4
External events	75.2 ± 10.9	15.3 ± 2.8
Other ν_μ & $\bar{\nu}_\mu$	89.6 ± 22.9	22.3 ± 3.5
ν_e & $\bar{\nu}_e$ from μ^\pm decay	425.3 ± 100.2	91.4 ± 27.6
ν_e & $\bar{\nu}_e$ from K^\pm decay	192.2 ± 41.9	51.2 ± 11.0
ν_e & $\bar{\nu}_e$ from K_L^0 decay	54.5 ± 20.5	51.4 ± 18.0
Other ν_e & $\bar{\nu}_e$	6.0 ± 3.2	6.7 ± 6.0
Unconstrained bkgd.	1590.6 ± 176.9	398.2 ± 49.7
Constrained bkgd.	1577.8 ± 85.2	398.7 ± 28.6
Total data	1959	478
Excess	381.2 ± 85.2	79.3 ± 28.6
0.26% (LSND) $\nu_\mu \rightarrow \nu_e$	463.1	100.0

mode and antineutrino mode [26]. See Supplemental Material [27] for more information on backgrounds. The upper limit of 1250 MeV corresponded to a small value of L/E and was chosen by the collaboration before unblinding the data in 2007. The lower limit of 200 MeV is chosen because we constrain the ν_e events with the CCQE ν_μ events and our CCQE ν_μ event sample only goes down to 200 MeV, as we require a visible Cherenkov ring from the muon. The estimated sizes of the intrinsic ν_e and gamma backgrounds are based on MiniBooNE event measurements and uncertainties from these constraints are included in the analysis. The intrinsic $\nu_e/\bar{\nu}_e$ background from muon decay is directly related to the large sample of observed $\nu_\mu/\bar{\nu}_\mu$ events, as these events constrain the muons that decay in the 50 m decay region. This constraint uses a joint fit of the observed $\nu_\mu/\bar{\nu}_\mu$ and $\nu_e/\bar{\nu}_e$ events, assuming that there are no substantial $\nu_\mu/\bar{\nu}_\mu$ disappearance oscillations. The other intrinsic ν_e background component, from kaon decay, is constrained by fits to kaon production data and SciBooNE measurements [28]. The intrinsic ν_e background from pion decay (1.2×10^{-4} branching ratio) and hyperon decay are very small. Other backgrounds from misidentified ν_μ or $\bar{\nu}_\mu$ [29,30] events are also constrained by the observed CCQE sample.

The gamma background from neutral-current (NC) π^0 production and $\Delta \rightarrow N\gamma$ radiative decay [31,32] are constrained by the associated large two-gamma sample (mainly from Δ production) observed in the MiniBooNE data, where π^0 measurements [33] are used to constrain the π^0 background. The π^0 background measured in the first and second neutrino data sets were found to be consistent, resulting in a lower statistical background uncertainty for the combined data. Other neutrino-induced single gamma production processes are included in the theoretical predictions, which agree well with the MiniBooNE estimates [31,34]. Single-gamma backgrounds from external neutrino interactions (“dirt” backgrounds) are estimated using topological and spatial cuts to isolate the events whose vertices are near the edge of the detector and point towards the detector center [35]. With the larger data set, the background from external neutrino interactions is now better determined to be approximately 7% larger, but with smaller uncertainty than in the previous publication [3]. A new technique to measure or constrain the gamma and dirt backgrounds based on event timing relative to the beam is in development.

Systematic uncertainties are determined by considering the predicted effects on the ν_μ , $\bar{\nu}_\mu$, ν_e , and $\bar{\nu}_e$ CCQE rates from variations of uncertainty parameters. The parameters include uncertainties in the neutrino and antineutrino flux estimates, uncertainties in neutrino cross sections, most of which are determined by *in situ* cross-section measurements at MiniBooNE [29,33], uncertainties from nuclear effects, and uncertainties in detector modeling and reconstruction. A covariance matrix in bins of E_ν^{QE} is

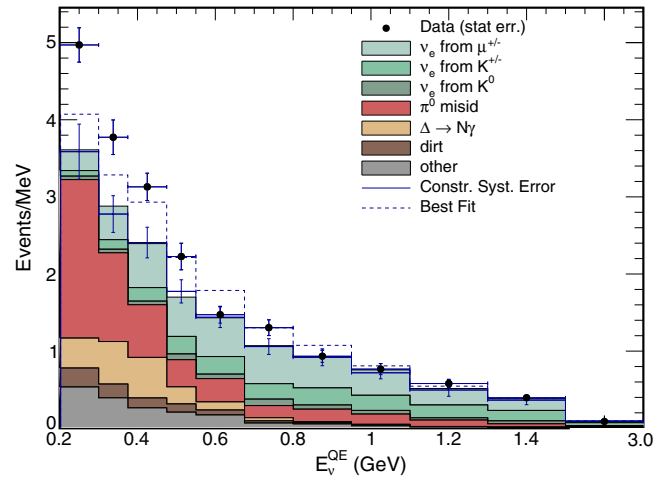


FIG. 1. The MiniBooNE neutrino mode E_ν^{QE} distributions, corresponding to the total 12.84×10^{20} POT data, for ν_e CCQE data (points with statistical errors) and background (histogram with systematic errors). The dashed curve shows the best fit to the neutrino-mode data assuming two-neutrino oscillations. The last bin is for the energy interval from 1500–3000 MeV.

constructed by considering the variation from each source of systematic uncertainty on the ν_e and $\bar{\nu}_e$ CCQE signal and background, and the ν_μ and $\bar{\nu}_\mu$ CCQE prediction as a function of E_ν^{QE} . This matrix includes correlations between any of the ν_e and $\bar{\nu}_e$ CCQE signal and background and ν_μ and $\bar{\nu}_\mu$ CCQE samples, and is used in the χ^2 calculation of the oscillation fits.

Table I also shows the expected number of events corresponding to the LSND best fit oscillation probability of 0.26%, assuming oscillations at large Δm^2 . LSND and MiniBooNE have the same average value of L/E , but MiniBooNE has a larger range of L/E . Therefore, the appearance probabilities for LSND and MiniBooNE should not be exactly the same at lower L/E values.

Figure 1 shows the E_ν^{QE} distribution for ν_e CCQE data and background in neutrino mode for the total 12.84×10^{20} POT data. Each bin of reconstructed E_ν^{QE} corresponds to a distribution of “true” generated neutrino energies, which can overlap adjacent bins. In neutrino mode, a total of 1959 data events pass the ν_e CCQE event selection requirements with $200 < E_\nu^{\text{QE}} < 1250$ MeV, compared to a background expectation of $1577.8 \pm 39.7(\text{stat}) \pm 75.4(\text{syst})$ events. The excess is then 381.2 ± 85.2 events or a 4.5σ effect. Note that the 162.0 event excess in the first 6.46×10^{20} POT data is approximately 1σ lower than the average excess, while the 219.2 event excess in the second 6.38×10^{20} POT data is approximately 1σ higher than the average excess. Figure 2 shows the excess events in neutrino mode from the first 6.46×10^{20} POT data and the second 6.38×10^{20} POT data (top plot). Combining the MiniBooNE neutrino and anti-neutrino data, there are a total of 2437 events in the $200 < E_\nu^{\text{QE}} < 1250$ MeV energy region, compared to a background

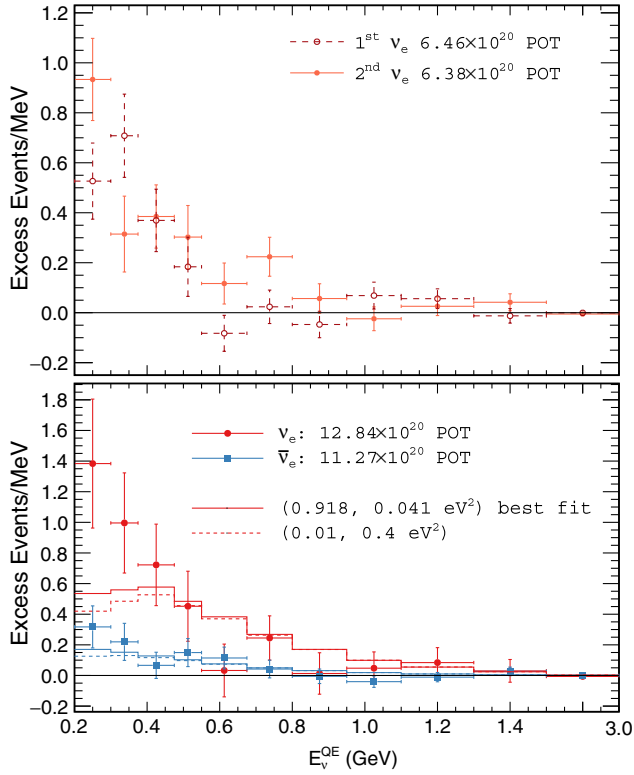


FIG. 2. The top plot shows the MiniBooNE event excesses in neutrino mode as a function of E_{ν}^{QE} from the first 6.46×10^{20} POT data and the second 6.38×10^{20} POT data. The bottom plot shows the total event excesses in both neutrino mode and antineutrino mode, corresponding to 12.84×10^{20} POT and 11.27×10^{20} POT, respectively. The solid (dashed) curve is the best fit (1σ fit point) to the neutrino-mode and antineutrino-mode data assuming two-neutrino oscillations. The last bin is for the energy interval from 1500–3000 MeV. Error bars include only statistical uncertainties for the top plot and both statistical and correlated systematic uncertainties for the bottom plot.

expectation of $1976.5 \pm 44.5(\text{stat}) \pm 88.5(\text{syst})$ events. This corresponds to a total ν_e plus $\bar{\nu}_e$ CCQE excess of 460.5 ± 99.0 events with respect to expectation or a 4.7σ excess. Figure 2 (bottom plot) shows the total event excesses as a function of E_{ν}^{QE} in both neutrino mode and antineutrino mode. The dashed curves show the two-neutrino oscillation predictions at the best-fit point ($\Delta m^2 = 0.041 \text{ eV}^2$, $\sin^2 2\theta = 0.92$), as well as at a point within 1σ of the best-fit point ($\Delta m^2 = 0.4 \text{ eV}^2$, $\sin^2 2\theta = 0.01$).

A two-neutrino model is assumed for the MiniBooNE oscillation fits in order to compare with the LSND data. However, the appearance neutrino experiments appear to be incompatible with the disappearance neutrino experiments in a $3 + 1$ model [10,12], and other models [15–19] may provide better fits to the data. The oscillation parameters are extracted from a combined fit of the observed E_{ν}^{QE} event distributions for muonlike and electronlike events using the full covariance matrix described previously in the full

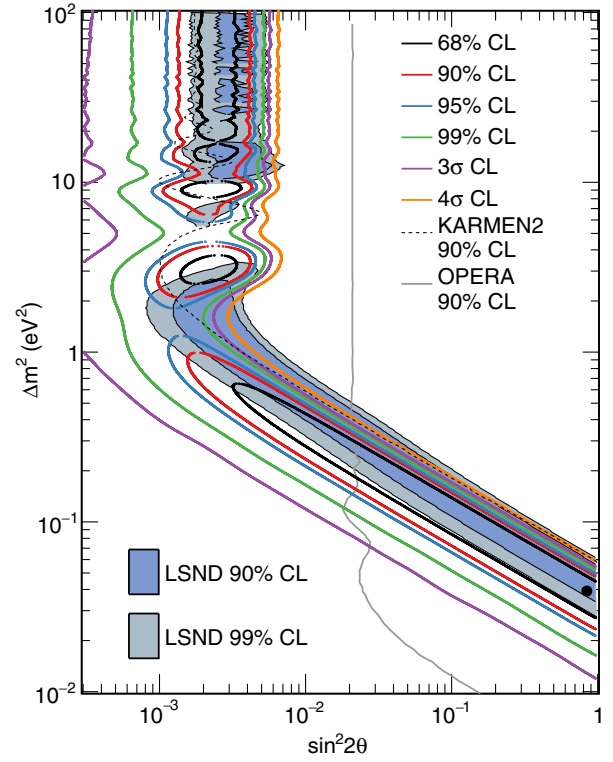


FIG. 3. MiniBooNE allowed regions in neutrino mode (12.84×10^{20} POT) for events with $200 < E_{\nu}^{\text{QE}} < 3000$ MeV within a two-neutrino oscillation model. The shaded areas show the 90% and 99% C.L. LSND $\bar{\nu}_{\mu} \rightarrow \bar{\nu}_e$ allowed regions. The black point shows the MiniBooNE best fit point. Also shown are 90% C.L. limits from the KARMEN [36] and OPERA [37] experiments.

energy range $200 < E_{\nu}^{\text{QE}} < 3000$ MeV. The fit assumes the same oscillation probability for both the right-sign ν_e and wrong-sign $\bar{\nu}_e$, and no ν_{μ} , $\bar{\nu}_{\mu}$, ν_e , or $\bar{\nu}_e$ disappearance. Using a likelihood-ratio technique [3], the confidence level values for the fitting statistic, $\Delta\chi^2 = \chi^2(\text{point}) - \chi^2(\text{best})$, as a function of oscillation parameters, Δm^2 and $\sin^2 2\theta$, is determined from frequentist, fake data studies. The fake data studies also determine the effective number of degrees of freedom and probabilities. With this technique, the best neutrino oscillation fit in neutrino mode occurs at $(\Delta m^2, \sin^2 2\theta) = (0.039 \text{ eV}^2, 0.84)$, as shown in Fig. 3. The χ^2/ndf for the best-fit point in the energy range $200 < E_{\nu}^{\text{QE}} < 1250$ MeV is $9.9/6.7$ with a probability of 15.5%. The background-only fit has a χ^2 probability of 0.06% relative to the best oscillation fit and a $\chi^2/\text{ndf} = 24.9/8.7$ with a probability of 0.21%. Figure 3 shows the MiniBooNE closed confidence level (C.L.) contours for ν_e appearance oscillations in neutrino mode in the $200 < E_{\nu}^{\text{QE}} < 3000$ MeV energy range.

Nuclear effects associated with neutrino interactions on carbon can affect the reconstruction of the neutrino energy, E_{ν}^{QE} , and the determination of the neutrino oscillation

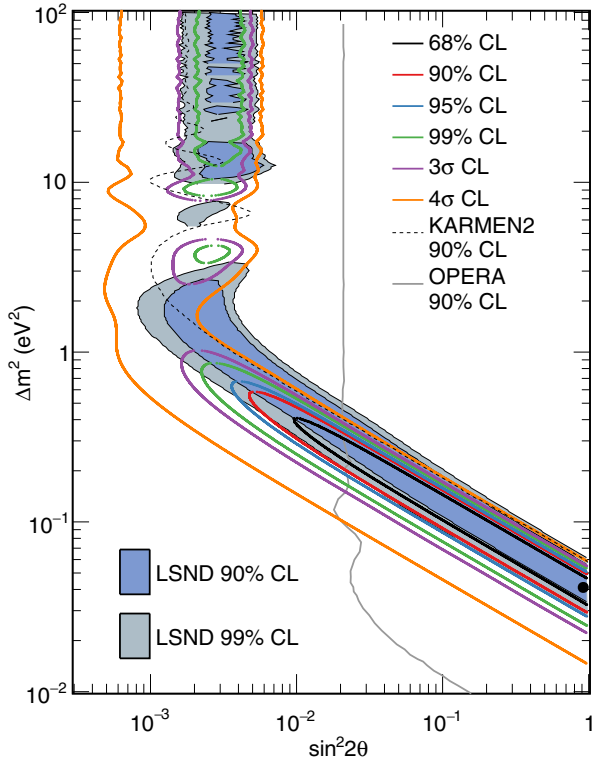


FIG. 4. MiniBooNE allowed regions for a combined neutrino mode (12.84×10^{20} POT) and antineutrino mode (11.27×10^{20} POT) data sets for events with $200 < E_\nu^{\text{QE}} < 3000$ MeV within a two-neutrino oscillation model. The shaded areas show the 90% and 99% C.L. LSND $\bar{\nu}_\mu \rightarrow \bar{\nu}_e$ allowed regions. The black point shows the MiniBooNE best fit point. Also shown are 90% C.L. limits from the KARMEN [36] and OPERA [37] experiments.

parameters [38]. These effects were studied previously [3,39] and were found to not affect substantially the oscillation fit. In addition, they do not affect the gamma background, which is determined from direct measurements of NC π^0 and dirt backgrounds.

Figure 4 shows the MiniBooNE allowed regions in both neutrino mode and antineutrino mode [3] for events with $200 < E_\nu^{\text{QE}} < 3000$ MeV within a two-neutrino oscillation model. For this oscillation fit the entire data set is used and includes the 12.84×10^{20} POT data in neutrino mode and the 11.27×10^{20} POT data in antineutrino mode. As shown in the figure, the MiniBooNE 1σ allowed region lies mostly within the LSND 90% C.L. band, which demonstrates good agreement between the LSND and MiniBooNE signals. Also shown are 90% C.L. limits from the KARMEN [36] and OPERA [37] experiments. The KARMEN2 90% C.L. limits are outside the MiniBooNE 95% C.L. allowed region, while the OPERA 90% C.L. limits disfavor the MiniBooNE allowed region below approximately 0.3 eV². The best combined neutrino oscillation fit occurs at $(\Delta m^2, \sin^2 2\theta) = (0.041 \text{ eV}^2, 0.92)$. The χ^2/ndf for the best-fit point in the energy range $200 < E_\nu^{\text{QE}} < 1250$ MeV

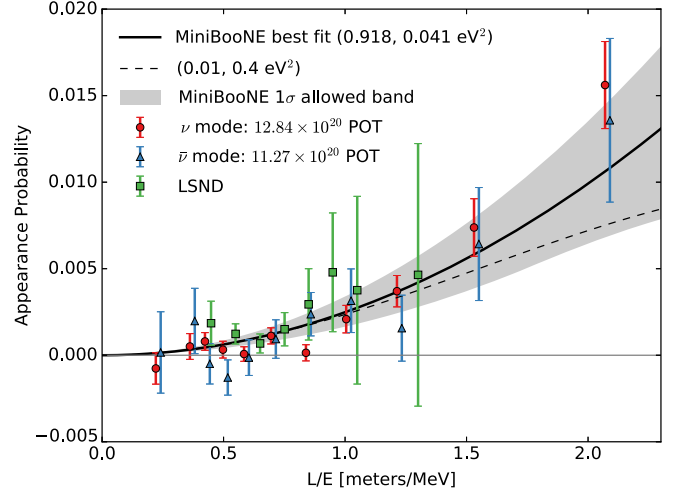


FIG. 5. A comparison between the L/E_ν^{QE} distributions for the MiniBooNE data excesses in neutrino mode (12.84×10^{20} POT) and antineutrino mode (11.27×10^{20} POT) to the L/E distribution from LSND [1]. The error bars show statistical uncertainties only. The curves show fits to the MiniBooNE data, assuming two-neutrino oscillations, while the shaded area is the MiniBooNE 1σ allowed band. The best-fit curve uses the reconstructed neutrino energy E_ν^{QE} for the MiniBooNE data. The dashed curve shows the example 1σ fit point.

is 19.4/15.6 with a probability of 21.1%, and the background-only fit has a χ^2 probability of 6×10^{-7} relative to the best oscillation fit and a $\chi^2/\text{ndf} = 47.1/17.3$ with a probability of 0.02%.

Figure 5 compares the L/E_ν^{QE} distributions for the MiniBooNE data excesses in neutrino mode and antineutrino mode to the L/E distribution from LSND [1]. The error bars show statistical uncertainties only. As shown in the figure, there is agreement among all three data sets. Assuming two-neutrino oscillations, the curves show fits to the MiniBooNE data described above. Fitting both MiniBooNE and LSND data, by adding LSND L/E data as additional terms, the best fit occurs at $(\Delta m^2, \sin^2 2\theta) = (0.041 \text{ eV}^2, 0.96)$ with a $\chi^2/\text{ndf} = 22.4/22.4$, corresponding to a probability of 42.5%. The MiniBooNE excess of events in both oscillation probability and L/E spectrum is, therefore, consistent with the LSND excess of events. The significance of the combined LSND (3.8σ) [1] and MiniBooNE (4.7σ) excesses is 6.0σ , which is obtained by adding the significances in quadrature, as the two experiments have completely different neutrino energies, neutrino fluxes, reconstructions, backgrounds, and systematic uncertainties.

In summary, the MiniBooNE experiment observes a total ν_e CCQE event excess in both neutrino and antineutrino running modes of 460.5 ± 99.0 events (4.7σ) in the energy range $200 < E_\nu^{\text{QE}} < 1250$ MeV. The MiniBooNE allowed region from a two-neutrino oscillation fit to the data, shown in Fig. 4, is consistent with the allowed region reported by

the LSND experiment [1]. On the other hand, a two-neutrino oscillation interpretation of the data would require at least four neutrino types and indicate physics beyond the three neutrino paradigm. The significance of the combined LSND and MiniBooNE excesses is 6.0σ . All of the major backgrounds are constrained by *in situ* event measurements, so nonoscillation explanations would need to invoke new anomalous background processes. Although the data are fit with a two-neutrino oscillation model, other models may provide better fits to the data. The MiniBooNE event excess will be further studied by the Fermilab short-baseline neutrino (SBN) program [40].

We acknowledge the support of Fermilab, the Department of Energy, and the National Science Foundation, and we acknowledge Los Alamos National Laboratory for LDRD funding.

*Deceased.

- [1] C. Athanassopoulos *et al.*, *Phys. Rev. Lett.* **75**, 2650 (1995); **77**, 3082 (1996); **81**, 1774 (1998); *Phys. Rev. C.* **54**, 2685 (1996); **58**, 2489 (1998); A. Aguilar *et al.*, *Phys. Rev. D* **64**, 112007 (2001).
- [2] A. A. Aguilar-Arevalo *et al.*, *Phys. Rev. Lett.* **98**, 231801 (2007); **102**, 101802 (2009); **105**, 181801 (2010).
- [3] A. A. Aguilar-Arevalo *et al.*, *Phys. Rev. Lett.* **110**, 161801 (2013).
- [4] G. Mention, M. Fechner, T. Lasserre, T. A. Mueller, D. Lhuillier, M. Cribier, and A. Letourneau, *Phys. Rev. D* **83**, 073006 (2011).
- [5] C. Giunti and M. Laveder, *Phys. Rev. C* **83**, 065504 (2011).
- [6] M. Sorel, J. M. Conrad, and M. H. Shaevitz, *Phys. Rev. D* **70**, 073004 (2004).
- [7] G. Karagiorgi, Z. Djurcic, J. M. Conrad, M. H. Shaevitz, and M. Sorel, *Phys. Rev. D* **80**, 073001 (2009); **81**, 039902(E) (2010).
- [8] G. H. Collin, C. A. Argüelles, J. M. Conrad, and M. H. Shaevitz, *Phys. Rev. Lett.* **117**, 221801 (2016).
- [9] C. Giunti and M. Laveder, *Phys. Lett. B* **706**, 200 (2011); *Phys. Rev. D* **84**, 073008 (2011).
- [10] S. Gariazzo, C. Giunti, M. Laveder, and Y. F. Li, *J. High Energy Phys.* **06** (2017) 135.
- [11] J. Kopp, M. Maltoni, and T. Schwetz, *Phys. Rev. Lett.* **107**, 091801 (2011); J. Kopp and P. A. N. Machado, *J. High Energy Phys.* **05** (2013) 050.
- [12] M. Dentler, A. Hernandez-Cabezudo, J. Kopp, P. Machado, M. Maltoni, I. Martinez-Soler, and T. Schwetz, *J. High Energy Phys.* **08** (2018) 010.
- [13] K. N. Abazajian *et al.*, arXiv:1204.5379.
- [14] J. M. Conrad, C. M. Ignarra, G. Karagiorgi, M. H. Shaevitz, and J. Spitz, *Adv. High Energy Phys.* **2013**, 163897 (2013).
- [15] J. Asaadi, E. Church, R. Guenette, B. J. P. Jones, and A. M. Szelc, *Phys. Rev. D* **97**, 075021 (2018); G. Karagiorgi, M. H. Shaevitz, and J. M. Conrad, arXiv:1202.1024; H. Pas, S. Pakvasa, and T. J. Weiler, *Phys. Rev. D* **72**, 095017 (2005); D. Doring, H. Paes, P. Sicking, and T. J. Weiler, arXiv:1808.07460.
- [16] V. A. Kostelecky and M. Mewes, *Phys. Rev. D* **69**, 016005 (2004); T. Katori, V. A. Kostelecky, and R. Tayloe, *Phys. Rev. D* **74**, 105009 (2006); J. S. Diaz and V. A. Kostelecky, *Phys. Lett. B* **700**, 25 (2011); *Phys. Rev. D* **85**, 016013 (2012).
- [17] S. N. Gninenko, *Phys. Rev. Lett.* **103**, 241802 (2009); S. N. Gninenko and D. S. Gorbunov, *Phys. Rev. D* **81**, 075013 (2010); Y. Bai, R. Lu, S. Lu, J. Salvado, and B. A. Stefanek, *Phys. Rev. D* **93**, 073004 (2016); Z. Moss, M. H. Moulai, C. A. Argüelles, and J. M. Conrad, *Phys. Rev. D* **97**, 055017 (2018); E. Baertuzzo, S. Jana, P. A. N. Machado, and R. Z. Funchal, arXiv:1807.09877; P. Ballett, S. Pascoli, and M. Ross-Lonergan, arXiv:1808.02915.
- [18] J. Liao and D. Marfatia, *Phys. Rev. Lett.* **117**, 071802 (2016).
- [19] M. Carena, Y.-Y. Li, C. S. Machado, and P. A. N. Machado, and C. E. M. Wagner, *Phys. Rev. D* **96**, 095014 (2017).
- [20] A. A. Aguilar-Arevalo *et al.*, *Phys. Rev. D* **79**, 072002 (2009).
- [21] A. A. Aguilar-Arevalo *et al.*, *Nucl. Instrum. Methods Phys. Res., Sect. A* **599**, 28 (2009).
- [22] R. B. Patterson, E. M. Laird, Y. Liu, P. D. Meyers, I. Stancu, and H. A. Tanaka, *Nucl. Instrum. Methods Phys. Res., Sect. A* **608**, 206 (2009).
- [23] A. A. Aguilar-Arevalo *et al.*, *Phys. Rev. D* **81**, 092005 (2010); *Phys. Rev. D* **88**, 032001 (2013).
- [24] A. A. Aguilar-Arevalo *et al.* (MiniBooNE Collaboration), *Phys. Rev. Lett.* **118**, 221803 (2017); arXiv:1807.06137.
- [25] A. A. Aguilar-Arevalo *et al.*, *Phys. Rev. D* **84**, 072005 (2011).
- [26] R. B. Patterson, Ph. D. thesis, Princeton University, 2007, http://www-boone.fnal.gov/publications/Papers/rbpatter_thesis.pdf.
- [27] See Supplemental Material at <http://link.aps.org/supplemental/10.1103/PhysRevLett.121.221801> for more information on backgrounds and plots showing agreement between data and the Monte Carlo simulation.
- [28] G. Cheng *et al.*, *Phys. Rev. D* **84**, 012009 (2011); C. Mariani, G. Cheng, J. M. Conrad, and M. H. Shaevitz, *Phys. Rev. D* **84**, 114021 (2011).
- [29] A. A. Aguilar-Arevalo *et al.*, *Phys. Rev. D* **81**, 092005 (2010); *Phys. Rev. Lett.* **100**, 032301 (2008).
- [30] A. A. Aguilar-Arevalo *et al.*, *Phys. Rev. D* **83**, 052007 (2011); *Phys. Rev. Lett.* **103**, 081801 (2009).
- [31] V. P. Efrosinin, Yu. G. Kudenko, and A. N. Khotjantsev, *Phys. At. Nucl.* **72**, 459 (2009); R. J. Hill, *Phys. Rev. D* **81**, 013008 (2010); *Phys. Rev. D* **84**, 017501 (2011); X. Zhang and B. D. Serot, *Phys. Lett. B* **719**, 409 (2013); *Phys. Rev. C* **86**, 035502 (2012); **86**, 035504 (2012); B. D. Serot and X. Zhang, *Phys. Rev. C* **86**, 015501 (2012).
- [32] E. Wang, L. Alvarez-Ruso, and J. Nieves, *Phys. Rev. C* **89**, 015503 (2014); *Phys. Lett. B* **740**, 16 (2015).
- [33] A. A. Aguilar-Arevalo *et al.*, *Phys. Rev. D* **81**, 013005 (2010); *Phys. Lett. B* **664**, 41 (2008).
- [34] D. Rein and L. M. Sehgal, *Phys. Lett.* **104B**, 394 (1981); S. S. Gershtein, Yu. Ya. Komachenko, and M. Yu. Khlopov, *Sov. J. Nucl. Phys.* **33**, 860 (1981); J. A. Harvey, C. T. Hill, and R. J. Hill, *Phys. Rev. Lett.* **99**, 261601 (2007); J. P. Jenkins and T. Goldman, *Phys. Rev. D* **80**, 053005 (2009); A. M. Ankowski, O. Benhar, T. Mori, R. Yamaguchi, and M. Sakuda, *Phys. Rev.*

- Lett. **108**, 052505 (2012); K. M. Graczyk, D. Kielczewska, P. Przewlocki, and J. T. Sobczyk, *Phys. Rev. D* **80**, 093001 (2009).
- [35] A. A. Aguilar-Arevalo *et al.*, *Phys. Rev. Lett.* **102**, 101802 (2009).
- [36] B. Armbruster *et al.*, *Phys. Rev. D* **65**, 112001 (2002).
- [37] N. Agafonova *et al.*, [arXiv:1803.11400](https://arxiv.org/abs/1803.11400).
- [38] M. Martini, M. Ericson, G. Chanfray, and J. Marteau, *Phys. Rev. C* **80**, 065501 (2009); M. Martini, M. Ericson, and G. Chanfray, *Phys. Rev. D* **85**, 093012 (2012); **87**, 013009 (2013); D. Meloni and M. Martini, *Phys. Lett. B* **716**, 186 (2012); J. Nieves, I. R. Simo, and M. J. Vicente Vacas, *Phys. Rev. C* **83**, 045501 (2011); J. Nieves, F. Sanchez, I. R. Simo, and M. J. Vicente Vacas, *Phys. Rev. D* **85**, 113008 (2012); O. Lalakulich, K. Gallmeister, and U. Mosel, *Phys. Rev. C* **86**, 014614 (2012); U. Mosel, O. Lalakulich, and K. Gallmeister, *Phys. Rev. Lett.* **112**, 151802 (2014); A. Meucci and C. Giusti, *Phys. Rev. D* **85**, 093002 (2012); G. D. Megias *et al.*, *Phys. Rev. D* **91**, 073004 (2015); P. Coloma and P. Huber, *Phys. Rev. Lett.* **111**, 221802 (2013); J. T. Sobczyk, *Phys. Rev. C* **86**, 015504 (2012).
- [39] M. Ericson, M. V. Garzelli, C. Giunti, and M. Martini, *Phys. Rev. D* **93**, 073008 (2016).
- [40] M. Antonello *et al.*, [arXiv:1503.01520](https://arxiv.org/abs/1503.01520).

3.1 Current Results

Since the publication above, MiniBooNE collected its final batch of data and published results in Ref [9]. Compared to the publication above, the data sample increased from 12.84×10^{20} protons-on-target to 18.75×10^{20} . The primary results were already presented in Section 2.1.2, but we reiterate them here.

In neutrino mode, 2870 events were observed, with an expectation of $2309.4 \pm 48.1(\text{stat.}) \pm 109.5(\text{syst.})$, giving an excess of $560.6 \pm 119.6(4.7\sigma)$. In antineutrino mode, 478 events were observed with an expectation of 400.6 ± 28.5 , giving an excess of 77.4 ± 28.5 . Combined, this gives a total excess of $638.0 \pm 52.1(\text{stat.}) \pm 122.2(\text{syst.})$, with a significance of 4.8σ , corresponding to a p-value of $p = 1.59 \times 10^{-6}$. The excess is plotted in Figure 2-2. If fitted to a 3+1 model, the p-value jumps to $p = 0.123$.

Chapter 4

Global Data Fits to Sterile Neutrino Models

In Chapter 2, we introduced a few experimental observations that have pointed toward the existence of sterile neutrinos, as well as introduced some sterile neutrino models. In this chapter we will test these sterile neutrino models against the global collection of SBL neutrino oscillation data.

For this study, we consider $P(\nu_e \rightarrow \nu_e)$, $P(\nu_\mu \rightarrow \nu_\mu)$, and $P(\nu_\mu \rightarrow \nu_e)$ CC neutrino and antineutrino oscillation channels. Assuming the 3+1 model, Equations (2.9) and (2.10) show that these oscillation channels are respectively sensitive to $|U_{e4}|^2$, $|U_{\mu4}|^2$, and $|U_{e4}||U_{\mu4}|$; the equations governing the different oscillation channels are not independent. Therefore, not only can preferred values of the mixing parameters be determined from global fits, the internal consistency of the models can also be tested. In fact, as we will see in Section 4.3, the minimal 3+1 sterile neutrino model suffers from internal inconsistencies that motivate the consideration of more complex models.

In this chapter we summarize the experiments that go into our fits, as well as the limits they have placed on their own. A table of the experiments in our fits is shown in Table 4.1. We then review the methodology of our fits, and end with the results.

The contents of this chapter can be seen as an update of the work in Ref. [34].

	$\nu_\mu \rightarrow \nu_e$	$\nu_\mu \rightarrow \nu_\mu$	$\nu_e \rightarrow \nu_e$
Neutrino	MiniBooNE (BNB) MiniBooNE(NuMI) NOMAD	SciBooNE/MiniBooNE CCFR CDHS MINOS	KARMEN/LSND Cross Section Gallium BEST
Antineutrino	LSND KARMEN MiniBooNE (BNB)	SciBooNE/MiniBooNE CCFR MINOS	Bugey NEOS DANSS PROSPECT STEREO Neutrino-4

Table 4.1: The collection of experiments that go into the global fits in this thesis.

4.1 Experiments

The experiments included in our fits fall into one of three groups: ν_e appearance ($P(\nu_\mu \rightarrow \nu_e)$ & $P(\bar{\nu}_\mu \rightarrow \bar{\nu}_e)$), ν_e disappearance ($P(\nu_e \rightarrow \nu_e)$ & $P(\bar{\nu}_e \rightarrow \bar{\nu}_e)$), and ν_μ disappearance ($P(\nu_\mu \rightarrow \nu_\mu)$ & $P(\bar{\nu}_\mu \rightarrow \bar{\nu}_\mu)$).

In this section, we give a short summary of each experience and their individual findings. For each experiment, we provide the 3+1 confidence regions released by the collaborations, if available. In Figures 4-6, 4-9, 4-16 and 4-24, we also provide the 3+1 confidence regions we recover in our implementation of these datasets for our global fits. Later we will look at what the combined data tells us.

4.1.1 $P(\nu_\mu \rightarrow \nu_e)$ & $P(\bar{\nu}_\mu \rightarrow \bar{\nu}_e)$

LSND [8]

The **L**iquid **S**cintillator **N**eutrino **D**etector (LSND) experiment ran 1993–1998 at the Los Alamos Neutron Science Center (LANSCE), searching for $\bar{\nu}_\mu \rightarrow \bar{\nu}_e$ oscillations. As reviewed in Section 2.1.1, the $\bar{\nu}_\mu$ beam was created by impinging a 798 MeV proton beam on a target and allowing the subsequent μ^+ 's to decay at rest into $\bar{\nu}_\mu$'s. The neutrinos would then propagate 30 m towards a cylindrical tank 8.3 m long by 5.7 m in diameter filled with 167 metric tons of liquid scintillator. The oscillated $\bar{\nu}_e$ would then inverse beta decay like $\bar{\nu}_e + p \rightarrow e^+ + n$, producing a signal from the positron followed by a coincident 2.2 MeV γ when the neutron captures. With this required coincident signal, LSND would select events with positron energies in the range $20 < E_e < 60$ MeV.

LSND observed an excess of $87.9 \pm 22.4 \pm 6.0$ events above background, corresponding to an oscillation probability of $(0.264 \pm 0.067 \pm 0.04)\%$. The 90% confidence region is shown in Figure 4-1b.

For our fits, we use the data shown in Figure 4-1a. Note that these data are a cleaner subset of the total LSND data. Events with $R_\gamma > 10$ are chosen, where R_γ is defined as the likelihood ratio that the neutron-captured γ observed is correlated to the initial signal versus accidental. Here, the event excess is $32.2 \pm 9.4 \pm 2.3$. More details on the R_γ selection can be found in Ref. [8].

The 3+1 results of our implementation of LSND is shown in Figure 4-6a.

KARMEN [35]

The **K**arlsruhe **R**utherford **M**edium **E**nergy **N**eutrino (KARMEN) experiment was another accelerator beam experiment similar to LSND, located at the spallation neutrino source ISIS at the Rutherford Laboratory in the UK, running 1997–2001. KARMEN searched for $\bar{\nu}_\mu \rightarrow \bar{\nu}_e$ oscillations using a 800 MeV proton beam to produce a DAR neutrino beam like LSND. The detector was placed 17.7 m away from the target and, unlike LSND, at an angle 100° off the proton beam, reducing beam backgrounds.

With a background prediction of 15.8 ± 0.5 events, KARMEN observed 15 events, well within expectations and finding no evidence for oscillations. Figure 4-2 plots

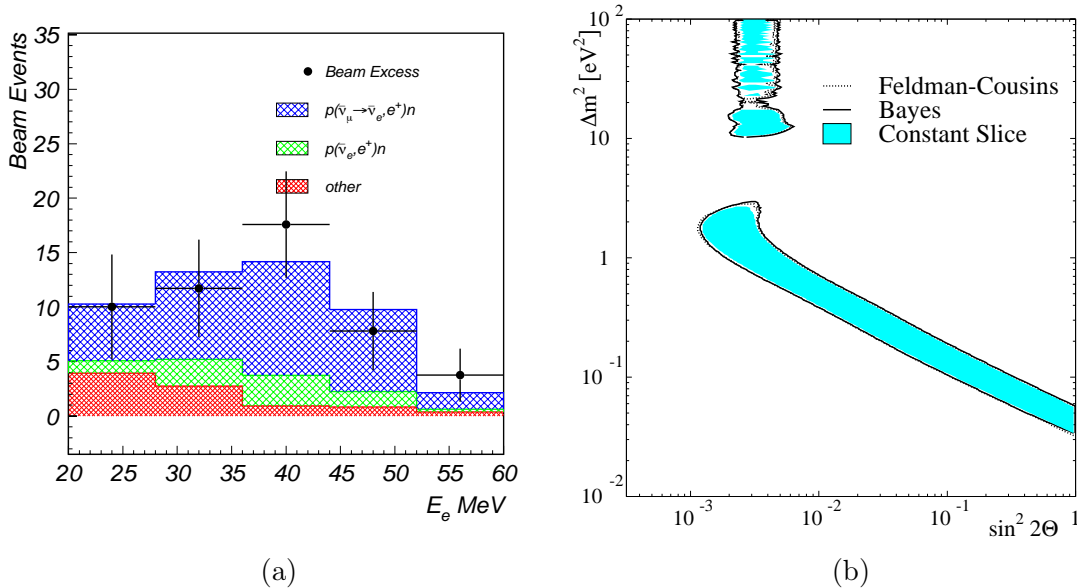


Figure 4-1: (a) The beam excess observed at LSND with the cut $R_\gamma > 10$. The red and green histograms are the expected beam-on backgrounds, and the blue histogram is the expected event rates with the best fit 3+1 oscillation hypothesis. (b) The best fit contours at the 90% confidence level. Figures from Ref. [8]

KARMEN’s 90% confidence level exclusion, compared with other experiments at the time. The 3+1 results of our implementation of KARMEN is shown in Figure 4-6b.

MiniBooNE (BNB) [9, 10]

The MiniBooNE experiment has already been described in detail in Chapter 3, and we simply refer to that chapter. The “BNB” in the experiment title refers to the Booster Neutrino Beam, which is the primary source of MiniBooNE’s neutrino flux.

The 3+1 results of our neutrino and antineutrino combined MiniBooNE fit is shown in Figure 4-6c.

MiniBooNE (NuMI) [36]

In addition to the BNB beam line, the MiniBooNE detector could also observe neutrinos from the NuMI beam line. The NuMI beam produces neutrinos for the MINOS detectors by accelerating 120 GeV protons into a carbon target. The MiniBooNE detector is located 745 m from the NuMI production target, and at an angle 6.3° off the NuMI beam axis. Using data collected in 2005–2007, MiniBooNE searched for possible $\nu_\mu \rightarrow \nu_e$ oscillations from the NuMI target. The data was selected to be in the energy range $0.2 < E_\nu < 3$ GeV, and is shown in Figure 4-3. The observed data falls within the expectation, but with large systematic uncertainties in the expectation. It’s noted that in the low energy region $E_\nu < 0.9$ GeV the data are systematically high at the 1.2σ level.

The 3+1 results of our implementation of MiniBooNE-NuMI is shown in Figure 4-6d.

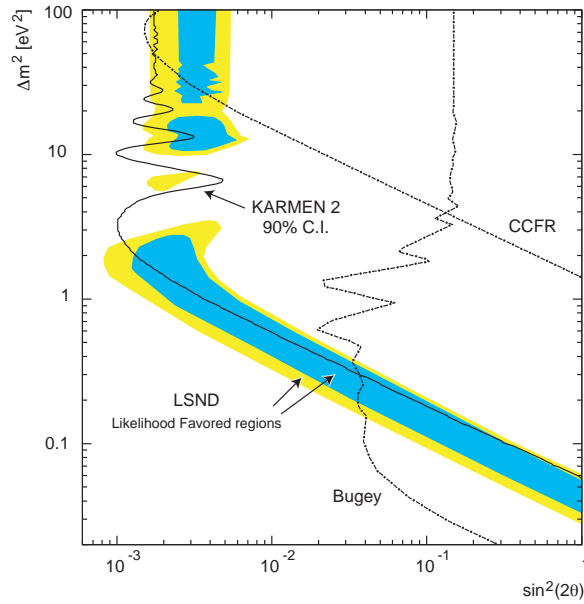


Figure 4-2: Comparison of KARMEN’s confidence region at the 90% confidence level with LSND’s. Included in this plot are exclusions from two other experiments, CCFR and Bugey. We discuss these experiments below. Figure from Ref. [35].

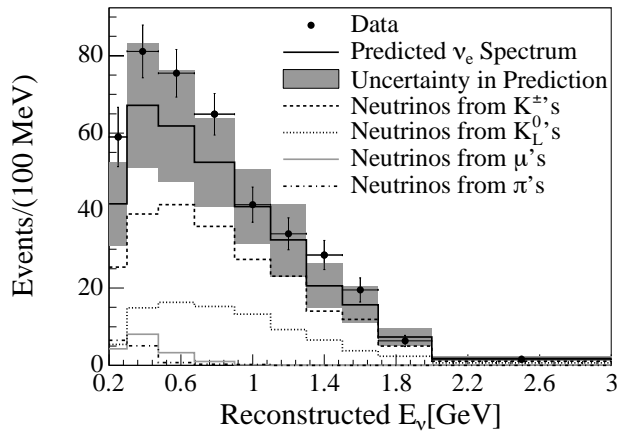


Figure 4-3: The observed ν_e event distribution in the MiniBooNE detector from the NuMI beam. While the observed data lies within the expectation, the expected distribution suffers from large systematic uncertainties. Figure from Ref. [36].

NOMAD [37]

The Neutrino Oscillation Magnetic Detector (NOMAD) experiment was designed to search for $\nu_\mu \rightarrow \nu_\tau$ oscillations using the neutrino beam produced by the 450 GeV proton synchrotron (SPS) at CERN. The proton beam impinged a series of beryllium rods, producing secondary particles which were then focused by two magnetic lenses and led into a 290 m decay tunnel. The neutrinos, on average, traveled 625 m before reaching the NOMAD detector. The detector was designed to identify electrons from $\tau^- \rightarrow e^- + \bar{\nu}_e + \nu_\tau$ decays. This allowed the detector to also search for $\nu_\mu \rightarrow \nu_e$ oscillations, motivated by the observations from LSND.

The NOMAD experiment conducted such a search using data collected 1995–1998. In order to reduce systematic uncertainties, the experiment studied the ratio $R_{e\mu}$ of ν_e to ν_μ CC interactions. Additionally, the experiment took into account the energy and radial distribution of the neutrino beam. The selected energy range extended up to 300 GeV, with a peak at ~ 40 GeV. This relatively large $\langle L \rangle / \langle E \rangle \sim 0.02$ gave NOMAD sensitivity to a larger Δm^2 compared to LSND. The data is binned as a function of visible energy, which is taken as an approximation of the neutrino energy.

The observed ratios $R_{e\mu}$ are shown in Figure 4-4. The observed data was consistent with the null hypothesis, and therefore excludes the LSND preferred parameter space at $\Delta m^2 \gtrsim 10 \text{ eV}^2$. The exclusion is shown in Figure 4-5.

The 3+1 results of our implementation of NOMAD is shown in Figure 4-6e.

4.1.2 $P(\nu_e \rightarrow \nu_e)$ & $P(\bar{\nu}_e \rightarrow \bar{\nu}_e)$

KARMEN/LSND (cross section) [38]

In addition to the $\bar{\nu}_\mu \rightarrow \bar{\nu}_e$ appearance analysis described above, both LSND and KARMEN conducted a measurement of the ν_e CC interaction cross section on ^{12}C [39–41]. Like $\bar{\nu}_e$ interactions, ν_e interactions can be tagged by a coincident signal. First, the incoming ν_e undergoes the IBD interaction $\nu_e + ^{12}\text{C} \rightarrow ^{12}\text{N}_{\text{gs}} + e^-$. Then, the ^{12}N ground state decays like $^{12}\text{N}_{\text{gs}} \rightarrow ^{12}\text{C} + e^+ + \nu_e$ with a Q-value of 16.3 MeV and a lifetime of 15.9 ms. The observed e^- , followed by a e^+ , allows the tagging of ν_e events, and a cross section measurement can be made.

In practice, the measured cross section will be *flux-averaged*, so that the measured quantity will depend on the flux knowledge. If the ν_e flux is low, then the measured cross section will be low compared to theoretical predictions. Therefore, the measured cross section can be used to place limits on the disappearance of the ν_e flux by comparing the measured cross section versus expectation.

The measured cross sections, compared to theoretical predictions, are shown in Figure 4-7a. No indication for oscillations is seen, and a limit is placed on $\nu_e \rightarrow \nu_e$ disappearance. Figure 4-7b shows the extracted limits.

The result of our 3+1 KARMEN/LSND cross section fit is shown in Figure 4-7b.

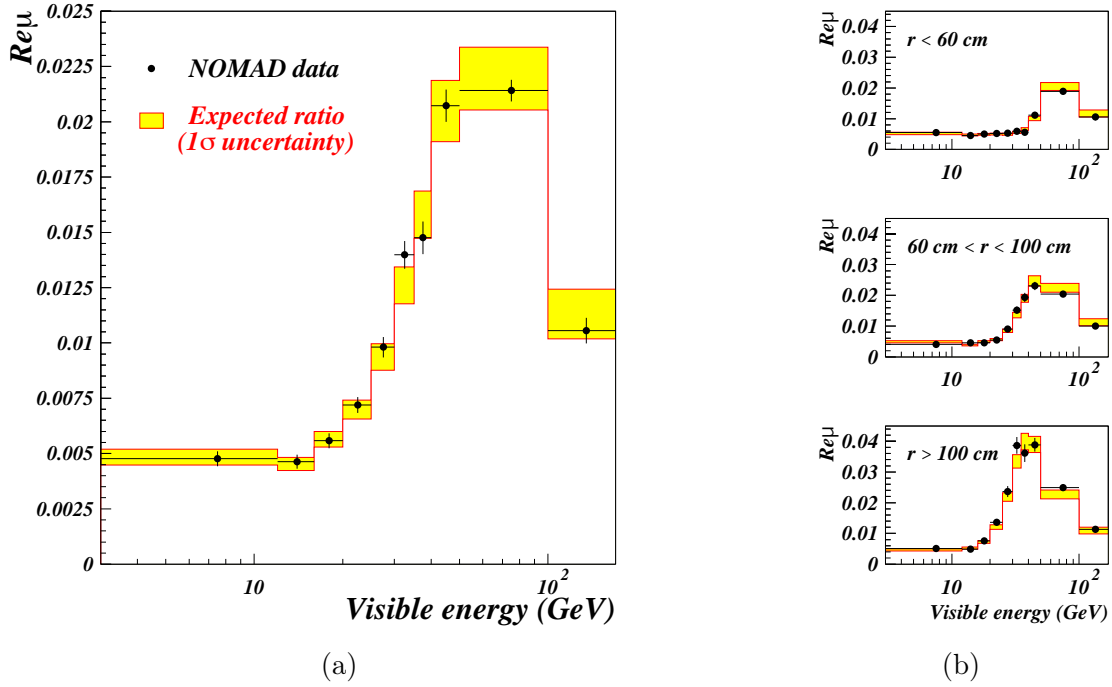


Figure 4-4: (a) The observed ratios $R_{e\mu}$ versus expectation at the NOMAD detector, with 1σ bands in yellow. (b) The observed ratios $R_{e\mu}$ and expectation, separated by radial distribution. Figures from Ref. [37].

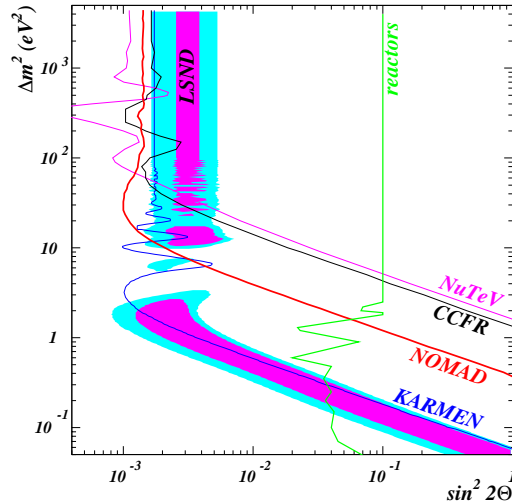
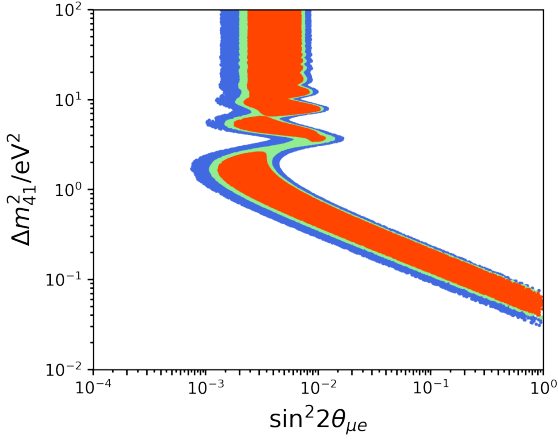
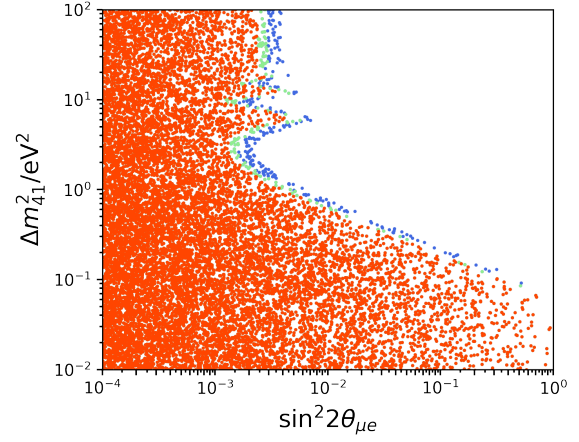


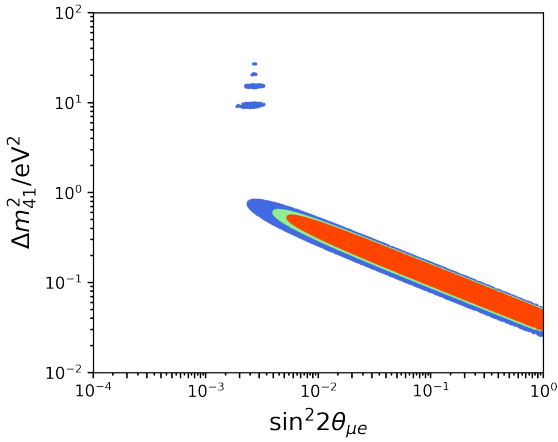
Figure 4-5: The 90% NOMAD exclusion region, compared with other SBL experiments available at the time of the NOMAD analysis. We have discussed several of these experiments in this section. Figure from Ref. [37].



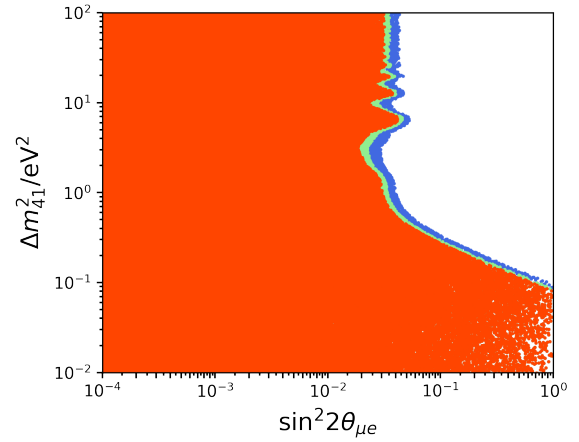
(a) LSND



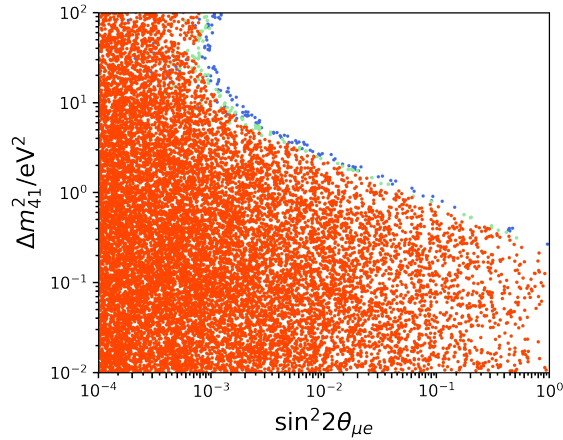
(b) KARMEN



(c) MiniBooNE (BNB)



(d) MiniBooNE (NuMI)



(e) NOMAD

Figure 4-6: 3+1 fits to the $\nu_\mu \rightarrow \nu_e$ & $\bar{\nu}_\mu \rightarrow \bar{\nu}_e$ appearance oscillation data used in our global fits. The 90%, 95%, and 99% confidence regions correspond to the red, green, and blue points respectively.

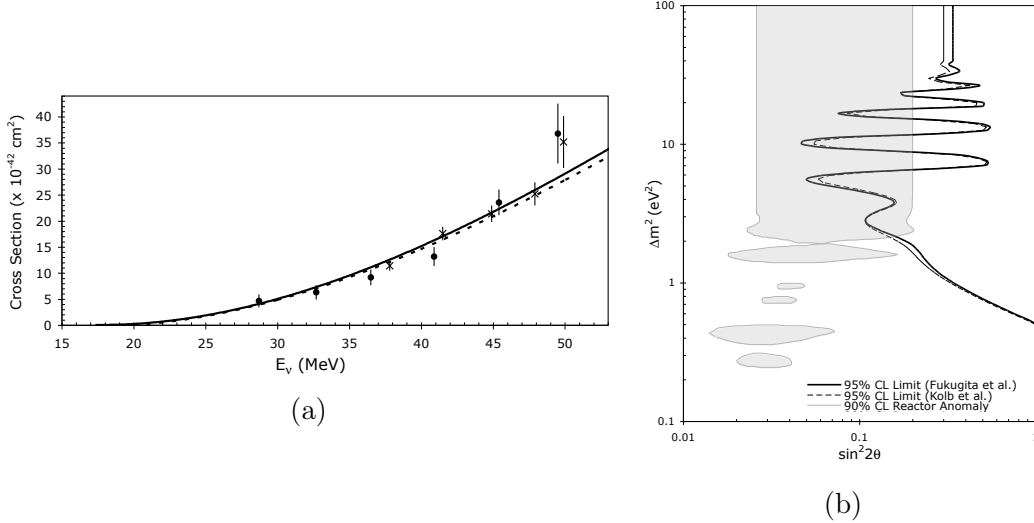


Figure 4-7: (a) The measured $\nu_e + {}^{12}\text{C} \rightarrow {}^{12}\text{N}_{\text{gs}} + e^-$ cross section for LSND (crosses) and KARMEN (points). The multiple lines correspond to different cross section predictions. (b) The 95% confidence level $\nu_e \rightarrow \nu_e$ disappearance limits. Each limit assumes a different interaction cross section model. The filled in grey contour corresponds to the RAA, which was discussed in Section 2.3. Figures from Ref. [38]

SAGE [23] & GALLEX [22]

While we discussed the Gallium anomalies in Section 2.4, we will review the results again here.

The **S**oviet-**A**merican **G**allium **E**xperiment (SAGE) and **G**allium **E**xperiment (GALLEX) were two ${}^{71}\text{Ga}$ -based detector experiments that measured solar neutrinos through the process $\nu_e + {}^{71}\text{Ga} \rightarrow {}^{71}\text{Ge} + e^-$. The produced ${}^{71}\text{Ge}$ would later be collected and counted. Both experiments ran calibration tests by placing radioactive neutrino sources within the detector.

GALLEX conducted two calibration runs with ${}^{51}\text{Cr}$ sources. One run was in 1994, and the other 1995–1996. Through electron capture the source would emit four mono-energetic lines of ν_e 's with differing rates: 747 keV (81.63%), 427 keV (8.95%), 752 keV (8.49%), and 432 keV (0.93%) [24]. SAGE also conducted two calibration runs, first with ${}^{51}\text{Cr}$ (1994–1995) and then with ${}^{37}\text{Ar}$. ${}^{37}\text{Ar}$ decays with two mono-energetic neutrino lines, one at 811 keV (90.2%) and another at 813 keV (9.8%) [42].

Combined, the observed ${}^{71}\text{Ge}$ production was a factor of $R = 0.87 \pm 0.05$ lower than expected. Collectively, these experiments are referred to as the ‘‘Gallium’’ experiments, and the anomalous data as the ‘‘Gallium anomalies.’’ The observed data are shown again in Figure 4-8 along with the results from BEST, which we discuss next.

The result of our SAGE and GALLEX 3+1 fit is shown in Figure 4-9b.

BEST [24, 25]

More recently, the **B**aksan **E**xperiment on **S**terile **T**ransitions (BEST) experiment ran

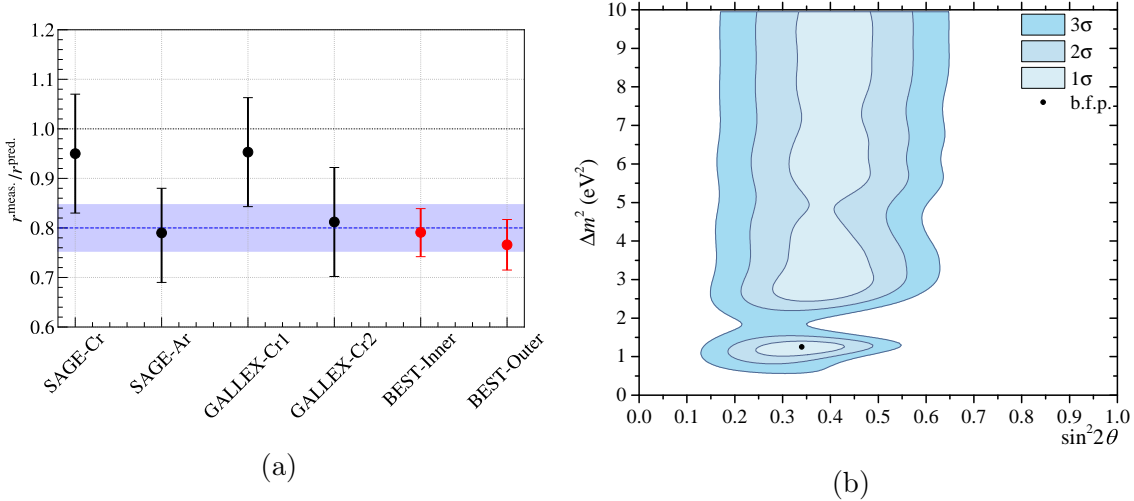


Figure 4-8: (a) The observed ^{71}Ge production rate over expectation for the various runs for SAGE, GALLEX, and BEST. Figure taken from Ref. [25]. (b) Allowed parameter regions of the combined SAGE, GALLEX, and BEST data for the 3+1 model. Figure taken from Ref. [24].

to follow-up on the Gallium anomalies. In 2019, a (3.414 ± 0.008) MCi ^{51}Cr source was placed in the center of a dual volume gallium detector. The inner spherical volume of diameter 133.5 cm held 7.5 t of Ga, while the outer cylindrical volume with dimension $(h, \rho) = (234.5, 109)$ cm held 40.0 t.

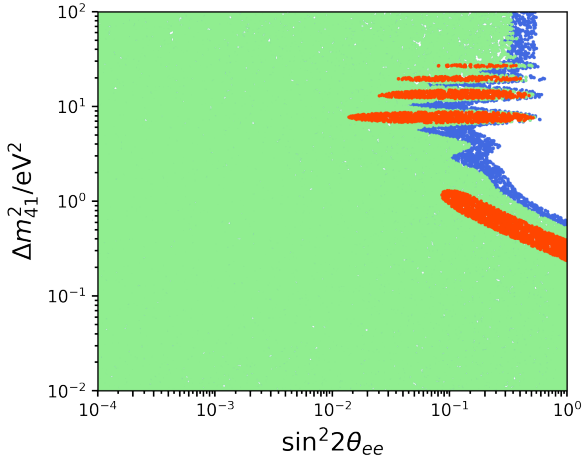
Like the previous Gallium anomalies, BEST observed a deficit of ^{71}Ge production rates in both volumes, with ratios of $R_{\text{in}} = 0.791 \pm 0.05$ for the inner volume and $R_{\text{out}} = 0.766 \pm 0.05$ for the outer volume. The rate ratio between the two volumes is 0.97 ± 0.07 , within unity. Therefore, an overall deficit is observed, but not an oscillation between volumes.

Combining these results with the previous Gallium anomalies give the 3+1 fit results shown in Figure 4-8b. In the oscillation hypothesis, a large mixing angle of $\sin^2 2\theta = 0.34$ is recovered for $\Delta m^2 \gtrsim 1$ eV 2 .

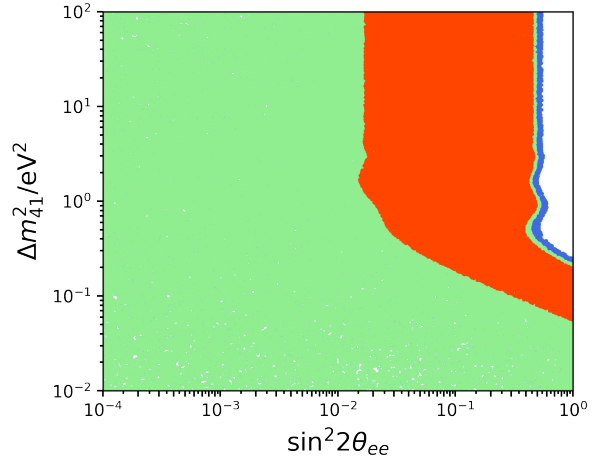
The result of our 3+1 fit for BEST is shown in Figure 4-9c.

Before moving on to the reactor experiments, let's discuss how the approach of these experiments have changed since the author first began with their thesis work.

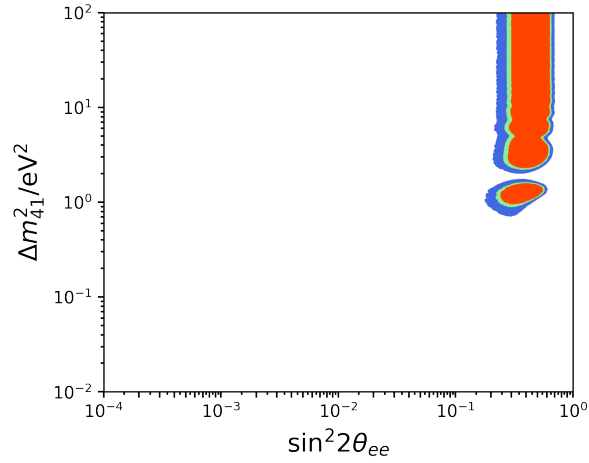
As discussed in Section 2.3, the Reactor Antineutrino Anomaly (RAA) has motivated the search for sterile neutrinos. But the RAA refers to a deficit compared to models, and reactor models are known to be both difficult to derive and incorrect. To avoid this limitation, modern reactor experiments try to measure oscillations over multiple baselines and compare the $\bar{\nu}_e$ spectral shape as a function of distance; this eliminates the need for prior flux knowledge. With a peak $\bar{\nu}_e$ observed energy of ~ 5 MeV, a multi-baseline detector would have to be placed ~ 5 m from the reactor core. This presents unique challenges, and we discuss these experiments below.



(a) KARMEN/LSND (cross section)



(b) SAGE & GALLEX



(c) BEST

Figure 4-9: The 3+1 fits to the $\nu_e \rightarrow \nu_e$ disappearance oscillation data sets used in our global fits.

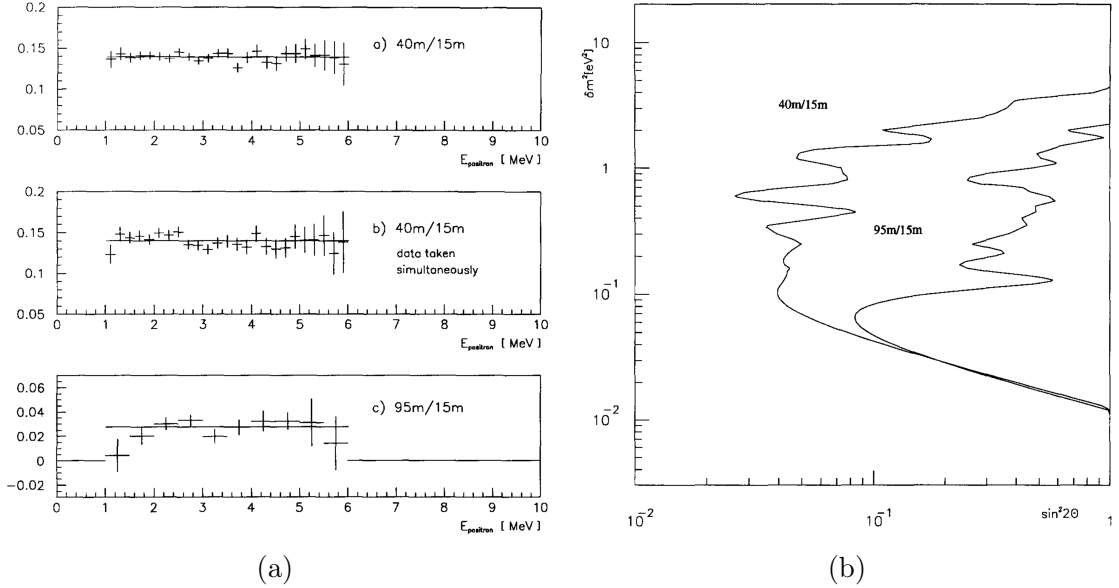


Figure 4-10: (a) The ratios of the observed Bugey data between the various detector baselines. The expected ratios, in the absence of oscillations, would be approximately $(15/40)^2 = 0.14$ for the 40m/15m comparison and $(15/95)^2 = 0.025$ for the 95m/15m comparison. The black lines are a fit to a constant line. (b) The 90% confidence level exclusion contours for two different detector comparisons. Figures from Ref. [43].

The 3+1 fits for the reactor experiments, as we have implemented them, are shown in Figure 4-16.

Bugey [43]

A neutrino oscillation search was conducted at the Bugey reactor complex in France using three ${}^6\text{Li}$ -loaded liquid scintillator detectors at distances of 15, 40, and 95 m from the reactor core. The collaboration did two analyses, one where the observed spectra was compared to nuclear models, and another where the spectra between baselines were compared. Previous publications [44, 45] from our group used the first analysis, but we have changed to using the latter in recent publications [34, 46].

The ratios of the observed data between the various baselines are shown in Figure 4-10a. The analysis finds no normalization difference between detectors nor spectral differences. The exclusions are shown in Figure 4-10b. Because the nearest detector was at 15 m, Bugey was primarily sensitive to lower Δm^2 .

Our 3+1 fit to Bugey is shown in Figure 4-16a.

DANSS [47]

The **D**etector of **A**ntineutrino Based on **S**olid **S**cintillator (DANSS) experiment is an ongoing reactor neutrino experiment located at the Kalinin Nuclear Power Plant in Russia. The detector is a highly segmented scintillator detector with a volume of $\sim 1\text{ m}^3$, placed on a movable platform so that the $\bar{\nu}_e$ spectra is measured at three distances, 10.7 m, 11.7 m, and 12.7 m from the reactor core center. The platform is

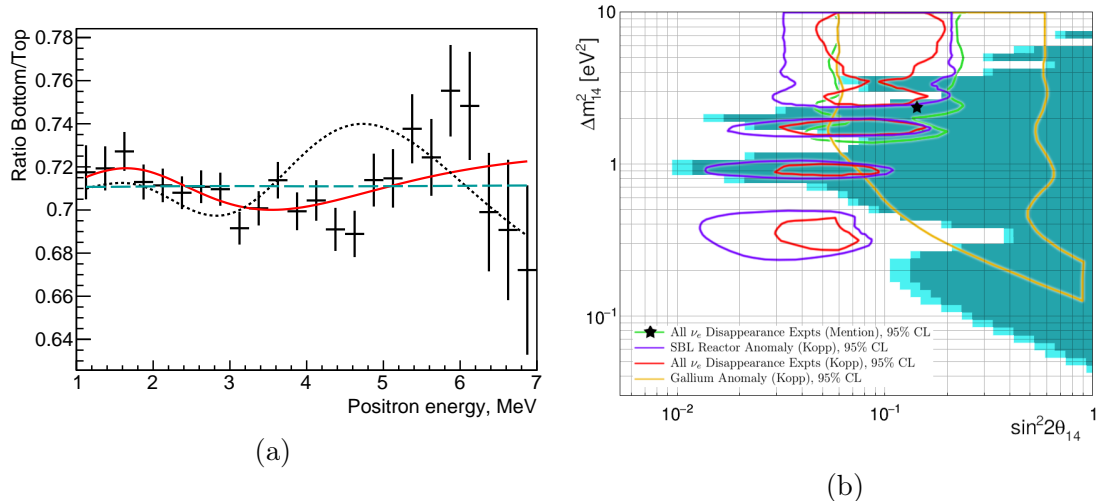


Figure 4-11: (a) The ratio of the observed positron energy spectra between the bottom (further) and top (nearer) detector positions. The dashed curve is the no-oscillation hypothesis, which is taken to be the ratio of the observed total rates between the bottom and top positions. The solid curve is the expectation from DANSS’s best fit point for oscillation: $\sin^2 2\theta = 0.05$ and $\Delta m^2 = 1.4 \text{ eV}^2$. The dotted curve is the expectation at DANSS from a fit to the RAA and Gallium (SAGE & GALLEX only) anomaly. (b) The 90% (cyan) and 95% (dark cyan) confidence level exclusion region for DANSS. Figures from Ref. [47].

placed under the reactor and moves vertically, so that the “top” position is nearer to the reactor, and the “bottom” position is further. The reactor core, in turn, is quite large: a cylindrical shape with dimensions $(h, \rho) = (3.7, 1.6) \text{ m}$.

DANSS conducts a shape-only analysis, where the spectra between the different positions are normalized before the ratios are taken. Therefore, DANSS searches for a spectral distortion from oscillations, without relying on reactor models.

For DANSS data taken 2016–2018, the results are shown in Figure 4-11b. A best fit oscillation point is found at $(\Delta m^2, \sin^2 2\theta) = (1.4 \text{ eV}^2, 0.05)$ with a $\Delta\chi^2 = 13.1$. The collaboration has yet to publish an analysis with a complete uncertainty treatment, so the significance of the measurement is still being studied. In Figure 4-11b, an exclusion curve is published.

We show our 3+1 fit to DANSS in Figure 4-16b.

NEOS/RENO [48]

The **N**eutrino **E**xperiment for **O**scillation at **S**hort **B**aseline (NEOS) experiment is an ongoing experiment at the Hanbit Nuclear Power Complex in Korea. The cylindrical liquid scintillator detector has dimensions $(h, \rho) = (1.21, 0.515) \text{ m}$ and sits $23.7 \pm 0.3 \text{ m}$ from the reactor core. The core, also cylindrical, has dimensions $(h, \rho) = (3.8, 1.55) \text{ m}$.

Unlike DANSS, the NEOS detector is a single volume and at a static position. To avoid systematic uncertainties from nuclear models, the analysis compares its data

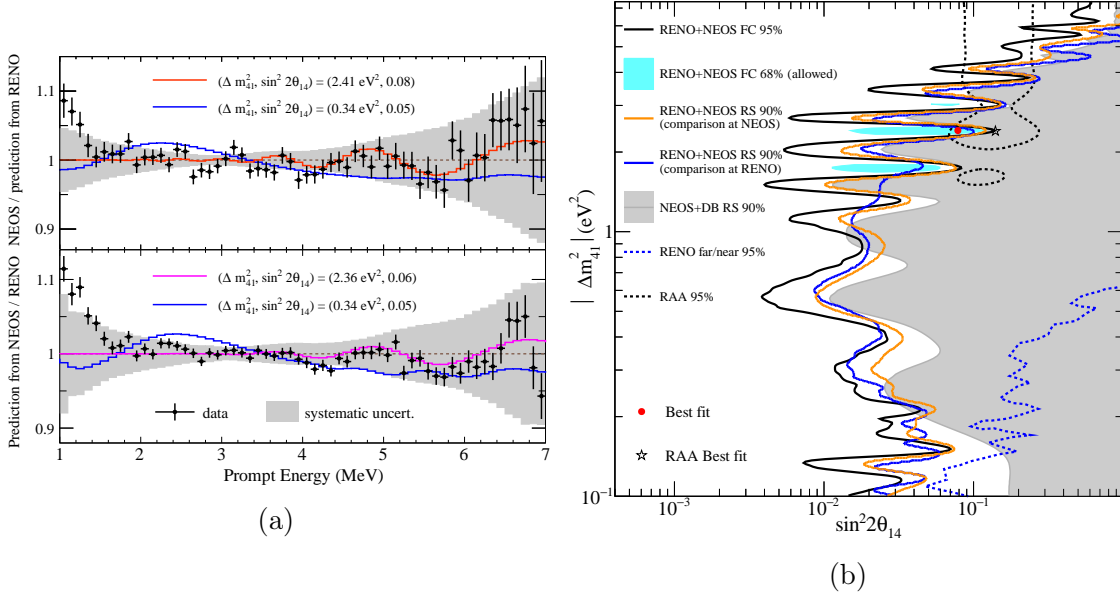


Figure 4-12: (a) Comparisons of the observed prompt energy spectra versus the expectation. In the upper plot, the NEOS data are compared to an expectation from the unfolded $\bar{\nu}_e$ spectra from RENO measurements. The lower plot shows the reverse: the RENO prompt spectra compared to an expectation from the unfolded $\bar{\nu}_e$ spectra from NEOS measurements. (b) Various exclusion limits by the NEOS collaboration. We only note the 95% (black line) and 68% (cyan filled) confidence levels of the NEOS/RENO joint analysis. The “NEOS+DB” contour is the exclusion obtained when NEOS used the unfolded Daya Bay $\bar{\nu}_e$ flux as their reference flux [49]. Figures from Ref. [48].

with a “reference flux” from a different experiment. This reference flux would ideally not contain spectral features from a $\Delta m^2 \sim 1 \text{ eV}^2$ e.g. if the flux was measured at a distance far beyond the oscillation length. Initially, NEOS used Daya Bay’s unfolded $\bar{\nu}_e$ flux measurement [49] as their reference flux, but has moved to a joint analysis with the **R**eactor **E**xperiment for **N**eutrino **O**scillation (RENO) collaboration. This is an improvement as the RENO detector lies in the same reactor complex as the NEOS detector, reducing systematic uncertainties relating to reactor complexes and reactor cores. The RENO detector is far enough from the reactor core (294 m) so that no shape information from a $\Delta m^2 \sim 1 \text{ eV}^2$ mass splitting would be discernible.

Current results from NEOS use 180 days of reactor-on and 45 days of reactor-off data collected in 2015–2016. The data from the joint analysis with RENO is shown in Figure 4-12a, and confidence regions in Figure 4-12b.

The best fit point is found at $(\Delta m^2, \sin^2 2\theta) = (2.41 \text{ eV}^2, 0.08)$, with a p-value of 8.2%. Therefore, NEOS does not see a significance signature for oscillations, but does have an allowed region at the 1σ level.

We show our 3+1 fit to NEOS/RENO in Figure 4-16c.

PROSPECT [50]

The **P**recision **R**eactor **O**scillation and **S**pectrum Experiment (PROSPECT) is an on-

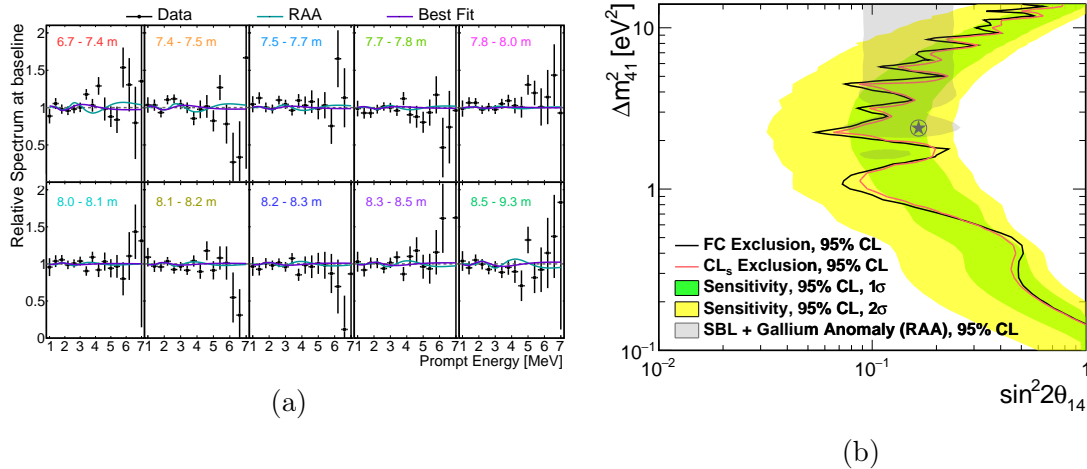


Figure 4-13: (a) The observed prompt energy spectra compared to expectation at PROSPECT. The prediction is normalized such that the spectra for a given energy bin is normalized (across baseline bins) to the data. (b) The 95% exclusion and sensitivities derived from PROSPECT. Two methods of calculating the exclusions and sensitivities are displayed. Figures from Ref. [50].

going reactor neutrino experiment located near the High Flux Isotope Reactor (HFIR) at Oak Ridge National Laboratory. Unlike the previous reactor experiments described, HFIR is a highly enriched uranium research reactor. This offers two benefits. First, the reactor core is compact, with dimensions $(h, \rho) = (0.508, 0.2175)$ m. This reduces the uncertainties in $\bar{\nu}_e$ propagation distances, and allows the detector to be placed closer to the reactor core. Second, the fission fraction of HFIR is always kept above 99% ²³⁵U. This simplifies the modeling of the reactor core, and reduces uncertainties that would arise from the reactor core's composition changing with time.

The PROSPECT detector is a rectangular volume with dimensions $2.0 \times 1.6 \times 1.2$ m³, subdivided into 154 optically isolated rectangular segments. The detector sits very close to the reactor core, with a center-to-center distance of 7.9 ± 0.1 m. This gives the detector a large baseline range compared to the center-to-center distance, ranging 6.7–9.2 m.

In 2018, PROSPECT collected 96 days of reactor-on data, and 73 days of reactor-off data. The results are shown in Figure 4-13a. In the analysis, the data are divided into 10 baseline bins and 16 prompt energy bins. For a given *energy* bin, the predicted $\bar{\nu}_e$ spectra is normalized (across baseline bins) to the total observed rate in that energy bin. Therefore, the analysis does not depend on the spectral shape of the true $\bar{\nu}_e$ reactor flux.

A best fit is found at $(\Delta m^2, \sin^2 2\theta) = (1.78 \text{ eV}^2, 0.11)$ with a $\Delta\chi^2 = 4$. MC simulations showed that this value of $\Delta\chi^2$ has a p-value of 0.57 with respect to the null hypothesis. Therefore, no significant evidence for oscillation is observed. Figure 4-13b plots the 95% confidence level of the data.

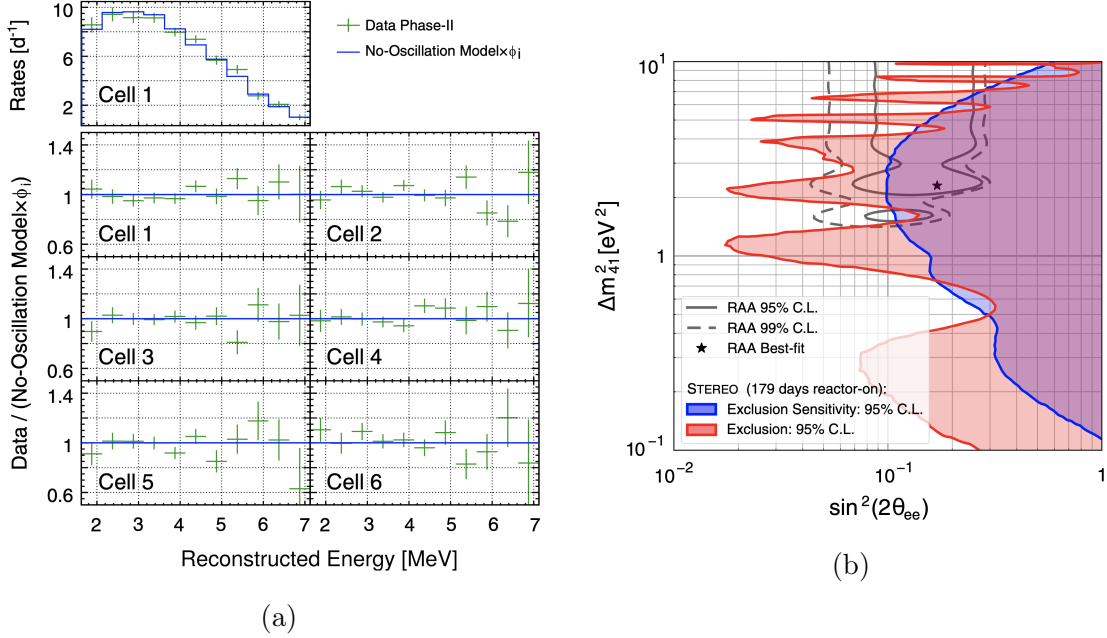


Figure 4-14: (a) The top-most plot shows the absolute comparison between the observed data in Phase II and the null hypothesis in the first cell. The remaining six plots show the relative comparison of the measured rates versus expectation for each cell in the detector. The normalization for each energy bin common across all cells is allowed to float. (b) The exclusion sensitivity and observed exclusion at the 95% confidence level is shown. Figures are taken from Ref. [51].

We show our 3+1 fit to PROSPECT in Figure 4-16d.

STEREO [51]

The STEREO experiment is an ongoing reactor neutrino experiment at the Institut Laue-Langevin (ILL) research center in Grenoble, France. Like other research reactors, the STEREO’s reactor is compact and composed of highly enriched ²³⁵U (93%). The STEREO detector is composed of six optically separated cells filled with liquid scintillator. The distinct cells allow the measurement of the $\bar{\nu}_e$ spectrum over baselines 9.4-11.2 m from the reactor core.

The STEREO experiment ran in two phases, with 179 days of total reactor-on time. Phases I and II were treated as two independent experiments, with the results of phase II shown in Figure 4-14a. Compared to pseudoexperiments, the observed p-value is 9%. Therefore, the no-sterile hypothesis cannot be rejected. The observed exclusion is shown in Figure 4-14b.

We show our 3+1 fit to STEREO in Figure 4-16e.

Neutrino-4 [52]

Neutrino-4 is an ongoing reactor neutrino experiment located near the SM-3 research nuclear reactor in Russia. Being a research reactor, the core is primarily ²³⁵U and compact, with dimensions $0.25 \times 0.42 \times 0.42$ m³.

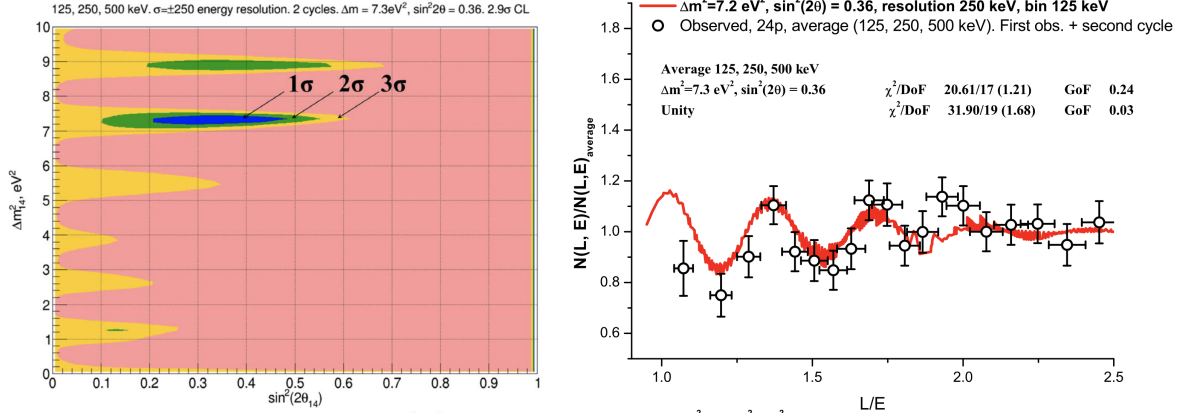


Figure 4-15: **Left:** The best fit contours reported by Neutrino-4. The best fit is found at $(\Delta m^2, \sin^2 2\theta) = (7.3 \text{ eV}^2, 0.36)$ with a 2.9σ significance. **Right:** The ratio of data versus expectation observed by Neutrino-4. The red line gives the expected signal at the best fit point. Figures from Ref. [52].

The detector, a 1.8 m^3 volume of liquid scintillator, is divided into 5×10 segments of dimensions $0.225 \times 0.225 \times 0.85 \text{ m}^3$ each. Further, the detector as a whole is placed on rails so that total baseline range sampled is 6–12 m from the reactor core. This also allows multiple subsegments of the detector to be placed at the same distance from the core, reducing detector calibration systematics.

In 2016–2020, Neutrino-4 recorded data for 720 days of reactor-on and 860 days of reactor-off. The results are shown in Figure 4-15. Neutrino-4 claims a significant signal for oscillations, with a best fit at $(\Delta m^2, \sin^2 2\theta) = (7.3 \text{ eV}^2, 0.36)$ at a significance of 2.9σ .

We show our 3+1 fit to Neutrino-4 in Figure 4-16f.

4.1.3 $P(\nu_\mu \rightarrow \nu_\mu)$ & $P(\bar{\nu}_\mu \rightarrow \bar{\nu}_\mu)$

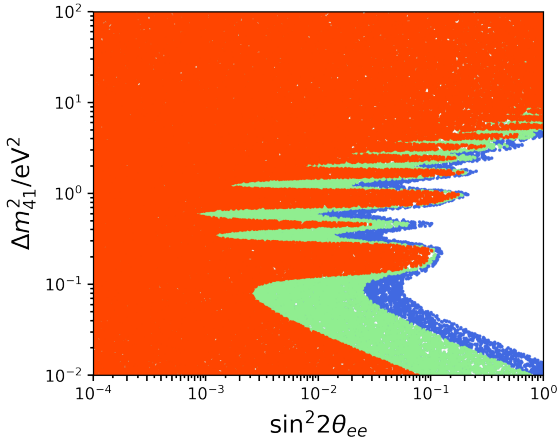
CDHS [53]

The CDHS collaboration conducted a $\nu_\mu \rightarrow \nu_\mu$ disappearance search using the CERN Super Proton Synchrotron (SPS) neutrino beam. The SPS impinged a 19.2 GeV proton beam onto a beryllium target, producing neutrinos with a peak flux at 1 GeV. The ν_μ 's would then be observed by two detectors, placed at 130 m and 885 m from the target. The detectors were composed of alternating planes of iron plates and scintillators.

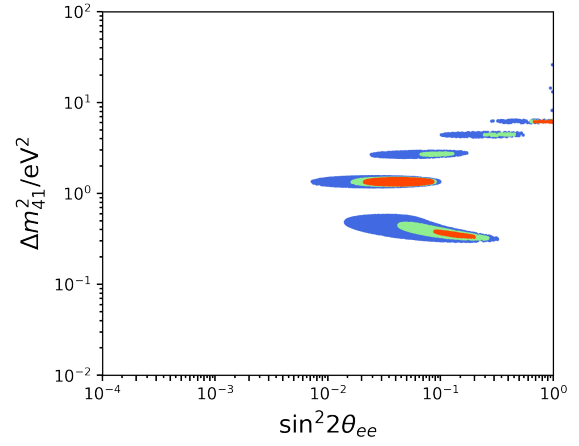
Unlike the other experiments listed in this section, CDHS did not bin their events by energy. Instead, CDHS sorted their events by the length traveled by the observed muons, acting as a proxy for ν_μ energy.

The observed ratios between the two detectors are shown in Figure 4-17a. No evidence for ν_μ disappearance was found between the two detectors. The extracted exclusion can be seen in Figure 4-17b.

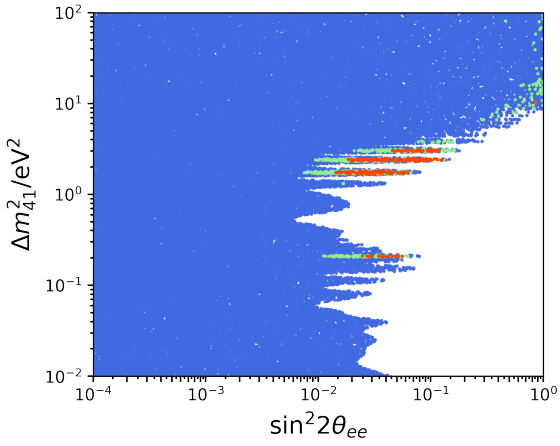
We show the results of our CDHS 3+1 fit in Figure 4-24a.



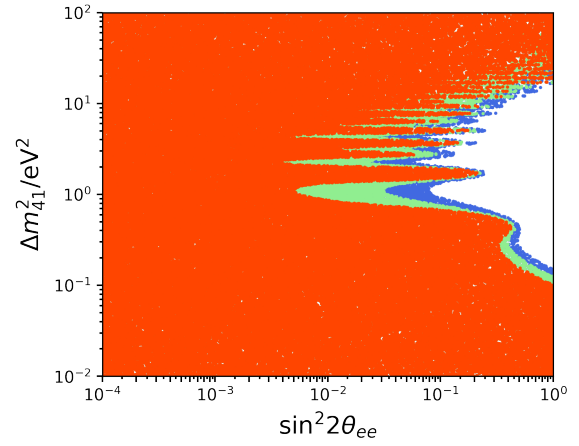
(a) Bugey



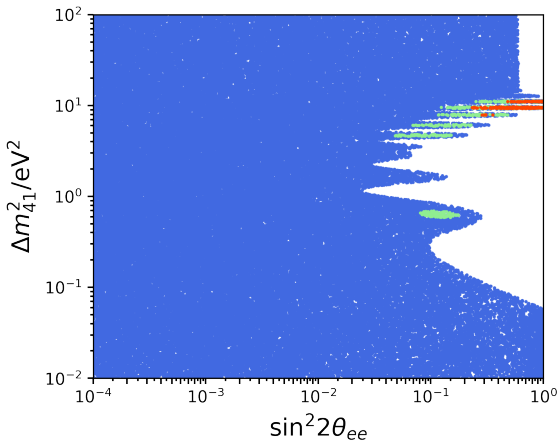
(b) DANSS



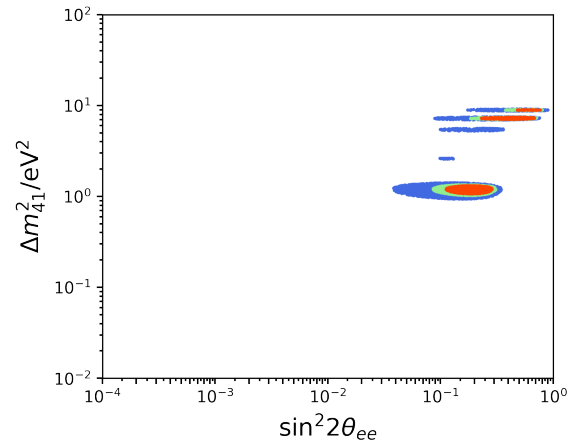
(c) NEOS/RENO



(d) PROSPECT



(e) STEREO



(f) Neutrino-4

Figure 4-16: The 3+1 fits to the $\bar{\nu}_e \rightarrow \bar{\nu}_e$ disappearance oscillation data used in our global fits.

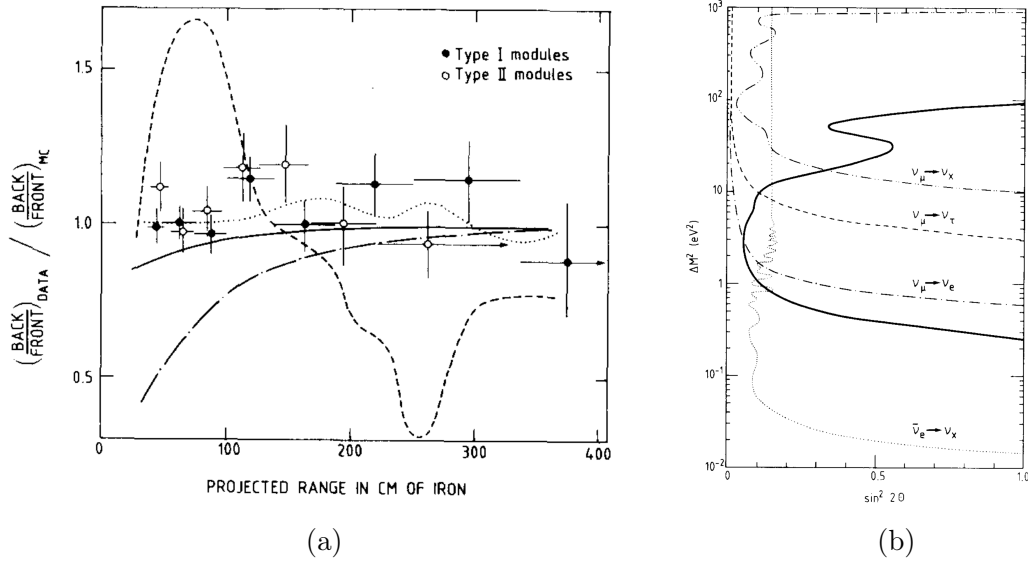


Figure 4-17: (a) The observed ratios of ν_μ events between the two CDHS detectors, as a function of muon track length. The different colored dots correspond to different subdetector types in the CDHS detectors. The different lines correspond to expectations for different sterile neutrino hypotheses. (b) The 90% confidence level from the CDHS observations, shown in the solid line. The remaining lines were the best limits, at the time, for other oscillation channels. Figures from Ref. [53].

CCFR84 [54]

The CCFR collaboration conducted a $\nu_\mu \rightarrow \nu_\mu$ and $\bar{\nu}_\mu \rightarrow \bar{\nu}_\mu$ disappearance search using two detectors in the Fermilab narrow band neutrino beam. The beam was tuned to provide data at five meson momentum settings (100, 140, 165, 200, and 250 GeV) for π^+ s and K^+ s, providing neutrinos between 40 and 230 GeV. The two detectors were placed 715 m and 1116 m from the midpoint of the decay pipe.

The observed ratios between the two detectors, for ν_μ and $\bar{\nu}_\mu$ data, are shown in Figure 4-18a. No evidence for oscillation was observed, and the 90% exclusion curves are shown in Figure 4-18b.

We show the results of our CCFR 3+1 fit in Figure 4-24b.

MiniBooNE/SciBooNE [55, 56]

In addition to the MiniBooNE $\nu_\mu \rightarrow \nu_e$ and $\bar{\nu}_\mu \rightarrow \bar{\nu}_e$ appearance analyses described earlier, MiniBooNE conducted $\nu_\mu \rightarrow \nu_\mu$ and $\bar{\nu}_\mu \rightarrow \bar{\nu}_\mu$ disappearance analyses jointly with the SciBooNE detector. The SciBooNE detector was located 100 m from the BNB neutrino production target, sharing the same neutrino flux as MiniBooNE. The SciBooNE detector was composed of three sub-detectors: a highly segmented scintillator tracker (SciBar), an electromagnetic calorimeter, and a muon range detector (MRD).

In the $\nu_\mu \rightarrow \nu_\mu$ analysis, events were collected in three ν_μ samples: SciBar-stopped events, MRD-stopped events, and MiniBooNE events. These three samples were fit simultaneously to an oscillation model. The data versus expectation can be seen in

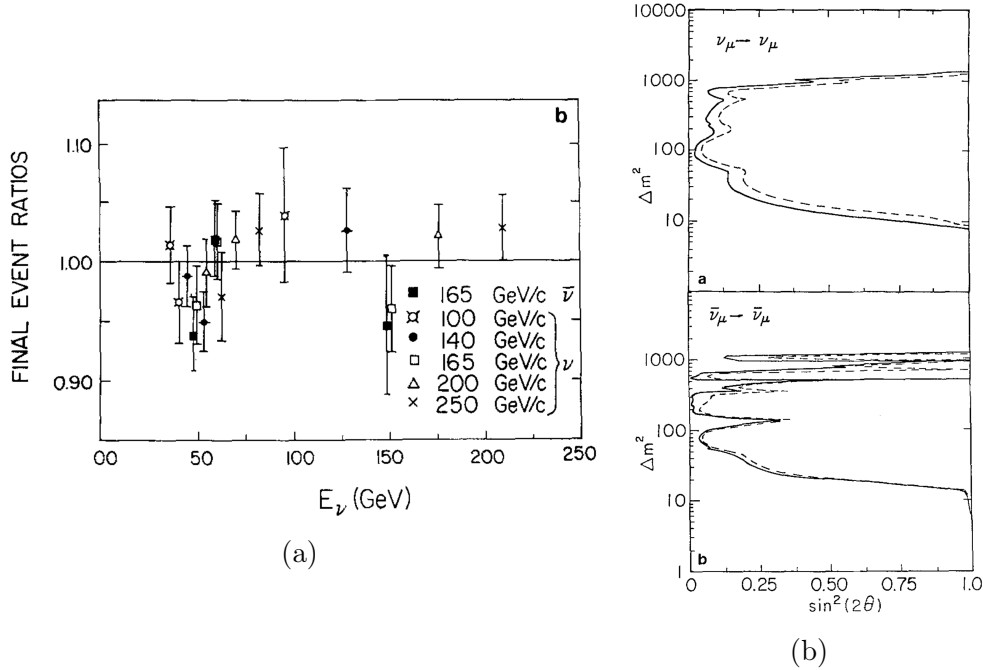


Figure 4-18: (a) The observed ratios of events seen between the far and near CCFR detectors. The plot shows both ν_μ and $\bar{\nu}_\mu$ data. (b) The 90% confidence level limits shown for ν_μ (top) and $\bar{\nu}_\mu$ (bottom) disappearance. The two lines in each plot corresponds to two different methods to draw the exclusions. Figures from Ref. [54].

Figure 4-19. The data gave a p-value over 50%, showing no evidence for oscillations. The exclusions are shown in Figure 4-20.

A similar analysis was conducted for $\bar{\nu}_\mu$ disappearance, using MiniBooNE data taken 2006–2012 and SciBooNE data taken 2007–2008. Like the ν_μ analysis, the $\bar{\nu}_\mu$ analysis used SciBar-stopped and MRD-stopped events. The data can be seen in Figure 4-21. Both detectors observed an excess compared to expectation, so no evidence for oscillations between the detectors was observed. The 90% exclusion is shown in Figure 4-22.

We show the results of our MiniBooNE/SciBooNE joint analysis 3+1 fit in Figure 4-24c.

MINOS-CC [58–60]

The **Main Injector Neutrino Oscillation Search** (MINOS) experiment was built to measure the standard model neutrino oscillation parameters using ν_μ and $\bar{\nu}_\mu$ oscillations. MINOS detected the neutrino flux from the NuMI beamline, with a near detector 1.04 km from the beam target and a far detector at 734 km. The detectors were magnetized, such that it could differentiate μ^- 's from μ^+ 's. The beam peaked at 3 GeV.

In our fits, we use both $\bar{\nu}_\mu \rightarrow \bar{\nu}_\mu$ and $\nu_\mu \rightarrow \nu_\mu$ oscillation channels from three different MINOS data sets. The first is the $\bar{\nu}_\mu \rightarrow \bar{\nu}_\mu$ oscillation data set, collected in two phases in 2009–2011 using the $\bar{\nu}_\mu$ -enhanced beam. The second data set is a $\bar{\nu}_\mu \rightarrow \bar{\nu}_\mu$ oscillation analysis using the 7% wrong-signed neutrinos in the ν_μ configuration. The last data set

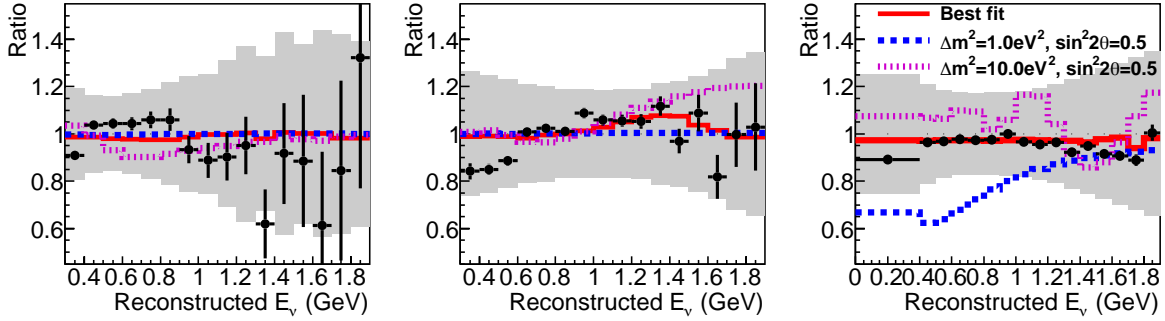


Figure 4-19: The ratio of observed ν_μ rates over expectation for, left to right, SciBar-stopped, MRD-stopped, and MinibooNE samples. Figures from Ref. [55].

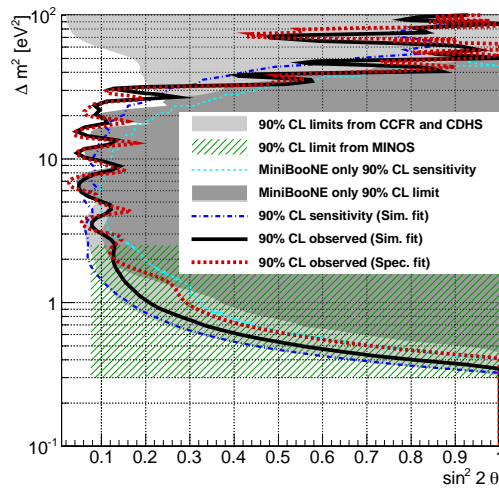


Figure 4-20: The 90% confidence level limit for the MiniBooNE/SciBooNE ν_μ disappearance joint fit. Figure from Ref. [55].

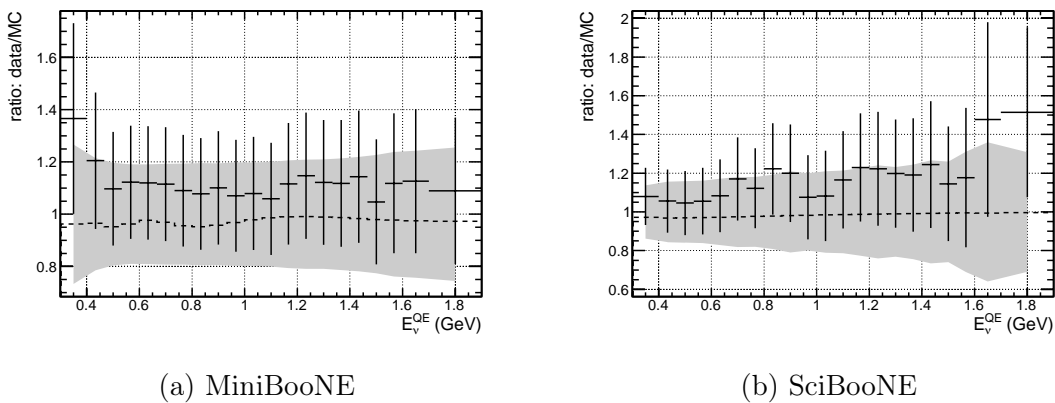


Figure 4-21: The ratios of observed over expected $\bar{\nu}_\mu$ events in MiniBooNE (left) and SciBooNE (right). No oscillation deficit was observed. Note that the y-axis does not start at 0. Figures from Ref. [56].

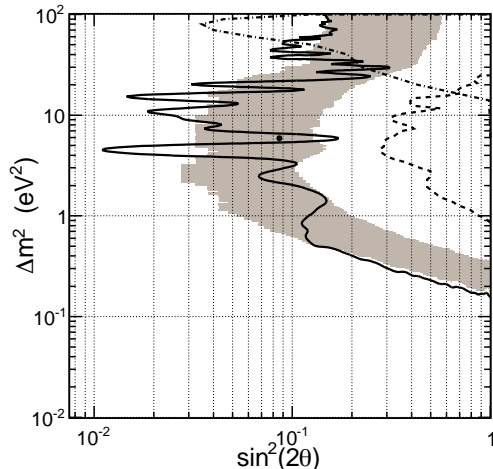


Figure 4-22: The 90% confidence level for the MiniBooNE/SciBooNE joint $\bar{\nu}_\mu$ disappearance analysis, shown in the solid line. The dashed line is the 90% confidence level from the 2009 MiniBooNE disappearance analysis [57] and the dot-dashed line is the 90% for CCFR. Figure from Ref. [56].

is the $\nu_\mu \rightarrow \nu_\mu$ oscillation analysis from 2016. In all three data sets, the observations in the near detector is used to predict the flux at the far detector given some model.

The three data sets are shown in Figure 4-23. The results of our MINOS fits are shown in Figure 4-24d.

4.2 Methodology

A thorough description of the methodology of our fits can be found in Ref. [34], but we summarize the significant points here.

For a particular model, a Markov Chain Monte Carlo (MCMC) is used to explore the parameter space. The algorithm follows that used by the `emcee` Python package [61], but with our own implementation in C++. The sampled parameters, for the models described in Section 2.5, are: Δm_{41}^2 , $|U_{e4}|$, and $|U_{\mu 4}|$ for the 3+1 model; Δm_{41}^2 , Δm_{51}^2 , $|U_{e4}|$, $|U_{e5}|$, $|U_{\mu 4}|$, $|U_{\mu 5}|$, and $\phi_{\mu e}$ for the 3+2 model; and Δm_{41}^2 , $|U_{e4}|$, $|U_{\mu 4}|$, and Γ for the 3+1+Decay model. For each model, we enforce the unitarity conditions $\sum_\alpha |U_{\alpha i}|^2 < 1$ for each mass index i , and $\sum_i |U_{\alpha i}|^2 < 1$ for each flavor index α . For each model, $\alpha \in \{e, \mu\}$; and $i \in \{4\}$ for both the 3+1 and 3+1+Decay models, while $i \in \{4, 5\}$ for the 3+2 model. We also impose the constraint $\Delta m_{41}^2 < \Delta m_{51}^2$ for the 3+2 model.

At each sampled point in the parameter space, two values are recorded: a χ^2 value and a log-likelihood. For the frequentist fits, the test statistic $\Delta\chi^2 = \chi^2(\vec{\theta}) - \chi_{\min}^2$ is used, where $\chi^2(\vec{\theta})$ is the χ^2 at some parameter set $\vec{\theta}$ and χ_{\min}^2 is the minimum χ^2 found in the parameter space. $\Delta\chi^2$ is assumed to follow a χ^2 distribution with degrees of freedom equal to the difference in degrees of freedom between the null model and the sterile model under consideration. When drawing two dimensional confidence regions, as have been shown in

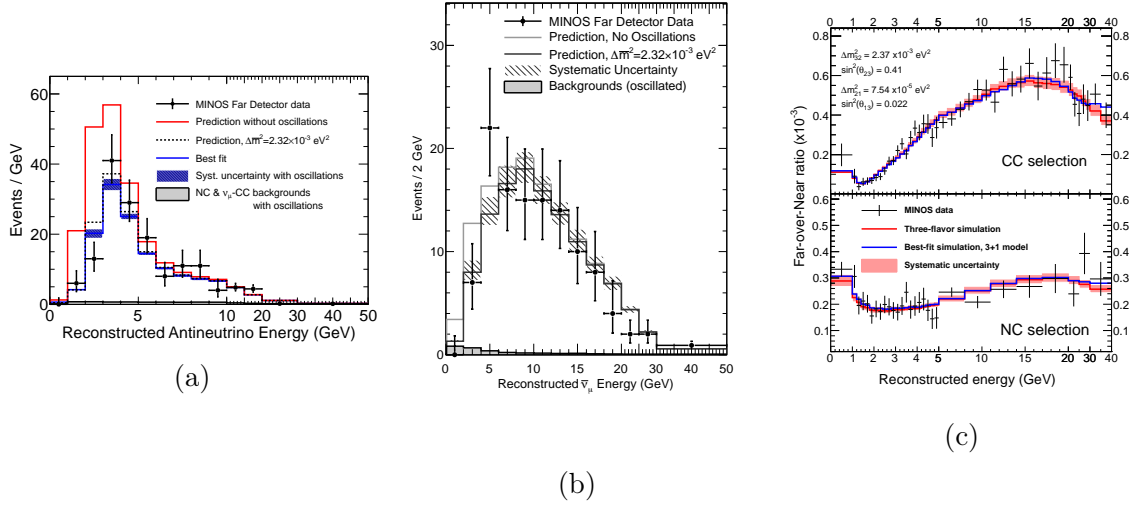


Figure 4-23: (a) The observed $\bar{\nu}_\mu$ spectra at the far detector in the $\bar{\nu}_\mu$ -enhanced beam configuration. In MINOS's analysis, the standard model parameters are fitted, not the sterile parameters. Figure from Ref. [59]. (b) The observed wrong-signed $\bar{\nu}_\mu$ spectra at the far detector in the ν_μ -enhanced beam configuration. Figure from Ref. [58]. (c) The observed ν_μ spectra ratio between the far and near detector. We only consider the CC sample in our fits. Figure from Ref. [60].

this chapter, the $\Delta\chi^2$ is profiled over the remaining dimensions, and the contours are drawn assuming two degrees of freedom unless otherwise stated.

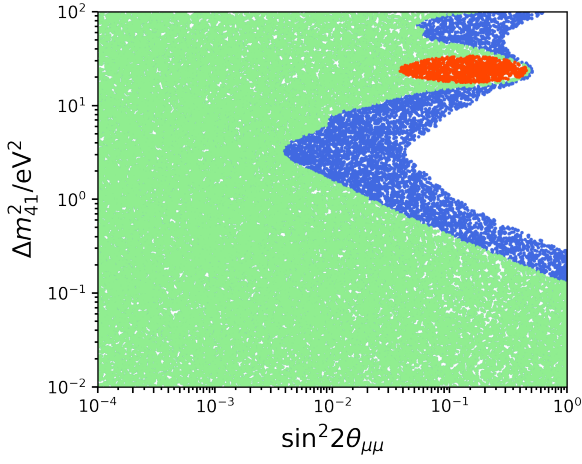
The log-likelihoods serve a dual purpose. First, the MCMC explores the parameters space guided by the log-likelihood. This allows a more efficient exploration of the parameter space, which would otherwise be computationally prohibitive if we were to scan in a grid over multiple dimensions (e.g. 7 dimensions for the 3+2 model). Second, the MCMC naturally samples the posterior, which allows the drawing of Bayesian credible regions. In our analysis, we use the python package `corner.py` [62] to draw these regions.

In addition to searching for the sterile parameters that best fit the data, we would also like to test the internal consistency of such a model. For example, in the 3+1 model, the three oscillation channels studied here, $\nu_\mu \rightarrow \nu_e$, $\nu_e \rightarrow \nu_e$, $\nu_\mu \rightarrow \nu_\mu$ (and their antineutrino analog), probe three different oscillation equations that depend on the mixing parameters differently:

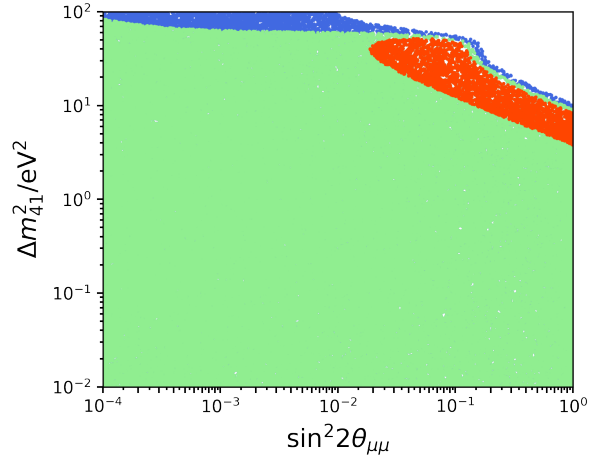
$$P(\nu_\mu \rightarrow \nu_e) = \sin^2 2\theta_{\mu e} \sin^2 \left(1.27 \Delta m_{41}^2 \frac{L}{E} \right) \quad (4.1)$$

$$P(\nu_e \rightarrow \nu_e) = 1 - \sin^2 2\theta_{ee} \sin^2 \left(1.27 \Delta m_{41}^2 \frac{L}{E} \right) \quad (4.2)$$

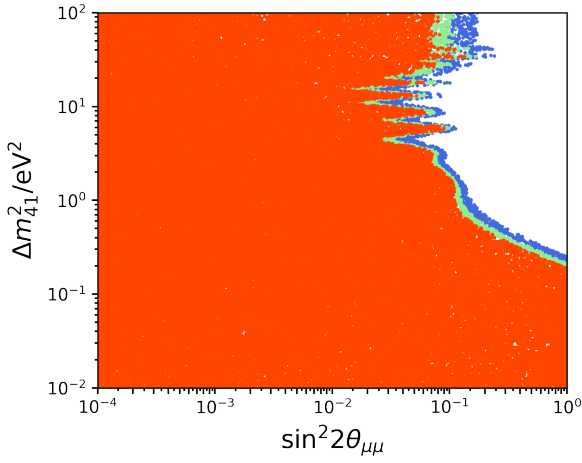
$$P(\nu_\mu \rightarrow \nu_\mu) = 1 - \sin^2 2\theta_{\mu\mu} \sin^2 \left(1.27 \Delta m_{41}^2 \frac{L}{E} \right), \quad (4.3)$$



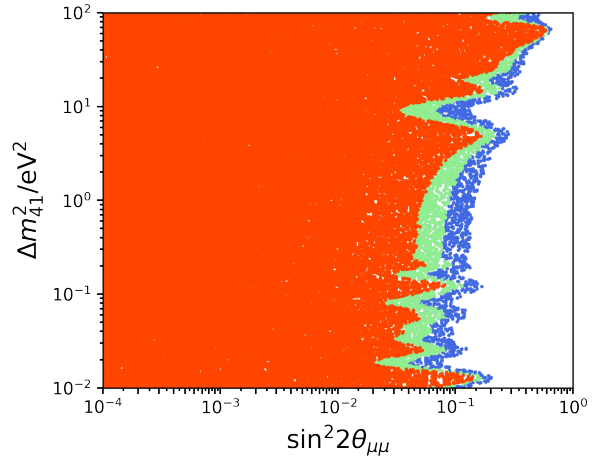
(a) CDHS



(b) CCFR



(c) MiniBooNE/SciBooNE



(d) MINOS

Figure 4-24: The 3+1 fits to the $\nu_\mu \rightarrow \nu_\mu$ and $\bar{\nu}_\mu \rightarrow \bar{\nu}_\mu$ disappearance experiments used in our global fits.

where the effective mixing angles $\sin^2 2\theta_{\alpha\beta}$ are given by

$$\sin^2 2\theta_{\mu e} = 4|U_{\mu 4}|^2|U_{e 4}|^2 \quad (4.4)$$

$$\sin^2 2\theta_{ee} = 4|U_{e 4}|^2(1 - |U_{e 4}|^2) \quad (4.5)$$

$$\sin^2 2\theta_{\mu\mu} = 4|U_{\mu 4}|^2(1 - |U_{\mu 4}|^2). \quad (4.6)$$

We can see that the three effective mixing angles depend on only two different mixing elements, $|U_{e 4}|^2$ and $|U_{\mu 4}|^2$. Therefore, the mixing angles are not independent and we can test if the different data sets provide consistent values.

We test this by splitting the data sets into two groups, an appearance and disappearance data set. The appearance data set would be sensitive to the product $|U_{\mu 4}|^2|U_{e 4}|^2$, while the disappearance data set would be composed of experiments that are sensitive to either $|U_{e 4}|^2$ or $|U_{\mu 4}|^2$. We then apply the Parameter Goodness of Fit (PG) test [63] on these data sets. We perform separate fits on the two data subsets, along with the fit to the global data set. We use the three minimum χ^2 's, χ_{glob}^2 , χ_{app}^2 , χ_{dis}^2 , to construct an effective

$$\chi_{\text{PG}}^2 = \chi_{\text{glob}}^2 - (\chi_{\text{app}}^2 + \chi_{\text{dis}}^2) \quad (4.7)$$

with an effective number of degrees of freedom

$$N_{\text{PG}} = (N_{\text{app}} + N_{\text{dis}}) - N_{\text{glob}}, \quad (4.8)$$

where N_x are the number of degrees of freedom for each subset. This χ_{PG}^2 is assumed to follow a χ^2 distribution with N_{PG} degrees of freedom, and the resulting p-value tells us the probability for the difference between the subsets to arise from chance if the underlying physics were consistent.

4.3 Results

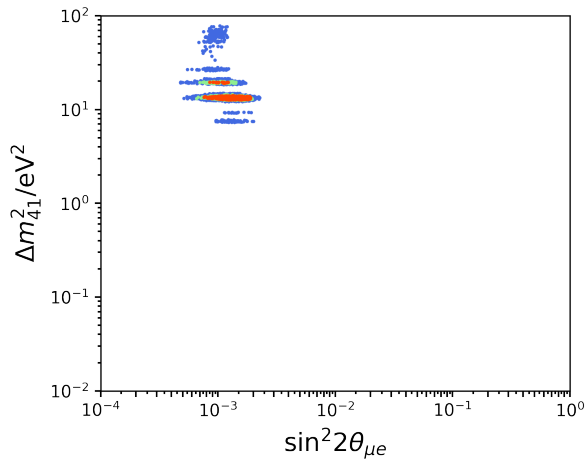
4.3.1 3+1 Model

We first fit the experiments listed in Section 4.1 to the 3+1 sterile model which we reviewed in Section 2.5.1. The results of this global fit are shown in Figure 4-25. The best fit mass-squared splitting is found at $\Delta m_{41}^2 = 13.1 \text{ eV}^2$, with mixing parameters $|U_{e 4}| = 0.30$ and $|U_{\mu 4}| = 0.065$. The best fit mixing parameters can also be written in terms of the effective mixing parameters $\sin^2 2\theta_{\mu e} = 0.0015$, $\sin^2 2\theta_{ee} = 0.32$, $\sin^2 2\theta_{\mu\mu} = 0.017$.

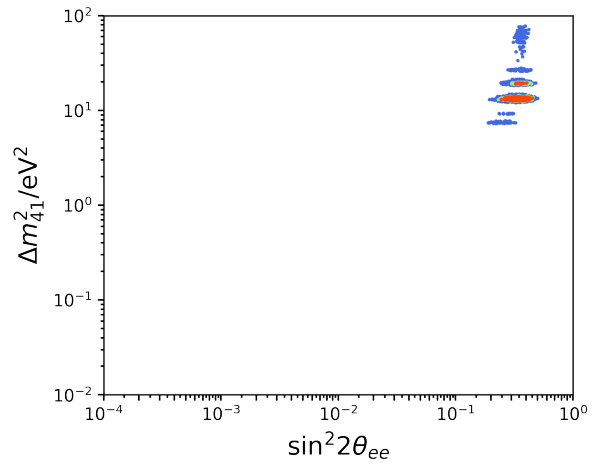
The improvement of the 3+1 model compared to the null is found to be $\Delta\chi^2 = 51$, with the addition of only 3 degrees of freedom. This substantial improvement has a p-value of $p = 4.9 \times 10^{-11}$ (6.6σ). Therefore, the experiments included in our fit strongly prefer a model like sterile neutrinos.

The results of the Bayesian fit can also be seen in Figure 4-26. Compared to the frequentist fit in Figure 4-25, we see good overlap between the regions, with the Bayesian contours being wider.

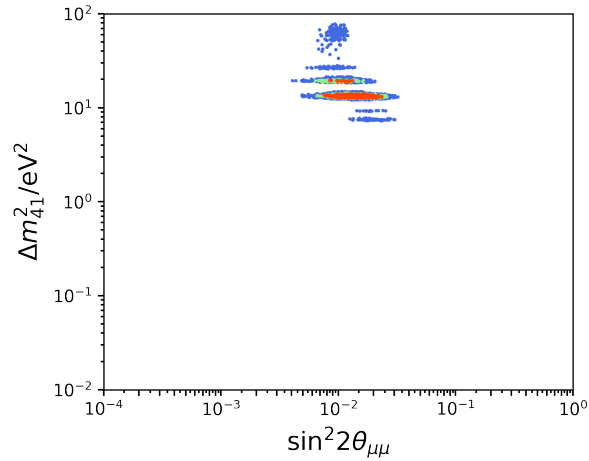
Before reporting on the tension, we would like to compare our current results with that from our previous review in Ref. [34]. We show in Figure 4-27 the frequentist 3+1 results from



(a)



(b)



(c)

Figure 4-25: Results of the 3+1 global fits. We plot the confidence regions in terms of three different, but not independent, mixing parameters: (a) $\sin^2 2\theta_{\mu e}$, (b) $\sin^2 2\theta_{ee}$, and (c) $\sin^2 2\theta_{\mu\mu}$. The confidence regions correspond to 90%, 95%, and 99% in red, green, and blue, respectively.

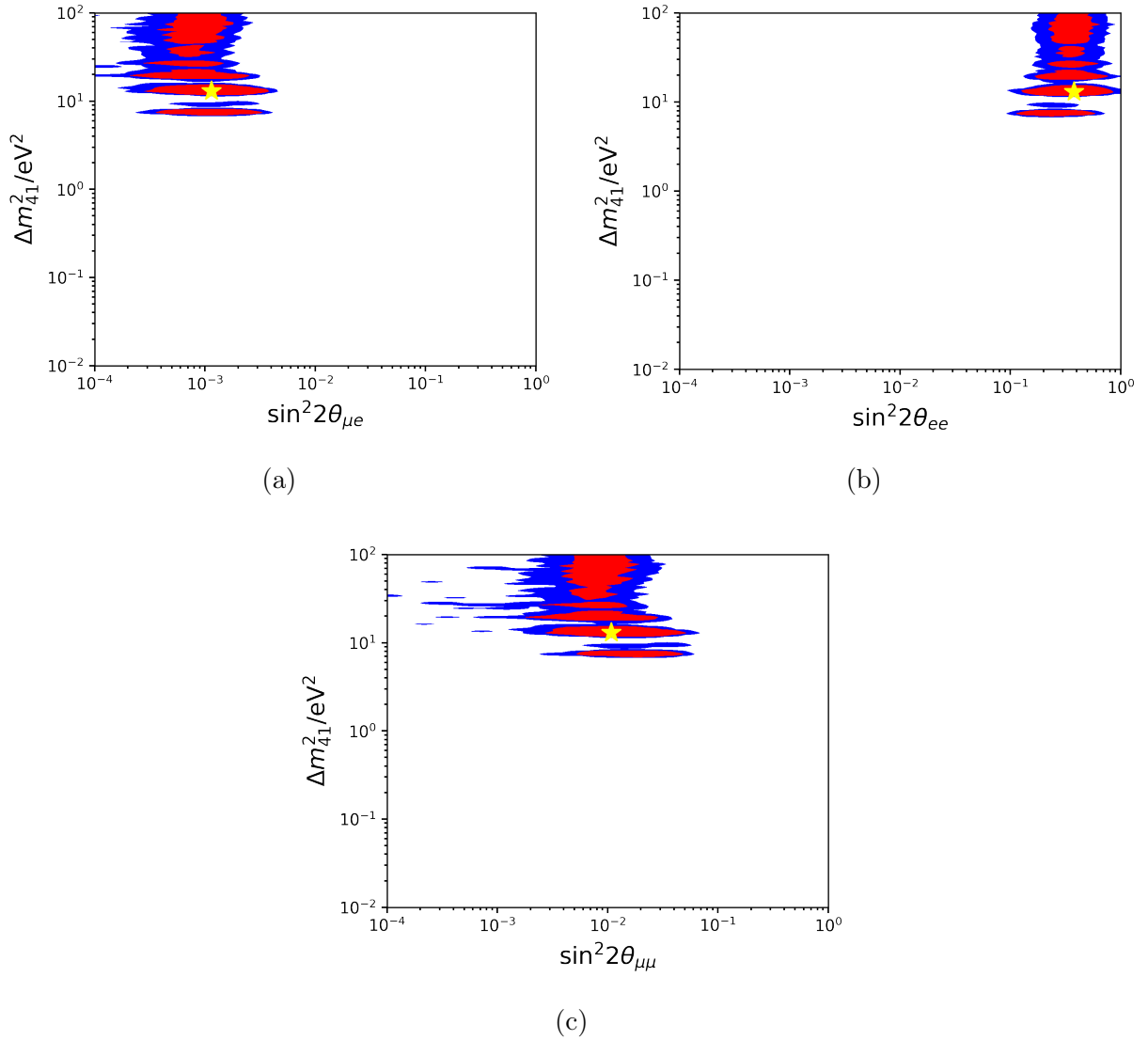


Figure 4-26: Results of the Bayesian 3+1 global fits. We plot the confidence regions in terms of three different, but not independent, mixing parameters: (a) $\sin^2 2\theta_{\mu e}$, (b) $\sin^2 2\theta_{ee}$, and (c) $\sin^2 2\theta_{\mu\mu}$. The credible regions correspond to 90% in red and 99% in blue.

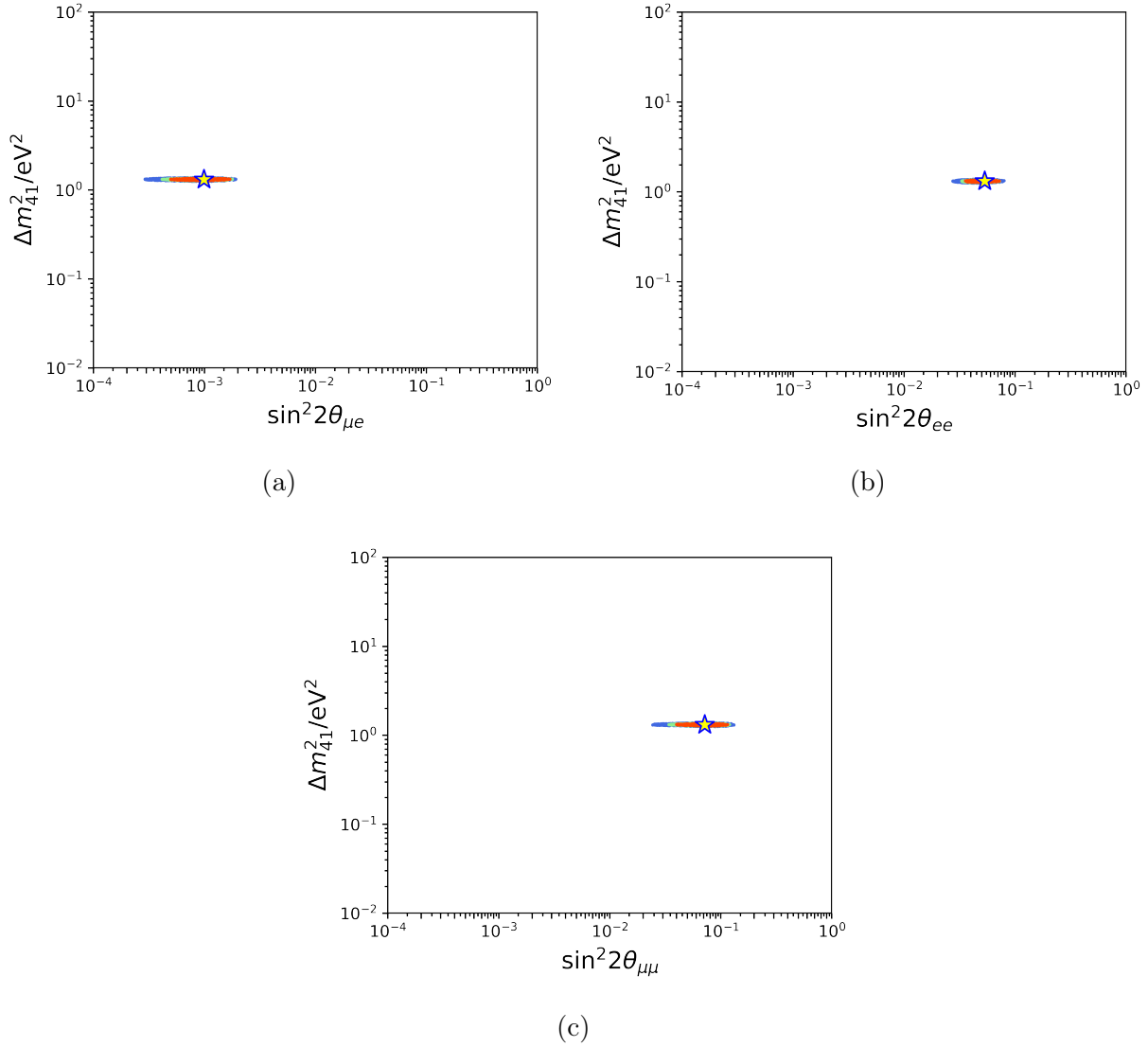


Figure 4-27: The frequentist global fit results from our previous review in Ref. [34].

that analysis, and in Figure 4-28 the Bayesian results. Comparing our current frequentist results in Figure 4-25 and the previous results in Figure 4-27, we find a substantial difference in the allowed Δm_{41}^2 values. We explain this change as being due to the addition of BEST, which had observed a 4σ deviation from the null model [25]. The previous best fit region is incompatible with the very strong signal observed by BEST, as can be seen by comparing Figure 4-27b and Figure 4-9c. Therefore, the $\Delta m_{41}^2 \approx 1.32 \text{ eV}^2$ best fit island found in Ref. [34] becomes disfavored. While no other islands were found in the previous frequentist fits, the Bayesian results from the previous fits, displayed in Figure 4-28, revealed higher mass splittings which the current fits are compatible with.

To test the internal consistency of this model, we calculate the tension by separating the data sets into two groups, as described above: the appearance and disappearance data sets. The appearance data are sensitive to the product $|U_{e4}||U_{\mu 4}|$, while the disappearance data

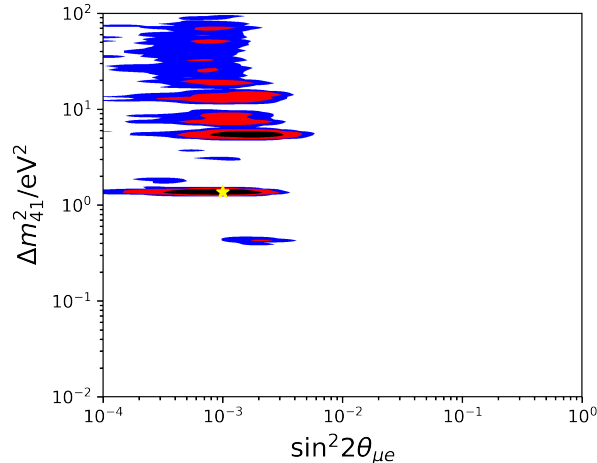


Figure 4-28: The Bayesian global fit results from our previous review in Ref. [34].

are individually sensitive to $|U_{e4}|^2$ or $|U_{\mu4}|^2$. The appearance-only and disappearance-only 3+1 fits are shown in Figure 4-29. Visually, we can already see that these two subsets of the data do not agree in parameter space. To quantify this tension, we will use the PG test. We find a test statistic value of $\chi_{\text{PG}}^2 = \chi_{\text{glob}}^2 - (\chi_{\text{app}}^2 + \chi_{\text{dis}}^2) = 728 - (79 + 619) = 30$, with degrees of freedom $k = (2 + 3) - 3 = 2$. This gives a p-value of $p = 3.1 \times 10^{-7} (5.1\sigma)$. Clearly, there exists an internal inconsistency within the 3+1 model despite the overall preference that the data has for the 3+1 model over the null model. This motivates the exploration of models more complex than the minimal 3+1 sterile neutrino model.

4.3.2 3+2 Model

We now consider the expanded 3+2 model, where we now have two sterile neutrino mass and weak states. In addition to the three parameters introduced in the 3+1 model, $(\Delta m_{41}^2, |U_{e4}|, |U_{\mu4}|)$, the parameters Δm_{51}^2 , $|U_{e5}|$, $|U_{\mu5}|$, and $\phi_{\mu e}$ are added in the 3+2 model, for a total of seven parameters.

Our fit finds the following best fit parameters: $\Delta m_{41}^2 = 2.2 \times 10^{-3} \text{ eV}^2$, $|U_{e4}| = 0.18$, $|U_{\mu4}| = 3.2 \times 10^{-4}$, $\Delta m_{51}^2 = 13.1 \text{ eV}^2$, $|U_{e5}| = 0.30$, $|U_{\mu5}| = 0.054$ and $\phi_{\mu e} = 0.78\pi$. At these parameter points, we find the improvement of the model compared to the null to be at $\Delta\chi^2 = 51$. We find, then, that the 3+2 model provides minimal improvement to the data, compared to the 3+1 model. In Figure 4-30a, we show the best fit regions in the Δm_{41}^2 vs Δm_{51}^2 plane. We can see that the 3+2 model ends up fitting Δm_{51}^2 to the Δm_{41}^2 values found in the 3+1 fit in Figure 4-25a, but leaves the other mass-squared splitting unconstrained. A similar feature is seen in Figure 4-30b, where we plot the best fit region in the $\sin(\phi_{\mu e})$ vs Δm_{51}^2 plane. Here, the data seems to be insensitive to the additional parameter $\phi_{\mu e}$. We conclude, therefore, that the 3+2 model provides negligible improvement to the data compared to the 3+1 model.

We use the PG test to test the consistency of the 3+2 model, following the same procedure as for the 3+1 model. We find a test statistic value of $\chi_{\text{PG}}^2 = \chi_{\text{glob}}^2 - (\chi_{\text{app}}^2 + \chi_{\text{dis}}^2) = 728 - (75 + 613) = 40$, with degrees of freedom $k = (5 + 6) - 7 = 4$. This gives a p-value

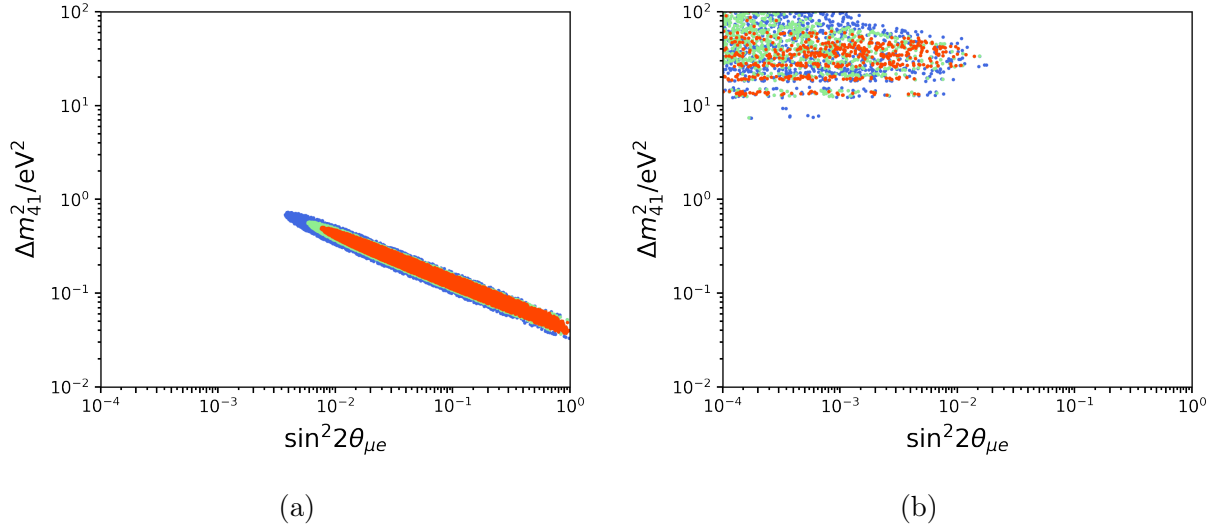


Figure 4-29: 3+1 fit results for (a) the appearance-only data sets and (b) the disappearance-only data sets.

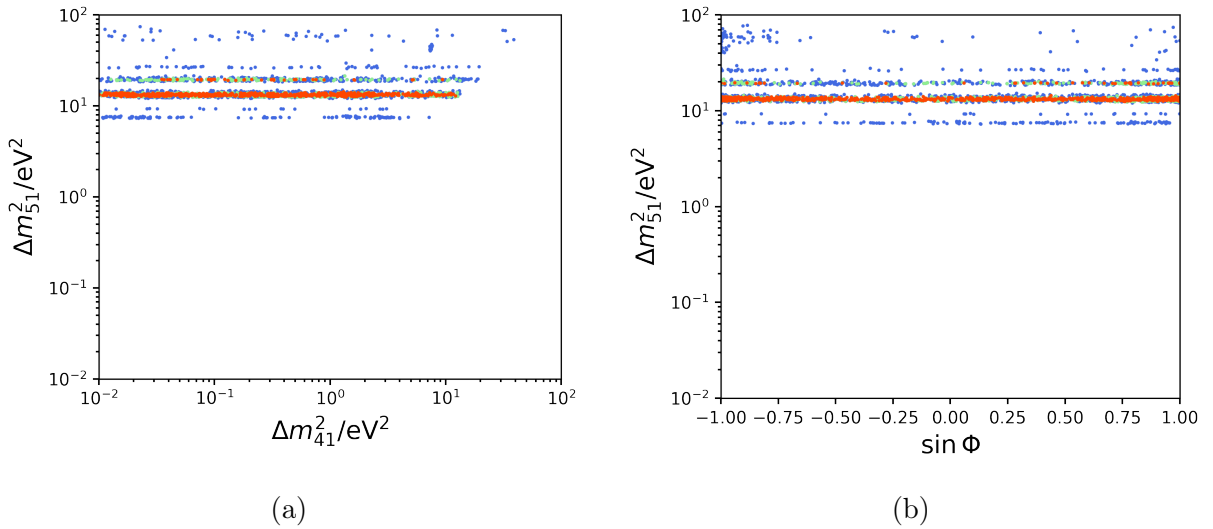


Figure 4-30: Results of the 3+2 global fits. (a) The best fit region in the Δm_{41}^2 vs Δm_{51}^2 plane. We can see that the fit finds preferred values of Δm_{51}^2 , but leaves Δm_{41}^2 unconstrained. The fitted values of Δm_{51}^2 are consistent with the values of Δm_{41}^2 found the in the 3+1 model. (b) The best fit region in the $\sin(\phi_{\mu e})$ vs Δm_{51}^2 plane. We see no sensitivity to the additional CP-violating parameter $\phi_{\mu e}$.

of $p = 4.3 \times 10^{-8}$ (5.5σ). Thus, we find that the 3+2 model actually worsens the tension compared to the 3+1 model.

4.3.3 3+1+Decay Model

We now consider the 3+1+Decay model described in Section 2.5.3. Here we have four dimensions to fit over. The first three are the same as the 3+1 case (Δm_{41}^2 , $|U_{e4}|$, $|U_{\mu 4}|$), with the fourth being the decay width Γ introduced in Section 2.5.3.

For this model, we show the results under two different conditions. In the first, we show the results with no bounds on Γ , to provide a fit that makes no model assumptions on the lifetime of ν_4 . In the second, we assume the decay width Γ is given specifically by Equation (2.21), and apply the condition that $g^2 < 4\pi$. This is to ensure that, in that particular model of Γ , we remain in the perturbative regime and that unitarity is preserved. This leads to the restriction that $\gamma \leq m_4/4$, or $\tau \geq 4/m_4$.

For the first case, we find a best fit at $\Delta m_{41}^2 = 1.4 \text{ eV}^2$, $|U_{e4}| = 0.3$, $|U_{\mu 4}| = 0.09$, and $\tau = 2.7 \text{ eV}^{-1}$. Written in terms of mixing angles, the best fit is found at $\sin^2 2\theta_{\mu e} = 0.0027$, $\sin^2 2\theta_{ee} = 0.34$, $\sin^2 2\theta_{\mu\mu} = 0.030$. The best fit confidence regions are shown in Figure 4-31, sliced in different intervals of τ . The contours are drawn assuming Wilks' theorem with three degrees of freedom. The first feature to notice is how different the preferred parameter space looks like when compared to the 3+1 case in Figure 4-25. In particular, the mass splitting drops down nearly an order of magnitude. Interestingly, this brings the Δm_{41}^2 to a value near that which was found in the previous 3+1 fit shown in Figure 4-27, but shifted to larger mixing angles. Another interesting feature is that the contour does not extend beyond $\tau > 0.8 \text{ eV}^{-1}$; therefore, there is a preference for a decaying sterile neutrino model versus a non-decaying sterile neutrino model.

To test the tension in this model, we once again utilize the PG test by separating the experiments into an appearance data set and a disappearance data set. We find a test statistic value of $\chi_{\text{PG}}^2 = \chi_{\text{glob}}^2 - (\chi_{\text{app}}^2 + \chi_{\text{dis}}^2) = 710 - (79 + 611) = 19$, with degrees of freedom $k = (3 + 4) - 4 = 3$. Compared to the 3+1 model, the tension is reduced from a χ_{PG}^2 of 30 to 19 with the 3+1+Decay model. This reduced tension corresponds to a p-value of $p = 2.7 \times 10^{-4}$ (3.6σ). While this is a substantial improvement compared to the tension for the 3+1 model, this tension is nonetheless troublesome. The confidence regions for the appearance and disappearance fits are shown in Figure 4-32 for the 95% confidence level.

For the case that we assume the specific decay width Γ as given in Equation (2.21) and restrict $g^2 < 4\pi$, we obtain the best fit point $\Delta m_{41}^2 = 1.35 \text{ eV}^2$, $|U_{e4}| = 0.3$, $|U_{\mu 4}| = 0.09$, and $\tau = 3.5 \text{ eV}^{-1}$. Written in terms of mixing angles, the best fit is found at $\sin^2 2\theta_{\mu e} = 0.0029$, $\sin^2 2\theta_{ee} = 0.32$, $\sin^2 2\theta_{\mu\mu} = 0.033$. We show in Figure 4-33 the best fit contours of this model with the coupling constant constraint. This time, only a single island exists, again with a preference for a finite lifetime.

We find a test statistic value of $\chi_{\text{PG}}^2 = \chi_{\text{glob}}^2 - (\chi_{\text{app}}^2 + \chi_{\text{dis}}^2) = 711 - (79 + 612) = 19$, with degrees of freedom $k = (3 + 4) - 4 = 3$. This gives the same p-value as the case with the unrestricted Γ . So while the preferred parameter space is significantly restricted when we place the bound $g^2 < 4\pi$, the best fit point remains similar and the relief in tension is the same. A comparison of the appearance and disappearance fits can be seen in Figure 4-34 for the 95% confidence level.

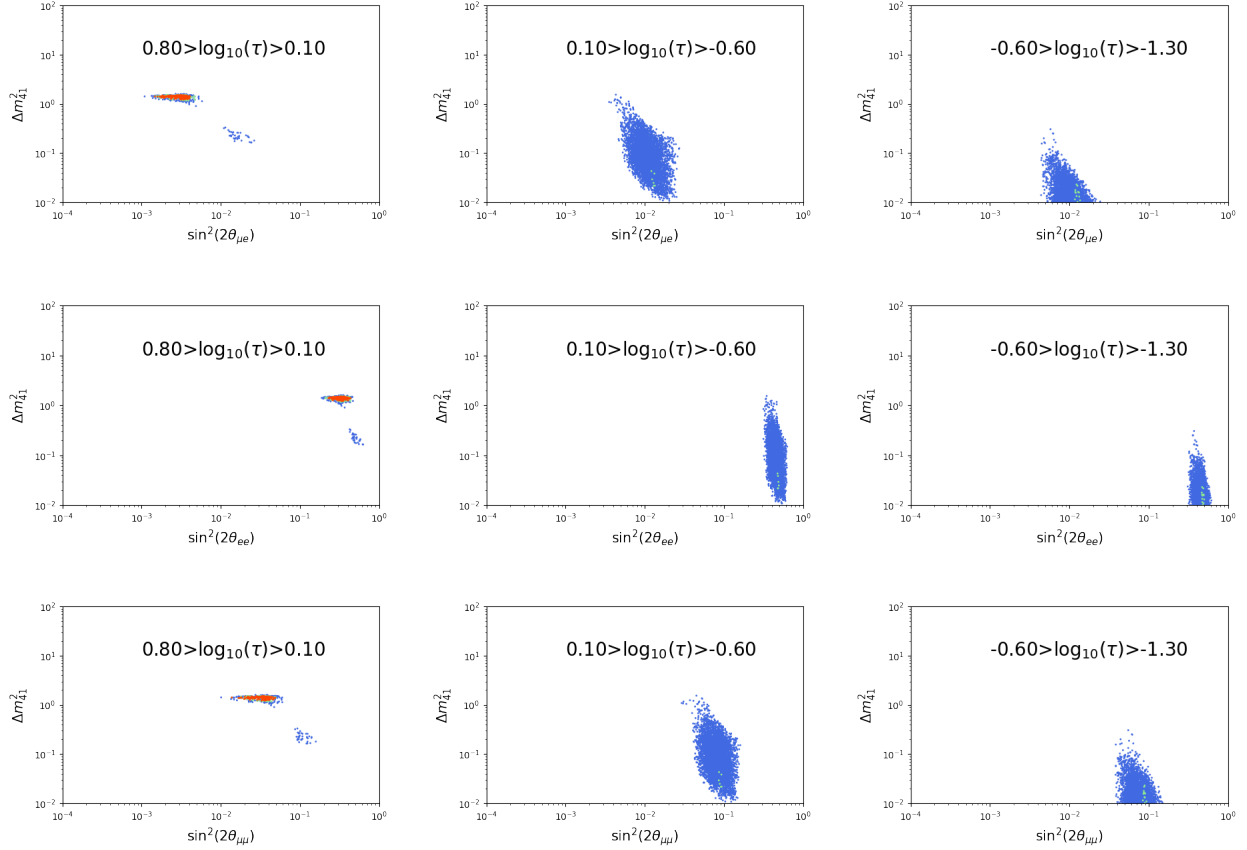


Figure 4-31: The results of the 3+1+Decay fits with no constraints on g^2 . The first row shows the changing confidence regions for $\sin^2 2\theta_{\mu e}$, the second for $\sin^2 2\theta_{ee}$, and the third for $\sin^2 2\theta_{\mu\mu}$. The columns are sliced into different intervals of lifetimes τ .

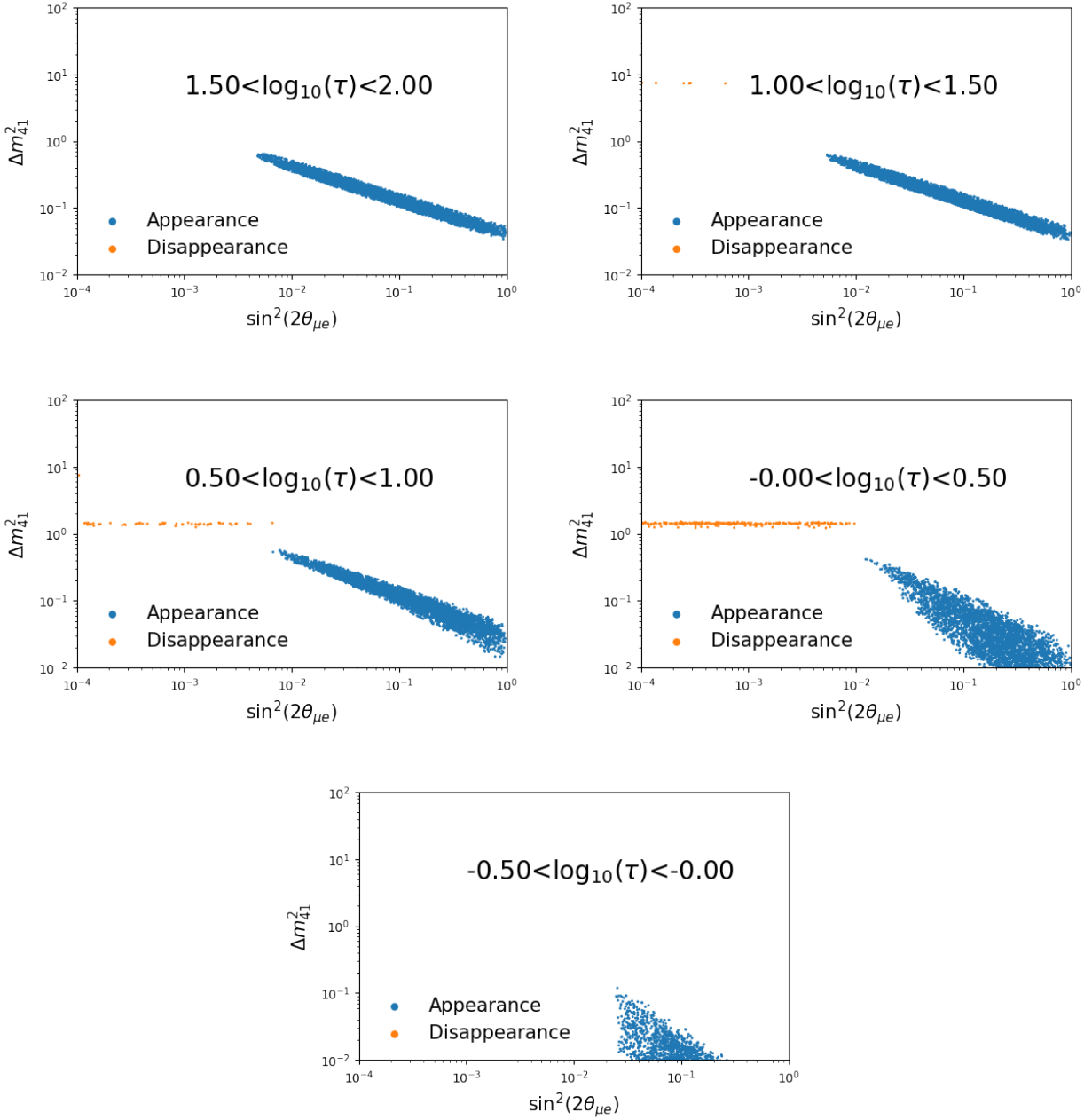


Figure 4-32: The confidence regions for the appearance and disappearance fits with the 3+1+Decay model at the 95% confidence level. Here, we place no restrictions on Γ .

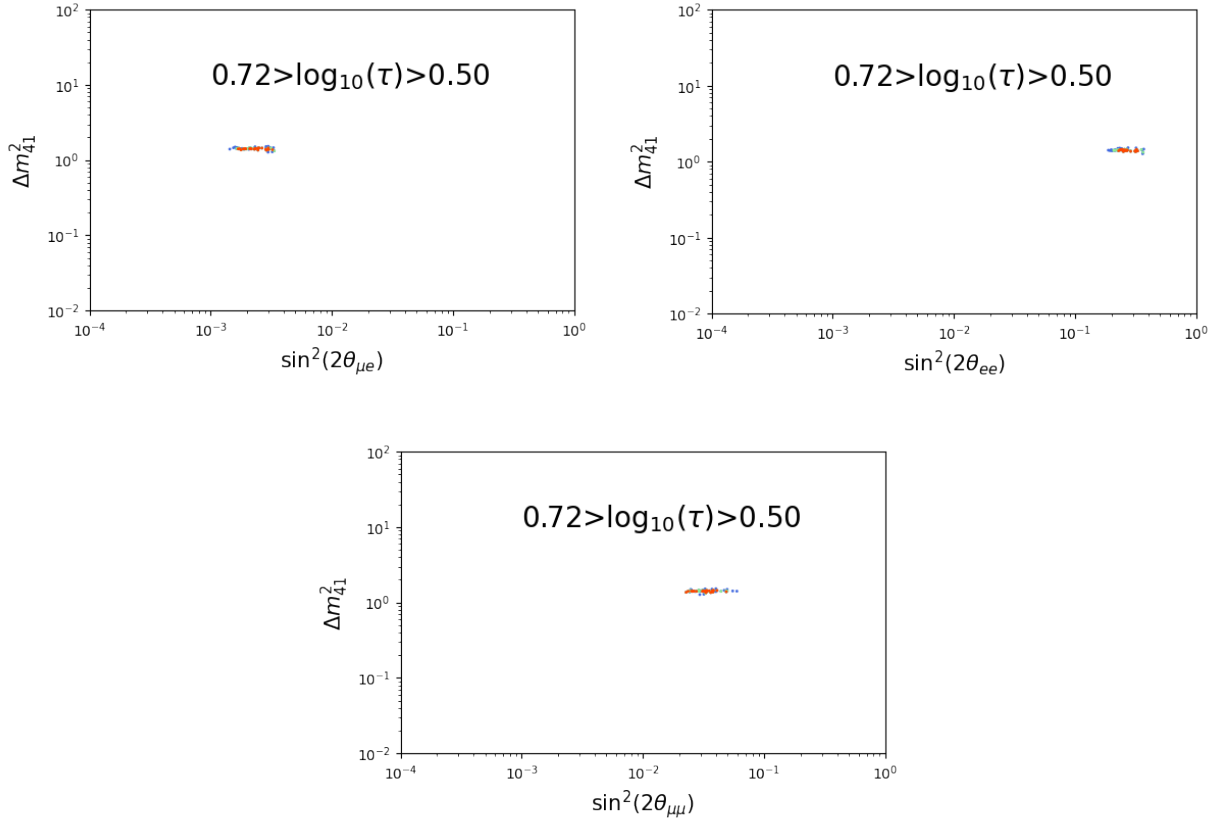


Figure 4-33: The best fit contours for the 3+1+Decay model when the constraint $g^2 < 4\pi$ is applied to the decay width Γ given in Equation (2.21).

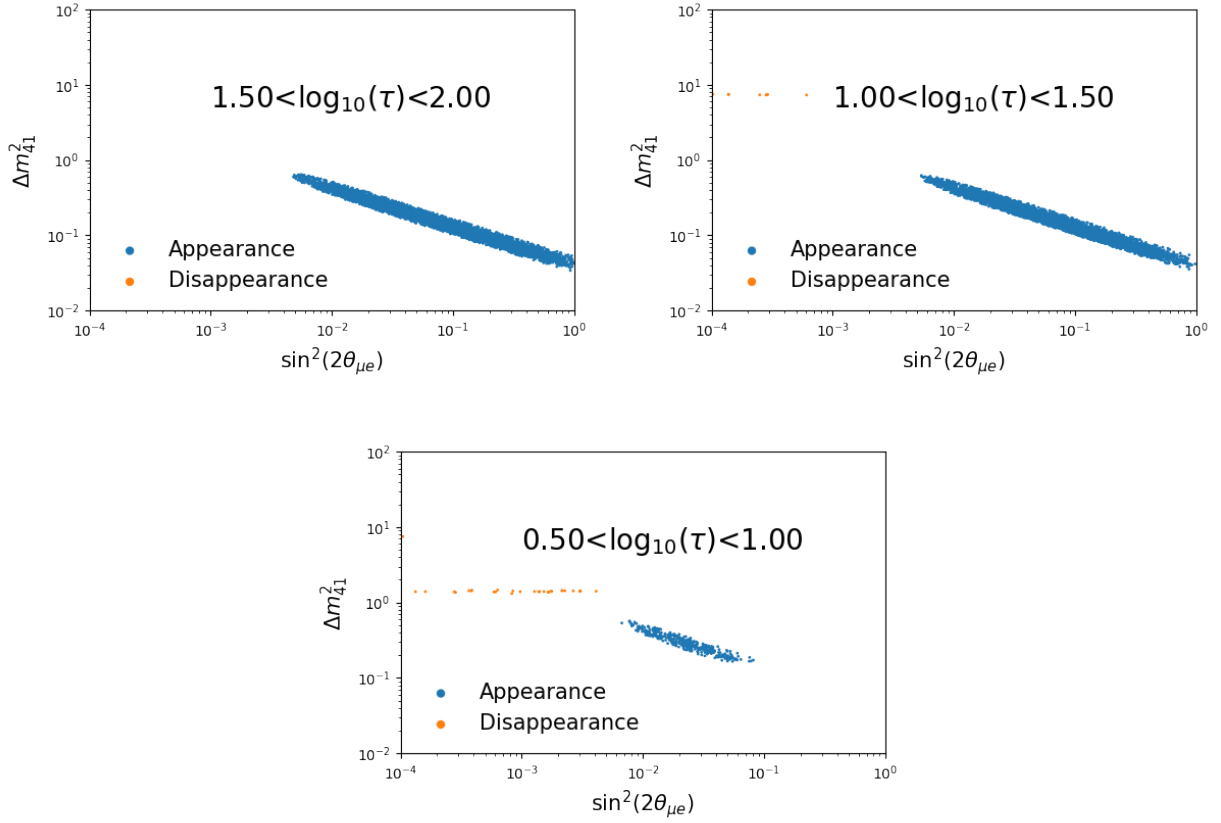


Figure 4-34: The confidence regions for the appearance and disappearance fits with the 3+1+Decay model at the 95% confidence level. The restriction $g^2 < 4\pi$ is placed here.

4.4 Discussion

The results of our global fits above give us a very confusing picture of the sterile neutrino model. We find that the data observed strongly prefer a minimal sterile neutrino mode, the 3+1 model, versus the SM picture; but irreconcilable tension exists within that model. Adding a second sterile state to the model, the 3+2 model, provides negligible improvement to the fit and worsens the tension. Expanding the picture into a more exotic model, the 3+1+Decay, provides some relief to the tension, but not enough to give us ease.

While simple sterile neutrino models are not able to give us a consistent picture, the various phenomena that can be explained by sterile neutrinos continues to encourage the development of novel models and new experimental techniques. In particular, we notice that while there exists experiments that observe something like $\nu_\mu \rightarrow \nu_e$ and $\nu_e \rightarrow \nu_e$ oscillations, there still has yet to be an experiment that observes $\nu_\mu \rightarrow \nu_\mu$ oscillations. Further, all the experiments listed above conduct measurements with vacuum oscillations. To continue exploring the sterile neutrino hypothesis, it would be interesting to search in unique ways. In the remaining chapters, we present an expansion of a sterile neutrino analysis that performs its search at a substantially higher energy than previous sterile neutrino searches and utilizing non-vacuum phenomena.

Chapter 5

Summary of the Previous Sterile Neutrino Search in IceCube

5.1 IceCube in a Nutshell

The IceCube Neutrino Observatory is a gigaton-scale neutrino detector embedded within the antarctic ice at 1450–2450 m below the surface [64]. The flagship purpose of IceCube is to search for point-sources of neutrinos outside of our solar system. For this thesis, though, we will restrict the discussion to the detector itself and the sterile neutrino analysis conducted with IceCube.

The detector is composed of 5160 digital optical modules (DOMs), which are the detector units embedded within the ice. Each DOM contains a photomultiplier tube (PMT) which points downwards, as well as a signal digitizer board. A schematic is shown in Figure 5-1. These DOMs are placed on 86 vertical strings, with 60 DOMs on each. The primary array of strings (78 strings) are arranged in an approximately triangular grid with 125 m horizontal spacing, and a vertical spacing of 17 m between DOMs. A subset of DOMs (8 strings), called DeepCore, are placed closer together, with an average inter-string spacing of 72 m and vertical DOM separation between 7 and 10 m. The dimensions of the detector were optimized to search for high-energy low-flux astrophysical neutrinos. A diagram of the detector is shown in Figure 5-2.

5.2 Sterile-Induced Neutrino Oscillation in Matter

In addition to astrophysical neutrinos, IceCube also detects neutrinos that are produced in the Earth’s atmosphere and later interact near the detector. As will be discussed in the next section, these atmospheric neutrinos are used to conduct a sterile neutrino search. This search utilizes the fact that these high-energy atmospheric neutrinos can travel through the Earth’s matter before reaching the detector, and that the presence of a sterile neutrino can modify matter-propagating neutrino oscillations beyond the modification expected from the SM (as in Section 1.4).

In this section, we discuss how these matter oscillations can be modified by the existence of a sterile neutrino. For this discussion, we again assume that the neutrinos are traveling

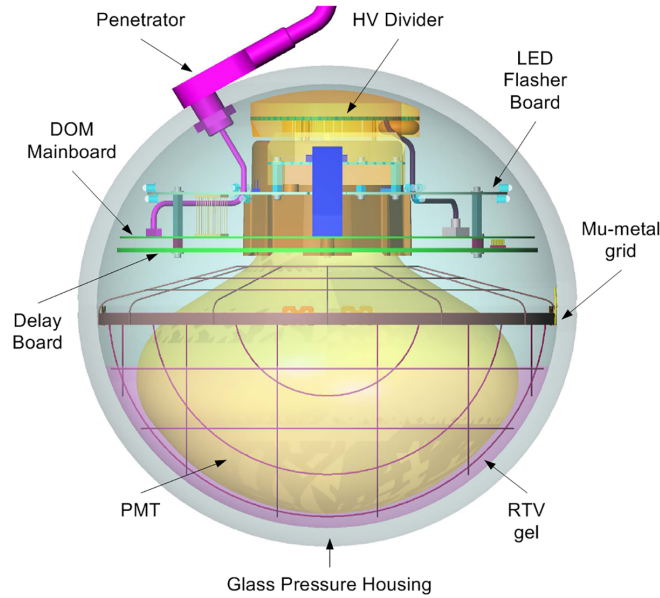


Figure 5-1: A schematic of one of the 5160 DOMs in IceCube. Note that the PMT points downwards.

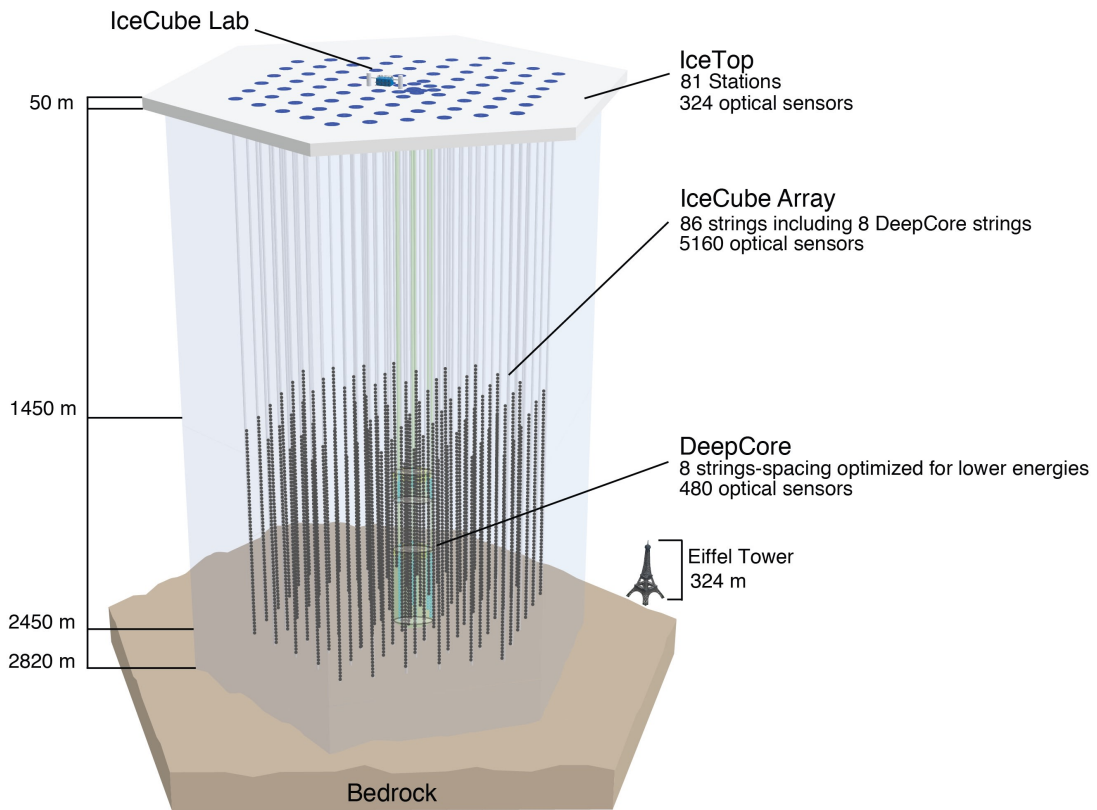


Figure 5-2: A diagram of the IceCube detector showing the distribution of the 86 strings and 5160 DOMs.

through a medium of constant density.

Like in Section 1.4, we start with the effective Hamiltonian in the flavor basis,

$$\mathcal{H}_F = \frac{1}{2E}(UM^2U^\dagger + \mathbb{A}). \quad (5.1)$$

Here,

$$\mathbb{M}^2 = \begin{pmatrix} 0 & 0 & 0 & 0 \\ 0 & \Delta m_{21}^2 & 0 & 0 \\ 0 & 0 & \Delta m_{31}^2 & 0 \\ 0 & 0 & 0 & \Delta m_{41}^2 \end{pmatrix}, \quad \mathbb{A} = \begin{pmatrix} A_{CC} + A_{NC} & 0 & 0 & 0 \\ 0 & A_{NC} & 0 & 0 \\ 0 & 0 & A_{NC} & 0 \\ 0 & 0 & 0 & 0 \end{pmatrix}, \quad (5.2)$$

where

$$A_{CC} \equiv 2EV_{CC} = 2\sqrt{2}EG_F N_e, \quad A_{NC} \equiv 2EV_{NC} = -\sqrt{2}EG_F N_n, \quad (5.3)$$

and N_n is the neutron density. In \mathbb{A} , we kept the NC terms. Note that the sterile component has neither CC nor NC terms.

In a two neutrino model, where we are considering only $\nu_\mu - \nu_s$ oscillations, we can simplify to

$$\mathbb{M}^2 = \begin{pmatrix} 0 & 0 \\ 0 & \Delta m^2 \end{pmatrix}, \quad \mathbb{A} = \begin{pmatrix} A_{NC} & 0 \\ 0 & 0 \end{pmatrix}. \quad (5.4)$$

We can see that our Hamiltonian ends up looking nearly identical to that derived in Section 1.4, so that the derived oscillation parameters can be obtained by making the replacement $A_{CC} \rightarrow A_{NC}$, or $N_e \rightarrow -N_n/2$, in Equations (1.30) to (1.35).

In this sterile-enhanced matter oscillation scenario, the resonant energy E_ν^R would be found at

$$E_\nu^R = -\frac{\Delta m^2 \cos 2\theta}{\sqrt{2}G_F N_n}. \quad (5.5)$$

If we assume that $\Delta m^2 > 0$ and $\theta < \pi/4$, then we get a negative value for E_ν^R . What this means is that the muon neutrino resonance can only be observed for antineutrinos, and not neutrinos.

In reality, a full oscillation treatment for four neutrinos propagating through varying density is required. For the work here and the remaining chapters, the neutrino propagation through the Earth is numerically calculated using the open-source neutrino oscillation calculator `nuSQuIDS` [65], which we describe more of later.

5.3 8-year Sterile Neutrino Search

As a result of the effect of matter oscillations discussed in Section 5.2, a sterile neutrino search can be conducted with IceCube that would not be possible with vacuum oscillations. Such an analysis has already been started and published [66, 67], which we will summarize in this section. In Chapters 6 and 7, we will discuss the continuation of this work and the final work of this thesis.

As discussed in the previous section, the existence of a sterile neutrino affects the oscilla-

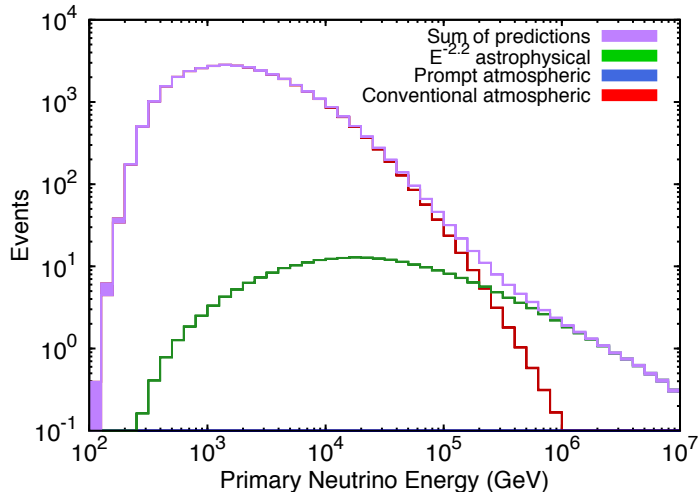


Figure 5-3: The best fit flux templates in the northern sky astrophysics ν_μ search in Ref. [68]. The atmospheric component is the sum of the conventional and prompt components, which we define later in Section 6.2.1. The prompt component fitted to zero. Supplemental figure from Ref. [68].

tion of the active neutrinos as they propagate through matter. As a reminder: regardless of the vacuum values of the mixing angles and mass-squared splittings, there exists a resonant energy for a given matter density that would result in maximal mixing for either neutrinos or antineutrinos. Refs. [66, 67] exploits this at IceCube, using the atmospheric muon antineutrinos produced around the Earth and which propagate through the Earth’s matter towards IceCube. That search is called Matter Enhanced Oscillations With Steriles (MEOWS). While “MEOWS” is not an official name, we will refer to the analysis as such in this thesis.

5.3.1 ν_μ Flux

Figure 5-3 shows the best fit template event rates for a northern sky astrophysical muon neutrino search conducted at IceCube [68]. The atmospheric muon neutrino event distributions (in red), are seen to peak at ~ 1 TeV.

In Figure 5-4, we show a series of oscillograms. Each plot shows the disappearance probability of atmospheric $\bar{\nu}_\mu$ after traversing through ‘the Earth’s matter, for some sterile parameters Δm_{41}^2 and $\sin^2 2\theta_{24}$. The x-axis gives the direction from which the neutrino is coming: $\cos\theta = -1$ refers to neutrinos that come from directly below the detector and traverse the Earth’s core, while $\cos\theta = 0$ refer to neutrinos from the horizon. For each plot, the disappearance in the upper left region is due to SM neutrino interactions at high energies with the Earth’s matter. The large disappearance seen in the $10^3 - 10^4$ GeV range is the resonant disappearance that is the result of the existence of a sterile neutrino state. This is the target signal for the sterile neutrino analysis in IceCube. As we can see, for typical sterile parameters considered, the resonant disappearance occurs at an energy near the peak muon neutrino flux seen in Figure 5-3.

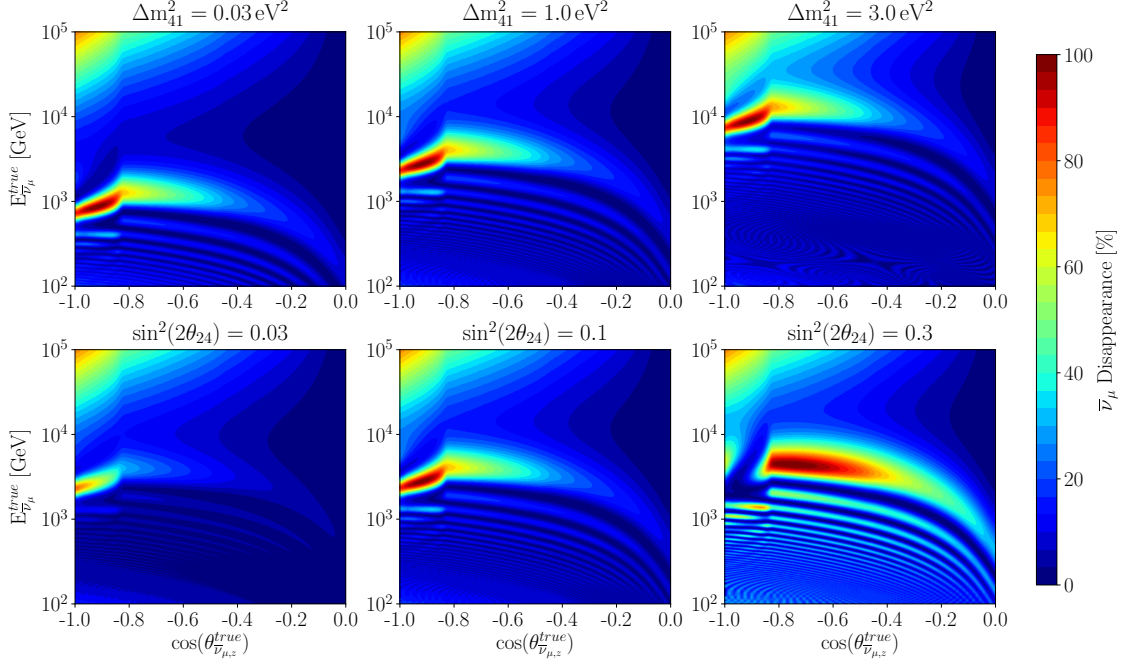


Figure 5-4: The expected disappearance of atmospheric $\bar{\nu}_\mu$ at the IceCube detector for various sterile neutrino parameters Δm_{41}^2 and $\sin^2 2\theta_{24}$. The top row keeps the mixing angle $\sin^2 2\theta_{24} = 0.1$ fixed with increasing Δm_{41}^2 from left to right. The bottom row keeps $\Delta m_{41}^2 = 1 \text{ eV}^2$ fixed with increasing $\sin^2 2\theta_{24}$ from left to right. Figure taken from Ref. [67].

5.3.2 ν_μ Interactions Near the Detector

When a ν_μ or $\bar{\nu}_\mu$ is near the detector, it can interact with the ice or bedrock. At the energies of interest, neutrinos undergo Deep Inelastic Scattering (DIS) [69]. Here, the neutrinos are of high enough energy that they can resolve the quarks individually in the nucleon. A tree-level diagram of a DIS scattering is shown in Figure 5-5. We refer to Ref. [69] for details on neutrino scattering.

With muons travelling at $\sim 1 \text{ TeV}$ through matter, they undergo various kinds of interactions. With the muon critical energy in ice being at 1.03 TeV , our muons of interest go through both ionization and radiative interactions. Examples of the latter are: bremsstrahlung, e^+e^- pair production, and photonuclear interactions [71]. The muon energy loss can be written as

$$\langle -dE/dx \rangle = a(E) + b(E)E, \quad (5.6)$$

where $a(E)$ is the ionization energy loss and $b(E)$ is the sum of the pair production, bremsstrahlung, and photonuclear contributions. An approximation of the average propagation distance can be calculated by integrating

$$R(E) = \int dE' [a(E') + b(E')E']^{-1}. \quad (5.7)$$

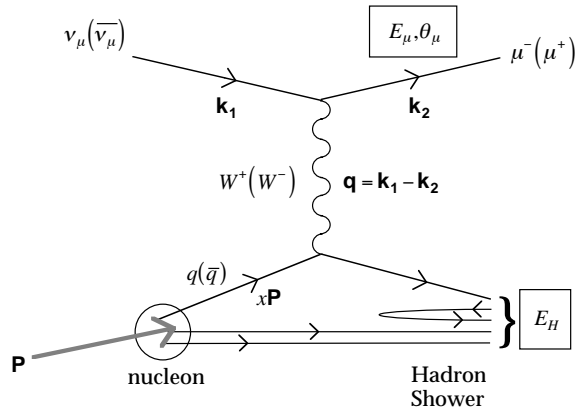


Figure 5-5: A deep inelastic scattering event of a $\nu_\mu/\bar{\nu}_\mu$ interacting with the quarks of a nucleon. The final products are a μ^-/μ^+ and a hadronic shower. Figure taken from Ref. [70].

This approximated range is called the “continuous-slowing-down-approximation” (CSDA) range. At higher energies, fluctuations in energy losses makes the CSDA range of limited use, but it can still provide an order of magnitude approximation for the distance travelled by a charged particle in a medium. For a μ of energy 1 TeV, the CSDA returns an average range of 2.4 km. Up at 10 TeV, the average range becomes 7.8 km. Therefore, a muon produced near IceCube will traverse a very long distance, over a kilometer long and frequently longer than the length of the detector. An IceCube event display is shown in Figure 5-6. There, a ν_μ undergoes a CC interaction near the center of the detector and the outgoing μ travels hundreds of meters to the left before exiting the detector.

In IceCube, a μ^+ track is indistinguishable to a μ^- track. Therefore, we cannot distinguish between a ν_μ CC event and a $\bar{\nu}_\mu$ CC event. In the context of observed events, we will thus use “ ν_μ ” to refer both ν_μ and $\bar{\nu}_\mu$ events.

5.3.3 Results

We summarize here the results of the previous sterile neutrino analysis in IceCube [66, 67]. Over a live-time of 7.634 years, 305 735 up-going ν_μ events were observed. These events were binned in terms of reconstructed energy and direction, and the sterile parameters Δm_{41}^2 and $\sin^2 2\theta_{24}$ were fitted. Two analyses were performed, a frequentist and a Bayesian analysis. The details of the frequentist analysis can be found in Section 7.3 in the context of the updated analysis, and the details for the Bayesian analysis can be found in Section 7.4.

The result of the frequentist analysis is shown in Figure 5-7. The best fit sterile parameters were found at $\Delta m_{41}^2 = 4.5 \text{ eV}^2$ and $\sin^2 2\theta_{24} = 0.10$, with a p-value of 8%. Therefore, no significant preference for sterile neutrinos was found.

The result of the Bayesian analysis is shown in Figure 5-8. The analysis was conducted by calculating the Bayes factor, as described in Section 7.4. At the best fit point of $\Delta m_{41}^2 = 4.5 \text{ eV}^2$ and $\sin^2 2\theta_{24} = 0.10$, a Bayes factor of $\log_{10} K = -1.03$ relative to null was found. According to Jeffreys’ scale, this constitutes a “strong” preference for the sterile model compared to the no-sterile model.



Event 5

Date: 12-Nov-10

Energy: 71.4 TeV

Topology: Track

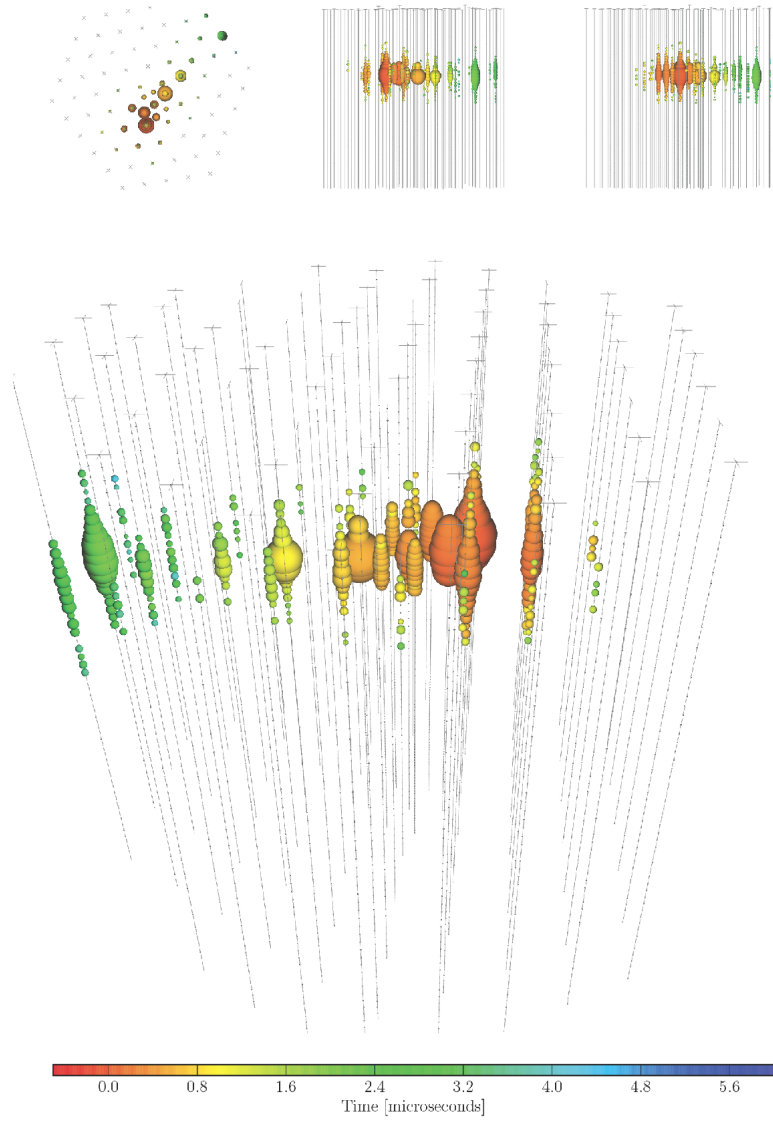


Figure 5-6: A ν_μ event observed in IceCube. Each colored sphere is a DOM that was hit. The size of the sphere corresponds to the energy deposited, and the color corresponds to the time when the DOM was hit. The event started near the center of the detector (red spheres), and moved left until exiting the detector.

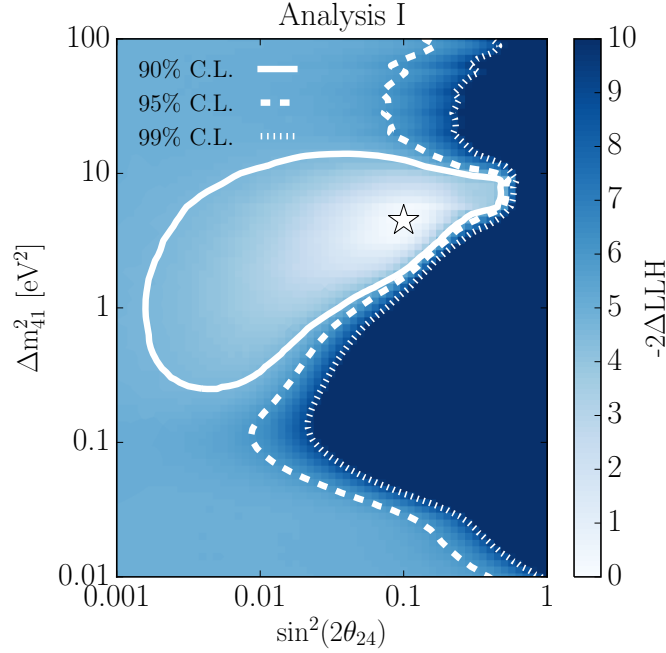


Figure 5-7: The best fit contour for the previous sterile neutrino analysis at IceCube. The best fit point was found at $\Delta m_{41}^2 = 4.5 \text{ eV}^2$ and $\sin^2 2\theta_{24} = 0.10$, with a p-value of 8%. Figure taken from Ref. [67].

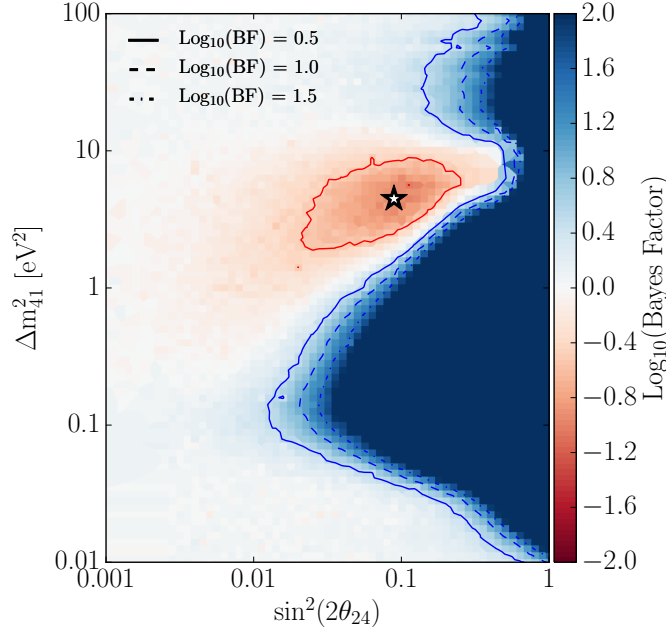


Figure 5-8: The result of the Bayesian fit in the previous sterile neutrino analysis at IceCube. At each point, the value of the Bayes factor relative to the null hypothesis is plotted. The point with the largest evidence was found at $\Delta m_{41}^2 = 4.5 \text{ eV}^2$ and $\sin^2 2\theta_{24} = 0.10$, with a Bayes factor of $\log_{10} K = -1.03$ relative to the no-sterile hypothesis. Figure taken from Ref. [66].

Chapter 6

MEOWS+ θ_{34}

The MEOWS analysis is unique amongst the sterile neutrino analyses in that it studies matter induced oscillations, as opposed to vacuum oscillations that the experiments listed in Section 4.1 explored. This provides an independent manner to search for sterile neutrinos, possibly shedding light on the difficulties with the sterile models discussed in Section 4.3.

As we noted in Chapter 4, a $\bar{\nu}_\mu \rightarrow \bar{\nu}_\mu$ vacuum disappearance experiment would only be sensitive to $|U_{\mu 4}|^2$ and Δm_{41}^2 for a 3+1 model. In matter oscillations, on the other hand, $\bar{\nu}_\mu \rightarrow \bar{\nu}_\mu$ depends on each of the new sterile neutrino parameters: $|U_{e4}|^2$, $|U_{\mu 4}|^2$, $|U_{\tau 4}|^2$, Δm_{41}^2 , δ_{14} , and δ_{24} . The mixing matrix elements can also be written in terms of the mixing angles θ_{14} , θ_{24} , θ_{34} . The relationship is given by

$$|U_{e4}|^2 = \sin^2 \theta_{14} \tag{6.1}$$

$$|U_{\mu 4}|^2 = \sin^2 \theta_{24} \cos^2 \theta_{14} \tag{6.2}$$

$$|U_{\tau 4}|^2 = \sin^2 \theta_{34} \cos^2 \theta_{24} \cos^2 \theta_{14}. \tag{6.3}$$

In the MEOWS analysis described in Section 5.3, a few simplifications were made. First, θ_{14} has a negligible effect on the atmospheric $\bar{\nu}_\mu$ disappearance through the Earth [72, 73], so θ_{14} was set to 0 (equivalently, $|U_{e4}|^2 = 0$), which made δ_{14} negligible as well. This leaves θ_{24} , θ_{34} , Δm_{41}^2 , and δ_{24} as the relevant sterile parameters. Finally, a choice was made to set $\theta_{34} = 0$ (equivalently, $|U_{\tau 4}|^2 = 0$), which also made δ_{24} negligible. This was done for computational reasons, with the justification that $\theta_{34} = 0$ is a conservative estimate.

The goal of our present work is to expand the MEOWS analysis to study the effects of a non-zero θ_{34} using the collected MEOWS neutrino sample. In fact, few experiments have placed limits on θ_{34} , and these existing limits remain weak. For example, the MINOS/MINOS+ experiments place a limit, at a fixed $\Delta m_{41}^2 = 0.5 \text{ eV}^2$, of only $\sin^2 \theta_{34} < 0.49$ ($\theta_{34} < 44^\circ$) at the 95% CL [74].

6.1 Oscillograms

Before discussing details of the analysis, we will see how θ_{34} affects $\bar{\nu}_\mu$ oscillations through the Earth. Figure 6-1 shows a series of oscillograms with increasing θ_{34} . Δm_{41}^2 and $\sin^2 2\theta_{24}$ are left constant at some representative value. For each pair of oscillograms, the left plot

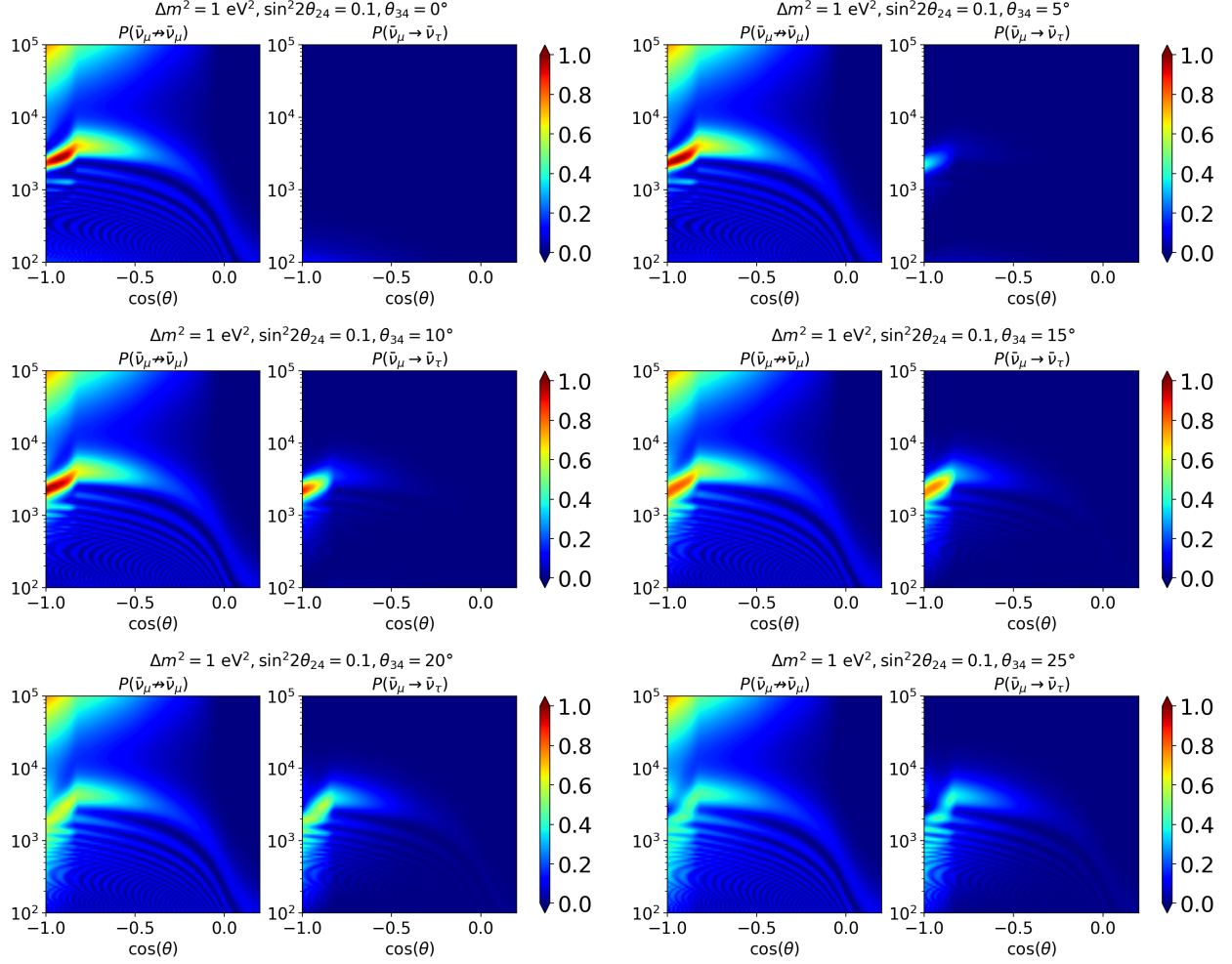


Figure 6-1: A series of oscillograms, where we show the expected $\bar{\nu}_\mu \rightarrow \bar{\nu}_\mu$ disappearance and $\bar{\nu}_\mu \rightarrow \bar{\nu}_\tau$ appearance for different values of θ_{34} . In each plot, we keep $\Delta m_{41}^2 = 1 \text{ eV}^2$ and $\sin^2 2\theta_{24} = 0.1$ constant.

shows the $\bar{\nu}_\mu$ disappearance. We can see how the resonance substantially changes with increasing θ_{34} , broadening and smearing into lower energies. Therefore, while $\theta_{34} = 0$ is the conservative selection, a proper fit to a 3+1 sterile model in IceCube has to take into account θ_{34} if it wants to accurately measure the hypothetical parameters.

Alongside each $\bar{\nu}_\mu$ disappearance plot, we also show the $\bar{\nu}_\mu \rightarrow \bar{\nu}_\tau$ appearance probability. With $\theta_{34} = 0$, $\bar{\nu}_\tau$ appearance is negligible. But with increasing θ_{34} , $\bar{\nu}_\tau$ appearance becomes significant. This appearance must be taken into account when doing our analysis.

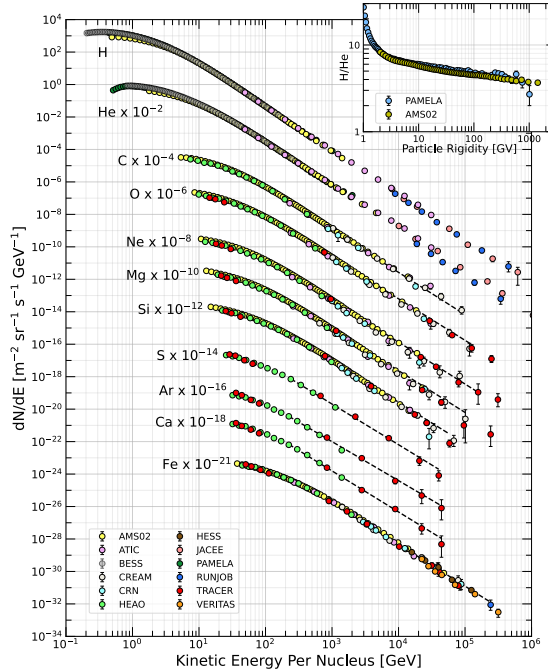


Figure 6-2: Fluxes of cosmic ray nuclei as a function of kinetic energy per nucleus. Figure taken from Ref. [75].

6.2 Neutrino Sources

6.2.1 Atmospheric Neutrinos

The neutrinos that the MEOWS analysis primarily detects are atmospheric muon neutrinos. These neutrinos are produced by the interactions of cosmic rays with the Earth’s atmosphere. Cosmic rays are primarily composed of hydrogen and helium nuclei, with a smaller proportion of heavier elements. Figure 6-2 shows the flux of various cosmic ray nuclei experimentally measured.

The spectra of these cosmic ray approximately follow a steeply falling power-law spectrum. Within our energy range of interest (several GeV up to 100 TeV), the intensity of primary nucleons is approximately given by

$$I_N(E) \approx 1.8 \times 10^4 (E/1 \text{ GeV})^{-\gamma} \text{ nucleon m}^{-2} \text{ s}^{-1} \text{ sr}^{-1} \text{ GeV}^{-1}, \quad (6.4)$$

where E is the energy per nucleon and $\gamma \approx 2.7$. These cosmic rays then collide with the Earth’s atmosphere, producing mesons that later decay into neutrinos (similar to how accelerating a proton beam into a target produces neutrinos at LSND and MiniBooNE). The flux evolution of cosmic rays and their daughter particles through the atmosphere are described by coupled cascade equations. Of interest for our analysis are the neutrino fluxes and the muon fluxes, the former of which is our source and the latter of which is a background.

The atmospheric neutrino flux is divided into two components a “conventional” component and a “prompt” component. The conventional component originates from the decay of

pions, kaons, and muons. The prompt component, on the other hand, originates from the decay of higher-mass charmed mesons. These charmed mesons decay quickly, before they have a chance to lose substantial energy interacting with the atmosphere. Therefore, the prompt neutrino component is in a higher energy range than the conventional component.

For the MEOWS analysis, the conventional flux is derived using the **Matrix Cascade Equation** (MCEq) package [76]. As inputs, MCEq takes in an initial cosmic ray model, a hadronic interaction model, and an atmospheric density profile. For the cosmic ray model, the Hillas-Gaisser 2012 H3a model [77] is used. As the cosmic rays collide with the atmosphere, the evolution of the secondary particles is guided by a hadronic interaction model. We use the SYBILL 2.3c model [78]. Finally, the evolution also depends on the atmospheric density profile of the Earth. Data from the Atmospheric Infrared Sounder (AIRS) on NASA’s Aqua satellite is used [79].

The prompt component is taken to be the one calculated in Ref. [80].

6.2.2 Astrophysical Neutrinos

In addition to atmospheric neutrinos, astrophysical neutrinos are taken into account. While their origin is unknown, IceCube has established the existence of a diffuse flux of astrophysical neutrinos. For this analysis, the astrophysical neutrino flux is taken to be isotropic with a falling power-law spectrum

$$\frac{dN_\nu}{dE} = \Phi_{\text{astro}} \times \left(\frac{E_\nu}{100 \text{ TeV}} \right)^{-\gamma_{\text{astro}}}, \quad (6.5)$$

with a nominal normalization $\Phi_{\text{astro}} = 0.787 \times 10^{-18} \text{ GeV}^{-1} \text{ sr}^{-1} \text{ s}^{-1} \text{ cm}^{-2}$ and a nominal spectral index of $\gamma_{\text{astro}} = 2.5$.

6.3 Neutrino Propagation Through the Earth

After calculating an initial neutrino flux at the Earth’s surface, we have to propagate this neutrino flux through the Earth. As mentioned earlier, this calculation is very difficult to do analytically taking into account the varying density profile of the Earth and the multiple neutrino flavors. We therefore use the **nuSQuIDS** package to numerically propagate the neutrinos through the Earth, given some sterile neutrino hypothesis. In addition to the difficult calculation of matter oscillations, **nuSQuIDS** also takes into account non-coherent interactions. These include flux attenuation from neutrinos interacting in the Earth; neutrino energy losses due to neutral current interactions; ν_e and ν_μ production from τ decays; and neutrino production from W^- decays in Glashow resonances.

nuSQuIDS also takes in as input the density profile of the Earth. Here, we use the Preliminary Reference Earth Model (PREM model) [81], which assumes a spherically symmetric Earth with density varying as a function of radius.

After propagating the neutrinos through the Earth with some sterile neutrino model, **nuSQuIDS** provides the final neutrino flux at the IceCube detector.

6.4 Neutrino Interactions Near the Detector

When a neutrino interacts in or near the detector, its interaction products are visible to the IceCube detector.

For a ν_μ CC interaction, the interaction products are an outgoing μ and a hadronic shower starting at the interaction point. As described in Section 5.3.2, a μ can travel long distances in the ice. If the muon traverses through the detector, it leaves behind a “track” of hit DOMs, as seen in Figure 5-6. For ν_μ CC events that occur outside the detector, the hadronic shower will not be visible and the detector would only be able to see the μ if it traverses through the detector.

For a ν_e CC interaction, the products are an outgoing e and a hadronic shower. The outgoing e will produce an electromagnetic shower which, like a hadronic shower, will remain close to the interaction point. This interaction will produce a roughly spherically symmetric distribution of hit DOMs, which is referred to as a “cascade.” An example of a cascade is shown in Figure 6-3.

For a NC interaction of any neutrino flavor ν_α , the interaction products are the ν_α and a hadronic shower. The outgoing ν_α is invisible to the detector, so the only signature is a cascade from the hadronic shower.

In summary: as seen by the detector, ν_μ CC events produce “tracks” from the μ traversing the detector, while ν_e CC and all-flavor NC events produce “cascades.”

The signature of a ν_τ CC interaction will depend on how the outgoing τ decays. Of interest for us is when the τ decays leptonically by $\tau \rightarrow \mu + \dots$, as this has the same event signature as a ν_μ event. This decay has a branching ratio of 18%. As seen in Figure 6-1, a non-zero θ_{34} can lead to significant $\nu_\mu \rightarrow \nu_\tau$ appearance, so these events have to be taken into account as well.

Simulated neutrino interaction points are chosen using the program `LeptonInjector` [82]. The injected energy follows some nominal flux. A related program, `LeptonWeighter` [82], allows the reweighting of events to some arbitrary flux after the simulation. This lets us use a single simulation set, which can be then reweighted for any neutrino flux at IceCube, i.e. any sterile neutrino hypothesis.

When a neutrino interaction point is selection, the secondary products are propagated through the rock and ice using the `PROPOSAL` software [83]. The deposited energy is accounted for by `PROPOSAL`, and the resulting photons are then propagated using the IceCube software `CLSim`. The photons are propagated until they are either absorbed or collected by a DOM.

For the ν_μ simulations, we use the same simulation set as the previous MEOWS analysis, corresponding to about 500 years of live time.

For the work in this thesis, we also generated a new set of ν_τ simulations. For this, we modified `PROPOSAL` to properly take into account the τ polarization when decaying into a μ . `PROPOSAL` typically propagates and decays particles assuming that they are unpolarized. τ^- 's (τ^+ 's), though, are very short-lived, and the weak interaction guarantees that they are produced in a left-(right-)handed chirality state. Therefore, they will decay polarized. The rest frame cross section for the μ^\pm energy and direction from a τ^\pm decay is [75, 84]

$$\frac{d^2\Gamma}{dx d\cos\vartheta} \propto [3 - 2x \pm |\mathbf{P}_\tau| \cos\vartheta(2x - 1)]x^2, \quad (6.6)$$



Event 12

Date: 27-Jun-11

Energy: 104.1 TeV

Topology: Shower

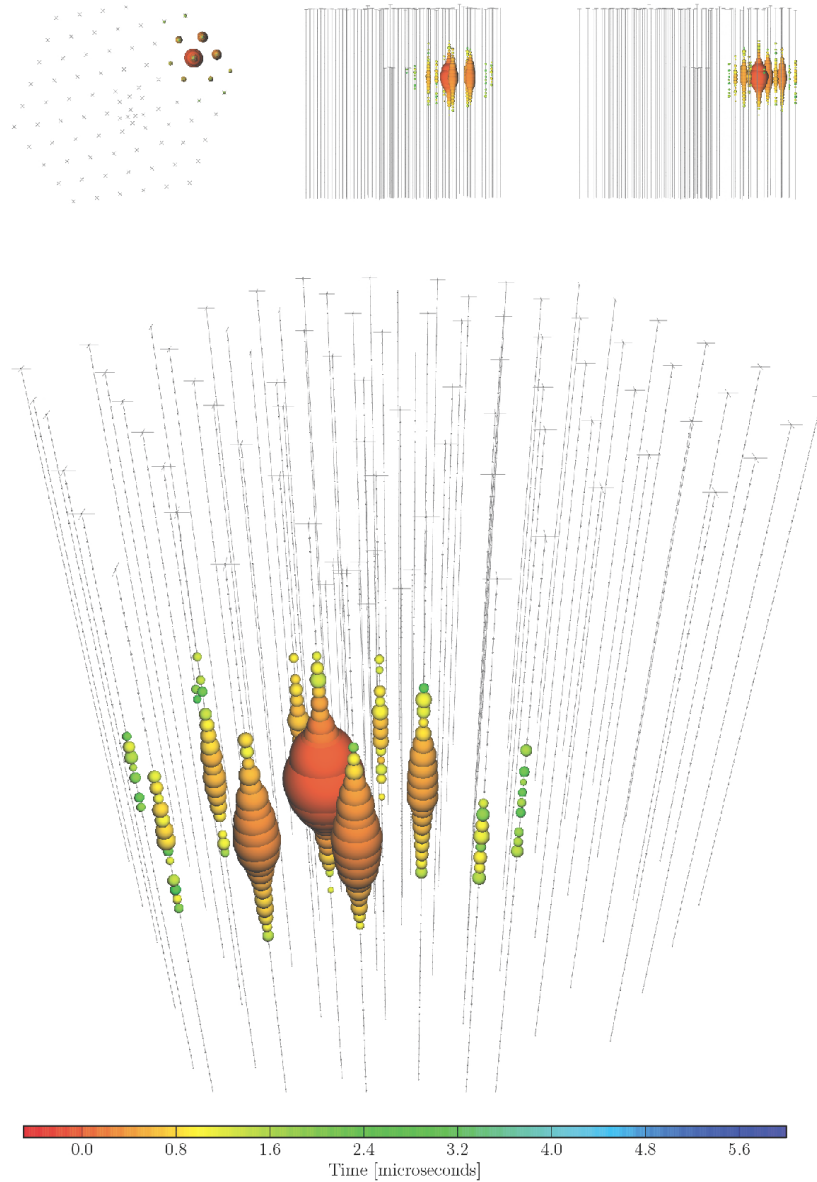


Figure 6-3: An example of a cascade event in IceCube. Unlike a track event, cascade events deposit their energy in an approximately spherical volume centered at the interaction point.

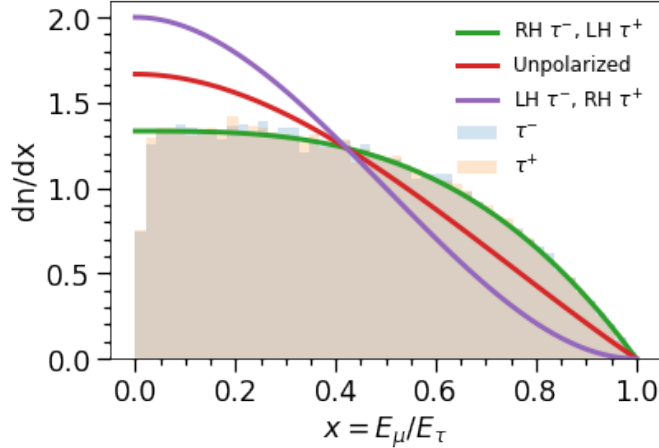


Figure 6-4: The expected ratio x of the energies between a μ and a τ , when the τ decays leptonically as $\tau \rightarrow \mu + \dots$. PROPOSAL typically assumes that all particles are unpolarized, so x would follow the red line. We added a correction to PROPOSAL to take into account that a ν_τ CC event would create polarized τ 's, and these τ 's would in turn decay polarized.

where $x \equiv 2E_\mu/m_\tau$, ϑ is the angle between the muon momentum and the τ spin, and $|\mathbf{P}_\tau|$ is the degree of τ polarization. The standard PROPOSAL code neglects the $\cos\vartheta$ dependent term, but we introduce it for our analysis. Looking at Equation (6.6), we can see that for left-handed (LH) τ^- and right-handed (RH) τ^- the muon is emitted preferentially in the direction of motion. Boosting to the lab frame, the μ^\pm energy distribution from a τ^\pm decay is given by [84]

$$F_{\tau^\pm \rightarrow \mu^\pm}(x) = \left(\frac{5}{3} - 3x^2 + \frac{4}{3}x^3 \right) \mp \mathbf{P}_\tau \left(\frac{1}{3} - 3x^2 + \frac{8}{3}x^3 \right). \quad (6.7)$$

The x distribution in the lab frame is shown in Figure 6-4. The green line corresponds to μ 's from completely polarized LH τ^- and RH τ^+ decays, and the purple line corresponds to μ 's from RH τ^- and LH τ^+ decays. The red line is the x distribution if we assumed that the τ 's were unpolarized when decaying. The histogram shows the results of our simulation after producing the muons as in Equation (6.6) and boosting to the lab frame. Without our correction, the simulation muon energy distribution would incorrectly follow the red line.

6.5 Muon Reconstruction

The observable of interest are muons traversing the detector, which produce tracks. The MEOWS analysis selected for tracks whether they begin inside or outside the detector. Tracks that originate outside of the detector are referred to as “through-going” tracks, while tracks that begin inside the detector are called “starting” tracks. While through-going muons provide worse energy reconstruction since the hadronic shower and initial track occur outside of the detector, they greatly increase the available statistics. Further contributing to the poor energy resolution is that these muons are likely to escape the detector, so the total energy

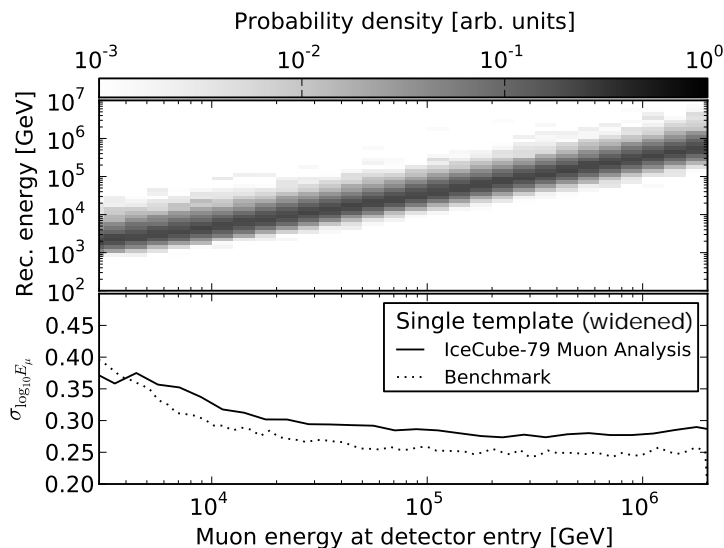


Figure 6-5: Energy reconstruction of muon tracks, as a function of the true muon energy when it entered the detector. Figure taken from Ref. [85].

of the muon is rarely contained entirely within the detector.

The energy reconstruction algorithm used is an internal IceCube algorithm called MuEX, used in an astrophysical neutrino search analysis [68] and described in more detail in Refs. [85, 86]. Figure 6-5 shows the reconstructed muon energy distribution as a function of the true muon energy when it enters the detector; the energy resolution is quite poor. Relative to the true neutrino energy on interaction, the energy resolution is even worse. We show in Figure 6-6 the reconstruction muon energy distribution compared to true ν_μ energy in the MEOWS simulation sample, and the reconstructed muon energy distribution compared to true ν_τ energy from our simulation.

The muon direction, on the other hand, is reconstructed well. Due to muons traversing such a large distance through IceCube, the large lever arm allows good reconstruction of the direction. This can be seen in Figure 5-6. Using the internal MPEfit algorithm, the direction is reliably reconstructed to better than 1° .

6.6 Event Selection

In this analysis we use the same event selection as the MEOWS analysis. The event selection was designed to obtain a very pure sample of ν_μ CC events. The IceCube detector, while being 1.5km under ice, still triggers 3000 times per second [87] due to penetrating atmospheric muons. These atmospheric muons constitute the largest backgrounds in the analysis. A detailed description of the cuts used are summarized in Ref. [67], but we will summarize here the more significant cuts.

At IceCube, the majority of the neutrino flux is composed of muon neutrinos. As discussed, ν_μ CC events produce a track in the detector, a very distinct signal compared to the

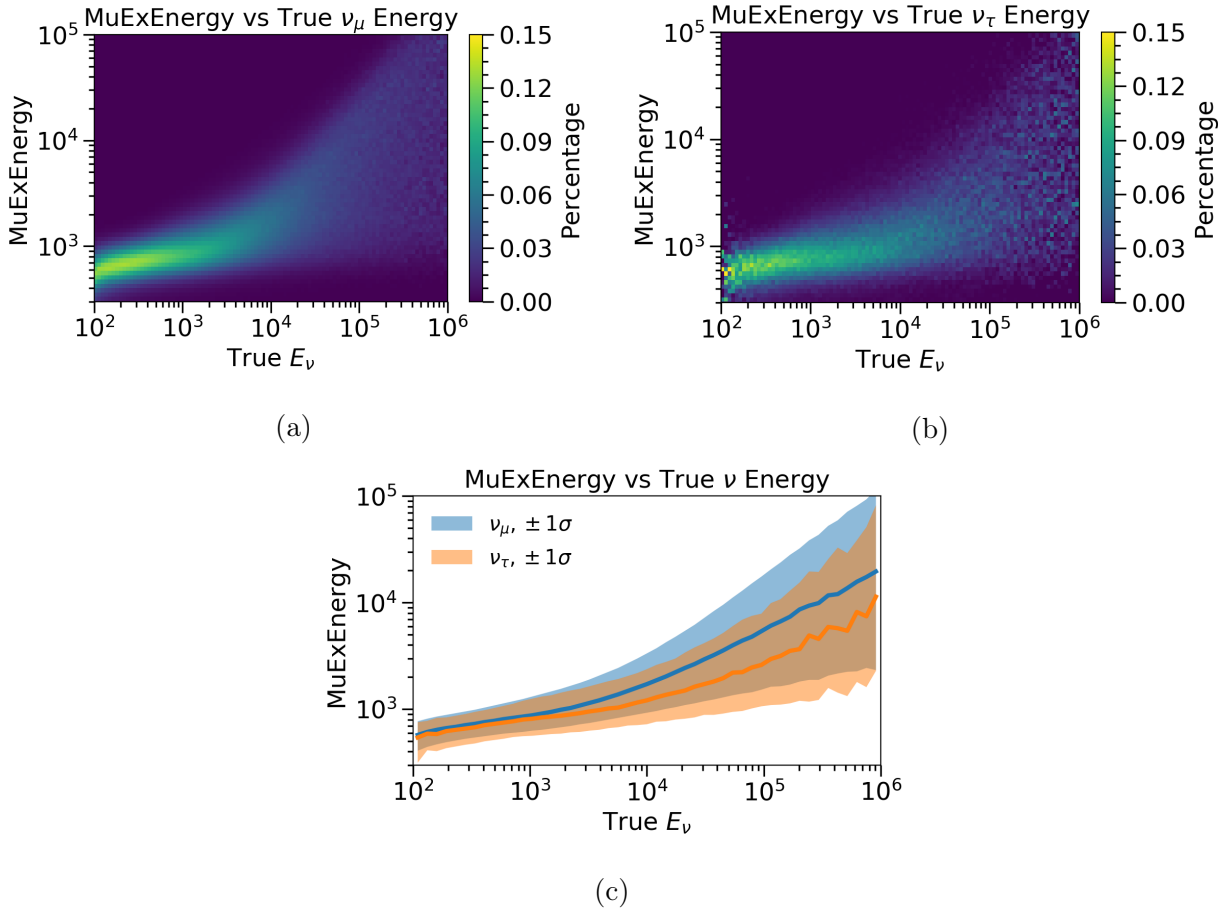


Figure 6-6: (a) The energy reconstruction of muons from ν_μ CC events as a function of true ν_μ energy. (b) The energy reconstruction of muons from ν_τ CC events followed by $\tau \rightarrow \mu\dots$ decays, as a function of true ν_τ energy. (c) A comparison of the muon energy reconstruction between ν_μ CC and ν_τ CC events. All plots use events that pass the MEOWS event selection.

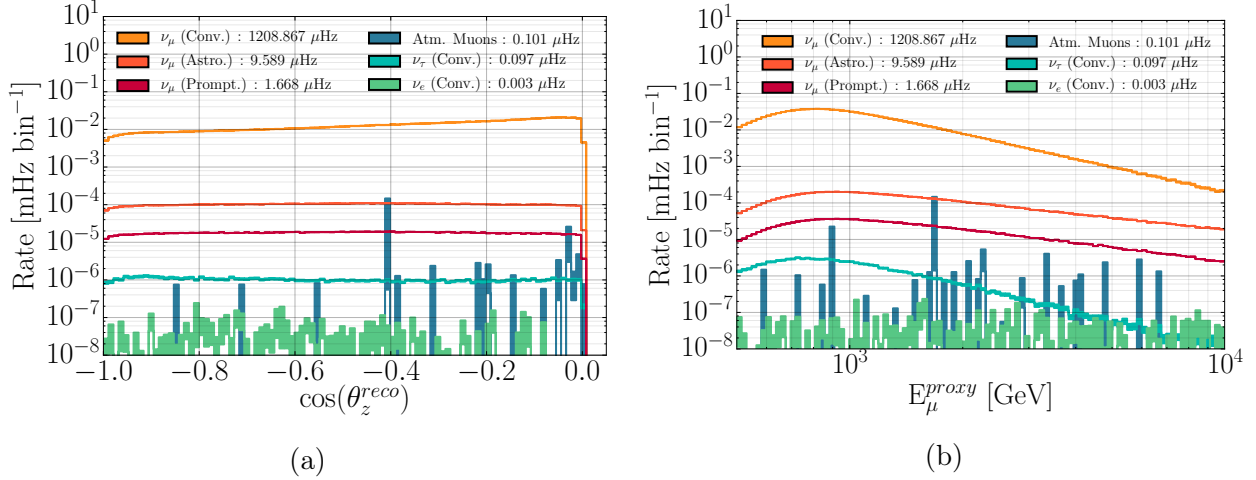


Figure 6-7: The expected event rates from different neutrino components and backgrounds that pass the final filter, assuming the no-sterile model. (a) The event rate as a function of reconstructed $\cos\theta$. (b) The rate as a function of reconstructed energy. Figures from Ref. [67].

cascades produced by ν_e and NC events. Therefore, the first step is IceCube’s muon filter, which removes non-track events. ν_τ CC events where the τ decays into a muon produces a near identical signal as a ν_μ CC event, so those will not be cut out.

Track events will then have their energies and direction fitted. A cut is applied so that the reconstructed energies fall within 500–9976 GeV. Outside of this range, the event count falls quickly, and the less understood astrophysical flux begins to dominate at higher energies.

At the horizon ($\cos\theta = 0$), IceCube already has 157km of water-equivalent shielding. While muons are highly penetrating, they are not so penetrating that they could traverse thousands of kilometers through the Earth. Therefore, any track reconstructed as coming from below the horizon ($\cos\theta < 0$) will very likely come from a ν_μ event instead of an atmospheric muon, and a cut is applied as such. If an above-horizon ($\cos\theta > 0$) atmospheric muon were to be misreconstructed as $\cos\theta < 0$, its fit would be poor and therefore still removable.

Ultimately, the event sample has a purity of 99.9%, with very few background events. The expected event distributions, as a function of reconstructed energy and zenith, are shown in Figure 6-7.

6.7 Systematic Parameters

The systematic treatment used in this analysis is near identical to the previous MEOWS analysis. The 18 systematic parameters can be divided into four categories: conventional flux parameters, detector parameters, astrophysics parameters, and cross section parameters. Each of these systematic parameters are implemented as nuisance parameters in our fits, with a prior associated with each one. Minor corrections to the systematic treatment come from a related MEOWS+Decay analysis in IceCube [3, 88]. They are: updated livetime from 7.6

years to 7.634 years; updated Barr parameter corrections (described in Section 6.7.1) using atmospheric data from the AIRS satellite; corrected Earth composition model that places the bedrock under IceCube at 3 km under the surface, rather than 30 km.

Here, we summarize each of the systematic parameters included in the MEOWS analysis, and which are also used in our updated analysis. More detailed descriptions of the systematic parameters can be found in Refs. [67, 89]. A table of all the systematic parameters with their central values and priors are listed in Table 6.1.

6.7.1 Conventional Flux Parameters

In Section 6.2.1, we discussed how a nominal conventional atmospheric flux is calculated assuming some cosmic ray model, hadronic interaction model, and atmospheric density model. A total of nine systematic parameters are used to parameterize the uncertainties in these models. The prompt component is not accounted for in the systematic parameters, as it is a subleading component in the energy range of interest and its uncertainty can be absorbed in the conventional component’s systematic uncertainties.

Conventional Normalization

A 40% normalization uncertainty is applied to the nominal conventional flux derived by MuEx.

Cosmic Ray Spectral Slope

The cosmic ray model used approximately follows a falling power-law spectrum. Uncertainties exist in the spectral shape of this cosmic ray flux, which translates into a spectral shape uncertainty in the produced neutrino flux. This is accounted for by the inclusion of a spectral shape correction term $\Delta\gamma$ in the conventional flux

$$\Phi(E_\nu; \Delta\gamma) = \Phi(E_\nu) \left(\frac{E}{2.2 \text{ TeV}} \right)^{-\Delta\gamma}, \quad (6.8)$$

where $\Phi(E_\nu)$ is the nominal conventional neutrino flux. $\Delta\gamma$ is centered at 0 and given a prior width of 0.03.

Barr Gradients (WP, WM, YP, YM, ZP, ZM)

The uncertainties in hadronic production are parameterized using the Barr parametrization [90]. In the Barr scheme, uncertainties in π^\pm and K^\pm production are grouped into different regions of incident particle energy E_i and $x_{\text{lab}} = E_s/E_i$, where E_s is the secondary total energy. Figure 6-8 shows how these regions are divided for π^\pm and K^\pm separately. Because the conventional flux is primarily composed of K^\pm and the energy range of interest begins in the hundreds of GeV, only the W, Y, and Z regions are considered. For the kaons, the regions for K^+ and K^- are treated separately, so a total of six Barr parameters are constructed: WP, WM, YP, YM, ZP, and ZM, where the “P” and “M” indicate if it’s for the positively charged or negatively charged kaons, respectively. These Barr parameters represent a modification to the K production rate at their respective E_i and x_{lab} . The uncertainties are: 40% for WP and WM, 30% for YP and YM, and $12.2\% \times \log_{10}(E_i/500 \text{ GeV})$ for ZP and ZM.

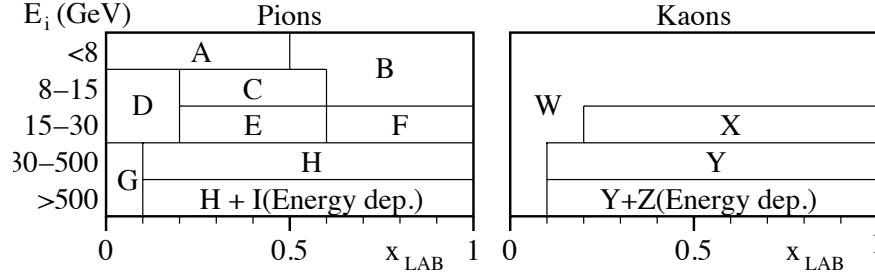


Figure 6-8: Different uncertainty regions for the meson production rate. The boundaries are chosen so that different regions correspond roughly to different physical effects. Figure taken from Ref. [90].

Atmospheric Density

Hadronic production and evolution will depend on the atmospheric density profile. A nominal profile is taken from the AIRS satellite [79]. Uncertainties provided by the AIRS satellite is used to perturb the density profile and extract the effect these uncertainties have on the atmospheric flux.

While only a single cosmic ray and hadronic interaction model were chosen to derive a nominal neutrino flux, several discrete models exist. It has been found that the combination of the systematic parameters above cover the different possible neutrino fluxes derived by different combinations of these models [3].

6.7.2 Detector Parameters

DOM Efficiency

The DOM efficiency parameter accounts for the correlated photon efficiency of the DOM's photocathodes globally, as well as any other external properties that may effectively reduce the overall photons detected by the DOMs in IceCube.

Ice Gradients

The ice in which IceCube is embedded has been deposited over the course of thousands of years under varying conditions. Therefore, the ice is not uniform and one must expect varying photon propagation properties as you move deeper into the ice. The uncertainty on this was parameterized with the "SnowStorm" method [91]. SnowStorm decomposes the depth dependent ice properties into Fourier modes, where lower order modes correspond to variations that span slowly across the height of the detector, and higher order modes correspond to variations that change rapidly. These variations are able to be decomposed into two parameters, which are simply called "ice gradient 0" and "ice gradient 1."

Hole Ice

The hole ice refers to the column of ice around the detector strings that were melted to install the DOMs and later refroze. This process changed the property of the ice immediately surrounding the DOMs, introducing an angular acceptance effect for photons approaching the DOMs. Notably, towards the central axis of the refrozen

columns, the ice is more opaque due to bubbles or impurities, affecting photons that are traveling straight up towards the DOMs. The effect of these upward-going photons is parameterized with the “forward hole ice” systematic.

6.7.3 Astrophysics Parameters

Towards higher energies, astrophysical neutrinos start to become a significant fraction of the neutrino flux, as can be seen in Figure 5-3. This astrophysical flux is assumed to be isotropic and equal for all three neutrino and antineutrino flavors. This flux is included and is given by

$$\frac{dN_\nu}{dE} = \Phi_{\text{astro}} \times \left(\frac{E_\nu}{100 \text{ TeV}} \right)^{-\gamma_{\text{astro}}}. \quad (6.9)$$

The two relevant astrophysical systematic parameters are the astrophysical normalization Φ_{astro} and the spectral correction $\Delta\gamma_{\text{astro}}$, which modifies the spectral index like $\gamma_{\text{astro}} = 2.5 + \Delta\gamma_{\text{astro}}$. The normalization is centered at

$$\Phi_{\text{astro}} = 0.787 \times 10^{-18} \text{ GeV}^{-1} \text{ sr}^{-1} \text{ s}^{-1} \text{ cm}^{-2} \quad (6.10)$$

and the spectral correction is centered at $\Delta\gamma_{\text{astro}} = 0$. The prior widths for the two parameters are correlated, but in one dimension they are both set to 0.36.

6.7.4 Cross Section Parameters

Neutrino Cross Section

As the neutrinos propagate through the Earth, their flux is affected by their interactions with the nucleons in the Earth. Uncertainties in the neutrino-nucleon cross section would therefore affect the expected neutrino flux at IceCube. These uncertainties are incorporated into the fit, with a 3% uncertainty for the neutrino cross section and a 7.5% uncertainty for the antineutrino cross section.

Kaon Cross Section

Mesons produced by cosmic rays travel for some distance before decaying. These interactions affect the final energy of these mesons before decaying, in turn affecting the daughter neutrino energies. The interaction cross section between kaons and nuclei have not been measured at these high energies. Therefore, a $\pm 7.5\%$ uncertainty is placed on the theoretical predictions of this cross section.

Conventional Flux Parameters	
Normalization ($\Phi_{\text{conv.}}$)	1.0 ± 0.4
Spectral shift ($\Delta\gamma_{\text{conv.}}$)	0.00 ± 0.03
Atm. Density	0.0 ± 1.0
Barr WP	0.0 ± 0.4
Barr WM	0.0 ± 0.4
Barr YP	0.0 ± 0.3
Barr YM	0.0 ± 0.3
Barr ZP	0.0 ± 0.12
Barr ZM	0.0 ± 0.12
Detector Parameters	
DOM Efficiency	0.97 ± 0.10
Hole Ice (p_2)	-1.0 ± 10.0
Ice Gradient 0	$0.0 \pm 1.0^*$
Ice Gradient 1	$0.0 \pm 1.0^*$
Astrophysics Parameters	
Normalization ($\Phi_{\text{astro.}}$)	$0.787 \pm 0.36^*$
Spectral shift ($\Delta\gamma_{\text{astro.}}$)	$0.0 \pm 0.36^*$
Cross Section Parameters	
Cross Section σ_{ν_μ}	1.00 ± 0.03
Cross Section $\sigma_{\bar{\nu}_\mu}$	1.000 ± 0.075
Kaon Energy Loss σ_{KA}	0.0 ± 1.0

Table 6.1: A table of the systematic parameters included in the previous MEOWS analysis and the current MEOWS+ θ_{34} analysis. The star indicates that the uncertainty is correlated with the adjacent starred parameter.

Chapter 7

Analysis Procedure and Results

7.1 Physics Parameters

In our analysis, we fit over both the physics and systematic parameters. For the physics parameters, the scan is done over a discrete 3-dimensional grid in $(\Delta m_{41}^2, |U_{\mu 4}|^2, |U_{\tau 4}|^2)$ -space. The physics point are sampled as follows: $\Delta m_{41}^2 \in [0.1, 50]$ eV², in steps of 0.1 in $\log_{10}(\Delta m_{41}^2)$ starting at $\Delta m_{41}^2 = 0.1$ eV² with 50 eV² appended at the end; $|U_{\mu 4}|^2 \in [0.001, 0.5]$, in steps of 0.1 in $\log_{10}(|U_{\mu 4}|^2)$ starting at $|U_{\mu 4}|^2 = 0.001$ with 0.5 appended at the end; and $|U_{\tau 4}|^2 \in [0.001, 0.5]$, in steps of 0.2 in $\log_{10}(|U_{\tau 4}|^2)$ starting at $|U_{\tau 4}|^2 = 0.001$ with 0.5 appended at the end.

While the previous MEOWS analysis presented their results in terms of $\sin^2 2\theta_{24}$, we choose to present our results in terms of $|U_{\mu 4}|^2$ and $|U_{\tau 4}|^2$. The connection between the mixing matrix parameters $|U_{\alpha i}|^2$ and mixing angles θ_{ij} are given in Equations (6.1) to (6.3).

Additionally, we choose to set $\delta_{24} = \pi$. We make this choice for two reasons. First, adding a fourth physics parameter to fit over would be too computationally expensive to be completed in a reasonable amount of time. Second, we found the choice of δ_{24} to have a small effect on the sensitivity when compared to the improvement obtained by the inclusion of θ_{34} . Increasing θ_{34} weakens the ν_μ disappearance while strengthening the $\bar{\nu}_\mu$ disappearance, resulting in a partial cancellation of the effect. Further, while the cancellation isn't exact, the fact that the conventional neutrino flux has more ν_μ than $\bar{\nu}_\mu$, and the ν_μ cross section is greater than the $\bar{\nu}_\mu$ cross section, means that increasing δ_{24} weakens the resonance effect. Therefore, setting δ_{24} to its maximal value, π , is the conservative choice.

7.2 Binning & Likelihood

The data is binned in two dimensions: reconstructed zenith $\cos\theta$ and reconstructed energy E . The zenith angle $\cos\theta$ ranges between -1 and 0 , with 20 bins of width 0.05. Here, $\cos\theta = -1$ corresponds to events coming from directly below the detector, and $\cos\theta = 0$ corresponds to events coming from the horizon. The reconstructed energy ranges from 500 to 9976 GeV, in 13 bins of width $\log_{10}(E/[\text{GeV}]) = 0.1$.

For a single bin, the Poisson likelihood

$$\mathcal{L}(\theta, \theta_\eta | k) = \frac{\lambda(\theta, \theta_\eta)^k e^{-\lambda(\theta, \theta_\eta)}}{k!} \quad (7.1)$$

gives the likelihood of observing k events, given an expectation of $\lambda(\theta, \theta_\eta)$, where θ is some set of physics parameters and θ_η is some set of systematic parameters.

When the expectation $\lambda(\theta, \theta_\eta)$ is determined through MC, finite simulations lead to an uncertainty in $\lambda(\theta, \theta_\eta)$. This is accounted for with an effective likelihood

$$\mathcal{L}_{\text{Eff}}(\theta, \theta_\eta | k) = \left(\frac{\mu}{\sigma^2}\right)^{\frac{\mu^2}{\sigma^2}+1} \Gamma\left(k + \frac{\mu^2}{\sigma^2} + 1\right) \left[k! \left(1 + \frac{\mu}{\sigma^2}\right)^{k + \frac{\mu^2}{\sigma^2} + 1} \Gamma\left(\frac{\mu^2}{\sigma^2} + 1\right) \right]^{-1}, \quad (7.2)$$

derived in Ref. [92]. μ and σ^2 are determined by the weights w of each MC event,

$$\mu = \sum_i w_i \quad \sigma^2 = \sum_i w_i^2. \quad (7.3)$$

In addition to the statistical likelihood, the prior likelihood of a set of systematic parameters θ_η is given by

$$\Pi(\theta_\eta) = \prod_\eta \frac{1}{\sqrt{2\pi\sigma_\eta^2}} e^{-\frac{(\theta_\eta - \Theta_\eta)^2}{2\sigma_\eta^2}}, \quad (7.4)$$

where Θ_η and σ_η are the prior central values and widths, respectively.

The final likelihood is given by the product of the effective likelihood and the prior likelihood

$$\mathcal{L}(\theta, \theta_\eta | k) = \mathcal{L}_{\text{Eff}}(\theta, \theta_\eta | k) \Pi(\theta_\eta). \quad (7.5)$$

For simplicity, we drop the k label.

7.3 Frequentist Analysis

In the frequentist analysis, the likelihood ratio

$$\Lambda = \frac{\sup_{\theta_\eta} \mathcal{L}(\theta_0, \theta_\eta)}{\sup_{\theta, \theta_\eta} \mathcal{L}(\theta, \theta_\eta)} \quad (7.6)$$

is used to construct the test statistic. In Equation (7.6), the “null” hypothesis θ_0 is compared to an alternative hypothesis where the physics parameters θ are free and $\theta_0 \in \theta$. In both models, the systematic parameters θ_η are set to maximize the likelihood. In this context, the “null” hypothesis does not necessarily have to be the null physics parameters ($\Delta m_{41}^2 = 0, |U_{\mu 4}|^2 = 0, |U_{\tau 4}|^2 = 0$).

At each sampled physics point θ , the negative likelihood is minimized over the systematic parameters θ_η . The minimization is done with the internal IceCube software **GolemFit** using the L-BFGS-B algorithm [93].

$\log_{10} K$	Evidence against null
>0	Null supported
$-1/2 - 0$	Not worth more than a bare mention
$-1 - -1/2$	Substantial
$-3/2 - -1$	Strong
$-2 - -3/2$	Very strong
<-2	Decisive

Table 7.1: Jeffreys scale, from Ref. [94].

We define the test statistic

$$\text{TS} \equiv -2 \log \Lambda = -2(\ell(\theta_0) - \ell(\hat{\theta})), \quad (7.7)$$

where

$$\ell(\theta_0) = \log[\sup_{\theta_\eta} \mathcal{L}(\theta_0, \theta_\eta)], \quad \ell(\hat{\theta}) = \log[\sup_{\theta, \theta_\eta} \mathcal{L}(\theta, \theta_\eta)]. \quad (7.8)$$

In this thesis, we assume Wilks' theorem, so that our test statistic TS follows a χ^2 -distribution with degrees of freedom equal to the difference in the number of parameters between the null and alternative hypothesis. In our case, this is 3.

The validity of Wilks' theorem is not guaranteed, and simulated pseudo-experiments have to be run to obtain the proper coverage. This is computationally expensive, and is not done in this thesis, but is planned for future publications. Despite possibly not following a χ^2 -distribution, we will refer to the TS as χ^2 , for simplicity.

7.4 Bayesian Analysis

In addition to the frequentist analysis described above, a Bayesian analysis is done using the Bayes factor

$$K = \frac{\mathcal{E}_i}{\mathcal{E}_j}, \quad (7.9)$$

where \mathcal{E} is the “evidence” for some model. The evidence is given by

$$\mathcal{E} = \int d\theta_\eta \mathcal{L}(\theta, \theta_\eta), \quad (7.10)$$

where $\mathcal{L}(\theta, \theta_\eta)$, as defined in Equation (7.5), includes the priors of the systematic parameters.

The Bayes factor quantifies the support of one model over another. Using the Bayes factor, we will compare the evidence of each physics parameter θ with the no-sterile neutrino hypothesis. In Equation (7.9), we will set the numerator \mathcal{E}_i as the no-sterile hypothesis. Therefore, a positive value of $\log_{10} K$ means a preference for the null model, while a negative value means a preference for the alternative model. A qualitative measure, called Jeffreys scale, of the strength of the evidence against the null model is given in Table 7.1, following Ref. [94].

7.5 Sensitivity

The sensitivity to the sterile parameters is calculated in two ways. The first is an approximate sensitivity referred to as the “Asimov” sensitivity [95]. In this method, the median sensitivity is estimated by the use of a single representative data set, as opposed to an ensemble of simulated experiments. The benefit is, of course, avoiding the computational limitations of simulating a large number of experimental trials. We used this method to conduct tests before we unblinded the data.

The Asimov data set is chosen to be the expected distribution of events assuming the null hypothesis and central value systematic parameters, with no statistical fluctuation. The median Asimov sensitivity is shown at the 99%, 95%, and 90% confidence levels in Figure 7-1. Figure 7-2 also shows the 95% confidence level for various values of $|U_{\tau 4}|^2$ overlaid on a single plot. Figure 7-1 and Figure 7-2 shows how the sensitivity of IceCube improves dramatically as the value of $|U_{\tau 4}|^2$ increases.

The second method of deriving the sensitivity is to run simulated experiments and finding the average exclusion sensitivities for the ensemble. The Asimov sensitivity described above is an approximation of this method, but is substantially faster to compute. Therefore, the more accurate method of deriving the sensitivities were not derived until after the results were unblinded.

We ran 400 trials and found the sensitivity distribution as shown in Figure 7-3. Plotted are the median sensitivity at the 95%, as well as the band that contains 95.45% (2σ) and 68.72% (1σ) of the sensitivity curves. We also include the Asimov sensitivity as shown previously in Figure 7-1. We find that the Asimov sensitivity did provide a near approximation of the sampled median sensitivity.

7.6 Pre-Unblinding Checks

Before fully unblinding the data, we ran a number of “blind” checks on the data to test for significant deviations from the model, without looking at parameters of interest. The steps taken, and the results, are:

1. We fit over the entire physics and systematic parameter space, keeping the results blind. At the best fit physics and systematic point, we run 10,000 realizations. For each realization, we fit for the systematic parameters at the injected physics point. We then compare the observed TS to the distribution of TS obtained from the ensemble test. We chose a p-value of $p=0.05$ to be a stopping condition. In Figure 7-4, we show the obtained TS, compared to the observed TS. We find a p-value of 0.82: Step 1 passed.
2. For each of the 260 analysis bins, we compare the observed likelihood to the distributions of likelihoods from the ensemble test of Step 1. Here, the likelihood used is a Poisson likelihood with the expected event counts taken to be the expectation from the best fit physics and systematic parameters. We chose that if six or more bins have a p-value corresponding to greater than 3σ , we would stop. At no single bin was a deviation of 3σ observed: Step 2 passed.

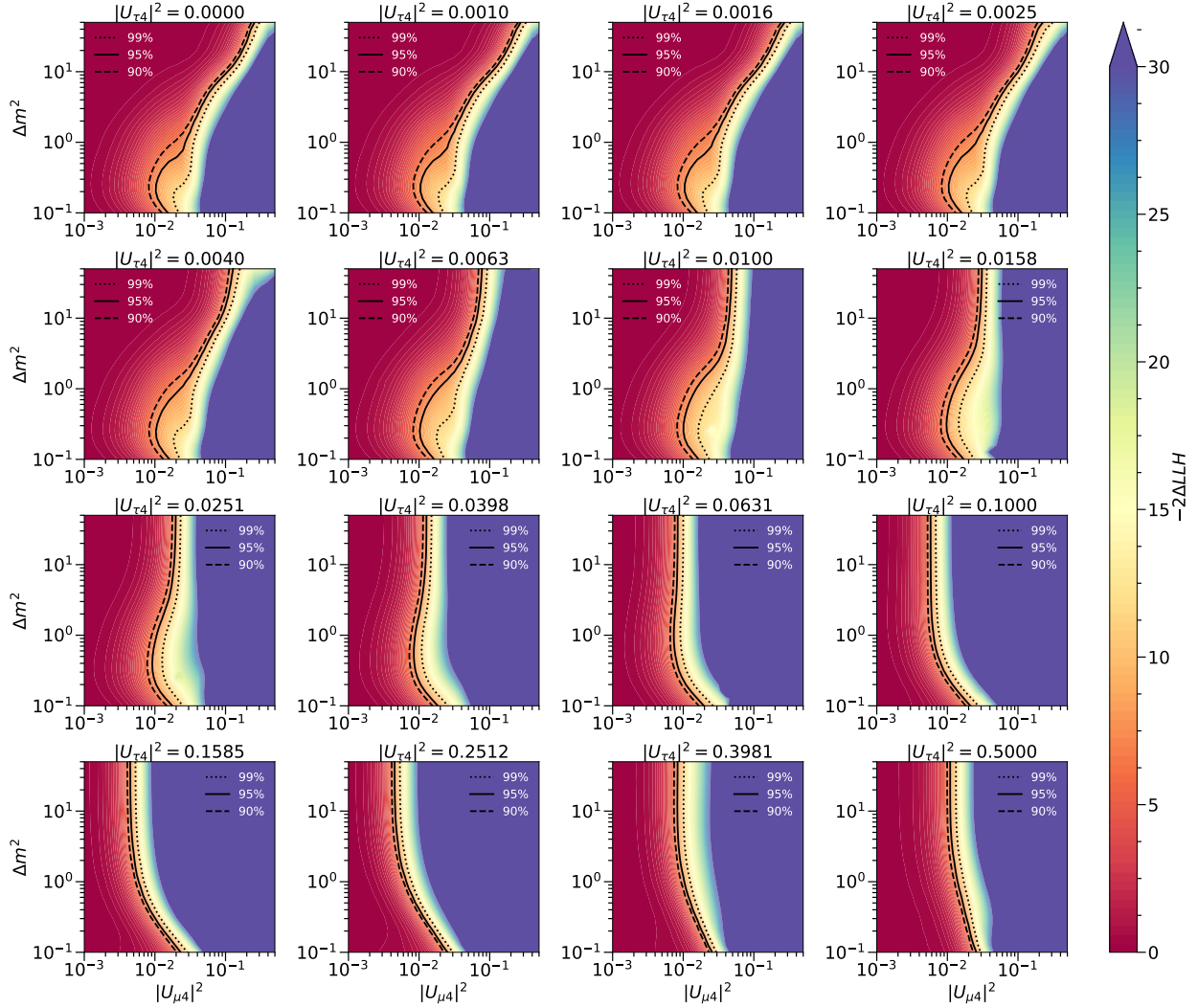


Figure 7-1: The expected sensitivities for the sterile parameters sampled. Each frame corresponds to a slice of $|U_{\tau 4}|^2$ sampled. The lines shown correspond to the 99%, 95%, and 90% confidence levels assuming Wilks' Theorem.

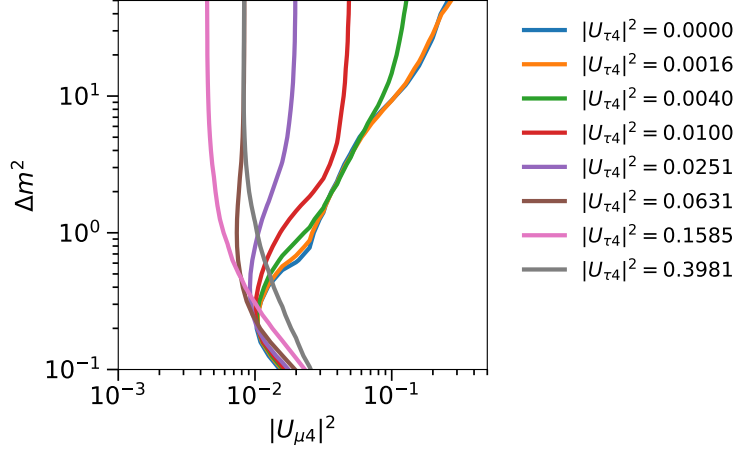


Figure 7-2: The expected sensitivities for the sterile parameters sampled. The 95% confidence level is shown for various values of $|U_{\tau 4}|^2$ sampled. As $|U_{\tau 4}|^2$ increases, the sensitivity to the sterile hypothesis improves dramatically.

3. If any systematic pulls more than 3σ or hits a bound, we stop. Figure 7-5 shows the best fit systematic parameters. No systematic pulls greater than 3σ or hit a bound: Step 3 passed.
4. We collapse the observation into two 1D distributions of reconstructed energy and zenith. If any bin pulls greater than 3σ , then we stop. No bins pulled greater than 3σ : step 4 passed.
5. We plot the 1D distributions from Step 4, and calculate a χ^2 comparing the data to the best fit expectation. We compare this χ^2 to the distribution of χ^2 obtained from the 10,000 simulated samples. Figure 7-6 shows these distributions. We found a p-value of $p=0.30$ and $p=0.39$ for the energy and zenith distribution, respectively: step 5 passed.

With the pre-unblinding tests completed and passing, we then fully unblinded the results.

7.7 Results

This section presents the results of this thesis analysis. The author and the IceCube collaboration intend to publish this result, which will lead to updates with higher-statistics tests and simulations.. However, the basic conclusions of the analysis presented here will not change.

7.7.1 Frequentist

For the frequentist scans, the results are shown in Figure 7-7. The confidence regions are drawn assuming Wilks' Theorem with 3 degrees of freedom, with the 90%, 95%, and 99% confidence levels shown. In Figure 7-7, the three dimensional parameter space is sliced

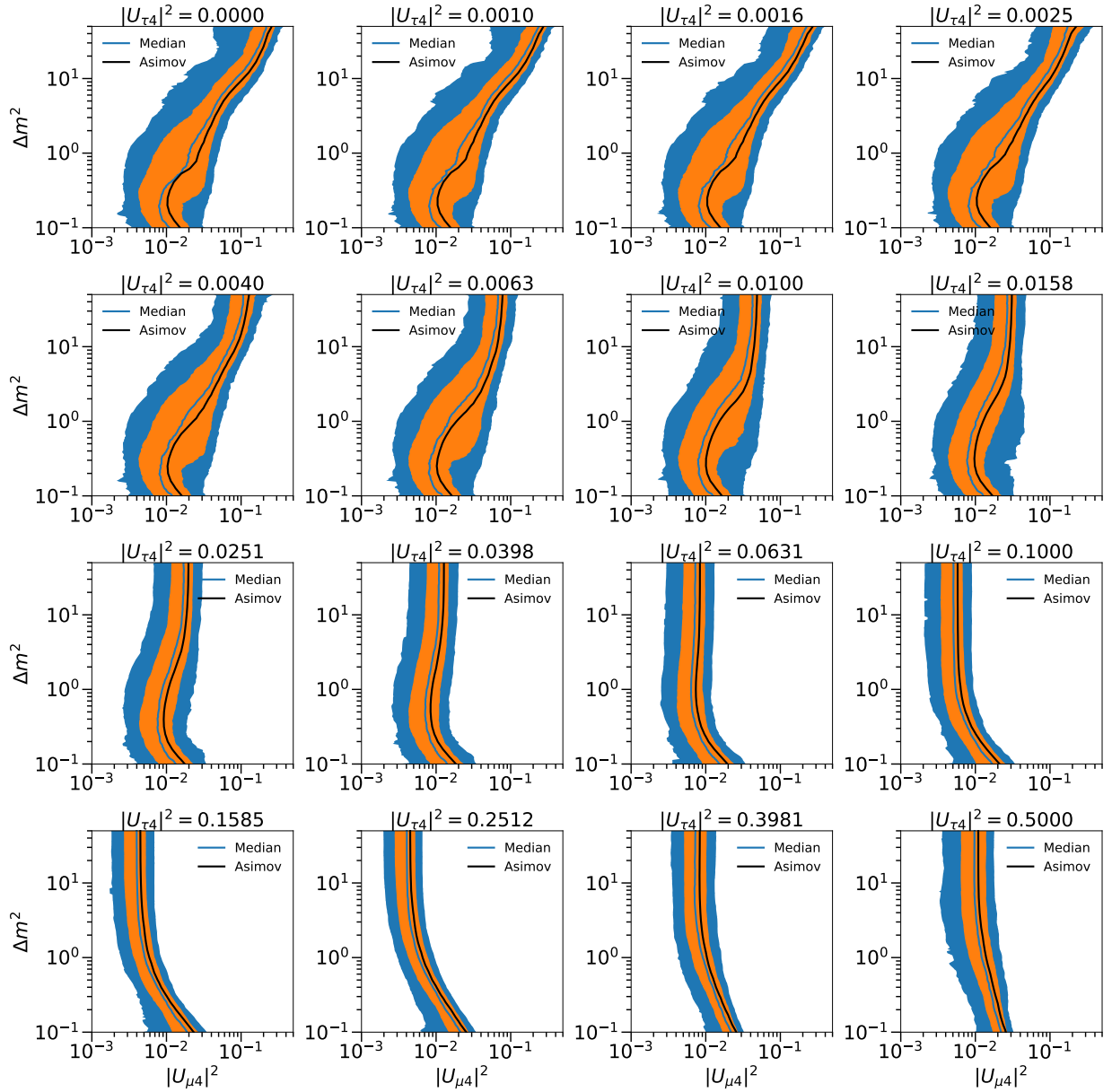


Figure 7-3: The sensitivity bands derived by generating 400 pseudoexperiments. The blue line is the median sensitivity at the 95% confidence level, while the orange and blue bands contain 95.45% (2σ) and 68.72% (1σ) of the sensitivity boundary, respectively. The black lines are the derived Asimov sensitivities.

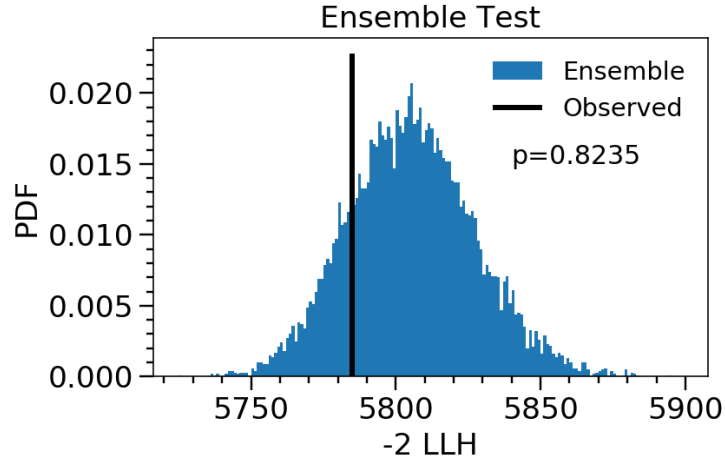


Figure 7-4: Step 1 of the pre-unblinding check. At the best fit physics and systematic point, 10,000 pseudoexperiments were injected. These pseudoexperiments then had the systematic parameters fitted at the best fit physics point. The plot shows the recovered distribution of the TS, and the black line shows the observed best fit TS.

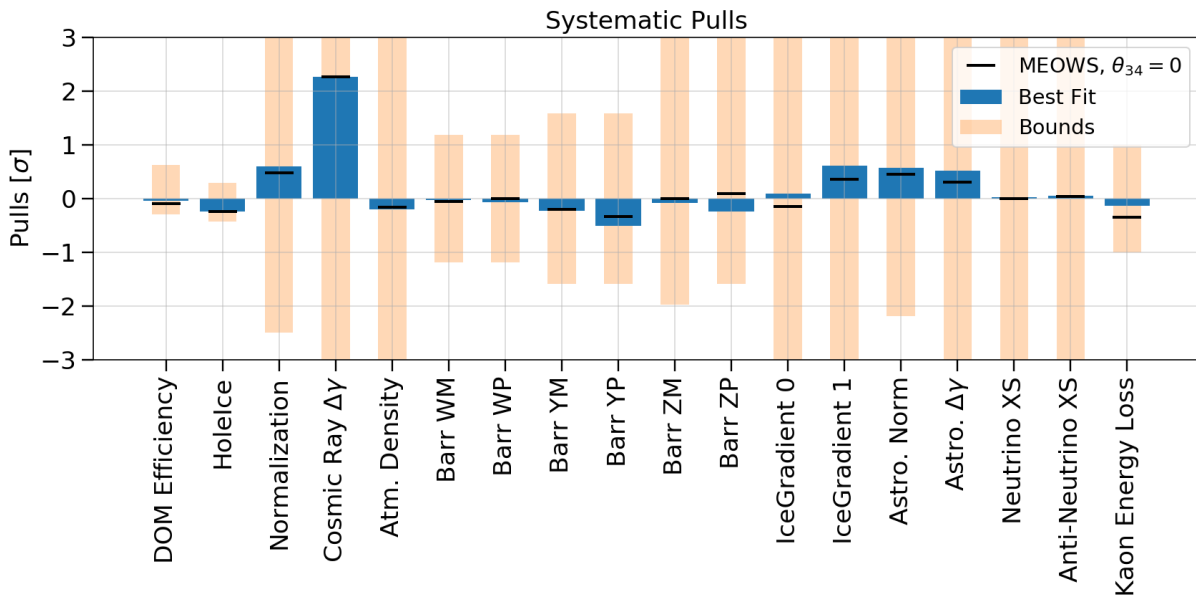


Figure 7-5: Step 3 of the pre-unblinding check. The plot shows the recovered best fit systematic parameters in blue, in terms of their pull. Not all parameters had bounds that extended beyond 3σ , so their ranges are shown by the orange bars. The black bars show the best fit systematic for the analysis in Refs. [66, 67].

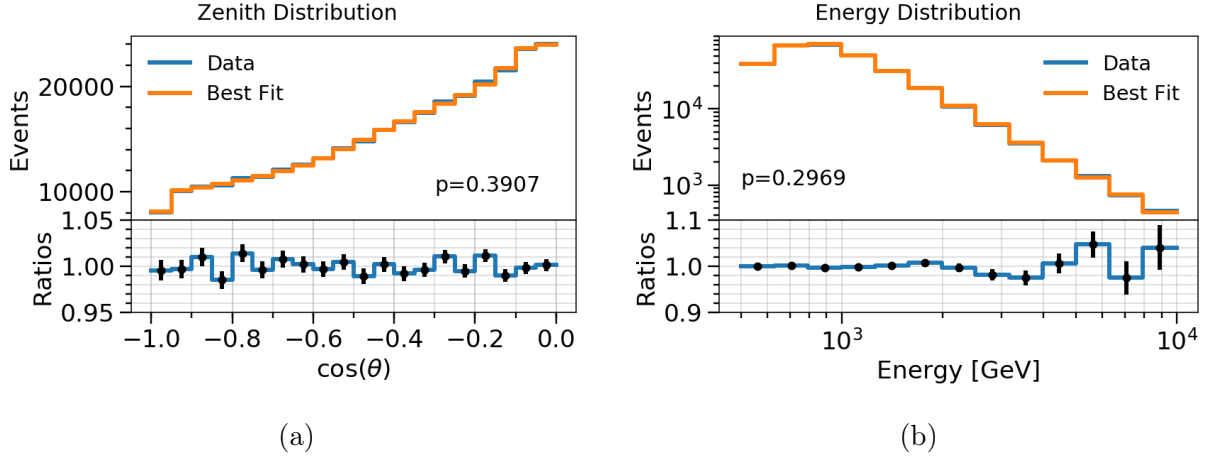


Figure 7-6: Results of step 5 of the pre-unblinding checks. (a) and (b) shows the 1D distributions of zenith and energy, respectively. The distribution of the data is shown along with the expectation at the best fit, and their ratio. The p-value is found by comparing the χ^2 to the obtained χ^2 distribution from the 10,000 pseudoexperiments.

into different frames of $|U_{\tau 4}|^2$. In Figure 7-8 and Figure 7-9, we also show the confidence regions sliced in Δm^2 and $|U_{\mu 4}|^2$, respectively. The best fit point is found at $\Delta m_{41}^2 = 5.0 \text{ eV}^2$, $|U_{\mu 4}|^2 = 0.04$, and $|U_{\tau 4}|^2 = 0.006$. At this point, we obtain a $\Delta\chi^2 = 7.7$. Assuming Wilks' Theorem with 3 degrees of freedom, this corresponds to a p-value of 5.2% (1.94σ). Using the pseudoexperiments generated to obtain the sensitivities in Figure 7-3, we can obtain a more accurate p-value of 2.7% (2.2σ).

In Figure 7-10, we show the data distribution. The pulls of the data, relative to the best fit physics and systematic parameters, are shown in Figure 7-11.

In Figure 7-12, we show the oscillogram at this best fit point, compared to the null.

We show in Figure 7-13a the percent difference between the expected event rate at the best fit versus the no-sterile hypothesis. In both cases, we use the best fit systematic parameters for each physics hypothesis. We can see here that, while the disappearance occurs mainly at true neutrino energies $E_\nu > 10 \text{ TeV}$ (see Figure 7-12), the signal appears below 10 TeV in reconstructed E_μ . In Figure 7-13b, we show the statistical pull that the best fit expectation has against the null best fit. Finally, in Figure 7-13c, we show the difference between the absolute value of the data pulls relative to the null fit versus the absolute value of data pulls relative to the best fit. This last figure reveals the bins that are pulling the best fit to the sterile parameters.

While a small number of experiments have conducted a multidimensional fit including θ_{34} , the author of this work is not aware of any that release the three (or more) dimensional confidence regions like in Figures 7-7 to 7-9. We therefore include two-dimensional confidence regions, profiled over the third dimension, to allow comparisons. In Figure 7-14, we show the confidence regions after profiling over each of the physics parameters, with the 90%, 95%, and 99% confidence levels drawn assuming Wilks' Theorem and two degrees of freedom.

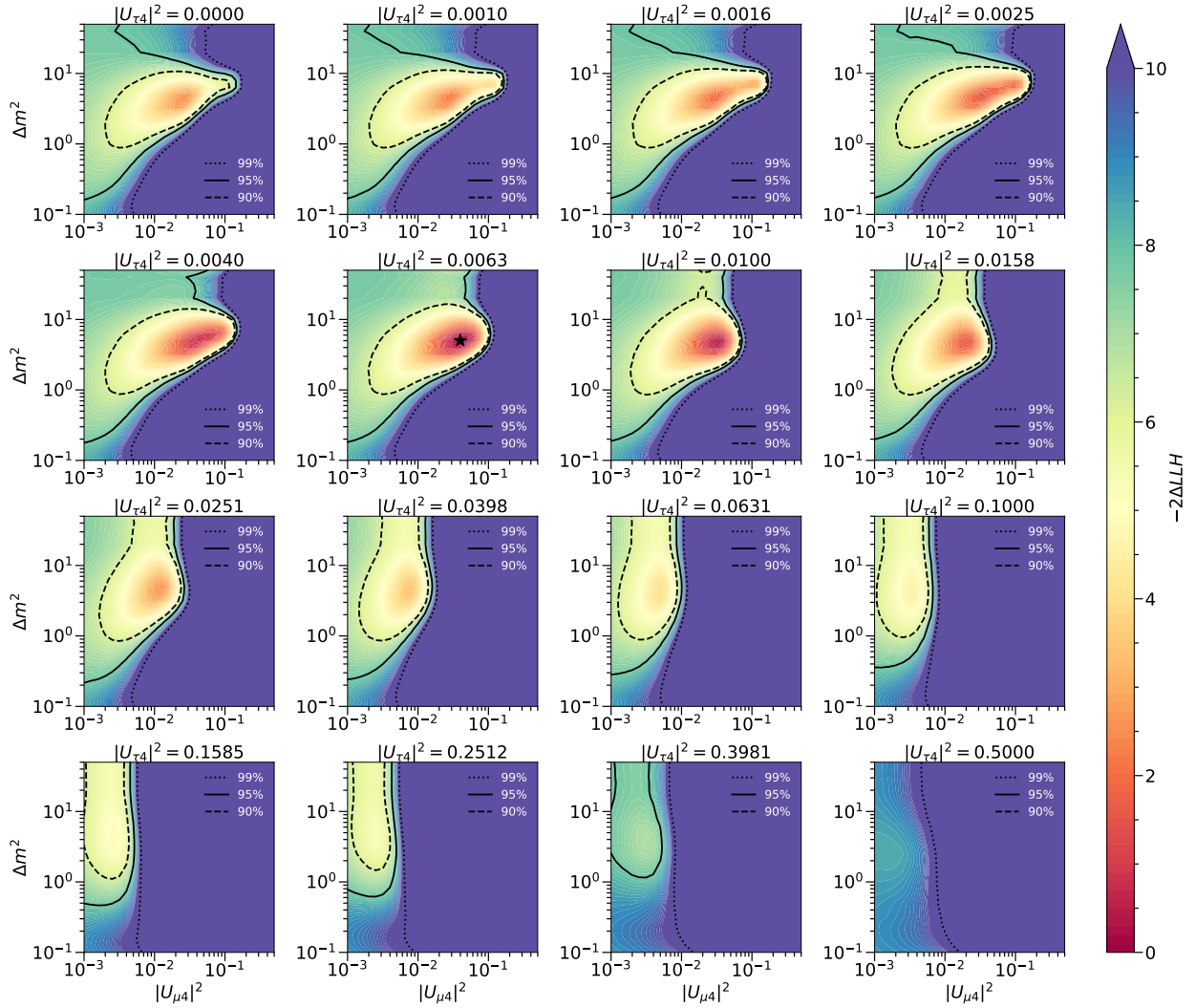


Figure 7-7: The observed confidence regions at 90%, 95%, and 99% confidence levels. The best fit point is labeled by a star. Here, the three dimensional parameter space is sliced into the sampled values of $|U_{\tau 4}|^2$.

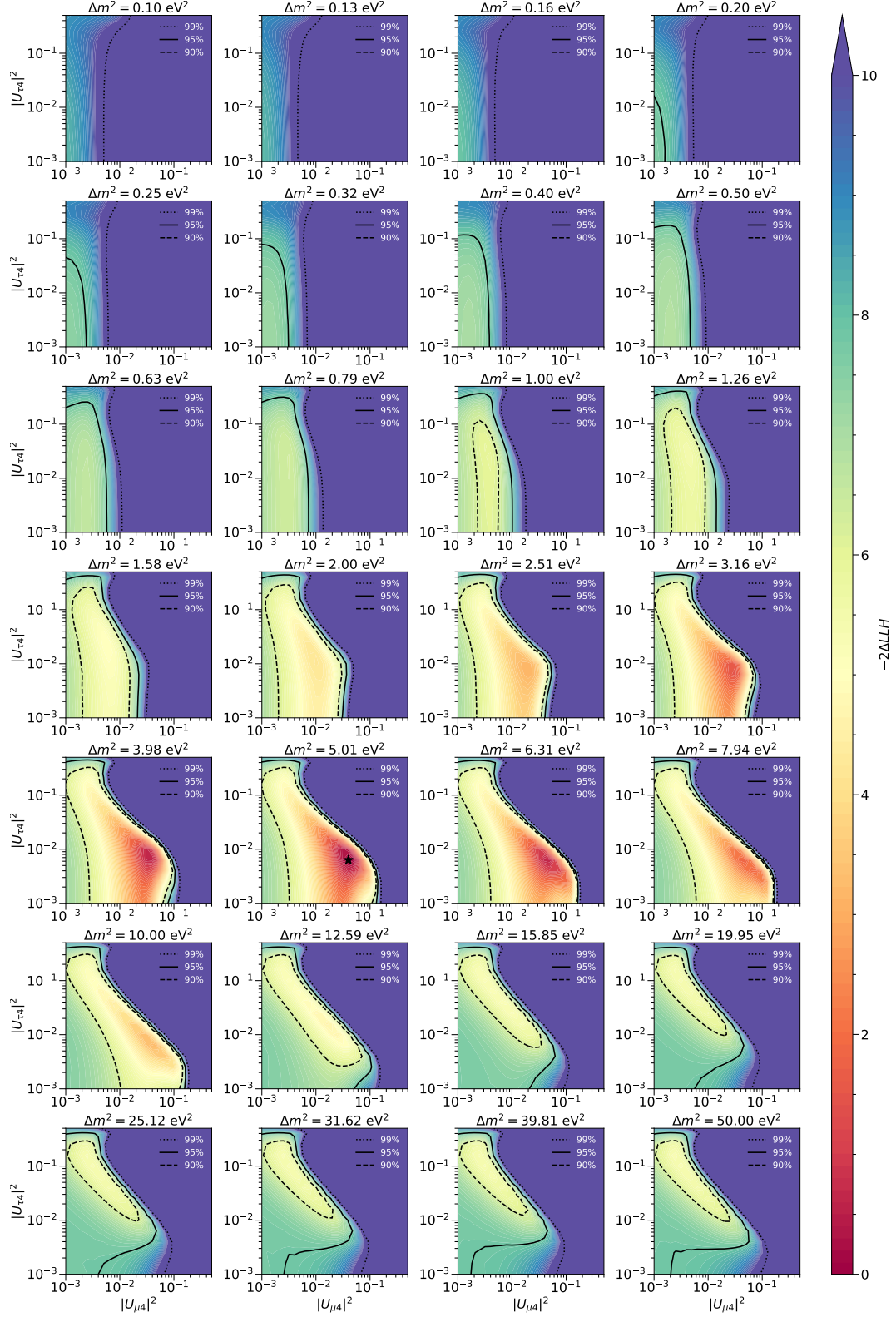


Figure 7-8: The observed confidence regions at 90%, 95%, and 99% confidence levels. The best fit point is labeled by a star. Here, the three dimensional parameter space is sliced into the sampled values of Δm^2_{41} .

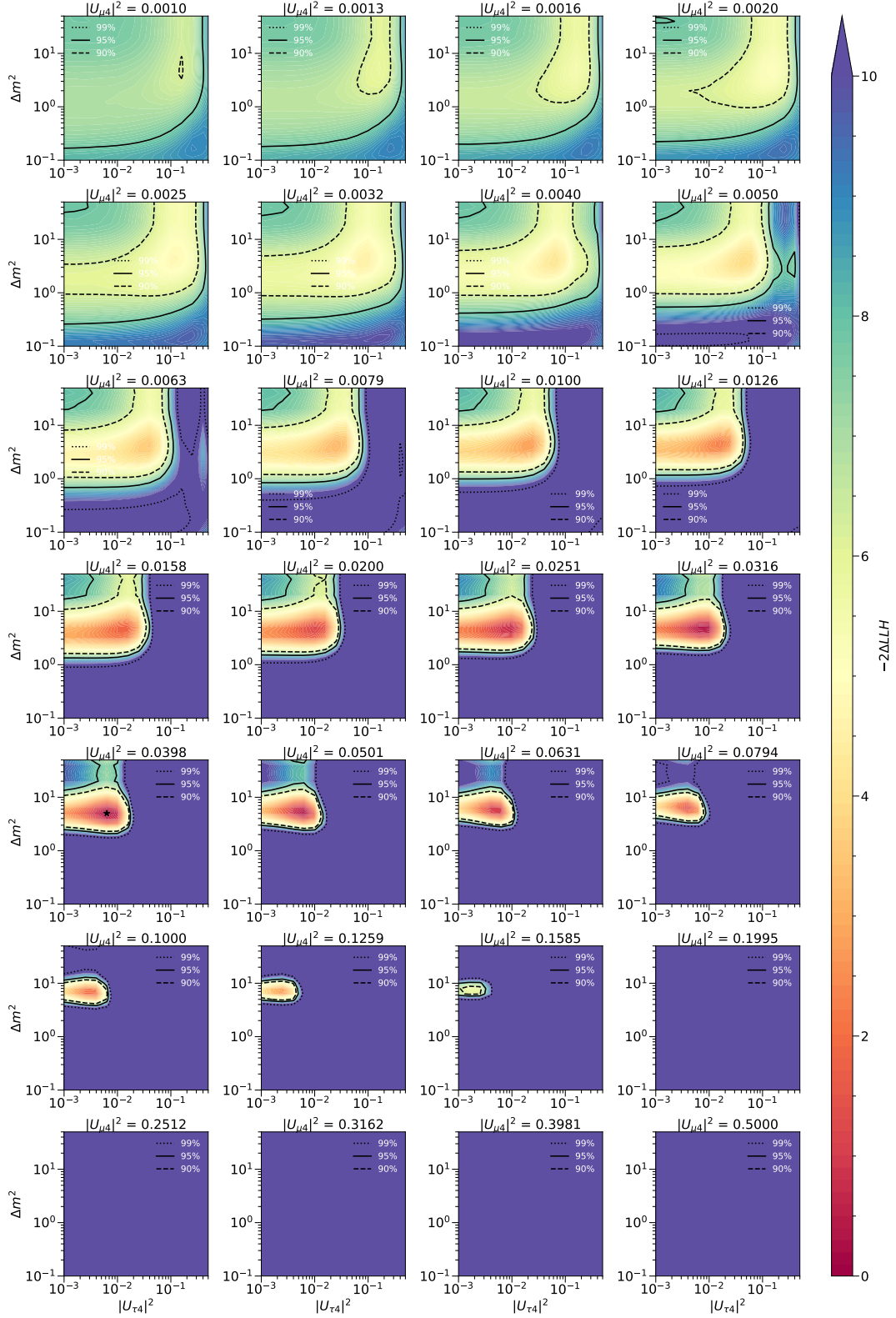


Figure 7-9: The observed confidence regions at 90%, 95%, and 99% confidence levels. The best fit point is labeled by a star. Here, the three dimensional parameter space is sliced into the sampled values of $|U_{\mu 4}|^2$.

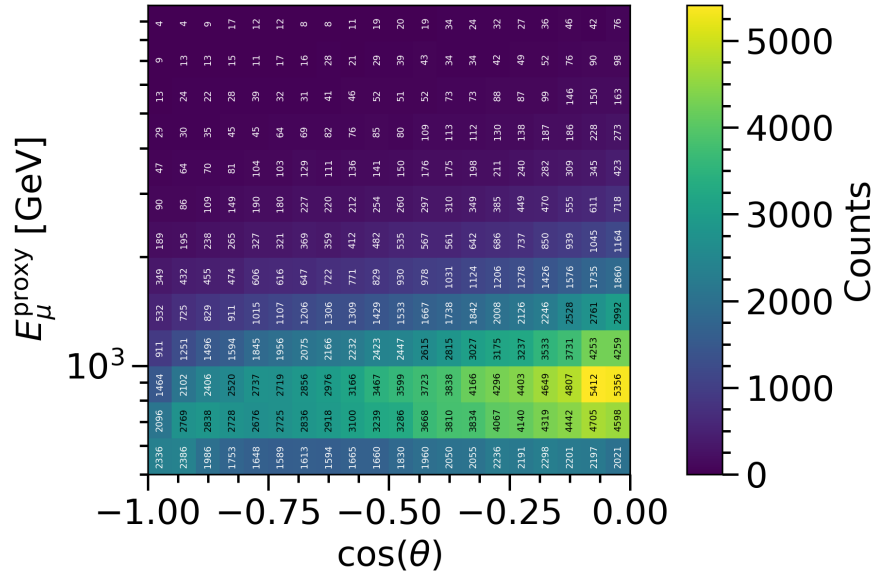


Figure 7-10: The distribution of events observed in the 7.634 year MEOWS sample.

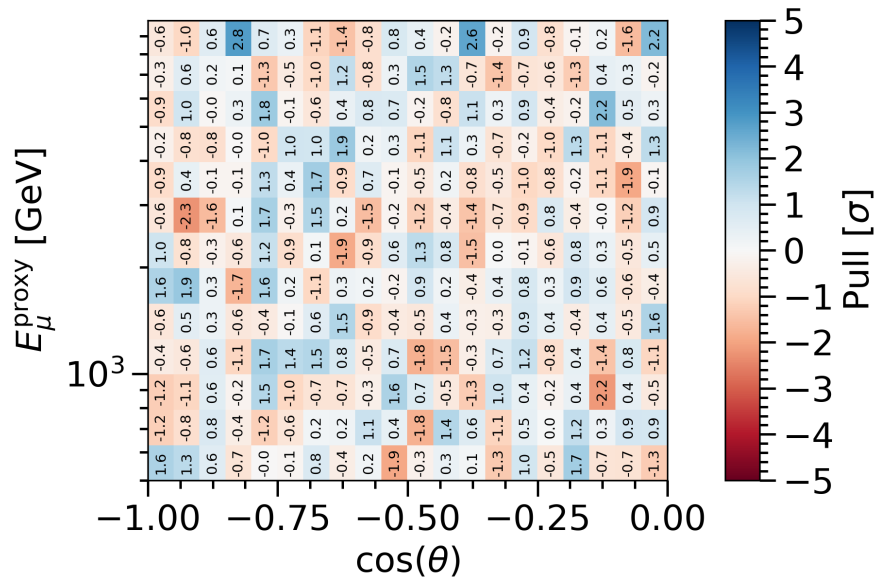


Figure 7-11: The statistical pulls of the data relative to the best fit physics and systematic parameters.

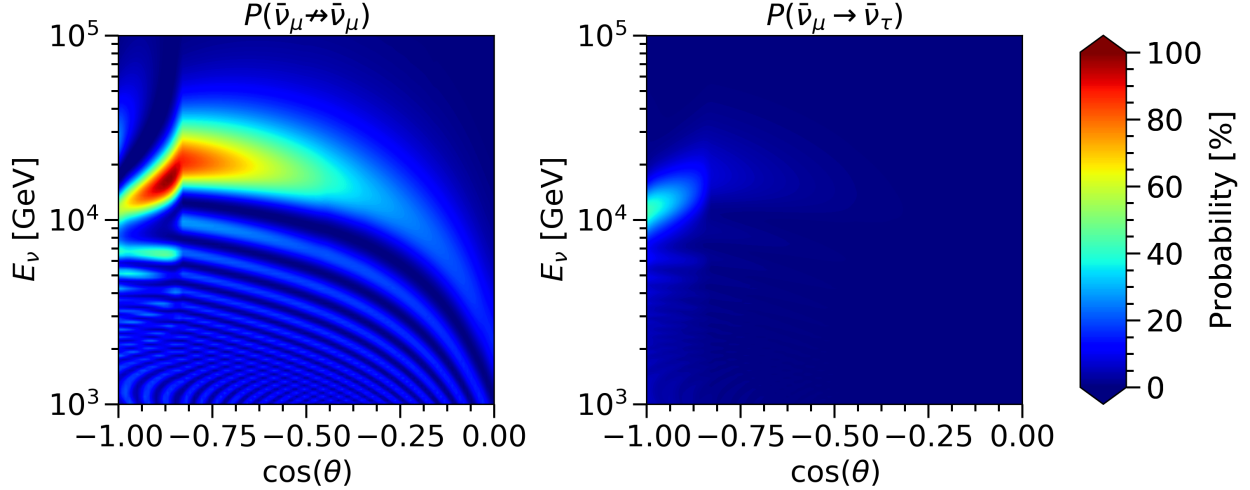


Figure 7-12: The oscillograms for $\bar{\nu}_\mu \rightarrow \bar{\nu}_\mu$ and $\bar{\nu}_\mu \rightarrow \bar{\nu}_\tau$ oscillations at the best fit point. The plot on the left shows the ratio of $\bar{\nu}_\mu$ flux at IceCube between the best fit model and the null model. The plot on the right shows the ratio of the expected $\bar{\nu}_\tau$ flux at the best fit model over the expected $\bar{\nu}_\mu$ flux with the null model.

7.7.2 Bayesian

For the Bayesian analysis, the result of the evidence calculations is shown sliced in $|U_{\tau 4}|^2$ in Figure 7-15. We also show the same results sliced by Δm_{41}^2 in Figure 7-16 and $|U_{\mu 4}|^2$ in Figure 7-17.

The point found with the largest evidence is $\Delta m_{41}^2 = 5.0 \text{ eV}^2$, $|U_{\mu 4}|^2 = 0.02$, and $|U_{\tau 4}|^2 = 0.006$. The observed Bayes factor, relative to the null model, was found to be $\log_{10} K = -1.56$. Following Jeffreys’ scale in Table 7.1, this corresponds to a “Very Strong” preference for the sterile model with respect to the non-sterile model. We note that the only other point to have a “Very Strong” preference for the sterile model, with $\log_{10} K = -1.55$, is found at the same point as the frequentist best fit: $\Delta m_{41}^2 = 5.0 \text{ eV}^2$, $|U_{\mu 4}|^2 = 0.04$, and $|U_{\tau 4}|^2 = 0.006$. A table of the best fit parameters from this analysis is provided in Table 7.2. The uncertainties in the nuisance parameters are obtained from the posterior distributions found at the best fit point. The posterior distributions for each nuisance parameter is shown in Figure 7-18, and the correlations between these parameters are shown in Figure 7-19.

7.8 Discussion

In this chapter we presented the results of an expanded sterile neutrino search in IceCube.

In the frequentist analysis, we find, under the assumption of Wilks’ Theorem, a p-value of 5.2%. While not reaching the usual standard of 2σ which the community frequently uses as the standard for a “signal,” it’s substantial enough to look at more closely. Interestingly, throwing pseudoexperiments has returned a p-value of only 2.7%, albeit with not enough realizations thrown to be confident in this value. As this thesis is being written, presented, and submitted, more pseudoexperiments are being simulated and fitted in order to achieve a more accurate p-value and possibly demonstrate a new experiment with a signal under the

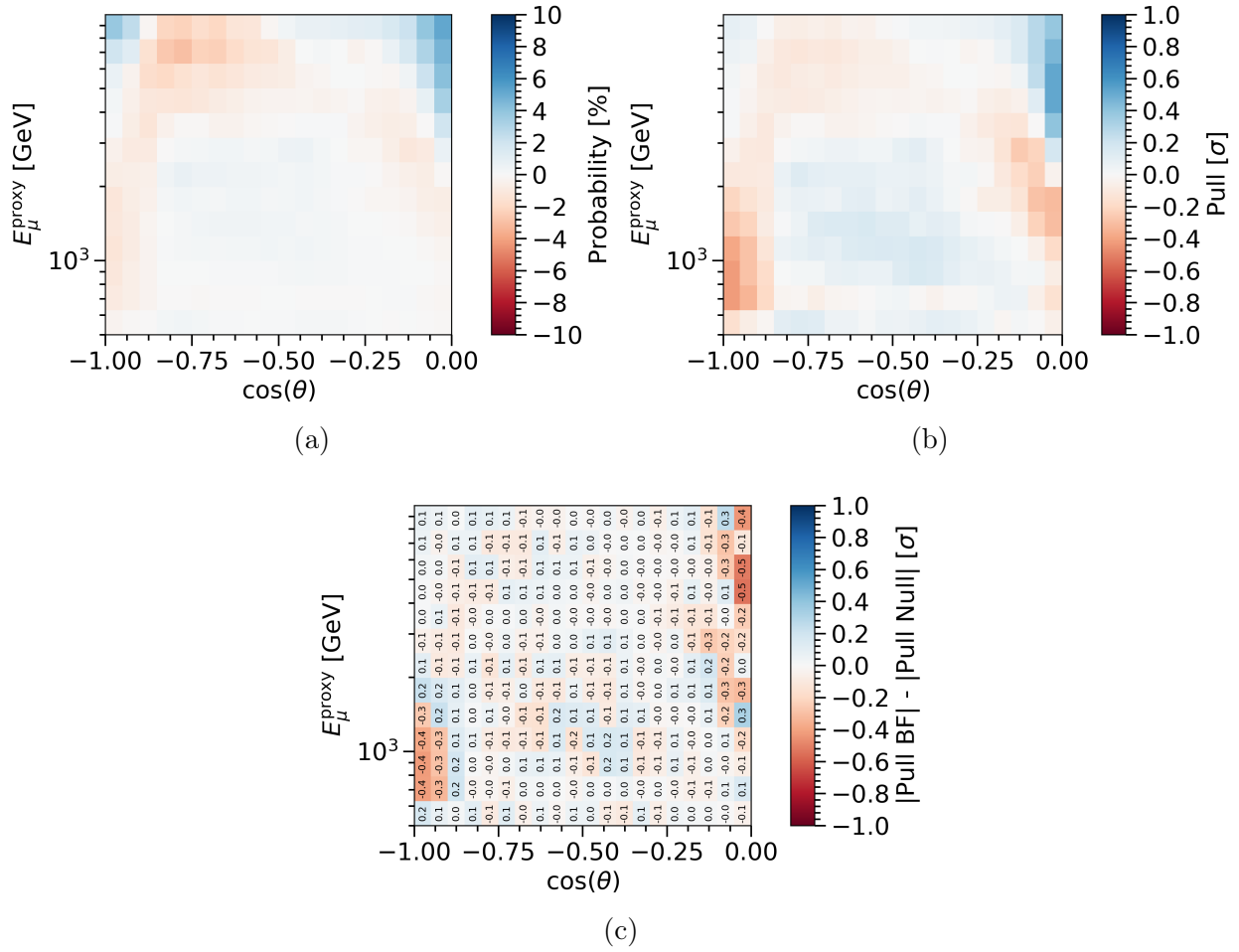
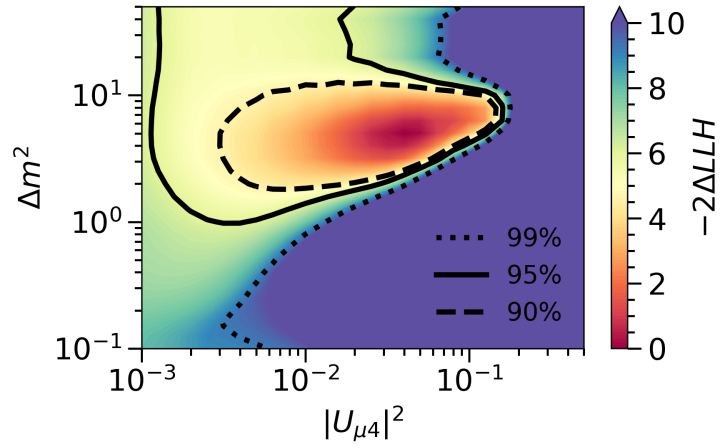
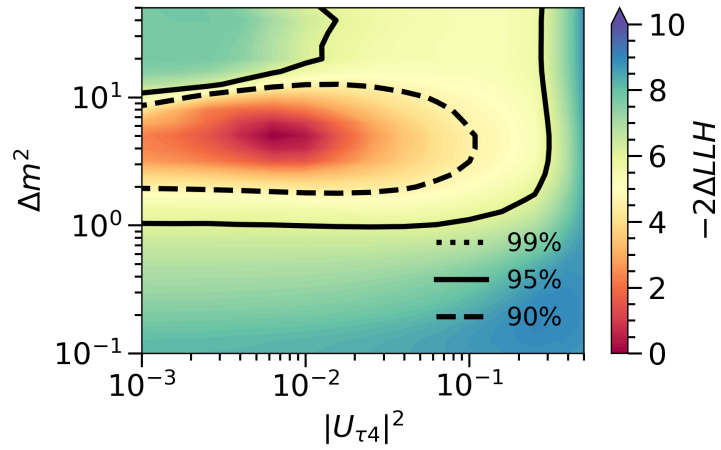


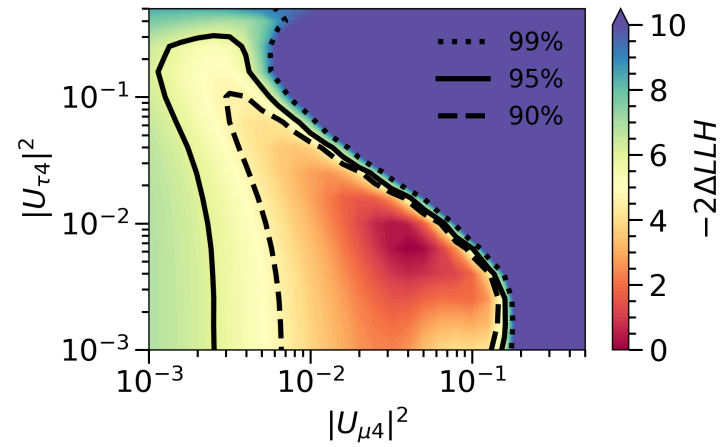
Figure 7-13: (a) The percent difference of expected events between the best fit sterile parameters versus the null. (b) The statistical pull of the expected event rate at the best fit sterile parameters relative to the null expected event rate. (c) The difference in the absolute values of the data pulls between the sterile and null model.



(a) Confidence regions with $|U_{\tau 4}|^2$ profiled.



(b) Confidence regions with $|U_{\mu 4}|^2$ profiled.



(c) Confidence regions with Δm_{41}^2 profiled.

Figure 7-14: The MEOWS+ θ_{34} results, profiled over each of the fitted physics parameters.

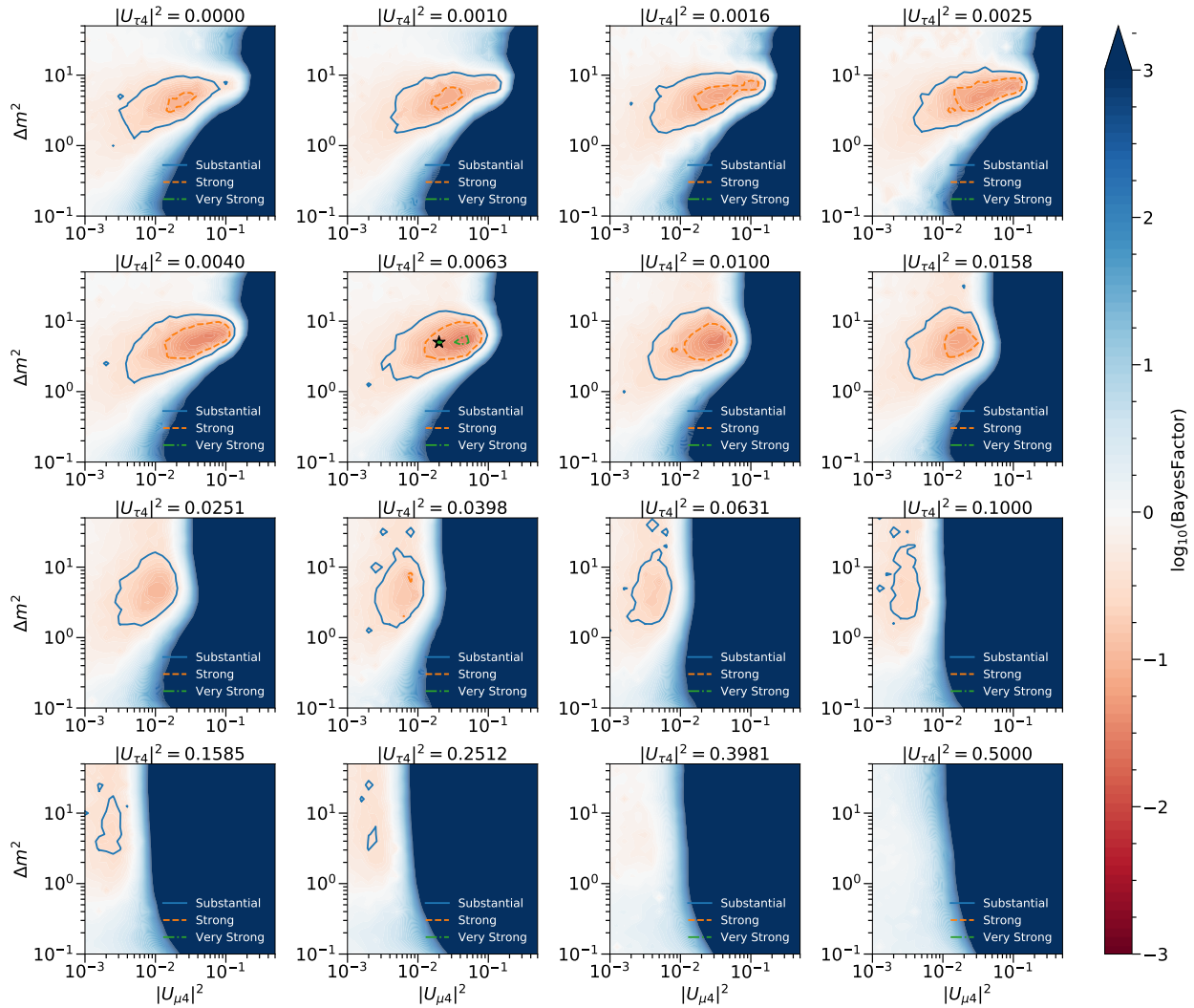


Figure 7-15: The result of the Bayesian fit, in slices of $|U_{\tau 4}|^2$. Here, the Bayes factor is calculated relative to the null hypothesis. A negative value corresponds to a preference to that hypothesis compared to the null. A positive value corresponds to a preference for the null.

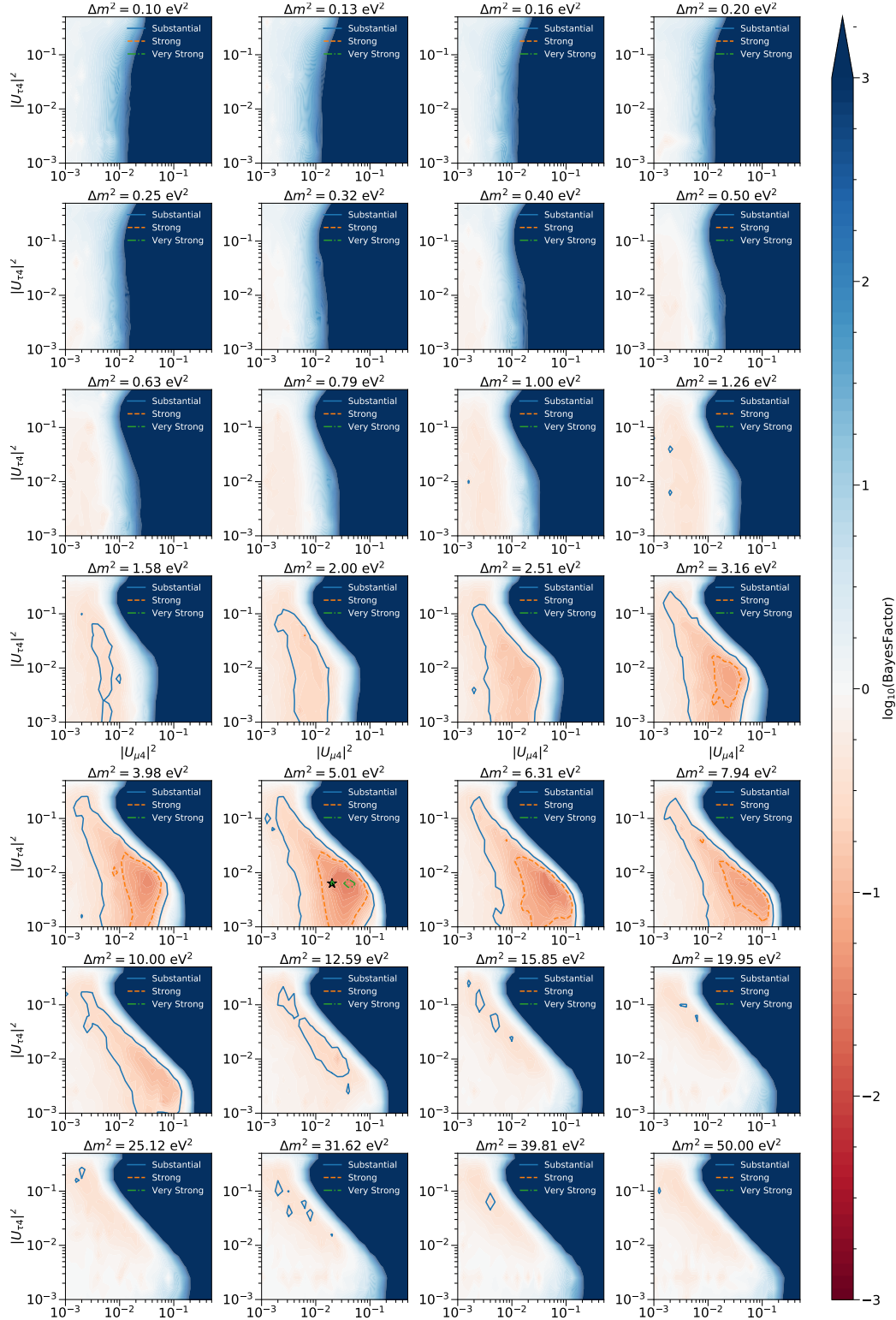


Figure 7-16: The result of the Bayesian fit, in slices of Δm_{41}^2 . Here, the Bayes factor is calculated relative to the null hypothesis. A negative value corresponds to a preference to that hypothesis compared to the null. A positive value corresponds to a preference for the null.

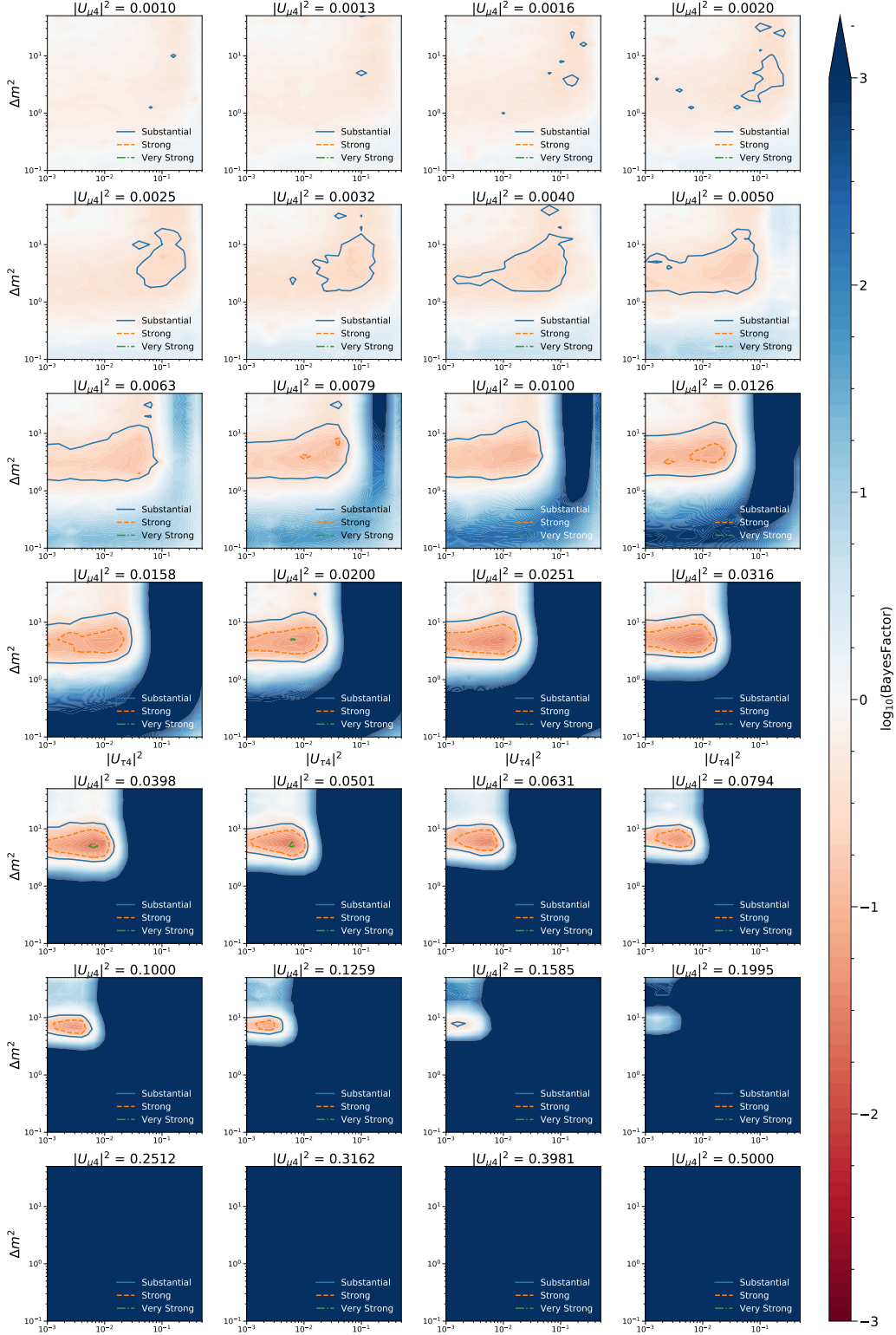


Figure 7-17: The result of the Bayesian fit, in slices of $|U_{\mu 4}|^2$. Here, the Bayes factor is calculated relative to the null hypothesis. A negative value corresponds to a preference to that hypothesis compared to the null. A positive value corresponds to a preference for the null.

Physics Parameters	
Δm_{41}^2	5.0 eV ²
$ U_{\mu 4} ^2$	0.02
$ U_{\tau 4} ^2$	0.006
Conventional Flux Parameters	
Normalization ($\Phi_{\text{conv.}}$)	1.179 \pm 0.054
Spectral shift ($\Delta\gamma_{\text{conv.}}$)	0.067 \pm 0.012
Atm. Density	-0.27 \pm 0.72
Barr WP	-0.01 \pm 0.28
Barr WM	-0.00 \pm 0.28
Barr YP	-0.13 \pm 0.16
Barr YM	-0.05 \pm 0.24
Barr ZP	0.016 \pm 0.088
Barr ZM	-0.00 \pm 0.11
Detector Parameters	
DOM Efficiency	0.9634 \pm 0.0049
Hole Ice (p ₂)	-3.33 \pm 0.43
Ice Gradient 0	-0.05 \pm 0.24
Ice Gradient 1	0.56 \pm 0.53
Astrophysics Parameters	
Normalization ($\Phi_{\text{astro.}}$)	0.91 \pm 0.21
Spectral shift ($\Delta\gamma_{\text{astro.}}$)	0.07 \pm 0.18
Cross Section Parameters	
Cross Section σ_{ν_μ}	1.000 \pm 0.030
Cross Section $\sigma_{\bar{\nu}_\mu}$	0.999 \pm 0.071
Kaon Energy Loss σ_{KA}	-0.21 \pm 0.91

Table 7.2: Best fit parameters found at the point with the largest evidence. The uncertainties for the nuisance parameters are obtained from the posterior distribution obtained at the best fit physics point.

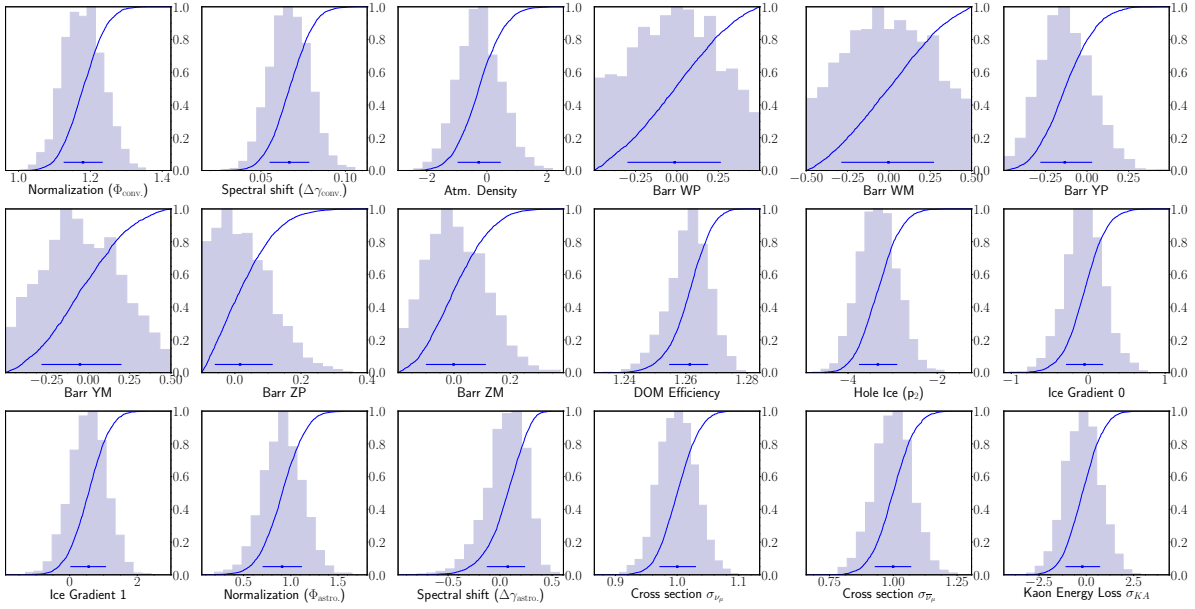


Figure 7-18: The posterior distributions for each nuisance parameter found at the best fit point. Included also is the cumulative distribution and the 1σ bounds of each parameter.

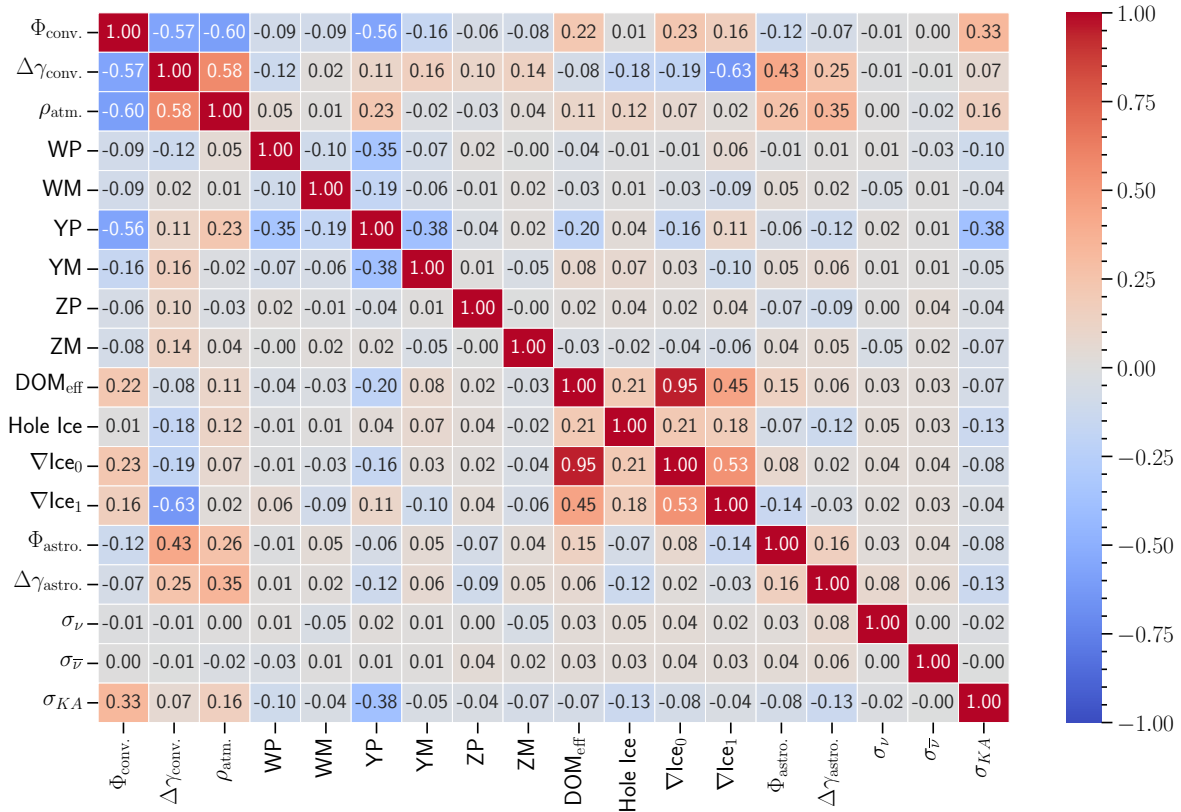


Figure 7-19: The correlations between the nuisance parameters in the posterior distribution for the best fit point.

3+1 sterile neutrino model. We will also conduct tests throughout the sampled parameter space to test if Wilks' Theorem is valid, to more accurately draw the confidence regions.

The Bayesian analysis, on the other hand, seems to show a clearer preference for the sterile model versus the null model, with a Bayes factor that indicates a “Very Strong” preference for the sterile model. With few other sterile neutrino experiments computing a Bayes factor, it's difficult to compare our results with the observation from other experiments. As this analysis moves forward towards publication, we will see if this observation holds up. If so, it will likely lead to further study and, possibly, further motivation to search for and study sterile neutrinos.

Chapter 8

Conclusion

In this work, we presented two analyses.

The first is an update to the sterile neutrino global fits. Fitting to the global data reveals a strong preference for a 3+1 model versus the null of 6.6σ . The best fit is at $\Delta m_{41}^2 = 13.1 \text{ eV}^2$, $|U_{e4}| = 0.30$, and $|U_{\mu 4}| = 0.065$. However, internal tensions make this model unviable. We explore two other models, 3+2 and 3+1+Decay. In the 3+2 model, we find no additional improvement to the fit compared to the 3+1 mode. In the 3+1+Decay, when the decay width Γ is left unconstrained, we find the best fit point at $\Delta m_{41}^2 = 1.4 \text{ eV}^2$, $|U_{e4}| = 0.3$, $|U_{\mu 4}| = 0.09$, and $\tau = 2.7 \text{ eV}^{-1}$. This model reduces the tension to 3.6σ , a substantial improvement over the 3+1 tension, but still too high.

In the second analysis, we expanded the previous MEOWS analysis to fit over the mixing parameter θ_{34} (or $|U_{\tau 4}|^2$). We do two different fits. In the frequentist fit, we find a best fit point at $\Delta m_{41}^2 = 5.0 \text{ eV}^2$, $|U_{\mu 4}|^2 = 0.04$, and $|U_{\tau 4}|^2 = 0.006$, with a p-value of 5.2% assuming Wilks' Theorem with 3 degrees of freedom. A more accurate p-value calculated with pseudoexperiments is currently indicating a lower p-value, but more trials need to be run confirm that value. The Bayesian fit, on the other hand, is seeing a stronger preference for the sterile model versus the null. The extracted Bayes factor of $\log_{10} < -1.56$ indicates a "Very Strong" preference for the sterile model, following Jeffreys' scale. The point with the largest evidence was found at $\Delta m_{41}^2 = 5.0 \text{ eV}^2$, $|U_{\mu 4}|^2 = 0.02$, and $|U_{\tau 4}|^2 = 0.006$, near the frequentist best fit point.

Appendix A

Specific Contributions

For the MiniBooNE analysis, my contributions included

- Running the data processing chain from start to finish.
- Analyzing reconstructed π^0 invariant mass to find energy shift in the PMTs since the previous data run.

With regards to the global fits, my contributions included

- Deriving the oscillation formulas for a neutrino decay width of Γ , and implementing them into the fitting software.
- Incorporating the various SBL experiments that released data since I started at MIT.
- Updated code to more exact oscillation formulae.
- Improved implementation of some already implemented experiments.

With respect to the IceCube analysis presented here, my contributions include

- Creating a ν_τ simulation set for the analysis.
- Implementing a modification in PROPOSAL to decay τ leptons as if they were polarized.
- Performing the sensitivity studies and analysis of the MEOWS+ θ_{34} search.

This work has been supported by the National Science Foundation.

Appendix B

Neutrino Oscillations Derivation

In this section, we will derive the oscillation formula for N neutrinos. We follow the derivation provided in Ref. [96], where we also generalize for an arbitrary number of neutrinos.

We write out our $N \times N$ mixing expression as

$$\begin{pmatrix} \nu_\alpha \\ \nu_\beta \\ \vdots \end{pmatrix} = \begin{pmatrix} U_{\alpha 1} & U_{\alpha 2} & \cdots \\ U_{\beta 1} & U_{\beta 2} & \cdots \\ \vdots & & \ddots \end{pmatrix} \begin{pmatrix} \nu_1 \\ \nu_2 \\ \vdots \end{pmatrix}. \quad (\text{B.1})$$

Assuming a unitary mixing matrix, we can also write our expression as

$$\begin{pmatrix} \nu_1 \\ \nu_2 \\ \vdots \end{pmatrix} = \begin{pmatrix} U_{\alpha 1}^* & U_{\beta 1}^* & \cdots \\ U_{\alpha 2}^* & U_{\beta 2}^* & \cdots \\ \vdots & & \ddots \end{pmatrix} \begin{pmatrix} \nu_\alpha \\ \nu_\beta \\ \vdots \end{pmatrix}. \quad (\text{B.2})$$

By defining

$$U \equiv \begin{pmatrix} U_{\alpha 1} & U_{\alpha 2} & \cdots \\ U_{\beta 1} & U_{\beta 2} & \cdots \\ \vdots & & \ddots \end{pmatrix}, \quad (\text{B.3})$$

we can write the unitarity condition $U^\dagger U = U U^\dagger = I$ as

$$(U U^\dagger)_{ij} = \sum_k U_{ik} U_{kj}^\dagger = \sum_k U_{ik} U_{jk}^* = \delta_{ij}. \quad (\text{B.4})$$

Let's assume that at $t = 0$, a neutrino of flavor α is produced, as shown in Figure B-1. Written in terms of its mass eigenstates, we have

$$|\psi(0)\rangle = |\nu_\alpha\rangle \equiv \sum_i U_{\alpha i}^* |\nu_i\rangle. \quad (\text{B.5})$$

Note that, since the produced neutrino in Figure B-1 appears as an adjoint spinor, the complex conjugates of the matrix elements are used in Equation (B.5).

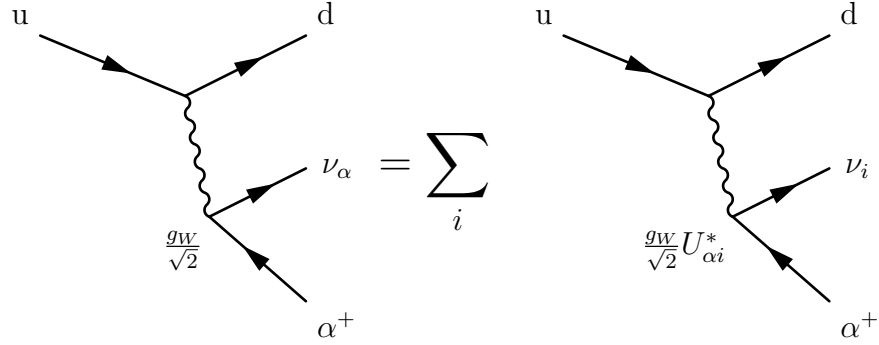


Figure B-1: The left side shows a β -decay to a neutrino of flavor α . The right side shows this same decay as a sum of contributions from the different mass eigenstates.

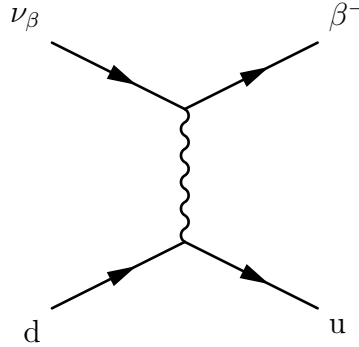


Figure B-2: Inverse β -decay interaction

Propagating these mass eigenstates as plane waves gives us the wavefunction

$$|\psi(\mathbf{x}, t)\rangle = \sum_i U_{\alpha i}^* |\nu_i\rangle e^{-i\phi_i}, \quad (\text{B.6})$$

where

$$\phi_i = p_i \cdot t = E_i t - \mathbf{p}_i \cdot \mathbf{x}. \quad (\text{B.7})$$

When this neutrino wavefunction later undergoes a charged current interaction at time t , as in Figure B-2, the interaction occurs in the flavor state, so we must expand the mass eigenstate terms to the corresponding weak eigenstates,

$$\begin{aligned} |\psi(\mathbf{x}, t)\rangle &= \sum_i U_{\alpha i}^* \left(\sum_{\gamma} U_{\gamma i} |\nu_{\gamma}\rangle \right) e^{-i\phi_i} \\ &= \sum_{\gamma} \left(\sum_i U_{\alpha i}^* U_{\gamma i} e^{-i\phi_i} \right) |\nu_{\gamma}\rangle \\ &= \sum_{\gamma} c_{\gamma} |\nu_{\gamma}\rangle, \end{aligned} \quad (\text{B.8})$$

where we have grouped together terms corresponding to the weak eigenstates $|\nu_\gamma\rangle$, and we define

$$c_\gamma \equiv \sum_i U_{\alpha i}^* U_{\gamma i} e^{-i\phi_i}. \quad (\text{B.9})$$

Note, again, that since the neutrino in Figure B-2 comes in as a spinor, the PMNS matrix elements are doubly-complex conjugated (i.e. the complex conjugation cancels out).

By writing out our propagated state as in Equation (B.8), we can easily obtain the probability of a produced ν_α oscillating and being detected as a ν_β .

$$P(\nu_\alpha \rightarrow \nu_\beta) = |\langle \nu_\beta | \psi(\mathbf{x}, t) \rangle|^2 \quad (\text{B.10})$$

$$= c_\beta c_\beta^* \quad (\text{B.11})$$

$$= \left| \sum_i U_{\alpha i}^* U_{\beta i} e^{-i\phi_i} \right|^2 \quad (\text{B.12})$$

We can expand Equation (B.12) by using the following identity:

$$\left| \sum_i z_i \right|^2 = \sum_{ij} z_i z_j^* \quad (\text{B.13})$$

$$= \sum_i |z_i|^2 + \sum_{i \neq j} z_i z_j^* \quad (\text{B.14})$$

$$= \sum_i |z_i|^2 + \sum_{i < j} (z_i z_j^* + z_i^* z_j) \quad (\text{B.15})$$

$$= \sum_i |z_i|^2 + 2 \sum_{i < j} \Re(z_i z_j^*). \quad (\text{B.16})$$

With Equation (B.16), we can write Equation (B.12) as

$$P(\nu_\alpha \rightarrow \nu_\beta) = \sum_i |U_{\alpha i}^* U_{\beta i}|^2 + 2 \sum_{i < j} \Re(U_{\alpha i}^* U_{\beta i} U_{\alpha j} U_{\beta j}^* e^{-i(\phi_i - \phi_j)}) \quad (\text{B.17})$$

We can also use Equation (B.16) on Equation (B.4) to write

$$\left| \sum_i U_{\alpha i}^* U_{\beta i} \right|^2 = \sum_i |U_{\alpha i}^* U_{\beta i}|^2 + 2 \sum_{i < j} \Re(U_{\alpha i}^* U_{\beta i} U_{\alpha j} U_{\beta j}^*) = \delta_{\alpha\beta}, \quad (\text{B.18})$$

which now lets us write Equation (B.17) as

$$P(\nu_\alpha \rightarrow \nu_\beta) = \delta_{\alpha\beta} + 2 \sum_{i < j} \Re(U_{\alpha i}^* U_{\beta i} U_{\alpha j} U_{\beta j}^* (e^{i(\phi_j - \phi_i)} - 1)), \quad (\text{B.19})$$

which we further expand into

$$\begin{aligned}
P(\nu_\alpha \rightarrow \nu_\beta) &= \delta_{\alpha\beta} + 2 \sum_{i<j} \Re(U_{\alpha i}^* U_{\beta i} U_{\alpha j} U_{\beta j}^*) (\cos(\phi_j - \phi_i) - 1) \\
&\quad - 2 \sum_{i<j} \Im(U_{\alpha i}^* U_{\beta i} U_{\alpha j} U_{\beta j}^*) \sin(\phi_j - \phi_i).
\end{aligned} \tag{B.20}$$

By defining $\Delta_{ji} = \frac{\phi_j - \phi_i}{2}$ and using trigonometric identities, we can rewrite

$$\cos(2\Delta_{ji}) - 1 = \cos^2(\Delta_{ji}) - \sin^2(\Delta_{ji}) - 1 \tag{B.21}$$

$$= -\sin^2(\Delta_{ji}) - (1 - \cos^2(\Delta_{ji})) \tag{B.22}$$

$$= -2 \sin^2(\Delta_{ji}). \tag{B.23}$$

Using this in Equation (B.20),

$$\begin{aligned}
P(\nu_\alpha \rightarrow \nu_\beta) &= \delta_{\alpha\beta} - 4 \sum_{i<j} \Re(U_{\alpha i}^* U_{\beta i} U_{\alpha j} U_{\beta j}^*) \sin^2(\Delta_{ji}) \\
&\quad - 2 \sum_{i<j} \Im(U_{\alpha i}^* U_{\beta i} U_{\alpha j} U_{\beta j}^*) \sin(2\Delta_{ji}).
\end{aligned} \tag{B.24}$$

The final step is to rewrite Δ_{ji} with physical quantities. From Equation (B.7) we can write

$$\Delta_{ji} = \frac{\Delta\phi_{ji}}{2} = (E_2 - E_1)T - (p_2 - p_1)L. \tag{B.25}$$

Let's assume that the momenta of the two neutrinos states ν_1 and ν_2 are equal¹, $p \equiv p_1 = p_2$. In this case

$$\begin{aligned}
\Delta\phi_{21} &= (E_2 - E_1)T \\
&= \left((p^2 + m_2^2)^{\frac{1}{2}} - (p^2 + m_1^2)^{\frac{1}{2}} \right) T \\
&= \left(p \left(1 + \frac{m_2^2}{p^2} \right)^{\frac{1}{2}} - p \left(1 + \frac{m_1^2}{p^2} \right)^{\frac{1}{2}} \right) T.
\end{aligned} \tag{B.26}$$

Because we assume that $m \ll p$, we are justified in doing the Taylor expansion

$$\left(1 + \frac{m^2}{p^2} \right)^{\frac{1}{2}} \approx 1 + \frac{m^2}{2p^2}. \tag{B.27}$$

¹While this simplifies the derivation, the resulting oscillation equations remain the same without this assumption [1].

When this approximation is inputted into Equation (B.26), we find

$$\begin{aligned}\Delta\phi_{21} &\approx \left(p \left(1 + \frac{m_2^2}{2p^2} \right) - p \left(1 + \frac{m_1^2}{2p^2} \right) \right) T \\ &= \frac{m_2^2 - m_1^2}{2p} T \\ &\approx \frac{m_2^2 - m_1^2}{2p} L.\end{aligned}\tag{B.28}$$

Where in the final step we use the approximation that $T = L$ because the neutrinos are traveling near the speed of light. With the final approximation $p = E$, we can write

$$\Delta\phi_{ji} = \frac{\Delta m_{ji}^2 L}{2E}.\tag{B.29}$$

Using Equation (B.29), we can write Equation (B.24) as

$$\begin{aligned}P(\nu_\alpha \rightarrow \nu_\beta) &= \delta_{\alpha\beta} - 4 \sum_{i<j} \Re(U_{\alpha i}^* U_{\beta i} U_{\alpha j} U_{\beta j}^*) \sin^2 \left(\frac{\Delta m_{ji}^2 L}{4E} \right) \\ &\quad - 2 \sum_{i<j} \Im(U_{\alpha i}^* U_{\beta i} U_{\alpha j} U_{\beta j}^*) \sin \left(\frac{\Delta m_{ji}^2 L}{2E} \right).\end{aligned}\tag{B.30}$$

Equation (B.30) is the final neutrino oscillation formula, written in natural units. In the field of neutrino physics, the standard is to give the mass-squared splitting Δm_{ji}^2 in units of eV, the energy E in GeV, and the distance L in kilometers. For the rest of this text we will use these units, unless otherwise stated. With these unit conversions in mind, Equation (B.30) can be rewritten as

$$\begin{aligned}P(\nu_\alpha \rightarrow \nu_\beta) &= \delta_{\alpha\beta} - 4 \sum_{i<j} \Re(U_{\alpha i}^* U_{\beta i} U_{\alpha j} U_{\beta j}^*) \sin^2 \left(1.27 \Delta m_{ji}^2 [\text{eV}] \frac{L[\text{km}]}{E[\text{GeV}]} \right) \\ &\quad - 2 \sum_{i<j} \Im(U_{\alpha i}^* U_{\beta i} U_{\alpha j} U_{\beta j}^*) \sin \left(2.54 \Delta m_{ji}^2 [\text{eV}] \frac{L[\text{km}]}{E[\text{GeV}]} \right).\end{aligned}\tag{B.31}$$

While Equation (B.31) has a term for each combination of Δm_{ij}^2 , they are not all independent. The relation between the different mass-squared splittings is given by

$$\Delta m_{ij}^2 = \sum_{k=i}^{j-1} \Delta m_k^2 \quad k+1,\tag{B.32}$$

so that there are only $N-1$ independent mass-squared splittings.

Appendix C

MiniBooNE Supplementary Material

We include here the Supplementary Material for the MiniBooNE publication presented in Chapter 3.

Supplementary Material: Significant Excess of Electron-Like Events in the MiniBooNE Short-Baseline Neutrino Experiment

A. A. Aguilar-Arevalo¹³, B. C. Brown⁶, L. Bugel¹², G. Cheng⁵, J. M. Conrad¹², R. L. Cooper^{10,15}, R. Dharmapalan^{1,2}, A. Diaz¹², Z. Djurcic², D. A. Finley⁶, R. Ford⁶, F. G. Garcia⁶, G. T. Garvey¹⁰, J. Grange⁷, E.-C. Huang¹⁰, W. Huelsnitz¹⁰, C. Ignarra¹², R. A. Johnson³, G. Karagiorgi⁵, T. Katori^{12,16}, T. Kobilarcik⁶, W. C. Louis¹⁰, C. Mariani¹⁹, W. Marsh⁶, G. B. Mills^{10,†}, J. Mirabal¹⁰, J. Monroe¹⁸, C. D. Moore⁶, J. Mousseau¹⁴, P. Nienaber¹⁷, J. Nowak⁹, B. Osmanov⁷, Z. Pavlovic⁶, D. Perevalov⁶, H. Ray⁷, B. P. Roe¹⁴, A. D. Russell⁶, M. H. Shaevitz⁵, J. Spitz¹⁴, I. Stancu¹, R. Tayloe⁸, R. T. Thornton¹⁰, M. Tzanov^{4,11}, R. G. Van de Water¹⁰, D. H. White¹⁰, D. A. Wickremasinghe³, E. D. Zimmerman⁴

(The MiniBooNE Collaboration)

¹University of Alabama; Tuscaloosa, AL 35487, USA

²Argonne National Laboratory; Argonne, IL 60439, USA

³University of Cincinnati; Cincinnati, OH, 45221, USA

⁴University of Colorado; Boulder, CO 80309, USA

⁵Columbia University; New York, NY 10027, USA

⁶Fermi National Accelerator Laboratory; Batavia, IL 60510, USA

⁷University of Florida; Gainesville, FL 32611, USA

⁸Indiana University; Bloomington, IN 47405, USA

⁹Lancaster University; Lancaster LA1 4YB, UK

¹⁰Los Alamos National Laboratory; Los Alamos, NM 87545, USA

¹¹Louisiana State University; Baton Rouge, LA 70803, USA

¹²Massachusetts Institute of Technology; Cambridge, MA 02139, USA

¹³Instituto de Ciencias Nucleares; Universidad Nacional Autónoma de México; CDMX 04510, México

¹⁴University of Michigan; Ann Arbor, MI 48109, USA

¹⁵New Mexico State University; Las Cruces, NM 88003, USA

¹⁶Queen Mary University of London; London E1 4NS, UK

¹⁷Saint Mary's University of Minnesota; Winona, MN 55987, USA

¹⁸Royal Holloway, University of London; Egham TW20 0EX, UK

¹⁹Center for Neutrino Physics; Virginia Tech; Blacksburg, VA 24061, USA

[†]Deceased

(Dated: September 26, 2018)

Appendix: Background Determination & Data vs Monte Carlo Comparisons

Almost all of the backgrounds in the electron-neutrino candidate event sample are determined directly from MiniBooNE data [26]. The muon-neutrino charged-current quasi-elastic (CCQE) observed data sample allows the background determination of both mis-identified ν_μ CCQE events from pion decay [28] and ν_e CCQE events from muon decay, as the neutrinos come from the same parent pion and ν_e and ν_μ cross sections are the same from lepton universality after correcting for charged lepton mass effects. The ν_e CCQE background from kaon decay was determined from external measurements and confirmed by data from the SciBooNE experiment [27]. In addition, the neutral current (NC) π^0 data sample allows the background determination of both NC π^0 events [32] and single gamma events from $\Delta \rightarrow N\gamma$ decays. Various theoretical estimates [30, 31] have confirmed the MiniBooNE single gamma background estimate. Fig. 1 shows a comparison of the single gamma background estimate from reference [31] with that of MiniBooNE, where good agreement is obtained. Single-gamma back-

grounds from external neutrino interactions (“dirt” backgrounds) are estimated using topological and spatial cuts to isolate the events whose vertices are near the edge of the detector and point towards the detector center [34]. These estimates have been confirmed by preliminary measurements of the absolute event time reconstruction of electron-neutrino candidate events, where a fit to the dirt event background using timing agrees within 10% with the background estimate using topological and spatial cuts.

In order to demonstrate that the MiniBooNE background estimates are reliable, various comparisons between the neutrino data, corresponding to 12.84×10^{20} protons on target (POT), and the Monte Carlo simulation have been performed to check and confirm the accuracy of the simulation. Fig. 2 shows an absolute comparison of the π^0 reconstructed mass distribution between the data and the simulation for NC π^0 events. Excellent agreement is obtained, and the ratio of the number of data events (42,483) to the number of Monte Carlo events (42,530) in the mass range from 80 to 200 MeV/c² is equal to 0.999. Fig. 3 shows an absolute comparison of

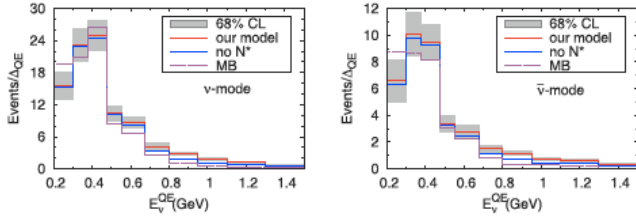


FIG. 1: A comparison of the single gamma background estimate from reference [31] with that of MiniBooNE, where good agreement is obtained.

the reconstructed neutrino energy distribution for CCQE events between the data and the simulation. Excellent agreement is also obtained, and the ratio of the number of data events (232,096) to the number of Monte Carlo events (236,145) is equal to 0.983.

In order to check the particle identification (PID) cuts, Figs. 4, 5, and 6 show comparisons between the data and simulation for the electron-muon likelihood distribution, the electron-pion likelihood distribution, and the gamma-gamma mass distribution. In each figure, distributions are shown after successive cuts are applied: no PID cut, electron-muon likelihood cut, electron-muon plus electron-pion likelihood cuts, and electron-muon plus electron-pion likelihood cuts and a gamma-gamma mass cut. The last plot in each figure shows distributions with the final event selection. The vertical lines show the range of energy-dependent cut values. Good agreement between the data and the simulation is obtained outside the cut values, while an excess of events is observed inside the cut values. Figs. 7 and 8 show the momentum and gamma-gamma opening angle distributions after successive cuts are applied. Good agreement is obtained between the data and Monte Carlo simulation for the no PID cut distributions, while event excesses are observed after the final event selection. These five plots also demonstrate that sidebands show good agreement between the data and simulation.

Fig. 9 shows the visible energy (E_{vis}) and $\cos \theta_e$ (U_z) distributions for the electron-neutrino candidate events in neutrino mode (top) and antineutrino mode (bottom). Also shown in the figures are the expectations from all known backgrounds and from the oscillation best fit. These distributions are important because the reconstructed neutrino energy, E_{ν}^{QE} , is determined from E_{vis} and U_z . A check on the spatial reconstruction is shown

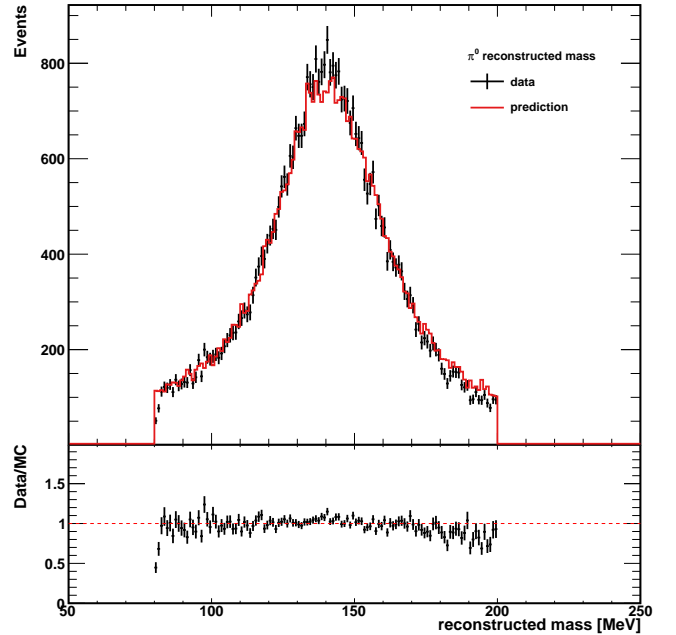


FIG. 2: An absolute comparison of the π^0 reconstructed mass distribution between the neutrino data (12.84×10^{20} POT) and the simulation for NC π^0 events (top). Also shown is the ratio between the data and Monte Carlo simulation (bottom). The error bars show only statistical uncertainties.

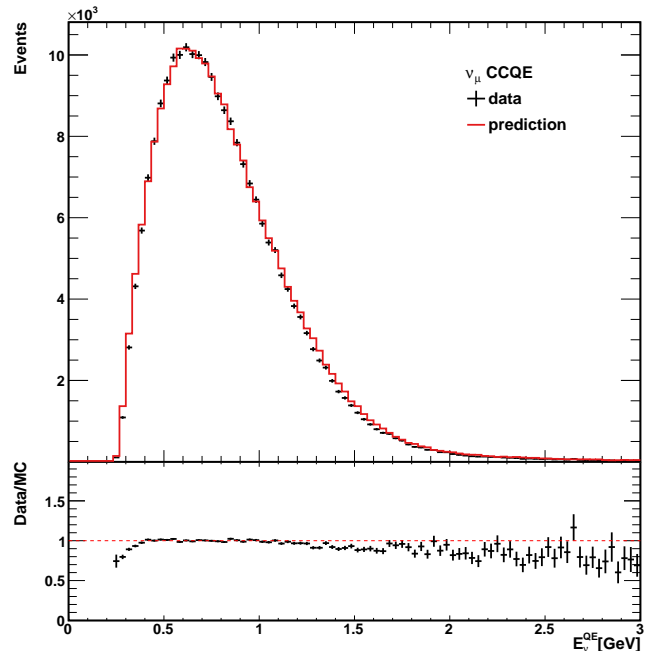


FIG. 3: An absolute comparison of the reconstructed neutrino energy distribution for CCQE events between the neutrino data (12.84×10^{20} POT) and the simulation (top). Also shown is the ratio between the data and Monte Carlo simulation (bottom). The error bars show only statistical uncertainties.

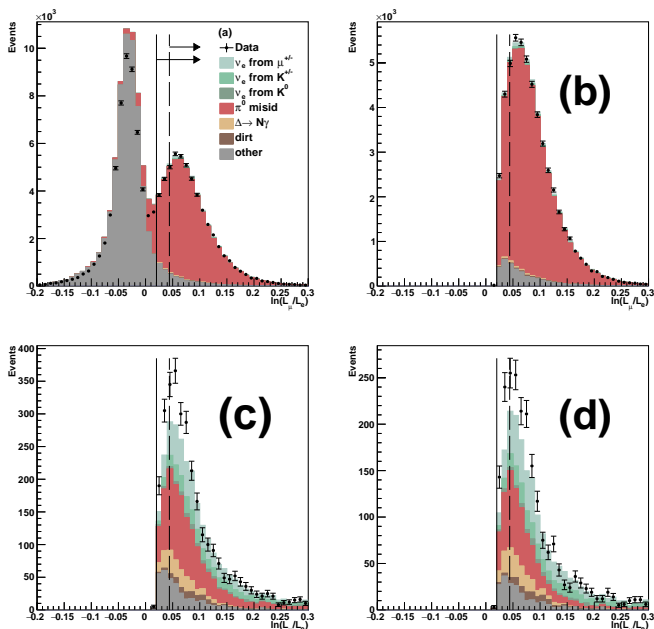


FIG. 4: Comparisons between the data and simulation for the electron-muon likelihood distribution after successive cuts are applied: (a) no PID cut, (b) electron-muon likelihood cut, (c) electron-muon plus electron-pion likelihood cuts, and (d) electron-muon plus electron pion likelihood cuts plus a gamma-gamma mass cut. The vertical lines in the figures show the range of energy-dependent cut values. The error bars show only statistical uncertainties.

in Fig. 10, where the radius reconstruction in the data is compared to the Monte Carlo simulation. As shown in the figure, the event excess is evenly distributed up to the 5m radius cut. A further check of the electron efficiency was obtained from the reconstruction of electron events in MiniBooNE that originated from the off-axis NUMI beam (P. Adamson et al., Phys. Rev. Lett. **102**, 211801 (2009)), as the intrinsic ν_e background was approximately ten times higher in the NUMI beam than in the BNB. The measured electron rate agreed with the simulation within errors.

Appendix: Stability Checks

Many checks have been performed on the data, including beam and detector stability checks. Fig. 11 shows the total number of neutrino events observed per 10^{17} POT over the lifetime of MiniBooNE in neutrino mode, antineutrino mode and beam-dump mode. The neutrino mode event rate of 100 events per 10^{17} POT has been stable to $< 2\%$ over the 15 year MiniBooNE running period. This is within the expected errors from time variations in BNB performance, such as target/horn change, beam rate monitoring, etc. A small change in the detector energy response between the first and second neutrino data set has been corrected by increasing the measured energy in the second data set by 2%. About half of the energy change is from PMT failures in the intervening years,

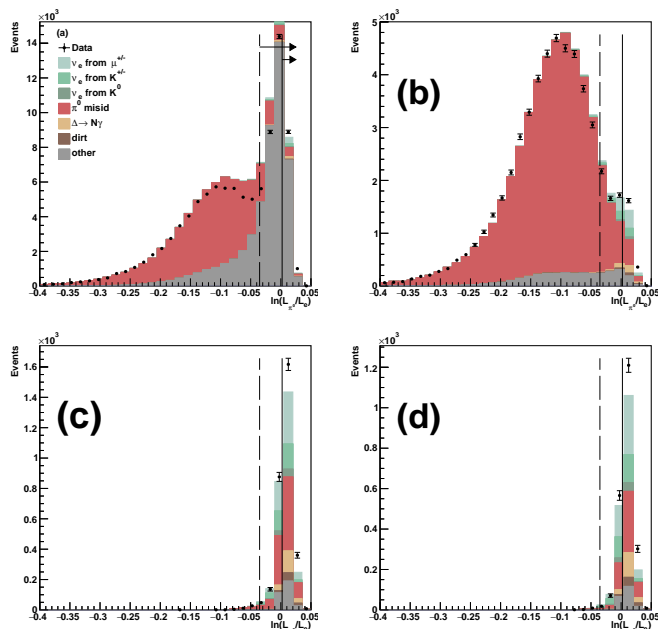


FIG. 5: Comparisons between the data and simulation for the electron-pion likelihood distribution after successive cuts are applied: (a) no PID cut, (b) electron-muon likelihood cut, (c) electron-muon plus electron-pion likelihood cuts, and (d) electron-muon plus electron pion likelihood cuts plus a gamma-gamma mass cut. The vertical lines in the figures show the range of energy-dependent cut values. The error bars show only statistical uncertainties.

and the remainder is within the detector response error from gain variations, oil properties, etc. With this energy correction, the first and second data sets are found to agree well. Fig. 12 compares the reconstructed ν_μ CCQE energy distributions for the second data set in 2016 and 2017 to the first data set, where good agreement is obtained. Likewise, Fig. 13 shows that the π^0 mass distribution has also not changed.

Appendix: Comparing New and Old Neutrino Data

Figs. 14 and 15 show the E_ν^{QE} distribution for ν_e CCQE data and background in neutrino mode over the full available energy range for the first 6.46×10^{20} POT data set and the second 6.38×10^{20} POT data set. Fig. 16 shows the ν_e CCQE data and background in antineutrino mode. Each bin of reconstructed E_ν^{QE} corresponds to a distribution of “true” generated neutrino energies, which can overlap adjacent bins. Note that the 162.0 event excess in the 6.46×10^{20} POT data is approximately 1σ lower than the average excess, while the 219.2 event excess in the 6.38×10^{20} POT data is approximately 1σ higher than the average excess. In antineutrino mode, a total of 478 data events pass the ν_e CCQE event selection requirements with $200 < E_\nu^{QE} < 1250$ MeV, compared to a background expectation of

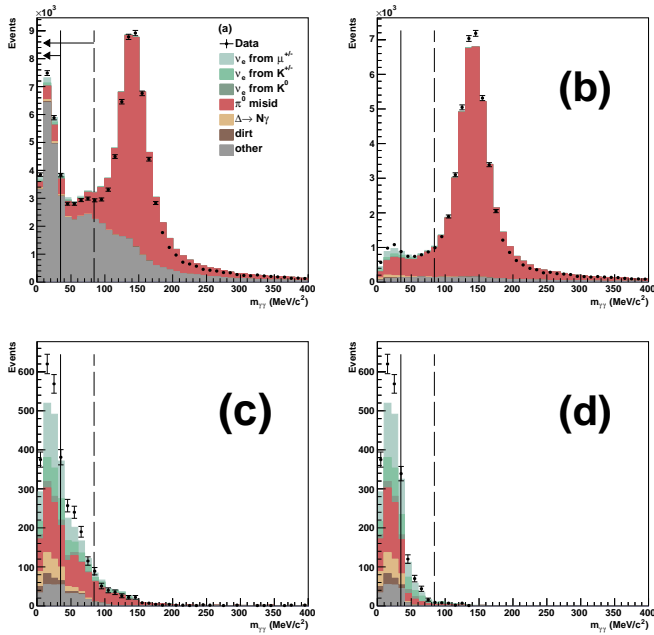


FIG. 6: Comparisons between the data and simulation for the gamma-gamma mass distribution after successive cuts are applied: (a) no PID cut, (b) electron-muon likelihood cut, (c) electron-muon plus electron-pion likelihood cuts, and (d) electron-muon plus electron pion likelihood cuts plus a gamma-gamma mass cut. The vertical lines in the figures show the range of energy-dependent cut values. The error bars show only statistical uncertainties.

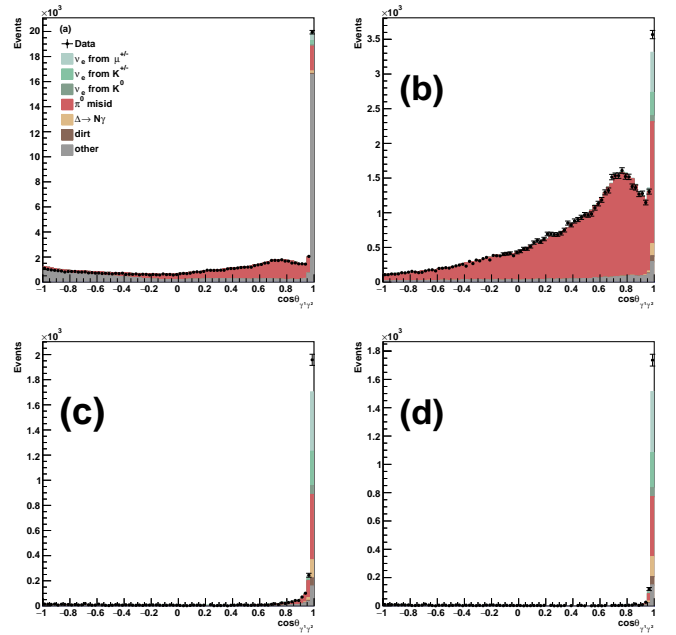


FIG. 8: Comparisons between the data and simulation for the gamma-gamma opening angle distribution after successive cuts are applied: (a) no PID cut, (b) electron-muon likelihood cut, (c) electron-muon plus electron-pion likelihood cuts, and (d) electron-muon plus electron pion likelihood cuts plus a gamma-gamma mass cut. The event excess occurs almost entirely for opening angles less than 13 degrees. The error bars show only statistical uncertainties.

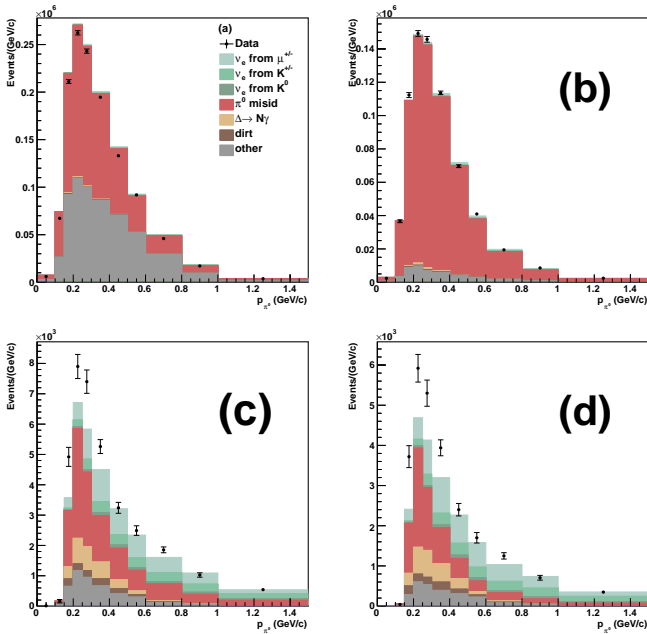


FIG. 7: Comparisons between the data and simulation for the momentum distribution after successive cuts are applied: (a) no PID cut, (b) electron-muon likelihood cut, (c) electron-muon plus electron-pion likelihood cuts, and (d) electron-muon plus electron pion likelihood cuts plus a gamma-gamma mass cut. The error bars show only statistical uncertainties.

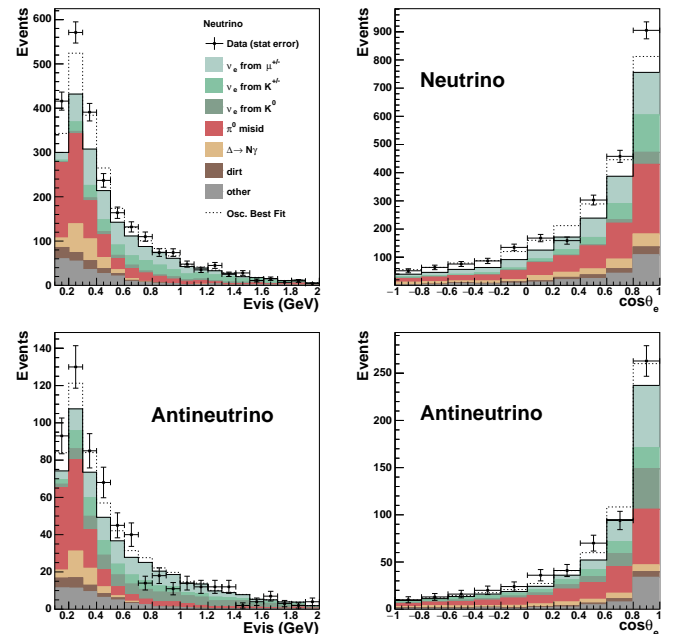


FIG. 9: The visible energy (E_{vis}) and $\cos\theta_e$ (U_z) distributions for the electron-neutrino candidate events in neutrino mode (top) and antineutrino mode (bottom). (The error bars show only statistical uncertainties.) Also shown in the figure are the expectations from all known backgrounds and from the oscillation best fit.

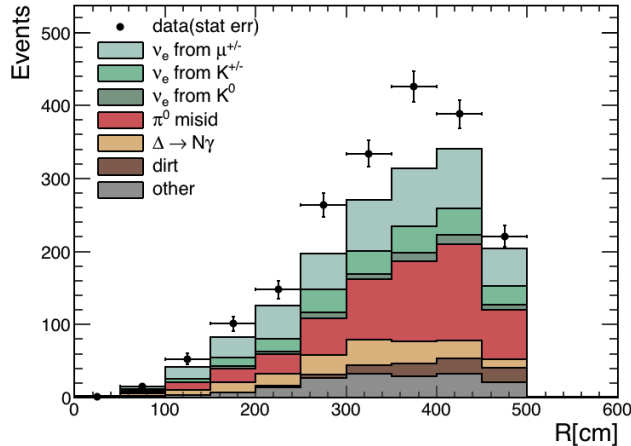


FIG. 10: The radius reconstruction in the data is compared to the Monte Carlo simulation. The event excess is evenly distributed up to the 5m radius cut.

$398.7 \pm 20.0(stat.) \pm 20.5(syst.)$ events. The excess is then 79.3 ± 28.6 events or a 2.8σ effect.

-
- [1] C. Athanassopoulos *et al.*, Phys. Rev. Lett. 75, 2650 (1995); 77, 3082 (1996); 81, 1774 (1998); Phys. Rev. C 54, 2685 (1996); 58, 2489 (1998); A. Aguilar *et al.*, Phys. Rev. D 64, 112007 (2001).
- [2] A. A. Aguilar-Arevalo *et al.*, Phys. Rev. Lett. 98, 231801 (2007); Phys. Rev. Lett. 102, 101802 (2009); Phys. Rev. Lett. 105, 181801 (2010).
- [3] A. A. Aguilar-Arevalo *et al.*, Phys. Rev. Lett. 110, 161801 (2013).
- [4] G. Mention, M. Fechner, T. Lasserre, T. A. Mueller, D. Lhuillier, M. Cribier, and A. Letourneau, Phys. Rev. D 83, 073006 (2011).
- [5] C. Giunti and M. Laveder, Phys. Rev. C 83, 065504 (2011).
- [6] M. Sorel, J. M. Conrad and M. H. Shaevitz, Phys. Rev. D 70, 073004 (2004).
- [7] G. Karagiorgi, Z. Djurcic, J. M. Conrad, M. H. Shaevitz and M. Sorel, Phys. Rev. D 80, 073001 (2009); D 81, 039902(E) (2010).
- [8] G.H. Collin, C.A. Argüelles, J.M. Conrad, and M.H. Shaevitz, Phys. Rev. Lett. 117, 221801 (2016).
- [9] C. Giunti and M. Laveder, Phys. Lett. B 706, 200 (2011); Phys. Rev. D 84, 073008, (2011).
- [10] S. Gariazzo, C. Giunti, M. Laveder, and Y.F. Li, arXiv:1703.00860 [hep-ph] (2017).
- [11] J. Kopp, M. Maltoni and T. Schwetz, Phys. Rev. Lett. 107, 091801 (2011); Joachim Kopp, Pedro A.N. Machado, Michele Maltoni, and Thomas Schwetz, JHEP 1305, 050, (2013).
- [12] Mona Dentler, Alvaro Hernandez-Cabezudo, Joachim Kopp, Pedro Machado, Michele Maltoni, Ivan Martinez-Soler, and Thomas Schwetz, arXiv:1803.10661 [hep-ph] (2018).
- [13] K. N. Abazajian *et al.*, arXiv:1204.5379 [hep-ph] (2012).
- [14] J. M. Conrad, C. M. Ignarra, G. Karagiorgi, M. H. Shaevitz, and J. Spitz, arXiv:1207.4765 [hep-ex] (2012).
- [15] J. Asaadi, E. Church, R. Guenette, B. J. P. Jones, and A. M. Szec, Phys. Rev. D 97, 075021 (2018); G. Karagiorgi, M. H. Shaevitz, and J. M. Conrad, arXiv:1202.1024; Heinrich Paes, Sandip Pakvasa, and Thomas J. Weiler, Phys. Rev. D 72, 095017 (2005); Dominik Doring, Heinrich Paes, Philipp Sicking, and Thomas J. Weiler, arXiv:1808.07460 [hep-ph] (2018).
- [16] V. A. Kostelecky and M. Mewes, Phys. Rev. D 69, 016005 (2004); T. Katori, V. A. Kostelecky, and R. Tayloe, Phys. Rev. D 74, 105009 (2006); Jorge S. Diaz and V. A. Kostelecky, Phys. Lett. B 700, 25 (2011); Jorge S. Diaz and V. A. Kostelecky, Phys. Rev. D 85, 016013 (2012).
- [17] S. N. Gninenko, Phys. Rev. Lett. 103, 241802 (2009); S. N. Gninenko and D. S. Gorbunov, Phys. Rev. D 81, 075013 (2010); Yang Bai, Ran Lu, Sida Lu, Jordi Salvado, and Ben A. Stefanek, Phys. Rev. D 93, 073004 (2016); Zander Moss, Marjon H. Moulai, Carlos Argüelles, Janet M. Conrad, Phys. Rev. D 97, 055017 (2018); Enrico Baertuzzo, Sudip Jana, Pedro A. N. Machado, and Renata Zukanovich Funchal, arXiv:1807.09877 [hep-ph] (2018); Peter Ballett, Silvia Pascoli, and Mark Ross-Lonergan, arXiv:1808.02915 [hep-ph] (2018).
- [18] Jiajun Liao and Danny Marfatia, Phys. Rev. Lett. 117, 071802 (2016).
- [19] Marcela Carena, Ying-Ying Li, Camila S. Machado, Pedro A. N. Machado, Carlos E. M. Wagner, Phys. Rev. D 96, 095014 (2017).
- [20] A. A. Aguilar-Arevalo *et al.*, Phys. Rev. D 79, 072002 (2009).
- [21] A. A. Aguilar-Arevalo *et al.*, Nucl. Instrum. Meth. A 599, 28 (2009).
- [22] R. B. Patterson *et al.*, Nucl. Instrum. Meth. A 608, 206 (2009).
- [23] A. A. Aguilar-Arevalo *et al.*, Phys. Rev. D 81, 092005 (2010); A. A. Aguilar-Arevalo *et al.*, Phys. Rev. D 88, 032001 (2013).
- [24] A. A. Aguilar-Arevalo *et al.* [MiniBooNE Collaboration], Phys. Rev. Lett. 118, no. 22, 221803 (2017); arXiv:1807.06137.
- [25] A. A. Aguilar-Arevalo *et al.*, Phys. Rev. D 84, 072005 (2011).
- [26] R. B. Patterson, Ph.D. Thesis, Princeton University (2007), <http://www-boone.fnal.gov/publications/Papers/rbpatther.thesis.pdf>.
- [27] G. Cheng *et al.*, Phys. Rev. D 84, 012009 (2011); C. Mariani, G. Cheng, J. M. Conrad and M. H. Shaevitz, Phys. Rev. D 84, 114021 (2011).
- [28] A. A. Aguilar-Arevalo *et al.*, Phys. Rev. D 81, 092005 (2010); Phys. Rev. Lett. 100, 032301 (2008).
- [29] A. A. Aguilar-Arevalo *et al.*, Phys. Rev. D 83, 052007 (2011); Phys. Rev. Lett. 103, 081801 (2009).
- [30] V. P. Efrosinin, Yu. G. Kudenko, and A. N. Khotjantsev, Phys. Atom. Nucl. 72, 459 (2009); Richard J. Hill, Phys. Rev. D 81, 013008 (2010); Richard J. Hill, Phys. Rev. D 84, 017501 (2011); Xilin Zhang and Brian D. Serot, Phys. Lett. B 719, 409 (2013); Phys. Rev. C 86, 035502 (2012); Phys. Rev. C 86, 035504 (2012); Brian D. Serot and Xilin Zhang, Phys. Rev. C 86, 015501 (2012).
- [31] E. Wang, L. Alvarez-Ruso, and J. Nieves, Phys. Rev. C 89, 015503 (2014); Phys. Lett. B 740, 16 (2015).

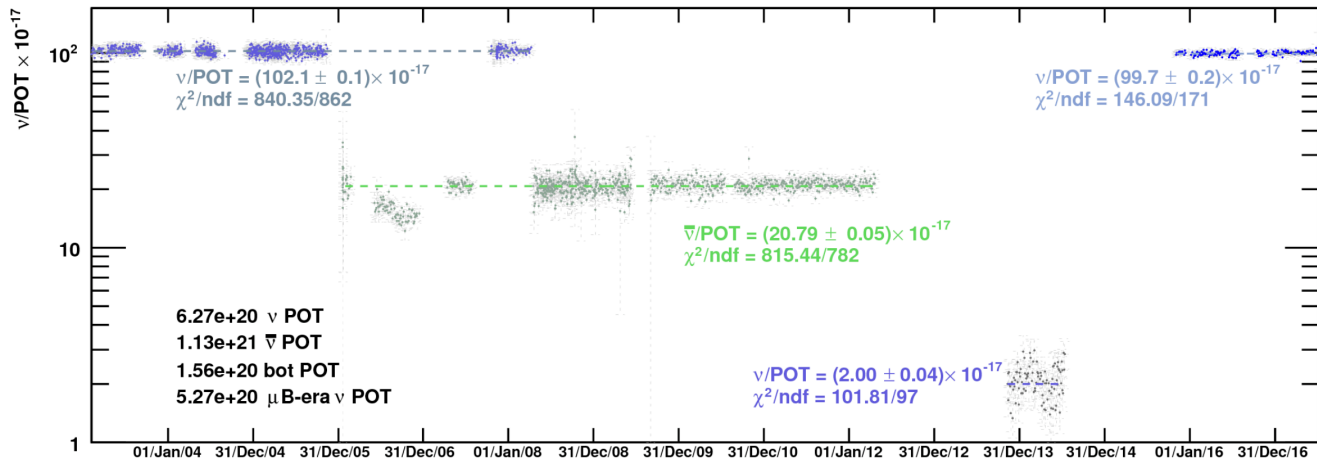


FIG. 11: The total number of neutrino events observed per 10^{17} POT over the lifetime of MiniBooNE in neutrino mode, antineutrino mode and beam-dump mode.

- [32] A. A. Aguilar-Arevalo *et al.*, Phys. Rev. D **81**, 013005 (2010); Phys. Lett. B. **664**, 41 (2008).
- [33] D. Rein and L. M. Sehgal, Phys. Lett. B. **104**, 394 (1981); S. S. Gershtein, Yu. Ya. Komachenko, and M. Yu. Khlopov, Sov. J. Nucl. Phys. **33**, 860 (1981); Jeffrey A. Harvey, Christopher T. Hill, and Richard J. Hill, Phys. Rev. Lett. **99**, 261601 (2007); J. P. Jenkins and T. Goldman, Phys. Rev. D **80**, 053005 (2009); Artur M. Ankowski, Omar Benhar, Takaaki Mori, Ryuta Yamaguchi, and Makoto Sakuda, Phys. Rev. Lett. **108**, 052505 (2012); K. M. Graczyk, D. Kielczewska, P. Przewlocki, J. T. Sobczyk, Phys. Rev. D **80**, 093001 (2009).
- [34] A. A. Aguilar-Arevalo *et al.*, Phys. Rev. Lett. **102**, 101802 (2009).
- [35] M. Martini, M. Ericson, G. Chanfray, and J. Marteau, Phys. Rev. C **80**, 065501 (2009); M. Martini, M. Ericson, and G. Chanfray, Phys. Rev. D **85**, 093012 (2012); Phys. Rev. D **87**, 013009 (2013); D. Meloni and M. Martini, Phys. Lett. B. **716**, 186 (2012); J. Nieves, I. R. Simo, and M. J. Vicente Vacas, Phys. Rev. C **83**, 045501 (2011); J. Nieves, F. Sanchez, I. R. Simo, and M. J. Vicente Vacas, Phys. Rev. D **85**, 113008 (2012); O. Lalakulich, K. Gallmeister, and U. Mosel, Phys. Rev. C **86**, 014614 (2012); Ulrich Mosel, Olga Lalakulich, and Kai Gallmeister, Phys. Rev. Lett. **112**, 151802 (2014); Andrea Meucci and Carlotta Giusti, Phys. Rev. D **85**, 093002 (2012); G. D. Megias *et al.*, Phys. Rev. D **91**, 073004 (2015); P. Coloma and P. Huber, Phys. Rev. Lett. **111**, 221802 (2013); Jan. T. Sobczyk, Phys. Rev. C **86**, 015504 (2012).
- [36] M. Ericson, M. V. Garzelli, C. Giunti, and M. Martini, Phys. Rev. D **93**, 073008 (2016).
- [37] B. Armbruster *et al.*, Phys. Rev. D **65**, 112001 (2002).
- [38] N. Agafonova *et al.*, arXiv1803.11400 [hep-ex] (2018).
- [39] M. Antonello *et al.*, arXiv:1503.01520 (2015).

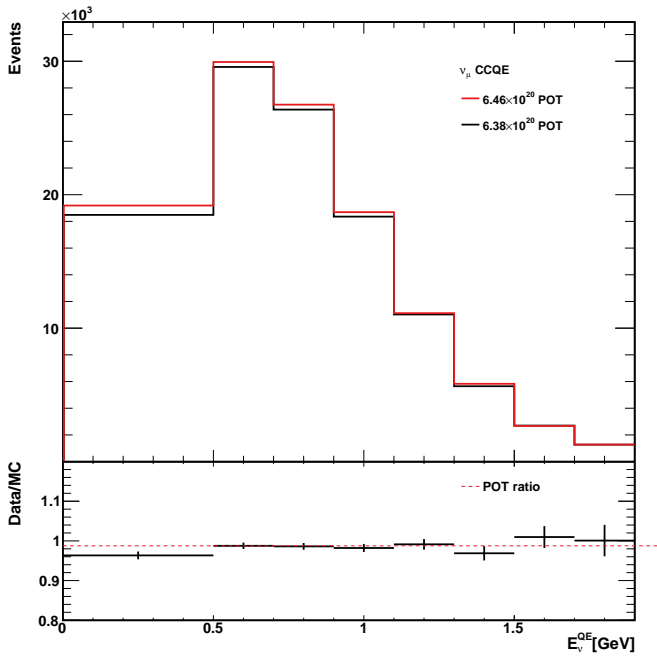


FIG. 12: The top plot shows a comparison between the reconstructed ν_μ CCQE energy distributions for the second data set in 2016 and 2017 (6.38×10^{20} POT) to the first data set (6.46×10^{20} POT). The bottom plot shows the ratio of the second data set to the first data set.

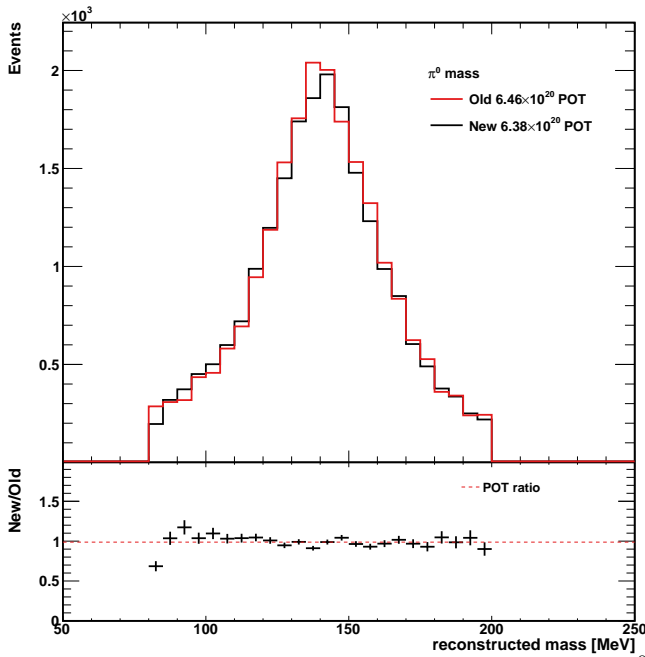


FIG. 13: The top plot shows a comparison between the π^0 mass distributions for the second data set in 2016 and 2017 (6.38×10^{20} POT) to the first data set (6.46×10^{20} POT). The bottom plot shows the ratio of the second data set to the first data set.

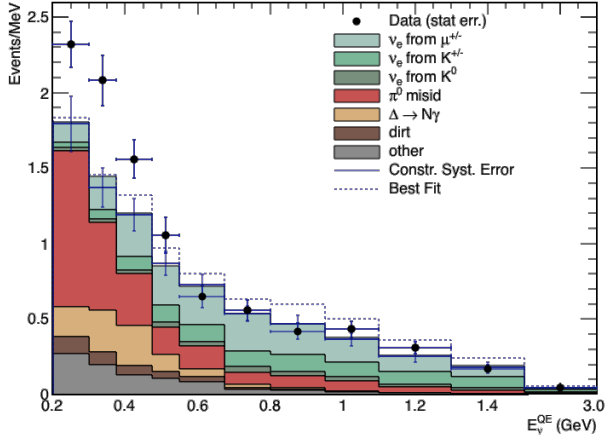


FIG. 14: The neutrino mode E_{ν}^{QE} distributions, corresponding to the first 6.46×10^{20} POT data set, for ν_e CCQE data (points with statistical errors) and background (histogram with systematic errors).

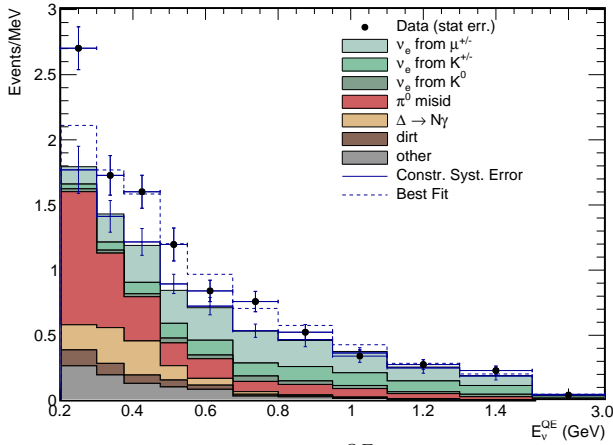


FIG. 15: The neutrino mode E_{ν}^{QE} distributions, corresponding to the second 6.38×10^{20} POT data set, for ν_e CCQE data (points with statistical errors) and background (histogram with systematic errors).

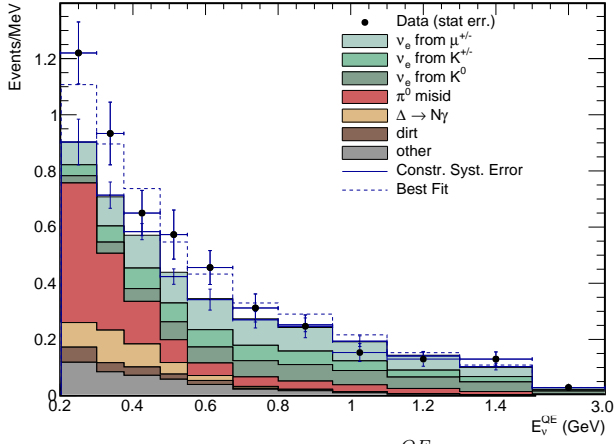


FIG. 16: The antineutrino mode E_{ν}^{QE} distributions, corresponding to the published 11.27×10^{20} POT data, for ν_e CCQE data (points with statistical errors) and background (histogram with systematic errors).

Bibliography

- [1] C. Giunti and C. W. Kim, *Fundamentals of Neutrino Physics and Astrophysics* (2007) (cit. on pp. 12, 14, 15, 128).
- [2] I. Esteban, M. C. Gonzalez-Garcia, M. Maltoni, T. Schwetz, and A. Zhou, “The fate of hints: updated global analysis of three-flavor neutrino oscillations”, *JHEP* **09**, 178 (2020), arXiv:2007.14792 [hep-ph] (cit. on pp. 12, 13).
- [3] M. H. Moulai, “Light, Unstable Sterile Neutrinos: Phenomenology, a Search in the IceCube Experiment, and a Global Picture”, PhD thesis (MIT, 2021), arXiv:2110.02351 [hep-ex] (cit. on pp. 13, 21, 94, 96).
- [4] L. Wolfenstein, “Neutrino oscillations in matter”, *Phys. Rev. D* **17**, 2369–2374 (1978), <https://link.aps.org/doi/10.1103/PhysRevD.17.2369> (cit. on p. 15).
- [5] S. P. Mikheyev and A. Y. Smirnov, “Resonance Amplification of Oscillations in Matter and Spectroscopy of Solar Neutrinos”, *Sov. J. Nucl. Phys.* **42**, 913–917 (1985) (cit. on p. 15).
- [6] S. P. Mikheev and A. Y. Smirnov, “Resonant amplification of neutrino oscillations in matter and solar neutrino spectroscopy”, *Nuovo Cim. C* **9**, 17–26 (1986) (cit. on p. 15).
- [7] D. O. Caldwell, ed., *Current aspects of neutrino physics* (2001) (cit. on p. 15).
- [8] A. Aguilar-Arevalo et al. (LSND), “Evidence for neutrino oscillations from the observation of $\bar{\nu}_e$ appearance in a $\bar{\nu}_\mu$ beam”, *Phys. Rev. D* **64**, 112007 (2001), arXiv:hep-ex/0104049 (cit. on pp. 17, 18, 42, 43).
- [9] A. A. Aguilar-Arevalo et al. (MiniBooNE), “Updated MiniBooNE neutrino oscillation results with increased data and new background studies”, *Phys. Rev. D* **103**, 052002 (2021), arXiv:2006.16883 [hep-ex] (cit. on pp. 18, 19, 39, 43).
- [10] A. A. Aguilar-Arevalo et al. (MiniBooNE), “Improved Search for $\bar{\nu}_\mu \rightarrow \bar{\nu}_e$ Oscillations in the MiniBooNE Experiment”, *Phys. Rev. Lett.* **110**, 161801 (2013), arXiv:1303.2588 [hep-ex] (cit. on pp. 18, 19, 43).
- [11] S. Schael et al. (ALEPH, DELPHI, L3, OPAL, SLD, LEP Electroweak Working Group, SLD Electroweak Group, SLD Heavy Flavour Group), “Precision electroweak measurements on the Z resonance”, *Phys. Rept.* **427**, 257–454 (2006), arXiv:hep-ex/0509008 (cit. on p. 20).
- [12] P. Huber, “Determination of antineutrino spectra from nuclear reactors”, *Phys. Rev. C* **84**, 024617 (2011), eprint: 1106.0687, <https://link.aps.org/doi/10.1103/PhysRevC.84.024617> (cit. on p. 20).

- [13] T. A. Mueller et al., “Improved Predictions of Reactor Antineutrino Spectra”, *Phys. Rev. C* **83**, 054615 (2011), arXiv:1101.2663 [hep-ex] (cit. on p. 20).
- [14] G. Mention, M. Fechner, T. Lasserre, T. A. Mueller, D. Lhuillier, M. Cribier, and A. Letourneau, “The Reactor Antineutrino Anomaly”, *Phys. Rev. D* **83**, 073006 (2011), arXiv:1101.2755 [hep-ex] (cit. on p. 20).
- [15] C. Giunti, Y. F. Li, C. A. Ternes, and Z. Xin, “Reactor antineutrino anomaly in light of recent flux model refinements”, (2021), arXiv:2110.06820 [hep-ph] (cit. on p. 22).
- [16] K. N. Abazajian et al., “Light Sterile Neutrinos: A White Paper”, (2012), arXiv:1204.5379 [hep-ph] (cit. on p. 22).
- [17] J. H. Choi et al. (RENO), “Observation of Energy and Baseline Dependent Reactor Antineutrino Disappearance in the RENO Experiment”, *Phys. Rev. Lett.* **116**, 211801 (2016), arXiv:1511.05849 [hep-ex] (cit. on p. 21).
- [18] F. P. An et al. (Daya Bay), “Measurement of the Reactor Antineutrino Flux and Spectrum at Daya Bay”, *Phys. Rev. Lett.* **116**, [Erratum: *Phys.Rev.Lett.* 118, 099902 (2017)], 061801 (2016), arXiv:1508.04233 [hep-ex] (cit. on p. 21).
- [19] Y. Abe et al. (Double Chooz), “Measurement of θ_{13} in Double Chooz using neutron captures on hydrogen with novel background rejection techniques”, *JHEP* **01**, 163 (2016), arXiv:1510.08937 [hep-ex] (cit. on p. 21).
- [20] L. Hayen, J. Kostensalo, N. Severijns, and J. Suhonen, “First-forbidden transitions in the reactor anomaly”, *Phys. Rev. C* **100**, 054323 (2019), arXiv:1908.08302 [nucl-th] (cit. on p. 21).
- [21] M. Estienne et al., “Updated Summation Model: An Improved Agreement with the Daya Bay Antineutrino Fluxes”, *Phys. Rev. Lett.* **123**, 022502 (2019), arXiv:1904.09358 [nucl-ex] (cit. on p. 21).
- [22] F. Kaether, W. Hampel, G. Heusser, J. Kiko, and T. Kirsten, “Reanalysis of the GALLEX solar neutrino flux and source experiments”, *Phys. Lett. B* **685**, 47–54 (2010), arXiv:1001.2731 [hep-ex] (cit. on pp. 21, 48).
- [23] J. N. Abdurashitov et al. (SAGE), “Measurement of the solar neutrino capture rate with gallium metal. III: Results for the 2002–2007 data-taking period”, *Phys. Rev. C* **80**, 015807 (2009), arXiv:0901.2200 [nucl-ex] (cit. on pp. 21, 48).
- [24] V. V. Barinov et al., “Results from the Baksan Experiment on Sterile Transitions (BEST)”, (2021), arXiv:2109.11482 [nucl-ex] (cit. on pp. 23, 48, 49).
- [25] V. V. Barinov et al., “A Search for Electron Neutrino Transitions to Sterile States in the BEST Experiment”, (2022), arXiv:2201.07364 [nucl-ex] (cit. on pp. 23, 48, 49, 67).
- [26] P. B. Pal and L. Wolfenstein, “Radiative Decays of Massive Neutrinos”, *Phys. Rev. D* **25**, 766 (1982) (cit. on p. 27).
- [27] J. F. Nieves, “Two Photon Decays of Heavy Neutrinos”, *Phys. Rev. D* **28**, 1664 (1983) (cit. on p. 27).

- [28] C. W. Kim and W. P. Lam, “Some remarks on neutrino decay via a Nambu-Goldstone boson”, *Mod. Phys. Lett. A* **5**, 297–299 (1990) (cit. on pp. 27, 28).
- [29] V. D. Barger, J. G. Learned, S. Pakvasa, and T. J. Weiler, “Neutrino decay as an explanation of atmospheric neutrino observations”, *Phys. Rev. Lett.* **82**, 2640–2643 (1999), arXiv:astro-ph/9810121 (cit. on p. 27).
- [30] S. Palomares-Ruiz, S. Pascoli, and T. Schwetz, “Explaining LSND by a decaying sterile neutrino”, *JHEP* **09**, 048 (2005), arXiv:hep-ph/0505216 (cit. on p. 28).
- [31] Z. Moss, M. H. Moulai, C. A. Argüelles, and J. M. Conrad, “Exploring a nonminimal sterile neutrino model involving decay at IceCube”, *Phys. Rev. D* **97**, 055017 (2018), arXiv:1711.05921 [hep-ph] (cit. on p. 28).
- [32] M. Lindner, T. Ohlsson, and W. Winter, “A Combined treatment of neutrino decay and neutrino oscillations”, *Nucl. Phys. B* **607**, 326–354 (2001), arXiv:hep-ph/0103170 (cit. on p. 28).
- [33] A. A. Aguilar-Arevalo et al. (MiniBooNE), “Significant Excess of ElectronLike Events in the MiniBooNE Short-Baseline Neutrino Experiment”, *Phys. Rev. Lett.* **121**, 221801 (2018), arXiv:1805.12028 [hep-ex] (cit. on p. 31).
- [34] A. Diaz, C. A. Argüelles, G. H. Collin, J. M. Conrad, and M. H. Shaevitz, “Where Are We With Light Sterile Neutrinos?”, *Phys. Rept.* **884**, 1–59 (2020), arXiv:1906.00045 [hep-ex] (cit. on pp. 41, 51, 61, 64, 67, 68).
- [35] B. Armbruster et al. (KARMEN), “Upper limits for neutrino oscillations $\bar{\nu}_\mu \rightarrow \bar{\nu}_e$ from muon decay at rest”, *Phys. Rev. D* **65**, 112001 (2002), arXiv:hep-ex/0203021 (cit. on pp. 42, 44).
- [36] P. Adamson et al. (MiniBooNE, MINOS), “Measurement of ν_μ and ν_e Events in an Off-Axis Horn-Focused Neutrino Beam”, *Phys. Rev. Lett.* **102**, 211801 (2009), arXiv:0809.2447 [hep-ex] (cit. on pp. 43, 44).
- [37] P. Astier et al. (NOMAD), “Search for $\nu_\mu \rightarrow \nu_e$ oscillations in the NOMAD experiment”, *Phys. Lett. B* **570**, 19–31 (2003), arXiv:hep-ex/0306037 (cit. on pp. 45, 46).
- [38] J. M. Conrad and M. H. Shaevitz, “Limits on Electron Neutrino Disappearance from the KARMEN and LSND ν_e - Carbon Cross Section Data”, *Phys. Rev. D* **85**, 013017 (2012), arXiv:1106.5552 [hep-ex] (cit. on pp. 45, 48).
- [39] B. E. Bodmann et al. (KARMEN), “Neutrino interactions with carbon: Recent measurements and a new test of electron-neutrino, anti-muon-neutrino universality”, *Phys. Lett. B* **332**, 251–257 (1994) (cit. on p. 45).
- [40] B. Armbruster et al., “KARMEN limits on electron-neutrino \rightarrow tau-neutrino oscillations in two neutrino and three neutrino mixing schemes”, *Phys. Rev. C* **57**, 3414–3424 (1998), arXiv:hep-ex/9801007 (cit. on p. 45).
- [41] L. B. Auerbach et al. (LSND), “Measurements of charged current reactions of nu(e) on 12-C”, *Phys. Rev. C* **64**, 065501 (2001), arXiv:hep-ex/0105068 (cit. on p. 45).
- [42] J. N. Abdurashitov et al., “Measurement of the response of a Ga solar neutrino experiment to neutrinos from an Ar-37 source”, *Phys. Rev. C* **73**, 045805 (2006), arXiv:nucl-ex/0512041 (cit. on p. 48).

- [43] Y. Declais et al., “Search for neutrino oscillations at 15-meters, 40-meters, and 95-meters from a nuclear power reactor at Bugey”, Nucl. Phys. B **434**, 503–534 (1995) (cit. on p. 51).
- [44] G. H. Collin, C. A. Argüelles, J. M. Conrad, and M. H. Shaevitz, “Sterile Neutrino Fits to Short Baseline Data”, Nucl. Phys. B **908**, 354–365 (2016), arXiv:1602.00671 [hep-ph] (cit. on p. 51).
- [45] G. H. Collin, C. A. Argüelles, J. M. Conrad, and M. H. Shaevitz, “First Constraints on the Complete Neutrino Mixing Matrix with a Sterile Neutrino”, Phys. Rev. Lett. **117**, 221801 (2016), arXiv:1607.00011 [hep-ph] (cit. on p. 51).
- [46] S. Vergani, N. W. Kamp, A. Diaz, C. A. Argüelles, J. M. Conrad, M. H. Shaevitz, and M. A. Uchida, “Explaining the MiniBooNE excess through a mixed model of neutrino oscillation and decay”, Phys. Rev. D **104**, 095005 (2021), arXiv:2105.06470 [hep-ph] (cit. on p. 51).
- [47] I. Alekseev et al. (DANSS), “Search for sterile neutrinos at the DANSS experiment”, Phys. Lett. B **787**, 56–63 (2018), arXiv:1804.04046 [hep-ex] (cit. on pp. 51, 52).
- [48] Z. Atif et al. (RENO, NEOS), “Search for sterile neutrino oscillation using RENO and NEOS data”, (2020), arXiv:2011.00896 [hep-ex] (cit. on pp. 52, 53).
- [49] Y. J. Ko et al. (NEOS), “Sterile Neutrino Search at the NEOS Experiment”, Phys. Rev. Lett. **118**, 121802 (2017), arXiv:1610.05134 [hep-ex] (cit. on p. 53).
- [50] M. Andriamirado et al. (PROSPECT), “Improved short-baseline neutrino oscillation search and energy spectrum measurement with the PROSPECT experiment at HFIR”, Phys. Rev. D **103**, 032001 (2021), arXiv:2006.11210 [hep-ex] (cit. on pp. 53, 54).
- [51] H. Almazán et al. (STEREO), “Improved sterile neutrino constraints from the STEREO experiment with 179 days of reactor-on data”, Phys. Rev. D **102**, 052002 (2020), arXiv:1912.06582 [hep-ex] (cit. on p. 55).
- [52] A. P. Serebrov et al., “Search for sterile neutrinos with the Neutrino-4 experiment and measurement results”, Phys. Rev. D **104**, 032003 (2021), arXiv:2005.05301 [hep-ex] (cit. on pp. 55, 56).
- [53] F. Dydak, G. Feldman, C. Guyot, J. Merlo, H.-J. Meyer, J. Rothberg, J. Steinberger, H. Taureg, W. von Rüden, H. Wachsmuth, H. Wahl, J. Wotschack, H. Blümer, P. Buchholz, J. Duda, F. Eisele, K. Kleinknecht, J. Knobloch, B. Pszola, B. Renk, R. Belusevic, B. Falkenburg, T. Flottmann, J. de Groot, C. Geweniger, H. Keilwerth, K. Tittel, P. Debu, A. Para, P. Perez, B. Peyaud, J. Rander, J. Schuller, R. Turlay, H. Abramowicz, and J. Królikowski, “A search for ν_μ oscillations in the Δm^2 range 0.3 – 90 eV²”, Physics Letters B **134**, 281–286 (1984), <https://www.sciencedirect.com/science/article/pii/0370269384906889> (cit. on pp. 56, 58).

- [54] I. E. Stockdale, A. Bodek, F. Borcharding, N. Giokaris, K. Lang, D. Garfinkle, F. S. Merritt, M. Oreglia, P. Reutens, P. S. Auchincloss, R. Blair, C. Haber, M. Ruiz, F. Sciulli, M. H. Shaevitz, W. H. Smith, R. Zhu, R. Coleman, H. E. Fisk, B. Jin, D. Levinthal, W. Marsh, P. A. Rapidis, H. B. White, and D. Yovanovitch, “Limits on muon-neutrino oscillations in the mass range $30 < \Delta m^2 < 1000 \text{ eV}^2/c^4$ ”, *Phys. Rev. Lett.* **52**, 1384–1388 (1984), <https://link.aps.org/doi/10.1103/PhysRevLett.52.1384> (cit. on pp. 58, 59).
- [55] K. B. M. Mahn et al. (SciBooNE, MiniBooNE), “Dual baseline search for muon neutrino disappearance at $0.5\text{eV}^2 < \Delta m^2 < 40\text{eV}^2$ ”, *Phys. Rev. D* **85**, 032007 (2012), [arXiv:1106.5685 \[hep-ex\]](https://arxiv.org/abs/1106.5685) (cit. on pp. 58, 60).
- [56] G. Cheng et al. (MiniBooNE, SciBooNE), “Dual baseline search for muon antineutrino disappearance at $0.1\text{eV}^2 < \Delta m^2 < 100\text{eV}^2$ ”, *Phys. Rev. D* **86**, 052009 (2012), [arXiv:1208.0322 \[hep-ex\]](https://arxiv.org/abs/1208.0322) (cit. on pp. 58, 60, 61).
- [57] A. A. Aguilar-Arevalo et al. (MiniBooNE), “A Search for muon neutrino and antineutrino disappearance in MiniBooNE”, *Phys. Rev. Lett.* **103**, 061802 (2009), [arXiv:0903.2465 \[hep-ex\]](https://arxiv.org/abs/0903.2465) (cit. on p. 61).
- [58] P. Adamson et al. (MINOS), “Search for the disappearance of muon antineutrinos in the NuMI neutrino beam”, *Phys. Rev. D* **84**, 071103 (2011), [arXiv:1108.1509 \[hep-ex\]](https://arxiv.org/abs/1108.1509) (cit. on pp. 59, 62).
- [59] P. Adamson et al. (MINOS), “An improved measurement of muon antineutrino disappearance in MINOS”, *Phys. Rev. Lett.* **108**, 191801 (2012), [arXiv:1202.2772 \[hep-ex\]](https://arxiv.org/abs/1202.2772) (cit. on pp. 59, 62).
- [60] P. Adamson et al. (MINOS), “Search for Sterile Neutrinos Mixing with Muon Neutrinos in MINOS”, *Phys. Rev. Lett.* **117**, 151803 (2016), [arXiv:1607.01176 \[hep-ex\]](https://arxiv.org/abs/1607.01176) (cit. on pp. 59, 62).
- [61] D. Foreman-Mackey, D. W. Hogg, D. Lang, and J. Goodman, “emcee: The MCMC Hammer”, *Publ. Astron. Soc. Pac.* **125**, 306–312 (2013), [arXiv:1202.3665 \[astro-ph.IM\]](https://arxiv.org/abs/1202.3665) (cit. on p. 61).
- [62] D. Foreman-Mackey, “Corner.py: scatterplot matrices in python”, *The Journal of Open Source Software* **1**, 24 (2016), <https://doi.org/10.21105/joss.00024> (cit. on p. 62).
- [63] M. Maltoni and T. Schwetz, “Testing the statistical compatibility of independent data sets”, *Phys. Rev. D* **68**, 033020 (2003), [arXiv:hep-ph/0304176](https://arxiv.org/abs/hep-ph/0304176) (cit. on p. 64).
- [64] M. G. Aartsen et al. (IceCube), “The IceCube Neutrino Observatory: Instrumentation and Online Systems”, *JINST* **12**, P03012 (2017), [arXiv:1612.05093 \[astro-ph.IM\]](https://arxiv.org/abs/1612.05093) (cit. on p. 77).
- [65] C. A. Argüelles, J. Salvado, and C. N. Weaver, “nuSQuIDS: A toolbox for neutrino propagation”, *Comput. Phys. Commun.* **277**, 108346 (2022), [arXiv:2112.13804 \[hep-ph\]](https://arxiv.org/abs/2112.13804) (cit. on p. 79).

- [66] M. G. Aartsen et al. (IceCube), “eV-Scale Sterile Neutrino Search Using Eight Years of Atmospheric Muon Neutrino Data from the IceCube Neutrino Observatory”, *Phys. Rev. Lett.* **125**, 141801 (2020), arXiv:2005.12942 [hep-ex] (cit. on pp. 79, 80, 82, 84, 106).
- [67] M. G. Aartsen et al. (IceCube), “Searching for eV-scale sterile neutrinos with eight years of atmospheric neutrinos at the IceCube Neutrino Telescope”, *Phys. Rev. D* **102**, 052009 (2020), arXiv:2005.12943 [hep-ex] (cit. on pp. 79–82, 84, 92, 94, 95, 106).
- [68] M. G. Aartsen et al. (IceCube), “Evidence for Astrophysical Muon Neutrinos from the Northern Sky with IceCube”, *Phys. Rev. Lett.* **115**, 081102 (2015), arXiv:1507.04005 [astro-ph.HE] (cit. on pp. 80, 92).
- [69] J. A. Formaggio and G. P. Zeller, “From eV to EeV: Neutrino Cross Sections Across Energy Scales”, *Rev. Mod. Phys.* **84**, 1307–1341 (2012), arXiv:1305.7513 [hep-ex] (cit. on p. 81).
- [70] J. M. Conrad, M. H. Shaevitz, and T. Bolton, “Precision measurements with high-energy neutrino beams”, *Rev. Mod. Phys.* **70**, 1341–1392 (1998), arXiv:hep-ex/9707015 (cit. on p. 82).
- [71] D. E. Groom, N. V. Mokhov, and S. I. Striganov, “Muon stopping power and range tables 10-MeV to 100-TeV”, *Atom. Data Nucl. Data Tabl.* **78**, 183–356 (2001) (cit. on p. 81).
- [72] S. Razzaque and A. Y. Smirnov, “Searching for sterile neutrinos in ice”, *JHEP* **07**, 084 (2011), arXiv:1104.1390 [hep-ph] (cit. on p. 85).
- [73] A. Esmaili, F. Halzen, and O. L. G. Peres, “Constraining Sterile Neutrinos with AMANDA and IceCube Atmospheric Neutrino Data”, *JCAP* **11**, 041 (2012), arXiv:1206.6903 [hep-ph] (cit. on p. 85).
- [74] P. Adamson et al. (MINOS+), “Search for sterile neutrinos in MINOS and MINOS+ using a two-detector fit”, *Phys. Rev. Lett.* **122**, 091803 (2019), arXiv:1710.06488 [hep-ex] (cit. on p. 85).
- [75] R. L. Workman et al. (Particle Data Group), “Review of Particle Physics”, *PTEP* **2022**, 083C01 (2022) (cit. on pp. 87, 89).
- [76] A. Fedynitch, R. Engel, T. K. Gaisser, F. Riehn, and T. Stanev, “Calculation of conventional and prompt lepton fluxes at very high energy”, *EPJ Web Conf.* **99**, edited by D. Berge, A. de Roeck, M. Mangano, and B. Pattison, 08001 (2015), arXiv:1503.00544 [hep-ph] (cit. on p. 88).
- [77] T. K. Gaisser, “Spectrum of cosmic-ray nucleons, kaon production, and the atmospheric muon charge ratio”, *Astropart. Phys.* **35**, 801–806 (2012), arXiv:1111.6675 [astro-ph.HE] (cit. on p. 88).
- [78] F. Riehn, H. P. Dembinski, R. Engel, A. Fedynitch, T. K. Gaisser, and T. Stanev, “The hadronic interaction model SIBYLL 2.3c and Feynman scaling”, *PoS ICRC2017*, 301 (2018), arXiv:1709.07227 [hep-ph] (cit. on p. 88).
- [79] Jet Propulsion Laboratory, “AIRS/AMSU/HSB Version 6 Level 3 Product User Guide”, Version 1.2 (2014) (cit. on pp. 88, 96).

- [80] A. Bhattacharya, R. Enberg, M. H. Reno, I. Sarcevic, and A. Stasto, “Perturbative charm production and the prompt atmospheric neutrino flux in light of RHIC and LHC”, *JHEP* **06**, 110 (2015), arXiv:1502.01076 [[hep-ph](#)] (cit. on p. 88).
- [81] A. M. Dziewonski and D. L. Anderson, “Preliminary reference earth model”, *Phys. Earth Planet. Interiors* **25**, 297–356 (1981) (cit. on p. 88).
- [82] R. Abbasi et al. (IceCube), “LeptonInjector and LeptonWeighter: A neutrino event generator and weighter for neutrino observatories”, *Comput. Phys. Commun.* **266**, 108018 (2021), arXiv:2012.10449 [[physics.comp-ph](#)] (cit. on p. 89).
- [83] J. H. Koehne, K. Frantzen, M. Schmitz, T. Fuchs, W. Rhode, D. Chirkin, and J. Becker Tjus, “PROPOSAL: A tool for propagation of charged leptons”, *Comput. Phys. Commun.* **184**, 2070–2090 (2013) (cit. on p. 89).
- [84] P. Lipari, “Lepton spectra in the earth’s atmosphere”, *Astropart. Phys.* **1**, 195–227 (1993) (cit. on pp. 89, 91).
- [85] M. G. Aartsen et al. (IceCube), “Energy Reconstruction Methods in the IceCube Neutrino Telescope”, *JINST* **9**, P03009 (2014), arXiv:1311.4767 [[physics.ins-det](#)] (cit. on p. 92).
- [86] C. Weaver, “Evidence for astrophysical muon neutrinos from the northern sky”, PhD thesis (Wisconsin U., Madison, Wisconsin U., Madison, 2015) (cit. on p. 92).
- [87] M. G. Aartsen et al. (IceCube), “Characterization of the Atmospheric Muon Flux in IceCube”, *Astropart. Phys.* **78**, 1–27 (2016), arXiv:1506.07981 [[astro-ph.HE](#)] (cit. on p. 92).
- [88] R. Abbasi et al. (IceCube), “First Search for Unstable Sterile Neutrinos with the IceCube Neutrino Observatory”, (2022), arXiv:2204.00612 [[hep-ex](#)] (cit. on p. 94).
- [89] S. N. G. Axani, “Sterile Neutrino Searches at the IceCube Neutrino Observatory”, PhD thesis (MIT, 2019), arXiv:2003.02796 [[hep-ex](#)] (cit. on p. 95).
- [90] G. D. Barr, T. K. Gaisser, S. Robbins, and T. Stanev, “Uncertainties in Atmospheric Neutrino Fluxes”, *Phys. Rev. D* **74**, 094009 (2006), arXiv:[astro-ph/0611266](#) (cit. on pp. 95, 96).
- [91] M. G. Aartsen et al. (IceCube), “Efficient propagation of systematic uncertainties from calibration to analysis with the SnowStorm method in IceCube”, *JCAP* **10**, 048 (2019), arXiv:1909.01530 [[hep-ex](#)] (cit. on p. 96).
- [92] C. A. Argüelles, A. Schneider, and T. Yuan, “A binned likelihood for stochastic models”, *JHEP* **06**, 030 (2019), arXiv:1901.04645 [[physics.data-an](#)] (cit. on p. 100).
- [93] C. Zhu, R. H. Byrd, P. Lu, and J. Nocedal, “Algorithm 778: l-bfgs-b: fortran subroutines for large-scale bound-constrained optimization”, *ACM Trans. Math. Softw.* **23**, 550–560 (1997), <https://doi.org/10.1145/279232.279236> (cit. on p. 100).
- [94] H. Jeffreys, *The Theory of Probability*, Oxford Classic Texts in the Physical Sciences (1939) (cit. on p. 101).

- [95] G. Cowan, K. Cranmer, E. Gross, and O. Vitells, “Asymptotic formulae for likelihood-based tests of new physics”, *Eur. Phys. J. C* **71**, [Erratum: *Eur.Phys.J.C* 73, 2501 (2013)], 1554 (2011), arXiv:1007.1727 [[physics.data-an](#)] (cit. on p. 102).
- [96] M. Thomson, *Modern Particle Physics* (Cambridge University Press, New York, 2013) (cit. on p. 125).